The Controlled Crystallisation

of High Strength Leucite Glass-Ceramics

By

Xiaohui Chen

A thesis submitted in fulfilment of the requirements for the degree of Doctor of Philosophy in

Institute of Dentistry, Queen Mary University of London

Institute of Dentistry, Bart's and the London School of Medicine and Dentistry,

Queen Mary University of London

June 2009

ABSTRACT

Leucite glass-ceramics are widely used in Dentistry, and show favourable aesthetics. Undesirable brittle failure however, is associated with uneven leucite crystal distribution, and the thermal mismatch between the glass matrix and larger leucite crystals. This thesis focuses on glass design and leucite microstructural control in order to produce high strength, aesthetic, reliable and processable leucite glass-ceramics. Glasses were designed using Appen Factors to control the thermal expansion coefficient, density and refractive index. Zirconia and niobium oxide were also introduced in to the glasses to investigate their nucleating effects on leucite crystallisation. Glasses were characterised using Dilatometry, Light Microscopy, Differential Scanning Calorimetry and High Temperature X-ray Diffraction. A series of two-step crystallisation heat treatments on all glasses were carried out to control the leucite crystal size, morphology and volume fraction. The biaxial flexural strength (BFS) of the experimental and commercial control IPS Empress Esthetic glass-ceramic was measured using the ball on ring test. Appen Factors were proven as a useful tool for glass design. Phase crystallisation and the crystallisation mechanisms in the leucite glass-ceramic system were dependant on the glass composition. Leucite crystallisation without the presence of titanium dioxide was possible. Leucite glass-ceramics with evenly distributed fine tetragonal leucite crystals (Mean (SD) 0.15 (0.09) μm^2) were achieved by ball milling of the parent glass followed by optimised two-step heat treatments. The glass-ceramic showed minimal matrix microcracking and a high BFS value of 252.4 (38.7) MPa and m value of 8.7, which is statistically higher than the IPS Empress Esthetics glass-ceramic with a BFS of 165.5 (30.6) MPa and m value of 6.3. Leucite crystal size, morphology and distribution depended on the parent glass composition and the thermal heat treatment. Highly crystallised leucite microstructures with orientated fibres, spheres and rosette shaped domains were synthesised based on different glass compositions, and showed a high BFS of 212.2 (28.2) MPa and m value of 8.5. High strength, reliable and translucent leucite glass-ceramics were successfully heat extruded to produce dental restorations.

ACKNOWLEDGEMENTS

I would like to thank my first supervisor Dr. M.J. Cattell for his first rate supervision and inspiration, without his selfless advice and guidance, the project would not have happened. I am also grateful for his tremendous help and advice besides research. Secondly, I would like to acknowledge my second supervisor Prof. R. Hill for his advice on Appen Factors, glass design, glass making, thermal analysis etc, his encouragement and discussion on the project.

I would like to thank Dr. T.C. Chadwick from Den-Mat Corporation for his discussion, suggestions and his industrial glass-ceramic fabrication expertise. I would to thank Dr. M. Philips in the British Standard Institution for the training provided on dilatometry, Dr. Z. Luklinska, Mr. M. Willis and Dr. K.M.Y. P'Ng in the School of Engineering and Materials Science for their expertise on microscopy, Dr. R.M. Williams in the Department of Biophysics in Relation to Dentistry for his help on X-ray diffraction analysis and structural refinement. Special appreciation also goes to Prof. W.S Marcenes for his advice on statistical analysis.

I am very grateful to the academic and technical staffs in the Institution of Dentistry for cultivating a friendly research environment. In particular, I would also like to express my acknowledgements to Prof. J.C. Elliott, Prof. D. Samarawickrama, Dr. M.P. Patel, Dr. S. Parker, Dr. P. Anderson, Mr. E.V. Greenidge, Mrs. M.R.M Woolcott, Mr. J. Cano and my colleague Mr. A. Theocharopoulos for their support. I would also like to express my acknowledgements to Ivoclar Vivadent, Dentsply and Jeneric Pentron in supplying materials for the project. Special thanks go to Den-Mat Corporation for their funding sponsored.

Finally, I will take this opportunity to thank my parents, sister and my boyfriend Mr. X. Cao for their love, continuous support and endless care, which makes me strong and confident.

LIST OF CONTENTS

LIST OF FIGURES

LIST OF TABLES

1 INTRODUCTION AND HISTORY

1.1 Introduction

Human permanent teeth are generally lost for the reasons of dental caries and periodontal disease (Guttorm et al., 1952). This lost tooth structure is normally replaced by a suitable dental material in order to fill the space, keep the teeth in the correct occlusal position and maintain oral health and confidence. Dental carries removal can produces the loss of sound enamel and dentine to give access to allow the removal of subsurface carries (Smith, 1986). The remaining tooth is next shaped (prepared) so that it can receive a dental restoration to replace the lost tooth structure. Tooth structure is a functionally graded material and is required to bear high loads and contact stresses with maximum biting forces up to 1000 N (He and Swain, 2008). Materials used to produce dental restorations therefore require high modulus, toughness and flexural strength to avoid failure (Kelly et al., 1996). Materials used to produce dental restorations include gold alloys, dental polymer composites and dental glass-ceramics (Anusavice, 2003). Leucite glass-ceramics are widely used in dentistry to produce aesthetic dental crown, bridge, inlay, onlay and veneer restorations. Various manufacturing methods such as sintering to metals, heat extrusion and computer aided design and machining are employed. However, all ceramic restorations are susceptible to brittle fracture and wear of the opposing teeth (Kelly et al., 1996). An ideal dental glass-ceramic material should have a high strength and reliability, a similar wear rate to human enamel and good chemical stability and aesthetics. Therefore, the development of leucite glass-ceramics which can fulfil low wear, high flexural strength, toughness and good aesthetics will be necessary and useful.

Leucite is a potassium alumino-silicate mineral that has corner linked four and six membered rings of SiO_4 tetrahedra, forming the structure of a (Si, Al)-O framework silicate (Deer et al., 1966). It is cubic at high temperature with low thermal expansion 11.7 - 12.8 x 10^{-6}/K (Hermansson and Carlsson, 1976) and tetragonal at low temperature with a relatively high thermal expansion around 20 - 25 x 10^{-6}/K (Rouf et al., 1978). A phase transformation occurs at around 605 - 625ºC (Mackert, 1988) and leads to a reversible 1.2% volume

change (Mackert and Evans, 1993) and crystal twinning (Palmer et al., 1988). Careful control of the difference in thermal expansion between the tetragonal leucite crystals and the glass matrix can be utilised to develop tangential compressive stresses around the crystals which were considered responsible for the significant strengthening in leucite glass-ceramics (Denry et al., 1996).

Leucite glass-ceramics can be produced by the controlled heating of a glass to nucleate and precipitate crystals in the glass matrix. Additional nucleating agents, glass composition and heat treatment influence the crystallisation (Rouf et al., 1978). Cubic leucite transforms to tetragonal during cooling. The mismatch of thermal expansion between the tetragonal leucite and the glass matrix (8 - 10 x 10^{-6}/K) (Vergano et al., 1967), leads to microcracking around large non uniform leucite crystals and clusters (Mackert and Williams, 1996), which have been linked to reduced strength of the glass-ceramics (Cattell et al., 1999). Microcracking can be minimised by a reduction in the mean leucite particle diameter to less than 4 μm (Mackert et al., 2001). The leucite crystal size therefore becomes a main concern, and the control of nucleation and crystallisation of leucite crystals is considered to influence the properties of the leucite glass-ceramics (Cattell et al., 2001).

Rouf et al., (1978) crystallised fine tetragonal leucite crystals (0.1 - 1 μm) in aluminosilicate glasses, whose modulus of rupture values were 200 - 300 MPa, but the high viscosity and opacity inhibit the manufacture and aesthetic applications. Ball milling followed by crystallisation heat treatments have been used to reduce the leucite crystal size and control its distribution (Cattell et al., 2005). A number of studies have shown that fine evenly distributed leucite crystals in the glass matrix may produce less microcracking and give improvement of flexural strength (Shareef et al., 1994, Cattell et al., 1997a). Controlled nucleation and crystallisation of these tetragonal leucite glass-ceramics by using ball milling and controlled heat treatments were carried out in this thesis to produce nano-sized leucite glass-ceramics, and to enhance their mechanical properties. This project also proposed modification of glass compositions to yield changes to their thermal properties and their relationship with the leucite crystals as a route to further increases in mechanical properties.

Appen Factors have been used in the literature to predict glass thermal expansion, density and refractive index and agree well with measured values (Park et al., 2008). It was decided to use this approach in this thesis to design new glasses for the production of leucite glass-ceramics, since thermal expansion of the residual glass and leucite content play important roles in the leucite glass-ceramic strength (Denry et al., 1996).

Therefore, the aims of the thesis were to design novel aluminosilicate glasses with tailored properties including thermal expansion coefficient, refractive index and density using Appen Factors. Explore the crystallisation kinetics of the experimental aluminosilicate glass formulations and control the leucite crystal size, morphology and volume fraction to produce high strength leucite glass-ceramics with controlled microstructures.

1.2 History and Background

Dental prostheses can be traced back to before Christianity and the earliest ceramic materials are thought to have been developed by Chinese ceramists as early as 1000AD. The first successful porcelain dentures were fabricated by Alexis Duchateau and Nicholas Dudois de Chemant in 1774, and the technique was presented by Duchateau in 1776 (Engelmeier, 2003). Porcelain single teeth which contained embedded platinum foils were introduced by Giuseppangelo Fonzi in 1808 (Kurdvk, 1999). Glass inlays were introduced by Herbst in 1882 with crushed glass frit fired in moulds made of plaster and asbestos (Jones, 1985). The first ceramic crown was introduced to Dentistry by Dr. Charles Land and patented in 1903 (Craig and Powers, 2002, Sukumaran and Bharadwaj, 2006). These crowns had excellent aesthetics, however, the low flexural strength led to unforeseen failure (Craig and Powers, 2002, Anusavice, 2003). Therefore, the feldspathic porcelains were not reliable without a high strength core.

The development of aluminous core and veneer porcelains was first introduced by adding crystalline alumina particles into feldspathic glass (McLean and Hughes, 1965). The aluminous porcelain was nearly twice as strong as dental porcelain, however, the opacity

and potential shrinkage need to be overcome. Thus the possibility of using glass-ceramics for dental applications was investigated to improve the dimensional accuracy, mechanical properties and aesthetic properties (MacCulloch, 1968).

Porcelain fused to metal (metal-ceramic) technology was first described by Brecker (1956), and patented by Weinstein *et al.,* (1962). McLean and Sced (1976) introduced a technique of fusing a platinum foil to the fit surface of aluminous porcelain in order to strengthen it. Gold coated platinum (Hopkins, 1981), palladium foil (Piddock *et al.*, 1986) and gold foil reinforced crowns were introduced (Hummert *et al.*, 1991) subsequently.

Cast glass converted to mica glass-ceramic (Adair and Grossman, 1984) and castable apatite ceramic (Hobo and Iwata, 1985) were used for restorations. A leucite-reinforced glass-ceramic material IPS Empress (Ivoclar Vivadent, Schaan, Liechtenstein) was first described by Wohlwend and Schärer (1990). It is placed into a pressing furnace, heated and then extruded into a mould to form dental restorations. The mechanical strength limits the material from the application of dental bridges (Höland et al., 2000). Lithium disilicate glass-ceramic (Empress 2) was introduced to achieve higher flexural strength (Höland et al., 2000) and fracture toughness (Thompson *et al.*, 1995). It is recommended for the fabrication of crowns and bridges up to second premolar, but requires a special connector design (Höland et al., 2000). In-ceram Alumina was developed by Sandoun. A high alumina (85%) powder slurry is applied to a porous refractory and sintered, then infiltrated with glass in a second firing process to produce a high strength core material (Qualtrough and Piddock, 1997). This is veneered with thermally compatible porcelain. Zirconia ceramics were also used as core materials and demonstrated higher strength (Chong *et al.*, 2002), however the zirconia core is more opaque (Heffernan *et al.*, 2002) and need to be veneered with porcelain to achieve aesthetics. Computer-assisted design and manufacturing (CAD/CAM) technology was introduced in Europe in 1980s. It consists of digital image generation, data acquisition, computer assisted milling and tooling systems (Yin *et al.,* 2005). Complex shapes of ceramic prostheses can be completed within a couple of hours by CAD/CAM using alumina, zirconia and glass-ceramic materials.

1.3 Structure of the Thesis

This thesis is organised in a classical way. Chapter 1 gives the history and background of dental ceramic restorative materials, and a general introduction about leucite glass-ceramics. Chapter 2 critically reviews the fundamental theory on glass, nucleation, glass-ceramics, mechanical milling, glass-ceramic processing and the techniques used during this study. Chapter 3 describes the materials and methods and Chapter 4 presents the experimental results according to different techniques used. Discussion on the experimental results and the relationship with the literature is given in Chapter 5. Conclusions of the thesis are given in Chapter 6, followed by the future work in Chapter 7. References used throughout the thesis are listed out in Chapter 8 and the Appendix is Chapter 9. Some of the work in this thesis is presented in the form of a US patent in Chapter 10.

2 LITERATURE REVIEW

2.1 Glasses

Glasses are inorganic product of fusion that have been cooled to a rigid condition without crystallising, according to American Society for Testing Materials (ASTM, 1941). During cooling, no discontinuous volume change is found at any temperature but a progressive increase in the viscosity is obtained. Although certain organic substances such as glucose or glycerol can undergo supercooling to form glasses, we are mainly concerned with the inorganic oxide glasses.

2.1.1 Glass Transition

When cooling a liquid or melt from high temperature, if crystallisation occurs, the liquid will freeze into a crystalline solid accompanied with a sudden decrease in volume at the solidification point (T_m), and then further thermal contraction (Fig. 2.1). The crystallisation phase generally is more stable than the glassy state. For some materials, crystallisation can be avoided if the cooling is sufficiently fast (Turnbull, 1969). The liquid continues as a supercooled liquid with a continuous decrease in volume and increase in viscosity. At a lower temperature the viscosity increases up to 10^{12} Pa·s, where the liquid behaves as a rigid glass, and the slope of the volume-temperature curve decreases close to that of the crystalline solid (Jones, 1956). The temperature is known as the glass transformation temperature (T_g), and is influenced by the cooling rate. Rapid cooling shifts the glass transition towards higher temperatures, resulting in higher specific volume, higher conductivity, lower refractive index and lower viscosity (Zarzycki, 1991). Whereas, slow cooling entitles the configurationally shrinkage to keep pace with the cooling, and leads to lower T_g and lower specific volume. Typically, the dependence of T_g upon cooling rate is relatively weak, about 3 - 5ºC with change in cooling rate at the same magnitude (Ediger et al., 1996).

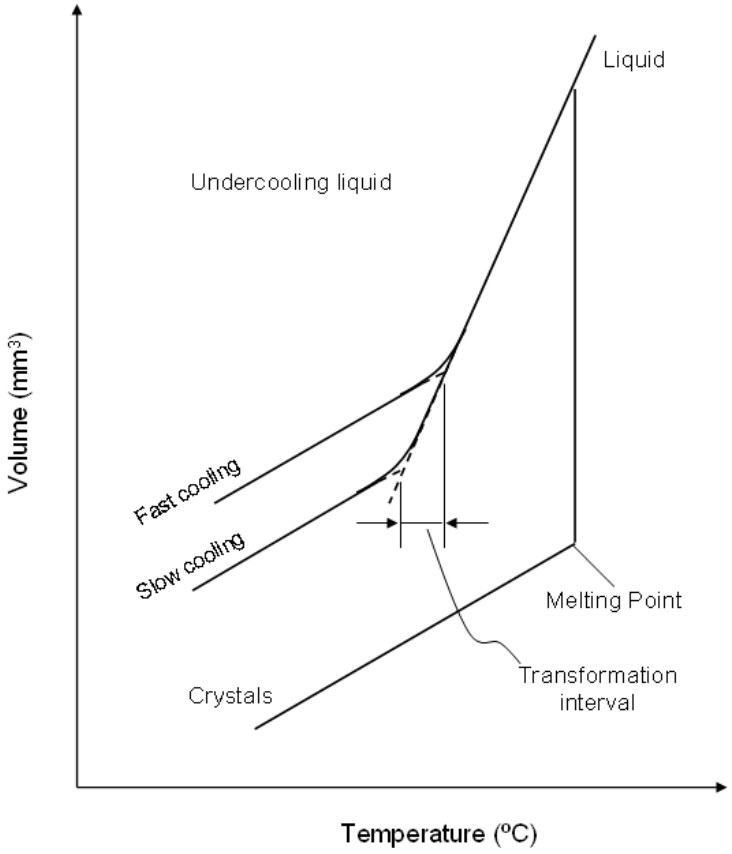

Fig. 2.1: Glass transition temperature (T_g) and its relationship with cooling rate (Jones, 1956).

2.1.2 Glass Structure

Different hypotheses on glass structure and the condition for glass formation were well developed. Goldschmidt (1926) suggested that the ability of an oxide to form a glass might be related to the size of cation and how the cation is surrounded. Based on simple oxides with stoichiometric formula A_mO_n, he advanced the empirical rules for glass formation, where the cation ionic radius and oxygen ionic radius ratio (r_A / r_O) fits between 0.2 and 0.4. The hypotheses imply a tetrahedral coordination of cation A, where the central cation (A) is surrounded by four oxygens at the corners of a tetrahedron. However, beryllia (BeO) whose radius ratio is very close to SiO_2, about 0.3, can never be prepared in the vitreous form (Zachariasen, 1932). Therefore, the ratio proposal is inadequate as the criterion for glass formation.

Zachariasen (1932) reconsidered the problem and established a random network theory of glass structure, which was reinforced by Warren's X-ray Diffraction study (1933). According to the random network theory, the atoms in the glass must be linked in a three-dimensional network where the interatomic forces and cation coordination number is essentially similar to its corresponding crystal. Different from the crystalline materials which have regular lattice structures with long-range order, the glass structure is a random network. A number of rules for the formation of an oxide glass were suggested (Zachariasen, 1932):

1. The coordinate number oxygen around the cation atom must be small.
2. An oxygen ion can not be shared by more than two cations.
3. The oxygen polyhedron must share only corners with each other, not on edges or faces.
4. At least three corners of each polyhedron must be shared with other polyhedra.

Many oxides both triangular (B_2O_3) and tetrahedral arrangements (SiO_2, P_2O_3, GeO_2, As_2O_5) satisfy the above rules. Those oxides which have the ability to build up a continuous three dimensional random network are designated as network formers. They can exist independently in the glassy state or in combination with some other oxides (Vargin, 1967). Glass formation becomes complex when more oxides get involved. Zachariasen (1932) modified the rules, for a complex oxide glass formation:

1. A sufficient percentage of cations surrounded by tetrahedral or oxygen triangles are present.
2. The tetrahedra or triangles should share corners only.
3. Oxygen atoms can only be bonded to two of these cations.

2.1.3 Glass Modifiers

Glass modifying oxides normally are incapable of building up a continuous network, but weaken the bonds within the glass network (Sun, 1947). The introduction of glass modifiers in to vitreous SiO_2, for example Na_2O, causes the rupture of Si-O-Si bonds in the continuous SiO_4 tetrahedral network. The bridging oxygen between two SiO_4 tetrahedra is replaced by two non-bridging oxygens, one of which is contributed by Na_2O. The Na^+ cations fill the hole or the interstices in the random network and balance the two negative charges on the non-bridging oxygen, so as to achieve electrical neutrality (Fig. 2.2). The increased asymmetry of the glass network leads to a reduction in the viscosity of the glass, and increase in the thermal expansion ($\alpha_{(T_0-T)}$). The Si-O-Si bridge rupture mechanism also applies to other alkali metal oxides and alkali earth metal oxides. It is found that the glass thermal expansion and room temperature glass density increase with alkali oxide concentration in binary silicate glasses (Shermer, 1956). The thermal expansion change also increases with the size of alkali cation (Shartsis et al., 1952, Shelby, 1976). Alkali metal oxides are used in dental glass-ceramics to modify the thermal expansion, glass transition temperature (T_g) and viscosity for suitable dental restoration applications.

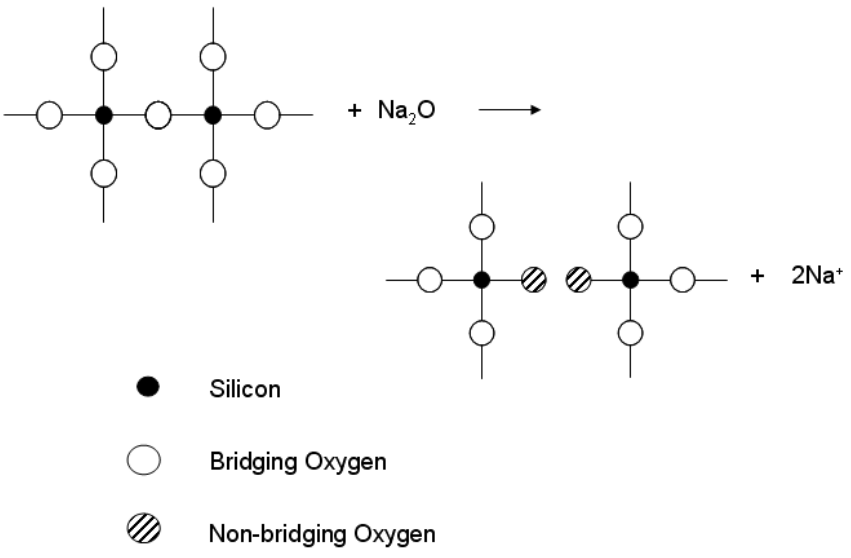

Fig. 2.2: Schematic of network modifier (Sun, 1947).

2.1.4 Intermediate Oxides

Certain oxides such as alumina are not capable to form glass networks themselves, however, depending on the glass composition, they can take part in the glass network or work as modifiers. This type of oxides is designated as intermediate oxides. As a typical intermediate oxide, aluminium ions in the alumina structure can be four or six coordinated with oxygen to form tetrahedral AlO_4 or octahedral AlO_6 groups, the tetrahedral AlO_4 group can replace the SiO_4 tetrahedron in glass (Day and Rindone, 1962). In order to achieve electroneutrality, an additional unit positive charge is required to balance the excess negative charge on the AlO_4 tetrahedron (Fig. 2.3). Thus, each molecule of aluminium oxide present in the glass requires the presence of one molecule of alkali oxide. This type of structural arrangement is widely recognised in many dental aluminosilicate glasses.

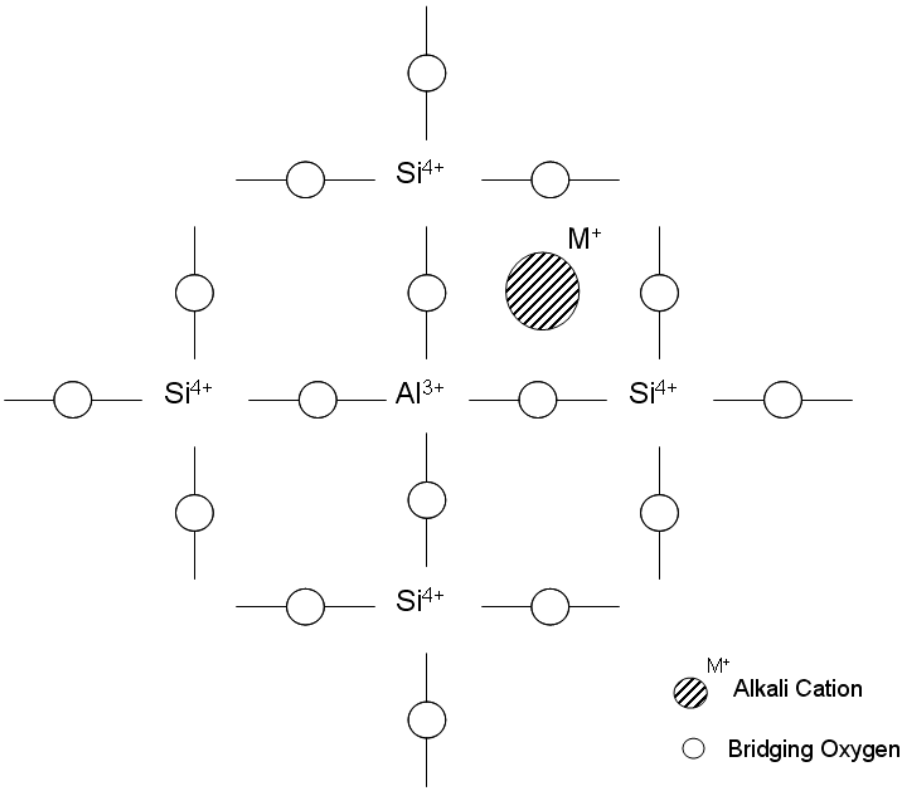

Fig. 2.3: Aluminium in a silicate network (Zarzycki, 1991).

2.1.5 Bonding of Oxides

Glass formation involves rupture of certain bonds and atomic rearrangement. The chemical bonding between the cation and the oxygen ion therefore plays an important role in glass formation. Sun (1947) studied the single bond energies from the heat of glass formation, and showed that the glass forming tendency of an oxide is directly related to the strength of bonds between the metal atoms and oxygen. He found that glass formers have strong bonds which link the atoms together to form a strong three-dimension network, and their bond strengths are above 334.72 kJ/mol. Modifying ions have bond strengths below 251.04 kJ/mol, and the intermediates have bond strengths between 251.04 and 334.72 kJ/mol. Nonetheless, the criterion is not without exception. Carbon dioxide (CO_2) has a single C-O bond strength of 502.08 kJ/mol, but does not form glass due to the weak intermolecular van der Waals forces. Rawson (1956) proposed the possibility of breaking bonds at melting temperature relies on both the bond strength and the available thermal energy indicated by melting temperature. He improved Sun's criterion by relating the glass formation in terms of the ratio of single bond energies and the melting point. Unfortunately, there are still numerous exceptions to this theory.

The interacting force (K) between cations and anions during solidification was studied. Field strength (F) was introduced to characterise the ability of a cation to form covalent bonds (Dietzel, 1942). According to Coulomb's law, the interacting force K:

$$K = \frac{Z_c Z_a e^2}{(r_c + r_a)^2} \tag{2.1}$$

Where Z_c and Z_a are the valences of cation and anion, e is the elementary charge, r_c and r_a are the ionic radii of cation and anion respectively. The field strength of a cation can be expressed as:

$$F = Z_c / a^2 \quad (2.2)$$

Where a is the distance between ions ($a = r_c + r_a$), therefore, higher field strength cations usually have a relatively small size and high valence. The field strength can be used as a guideline to estimate the category of cations. Cations with field strength between 0.1 and 0.4 work as network modifiers, between 0.5 and 1.0 behave as intermediates, whereas those with field strength larger than 1.4 are considered as network formers (Vogel, 1985, Vargin, 1967). However, the field strength criterion is based on the hypothesis where ions behave as rigid spheres. Exceptions were suggested when symmetric configurations are formed (Uhlmann and Yinnon, 1983).

Pauling (1932) suggested the properties of bonding between two atoms are determined by the difference in their electronegativity. Different criterion for glass formation based on electronegativity was advanced by Stanworth (1946), where network formers are suggested to have electronegativities between 1.8 eV and 2.2 eV, whereas network modifiers have electronegativities less than 1 eV.

All these criteria have been proven as useful tools to predict the possibility of glass formation and the structure property relationships for glass. However, they are limited within the field of oxides, and have exceptions respectively. According to different criterions, the relative ranking of glass forming oxide differs (Sun, 1947, Dietzel, 1942, Stanworth, 1971). Therefore, they may not be entirely reliable for the prediction of glass formation.

2.1.6 Relationship between Glass Properties and Glass Composition

Glass properties including thermal expansion, glass transition (T_g), density and refractive index (R.I.) have a relationship with its constituent parts. Different empirical methods (Winkelmann and Schott, 1894, Appen, 1956, English and Turner, 1927, Huggins and Sun, 1943, Takahashi, 1953, Priven, 1986) were formulated based on the hypotheses that glass properties are simply a linear function of composition. The glass properties can therefore be

calculated:

$$X = \alpha_1 p_1 + \alpha_2 p_2 + \cdots + \alpha_n p_n = \sum_{i=1}^{n} \alpha_i p_i \qquad (2.3)$$

where X represents the properties of glass, α_i is the corresponding characteristic factor of each oxide to the glass, and p_i represents the concentration of the individual oxide. According to the way the oxide concentration p_i is expressed, these models can be ranked in different categories. The methods by Winkelmann and Schotts (1894), Huggins and Sun (1943), English and Turner (1927) are based on weight percentage, which allows straight forward calculation of the oxide glass batch. Appen (1956) expressed the oxide concentration in mole percentage, which gives the access to easily link the glass properties with the glass structure. Considering the compositional dependent properties of glass are not quite linear over a wide compositional range, he first introduced partial coefficients to modify the oxide characteristic factors according to a specific compositional range. Higher accuracy was achieved, and the idea was widely accepted by other scientists. The volume based method was first suggested by Demkina (1960), which simplifies the form of property concentration dependences and shows higher accuracy for certain glass composition (Priven, 1988). Priven (2004) proposed a new general method for calculating the properties of oxide glass by replacing the thermodynamic characteristics with empirical parameters, which allows the application of wider composition ranges. Systematic comparisons of these methods were not available until the development of the experimental based glass properties database MDL Sciglass. A comparison of different methods on different glass properties were carried out with the assistance of the MDL Sciglass information system and the methods by Appen and Priven were proven to be the most promising ones (Priven and Mazurin, 2003, Priven, 2004). Calculation using Appen Factors is considered as one of the best methods for the prediction of silicate glass properties, when the silica content is over 50% (Scholze and Lakin, 1991, Priven and Mazurin, 2003). However, it only covers a significantly narrow compositional area (Priven, 2004). The Appen Factors given in Table

9.1 in Appendix were used as a guideline to modify the glass compositions and make predictions of the glass properties in this study.

2.2 The Mechanism of Crystallisation

Crystallisation is a process by which the regular lattices of a crystal with long range order are generated from a less well-ordered liquid (McMillan, 1979). Crystallisation of glass consists of nucleation and subsequent crystal growth. Nucleation involves the formation of embryos of longer range atomic order than those in the liquid phase. These embryos need to achieve a critical size in order to grow spontaneously into stable nuclei. Nucleation can be homogeneous or heterogeneous.

2.2.1 Homogeneous Nucleation

Nucleation from a homogeneous phase is called homogeneous nucleation (Kingery et al., 1976). Embryos are randomly generated throughout the liquid phase due to local thermal fluctuations in the liquid structure. The formation of nuclei requires the formation of an interface between the two phases, therefore, an increase in free energy is required to overcome the nucleation barrier.

In a given supercooled liquid system, during nucleation, there are two contributions to the free energy change. One arises from the formation of the interface between the embryo and the liquid phase which leads to an increase of the interfacial free energy, and another from the rearrangement of the atoms within the embryo, which brings in a reduction of the volume free energy. The free energy change ΔG for a spherical embryo of radius r is given by:

$$\Delta G = -\frac{4}{3}\pi r^3 \Delta G_v + 4\pi r^2 \gamma_{SL} \qquad (2.4)$$

Where ΔG_v is the volume free energy change due to the phase transformation from liquid to solid and γ_{SL} is the solid/liquid interfacial free energy per unit area. The free energy

increase due to the elastic strains arising from the volume change during the melting process is negligible (Kingery et al., 1976), which has not been taken into account in Equation (2.4). The interfacial energy term ($4\pi r^2\gamma_{SL}$) in Equation (2.4) predominates for very small embryos, and results in unstable embryos. As the size of embryos increase, the interfacial energy becomes a smaller fraction of the total energy change. Once the radius has its critical value r^*, the volume free energy term ($-\frac{4}{3}\pi r^3\Delta G_v$) becomes predominant and further growth leads to an increased reduction of the overall free energy and produces a more stable system (Fig. 2.4). The free energy change has its maximum value at r^*, where embryos can be termed as nuclei. The critical radius r^* can be derived by differentiating Equation (2.5):

$$r^* = 2\gamma_{SL} / \Delta G_v \tag{2.5}$$

Embryos which have a radius less than the critical radius r^* are called subcritical embryos, those of radius r^* and larger are named critical and supercritical nuclei (Kingery et al., 1976). Critical nuclei can either indefinitely grow larger or dissolve in the liquid phase, so as to lower the free energy of the critical nuclei. The maximum free energy change for the formation of a critical nucleus is:

$$\Delta G^* = \frac{16}{3}\frac{\pi\gamma_{SL}{}^3}{\Delta G_v{}^2} \tag{2.6}$$

The maximum free energy change for the formation of a critical nucleus expressed in Equation (2.6) can also be termed as the thermodynamic energy barrier to nucleation.

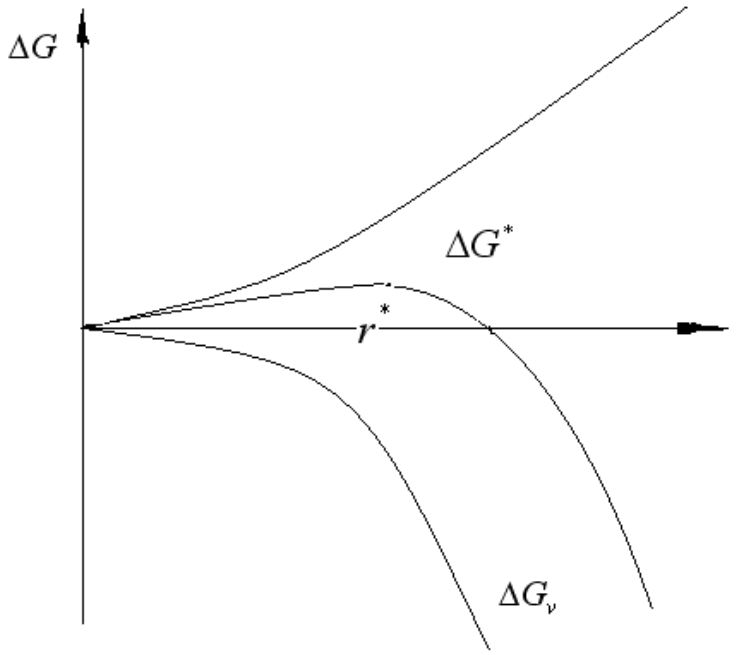

Fig. 2.4: The free energy change for the growth of an embryo of radius r.

The volume free energy change ΔG_v is considered as the driving force which determines the ability of nucleation. According to the definition of the Gibbs free energy, the volume free energy change can be given as:

$$\Delta G_v = \Delta H_v - T\Delta S_v \tag{2.7}$$

Where ΔH_v and ΔS_v are respectively the differences between the enthalpy and entropy between the solid and the liquid phase per unit volume. They were considered independent to temperature near the melting temperature T_m, and at the melting temperature:

$$\Delta G_v = \Delta H_f - T_m \Delta S_f = 0 \tag{2.8}$$

Where ΔH_f and ΔS_f are the enthalpy and entropy of fusion per unit volume, hence:

$$\Delta S_f = \frac{\Delta H_f}{T_m} \tag{2.9}$$

Substituting Equation (2.9) into Equation (2.7), the volume free energy change can be given:

$$\Delta G_v = \Delta H_f - T\frac{\Delta H_f}{T_m} = \frac{\Delta H_f}{T_m}\Delta T \tag{2.10}$$

Where ΔT is the degree of supercooling below the liquids temperature, $\Delta T = T_m - T$. For a larger degree of supercooling, the volume free energy change was expressed by Hoffman (1958) as:

$$\Delta G_v = \frac{\Delta H_f}{T_m}\frac{T}{T_m}\Delta T \tag{2.11}$$

Calorimetric measurement can be used to estimate the heat of fusion and the melting point. The approximation of the volume free energy change calculated based on Equation (2.10) and Equation (2.11) were overestimated and underestimated respectively (Takahashi and Yoshio, 1973).

The homogenous nucleation rate (the number of nuclei produced in a unit volume per unit time) in a condensed system was derived by Turnbull and Fisher (1949):

$$I = A\exp[-\frac{(\Delta G^* + Q)}{kT}], \text{ where } A = n_v(kT/h) \tag{2.12}$$

The terms ΔG^* is the thermodynamic free energy barrier to nucleation, Q is the activation energy for diffusion of molecules across the phase boundary, which was termed as the kinetic free energy barriers to nucleation. k represents the Boltzmann constant, T is

the absolute temperature, n_v is the number of atoms per unit area, and h is Planck's constant. The above equation was suggested for short-range nucleation processes, as nucleation involving more than one component was expected for longer range diffusion. Substituting Equations (2.6) and (2.10) into Equation (2.12) gives the temperature dependent homogenous nucleation rate:

$$I = A\exp(-\frac{16\pi\gamma_{SL}{}^3 T_m^2}{3kT\Delta H_f{}^2 \Delta T^2})\exp(-\frac{Q}{kT}) \tag{2.13}$$

The kinetic barrier Q can be expressed in terms of an effective diffusion coefficient D given by:

$$D = D_0 \exp(-Q/kT) \tag{2.14}$$

$D_0 = kT\lambda^2/h$, λ is the jump distance (quantity of the order of atomic dimensions). In the liquid phase, the diffusion coefficient is a function of viscosity (η), as described by the Stokes-Einstein Equation (James, 1985):

$$D = kT/3\pi\lambda\eta \tag{2.15}$$

The nucleation rate can be described as:

$$I = \frac{n_v kT}{3\pi\eta\lambda^3}\exp(-\frac{16\pi\gamma_{SL}{}^3 T_m^2}{3kT\Delta H_f{}^2 \Delta T^2}) \tag{2.16}$$

Therefore, the nucleation rate is a function of supercooling. The exponential term increases with increased supercooling. However, the viscosity of the supercooled liquid increases rapidly which contributes to a rapid reduction of the pre-exponential term in Equation (2.16). Taking the viscosity change into account, the increase in η leads to decrease in the nucleation rate I, which offsets the increased magnitude of the thermodynamic energy

barrier for nucleation. Therefore, the nucleation rate has a maximum value with supercooling as shown in Fig. 2.7. The nucleation rate is either zero or very small initially, and increases to a steady rate where the number of nuclei increases linearly with an increase in nucleation time. With further increased nucleation time, the number of nuclei per unit volume becomes almost constant (McMillan, 1979). The nucleation rate for homogenous nucleation calculated using Equation (2.16) assumed that an equilibrium distribution of subcritically sized embryos are present, and no volume and composition change occurs with the nucleation (Barsoum, 1997). However, crystal nucleation often occurs heterogeneously on impurity or container walls, rarely by homogenous nucleation, and volume and compositional change commonly exists during nucleation (Barsoum, 1997).

2.2.2 Heterogeneous Nucleation

The formation of nuclei of a new phase on the interface of an already existing phase is called heterogeneous nucleation (James, 1985). The presence of impurities and the strained lattice reduce the thermodynamic energy barrier for nucleation, as there is a reduction in the interfacial free energy between the liquid and solid.

A spherical cap shaped nucleus of phase β forms on a flat substrate with a contact angle θ as illustrated in Fig. 2.5, at equilibrium;

$$\gamma_1 = \gamma_2 + \gamma_3 \cos\theta \text{ , } (0 \le \theta \le \pi) \qquad (2.17)$$

Where γ_1 is the interfacial energy between the substrate and liquid, γ_2 is the interfacial energy between the heterogeneity nucleus and the substrate, and γ_3 is the interfacial energy between the heterogeneity nucleus and liquid.

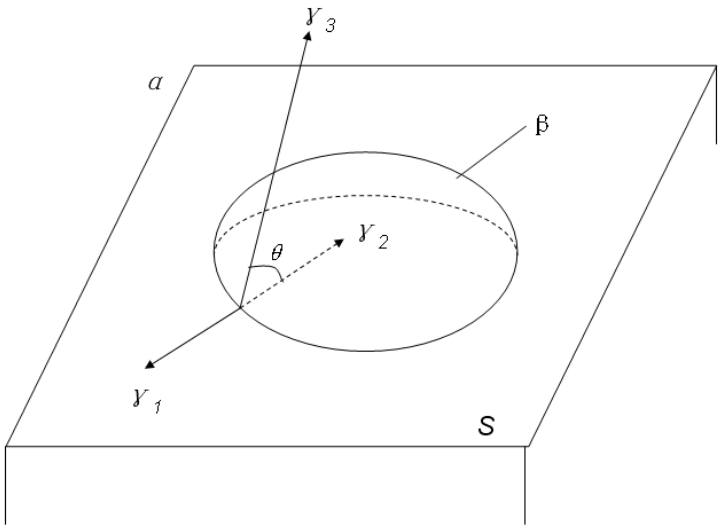

Fig. 2.5: Spherical cap model of heterogeneous nucleation.

The free energy of forming a critical-size nucleus can be expressed as:

$$\Delta G_{het} = \Delta G^{*}_{\text{hom}} f(\theta) \tag{2.18}$$

Where

$$f(\theta) = \frac{(2+\cos\theta)(1-\cos\theta)^2}{4} \tag{2.19}$$

For any contact angle less than 180º, the activation energy of heterogeneous nucleation is smaller than for homogeneous nucleation, and decreases as θ gets close to 0º (complete wetting), which results in reduction of the critical nucleus size. In practice, the solid surface is not perfectly flat due to surface roughening. Nuclei could fill cavities in the solid surface, and then the total surface energy change becomes negative.

The heterogeneous nucleation rate can be expressed (Christian, 1975) as:

$$I_{het} = \frac{n_s kT}{h} \exp[-\frac{f(\theta)\Delta G_{\text{hom}} + Q}{kT}] \tag{2.20}$$

Where n_s is the number of the atoms of the liquid in contact with the impurity surface per unit area. Therefore, the heterogeneous nucleation rate depends on the contact angles. Fletcher (1958, 1959) proposed that the activation energy for heterogeneous nucleation $\Delta G_{het} = \Delta G_{\text{hom}} g(\theta, x)$, where g is a function of contact angle θ and x, $x = R / r^*$, r^* is the critical nucleus radius for homogeneous nucleation, and R is the radius for the spherical cap. A surface with larger spherical cap radius R results in smaller activation energy and higher tendency to form nuclei. Thus the curvature (R) of the impurity surface is also an important factor for heterogeneous nucleation.

According to the classical nucleation theory, crystal nucleation rate is temperature dependent and mainly governed by the nucleus/liquid interfacial energy. However, quantitative discrepancies between the experimental nucleation rate and those predicted by classical nucleation theory were reported. This could be explained as the classical nucleation theory did not take into account several effects, such as the size or temperature dependence of the nucleus/liquid surface energy (Fokin and Zanotto, 2000), elastic strain energy generated due to the density difference between the crystals and glass (Schmelzer et al., 1993, Schmelzer et al., 2004) and the deviation of the glass and nucleus composition during crystallisation (Fokin et al., 2003).

It was suggested that elastic strain can partially or fully diminish the thermodynamic driving force for the crystallisation, which can therefore increase the thermodynamic barrier ΔG^* for nucleation (Schmelzer et al., 1993, Fokin and Zanotto, 2000, Fokin et al., 2005) and decrease the nucleation rate (Schmelzer et al., 2004). Fokin et al., (2003) demonstrated a continuous variation in glass and crystal compositions during crystallisation. They also suggested the variation in the nucleus composition facilitates the reduction of thermodynamic barrier ΔG^* for nucleation by decreasing the nucleus/liquid interfacial energy and leads to increase in nucleation rate.

2.2.3 Nucleating Agents

Nucleating Agents are usually capable of existing in the glass in the form of particles of colloidal dimensions (McMillan, 1979), precipitated during cooling or reheating. They increase the driving force of nucleation or lower the interfacial tension, so as to promote nucleation. They may also work as nuclei for crystal growth. Different nucleating agents such as titanium dioxide (TiO_2), phosphorous pentoxide (P_2O_5), zirconium dioxide (ZrO_2), fluorides and some metals (Ni, Cr, Cu, Ag and pt) are used in the production of glass-ceramics (McMillan, 1979).

Silicate glass is built up of SiO_4 tetrahedra which can integrate with foreign structural units. The SiO_4 structure may be stable at low concentration of intrusive oxide and produce a single-phase glass. When the concentration of the added oxide exceeds a critical limit, the disruptive effect of the oxides leads to separation of the structure into two phases in order to lower the total free energy. A single phase system can form in which the SiO_4 tetrahedra is considered as being dissolved in the network of the added oxide (McMillan, 1979). Titanium dioxide has proved to be a good nucleating agent, which is effective in a variety of glasses with a weight percent of 2 to 20 (Stookey, 1960). Titanium ions (Ti^{4+}) were suggested having 4-fold coordination with oxygen in the silicate network. During cooling, the coordination number of Ti^{4+} increased up to six and acted as a glass modifier, reduced the viscosity and facilitated other cation diffusion towards nucleation and crystal growth (Barbieri et al., 1997). The introduction of titanium dioxide (TiO_2) can also lead to phase separation (Weyl, 1951, Maurer, 1962, Khater and Idris, 2007), which can act as nucleation sites. Zirconia (ZrO_2) has been used for the crystallisation of leucite (Hermansson and Carlsson, 1978). It was also suggested the addition of ZrO_2 increased viscosity in the Li_2O-SiO_2-Al_2O_3-K_2O-P_2O_5 system, hampered the growth of lithium metasilicate and increased translucency in the glass-ceramic (Apel et al., 2007). Niobium oxide (Nb_2O_5) was also proven to prevent the crystal growth of fluorapatite glass-ceramics (Denry et al., 2005).

2.2.4 Crystal Growth

Once a stable nucleus has formed either by homogeneous or heterogeneous nucleation, it tends to grow. The growth rate depends on the diffusion rate of atoms towards the liquid-crystal interface, how the atoms cross the interface (Zarzycki, 1991) and the rate of heat flow away from the liquid-crystal interface (Strnad, 1986). The nature of the interface therefore plays an important role in determining the crystallites growing kinetic and their subsequent morphology (Kingery et al., 1976). Jaskson (1967) related the nature of the interface to the entropy of fusion (ΔS). Materials with small entropies of fusion ($\Delta S < 2R$, where R is the gas constant) are expected to have a rough growing interface on an atomic scale, and a more isotropic growth rate. In contrast, materials with larger entropy changes ($\Delta S > 4R$) have a smoother interface and a more anisotropic growth rate.

According to Turnbull (1956), the crystal-liquid interface may be represented by two potential wells separated by the jump distance λ, which can also be termed as the interatomic separation. An atom in the crystal structure has a lower free energy than the corresponding atoms in the liquid state, therefore the molar free energy change corresponding to crystallisation is:

$$\Delta G_v = G_c - G_l \tag{2.21}$$

Where G_c is the free energy of the crystal, and G_l is the free energy of the liquid state. In order to cross the liquid-crystal interface (Fig. 2.6), a free energy of activation $\Delta G^{"}$ is required to overcome the energy barrier. The frequency (v_{ls}) for an atom to cross the liquid-crystal interface can be expressed:

$$v_{ls} = v\exp(-\Delta G^{"}/RT) \tag{2.22}$$

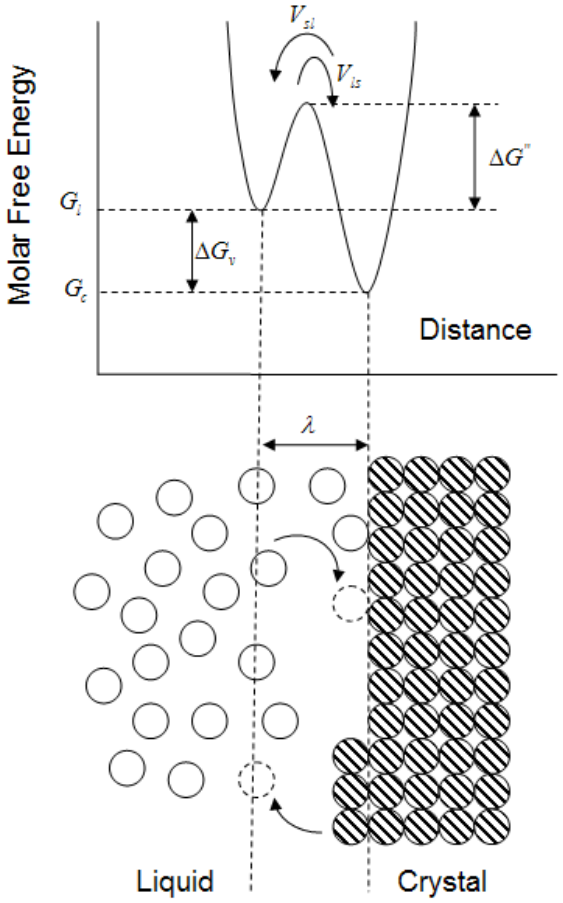

Fig. 2.6: Growth mechanism controlled by the interface (Zarzycki, 1991).

The activation energy for crossing the crystal-liquid interface is $\Delta G^{"} - \Delta G_v$, and the frequency for an atom to cross the crystal-liquid interface is:

$$v_{sl} = v \exp(-\frac{\Delta G^{"} - \Delta G_v}{RT}) \tag{2.23}$$

Where v is the fundamental vibration frequency at the crystal-liquid interface.

The crystal growth rate is proportional to the difference between the frequencies of the liquid to crystal transitions and the crystal to liquid transitions. The crystal growth rate can therefore be given by:

$$u = f\lambda v \exp(-\frac{G^{"}}{RT})(1-\exp\frac{\Delta G_v}{RT}) \quad (2.24)$$

Where f is the fraction of sites on the surface which are available for growth ($0 < f < 1$). Turnbull (1956) commented that nucleation is controlled by relatively short-distance arrangements near the nucleus, and the growth is controlled by long range distribution. Therefore the activation energy $\Delta G^{"}$ for the movement of an atom across the interface is not necessarily equal to or the same order of magnitude as the activation energy ΔG_v for nucleation. Turnbull and Cohen (1958) suggested that for simple substances, the activation energy $\Delta G^{"}$ for the crystal growth is close to that for viscous flow. Substituting Equation (2.14) and the Stokes-Einstein Equation (2.15) into Equation (2.24), the growth rate can be expressed as:

$$u = f\frac{hvT}{3\pi\lambda^2\eta}(1-\exp\frac{\Delta G}{RT}) \quad (2.25)$$

Viscosity plays an important role on the crystal growth rate. A rapid increase in viscosity with decrease in temperature results in the decrease of the growth rate.

2.2.5 The Nucleation Rate and Growth Rate with Temperature

The nucleation rate I and the growth rate u are the two predominant parameters for glass crystallisation and both of them are temperature dependent as shown in Fig. 2.7 (Tamman, 1925). There is a metastable zone (T_2 - T_m) below the melting temperature (T_m), in which nuclei do not form at a detectable rate. The initial nuclei formation occurs between T_2 and T_4, below which the liquid viscosity is high. Below this metastable zone, the crystallisation depends on the overlapping of the nucleation rate and the crystallisation rate. If both nucleation rate I and the growth rate u are too low, the crystallisation will be negligible and then the liquid will transform into glass. High nucleation rate I and low

growth rate u results in partially crystalline materials with fine grains, whereas low nucleation rate I and high growth rate u leads to a small amount of large crystals distributed in the glass. High nucleation rate I and high growth rate u can result in fully crystalline materials. Different nucleation and growth rates lead to different material structures, which contribute to the material properties. Careful control of the nucleation and growth rate becomes important, especially in the glass and glass-ceramic industry, to achieve the required properties.

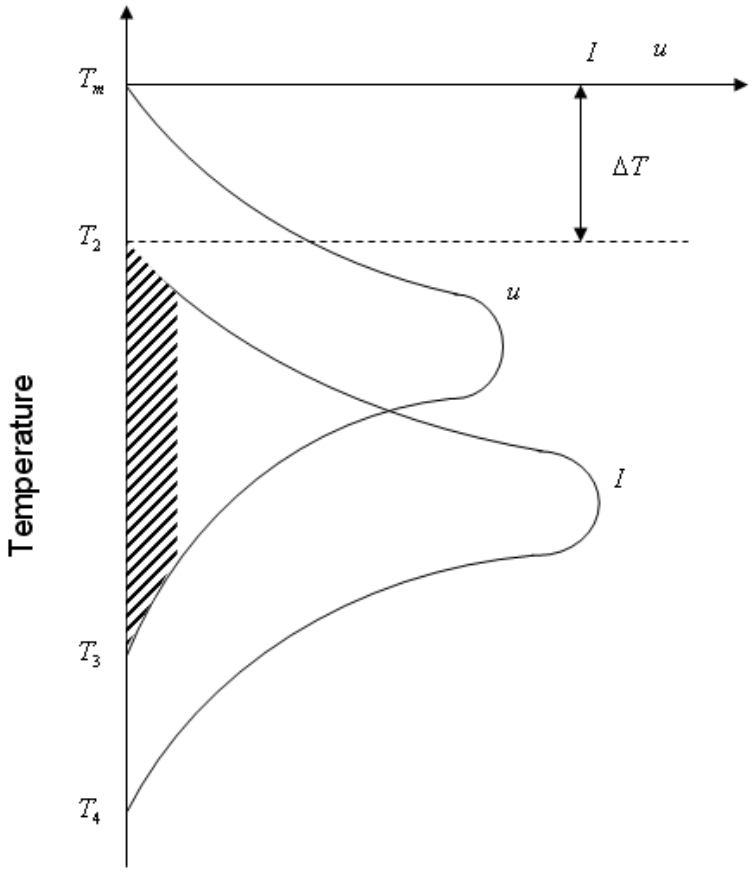

Fig. 2.7: Variations of the nucleation rate and growth rate with temperature (Zarzycki, 1991).

2.3 Phase Separation

Supercooled liquids within certain compositional ranges and temperatures can separate into two immiscible liquid phases of markedly different compositions, instead of forming a homogenous single liquid phase (Zarzycki, 1991). Those regions are due to immiscibility and the initial unmixing of the liquid glass compositions. Glass-forming systems such as silicate or borosilicate glass forming systems encounter immiscibility regions. Phase separation can be achieved by spinodal decomposition or nucleation and growth (James, 1985).

Phase separation can be explained in terms of a binary solution of components A and B at constant temperature. For a simple statistical model in which atoms A and B are randomly mixed on a regular lattice, the free energy of mixing ΔG_m at constant temperature T can be expressed in terms of the entropy ΔS_m and the enthalpy ΔH_m of the mixing (James, 1975):

$$\Delta G_m = \Delta H_m - T\Delta S_m \tag{2.26}$$

Assuming the entropy of the mixing ΔS_m is that of an ideal solution where the enthalpy ΔH_m equals the entropy:

$$\Delta S_m = -R[x \ln x + (1-x)\ln(1-x)] \tag{2.27}$$

And the entropy change is assumed to equal the energy change:

$$\Delta H_m = \alpha x(1-x) \tag{2.28}$$

Where x is the molar fraction of phase B, R refers to the universal gas constant, and α is given by: $\alpha = NZ[E_{AB} - (E_{AA} + E_{BB})/2]$, where E_{AA}, E_{BB} and E_{AB} are the energies

of the various bonds between atoms, N is the Avogadro's number, and Z is the coordination number of each atom. Therefore the free energy of mixing ΔG_m can be expressed as:

$$\Delta G_m = \alpha x(1-x) + RT[x\ln x + (1-x)\ln(1-x)] \tag{2.29}$$

If the energy of A-B bond is greater than the energy of A-A and B-B bonds, the enthalpy is negative and the mixing is completely miscible. If the A-B bond is weaker than the A-A and B-B bonds, there is a tendency for atoms to separate into two different phases which lower the free energy of the solution.

2.3.1 Spinodal Decomposition

In a binary system A-B, the free energy versus composition curves is shown in Fig. 2.8 B. If the energy curve has a negative curvature ($\delta G = d^2G/dx^2 < 0$), a small fluctuation in composition below the peak consolute temperature T_c, results in a reduction of the free energy G_0 (Fig. 2.8 B), which contributes to A-rich and B-rich regions spontaneously (Cahn, 1968). Therefore:

$$\delta G = d^2G/dx^2 = 0 \tag{2.30}$$

The two corresponding critical points are called spinodal points (c and d in Fig. 2.8 B). The locus of those points corresponding to $\delta G = 0$ in the temperature-composition diagram is known as the chemical spinodal.

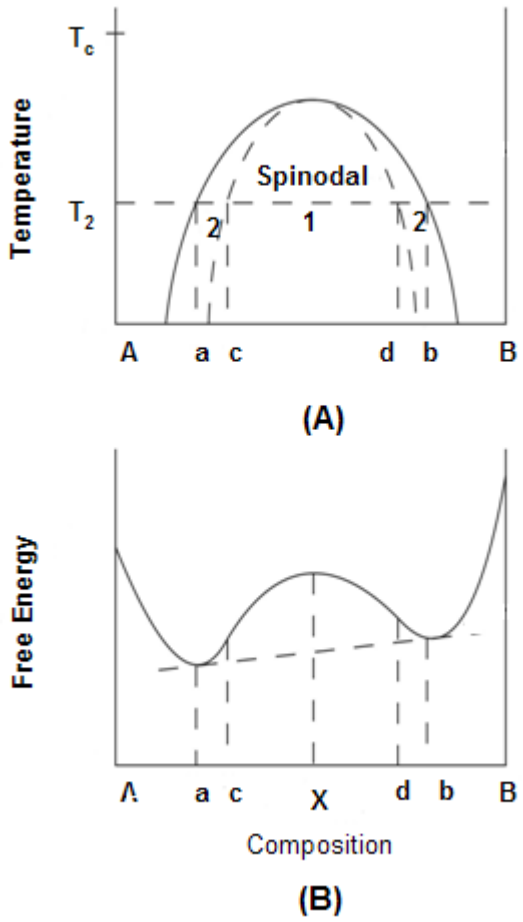

Fig. 2.8: Free energy versus composition diagram (A) and corresponding phase diagram (B) (Cahn, 1968).

The spinodal splits the diagram into two regions, region 1 consists of the initial composition and lies between the chemical spinodal where $\delta G < 0$. The system is unstable and infinitesimal fluctuations in composition occur spontaneously so as to achieve a more stable phase with lower free energy. The phase separation system is controlled solely by diffusion, and the process is named spinodal decomposition by Cahn (1968). With increased time, the phase separation is kinetically preferred and the concentration of the two phases varies with time. The initially diffuse interfaces tend to become progressively sharp. The diffusion within spinodal decomposition is called up-hill diffusion as illustrated in Fig. 2.9 (A) (Zarzycki, 1970, James, 1975). Therefore, small clusters occur periodically, and result in a relatively even distribution in an interconnected structure.

2.3.2 Phase Separation by Nucleation and Growth

If a glass composition lies in region 2 (Fig. 2.8 A) where $\delta G > 0$, the system is stable towards small fluctuations in composition. This results in an increase of free energy, but the system is metastable towards formation of nuclei whose composition is different from the matrix, which leads to a reduction of the system free energy. In contrast to spinodal decomposition, the composition of the nucleation phase does not change according to the time during the phase nucleation and growth. The second phase has sharp interfaces initially, and growth at the expense of matrix concentration. The second phase tends to be spherical with a random distribution (James, 1975).

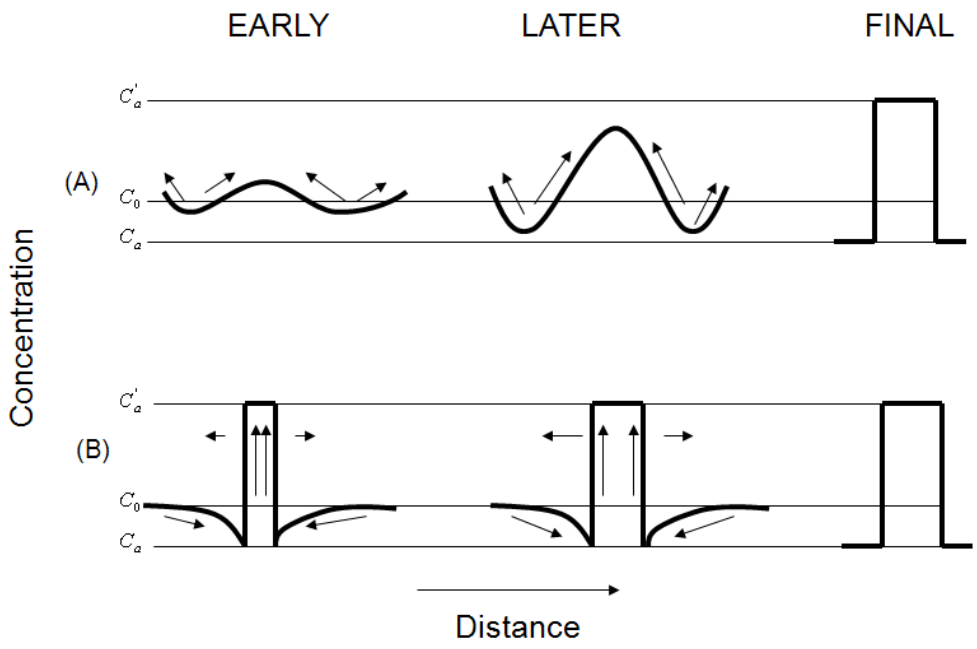

Fig. 2.9: Composition fluctuation in terms of time (A) spinodal decomposition (B) nucleation and growth (Zarzycki, 1991).

2.4 Glass-Ceramics

2.4.1 General Introduction

Glass-ceramics are polycrystalline solids produced by the controlled crystallisation of glass (Stookey, 1959). In dentistry, glass-ceramic powders or monoliths are produced and further sintered, heat extruded or machined in the dental laboratory for clinical applications.

The idealised steps used in processing a glass-ceramic are illustrated schematically by the temperature-time cycle shown in Fig. 2.10. A homogeneous glass is initially heated and formed at high temperature and then cooled to ambient temperature, followed by shaping. Some phase-separated domains or nucleated phases might present in the glass (Kingery et al., 1976). The glass is then heated from room temperature to the optimum nucleation temperature T_N, and then typically held at this temperature for 1 - 2 hours. A slow heating rate (2ºC to 5ºC/min) is generally used to avoid high temperature gradients which can lead to thermal shock of the glass. The nucleation temperature normally lies between the glass transition temperature (T_g) and 50ºC above T_g, and corresponds to a viscosity in the range of 10^{10} to 10^{11} Pa·s (McMillan, 1979). Hing and McMillan (1973) suggested a diffusion controlled coarsening process might occur during the nucleation treatment. The idea was validated by McMillan (1974), who found there is an optimum nucleation duration for producing fine-grained glass-ceramic. The optimum nucleation temperature (Harper et al., 1970) and nucleation duration can be determined by experimentation (Park et al., 2003).

Following the nucleation stage, the glass is further heated at a controlled rate up to the maximum crystallisation temperature (T_C), for the maximum development of the major crystalline phase without deformation of the material by viscous flow. The maximum crystallisation temperature (T_C) has been suggested 25 to 50ºC below the re-dissolution temperature of the crystalline phase (McMillan, 1979, Zarzycki, 1991). Once the maximum crystallisation temperature is achieved, the glass will be held for a suitable period, to permit crystal growth upon the nuclei to the size required, then the glass-ceramic can be cooled

down to room temperature.

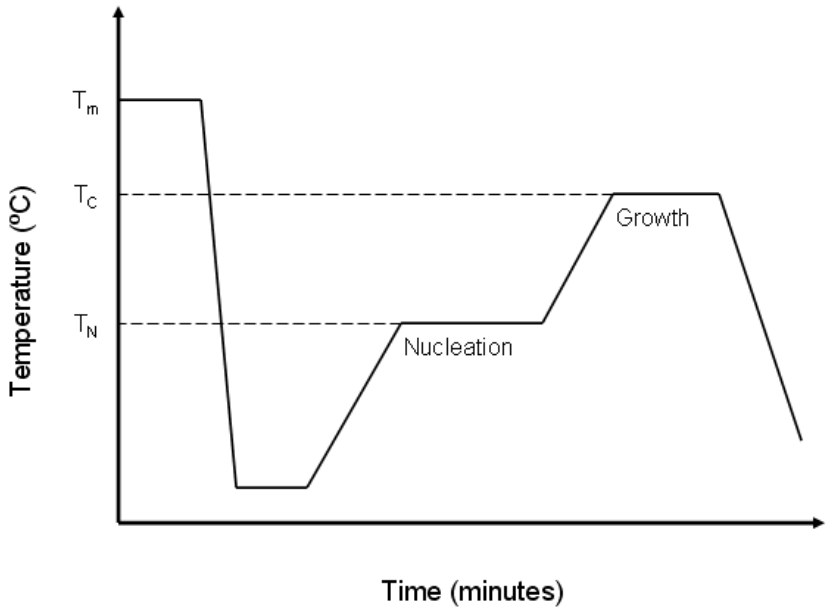

Fig. 2.10: Heat treatment schedule for a glass-ceramic.

The structure of the glass-ceramics and the volume fraction of the crystalline phase are determined by the initial glass composition, the stoichiometry of the crystalline phase and the crystallisation heat treatment. Heating rate also plays an important role on the structure of the glass-ceramics. If the nucleation rate I is high, the crystal growth rate u may not be sufficiently rapid with a high heating rate, therefore, the glass will end up with partially crystalline material with fine grains. Slow heating alternatively leads to a progressive change in the glass composition, stress relaxation by the viscous flow in the glass, and avoids deformation, contributing to a high volume of crystalline phase.

Glass-ceramics produced by controlled crystallisation demonstrate excellent mechanical and physical properties including mechanical strength, hardness, chemical durability and abrasion resistance (Stookey, 1959, McMillan, 1979). It is suggested the strength of glass-ceramics is influenced by the degree of crystallinity, and the crystal size. A fine crystalline phase has proved to inhibit crack propagation and resulted in higher strength (Miyata and Jinno, 1972). Glass-ceramics can be opaque due to the refractive index

differences between the crystalline phase and the residual glass. Transparency of glass-ceramics can be achievable by reducing the size of the crystalline phase or matching the refractive indices (Beall and Duke, 1969). Therefore, translucency glass-ceramics suitable for dental aesthetic applications are achievable. The thermal expansion of glass-ceramic can be modified by a controlled crystallisation heat treatment, and the degree of crystallinity. In dentistry, glass-ceramics with different thermal expansion have been prepared by controlling the crystallisation to get thermal compatibility with metal, alumina or zirconium substructures (Kelly, 1997, McLean, 2001).

2.4.2 Leucite Glass-Ceramics

Leucite ($K_2O{\cdot}Al_2O_3{\cdot}4SiO_2$) is a potassium alumino-silicate mineral that has corner linked four and six membered rings of SiO_4 tetrahedra, forming the structure of a (Si, Al)-O framework silicate (Fig. 2.11). Two different cation sites are present in the structure, the larger site contains 16 positions coordinated by 12 oxygens and is in line with channels formed by six-membered rings. The second site contains 24 positions among which only 16 are occupied, and each position is coordinated by four coplanar oxygens of the framework and two occupants of the larger sites (Deer et al., 1966). The larger sites are normally filled by potassium, rubidium or cesium, and the smaller sites are vacant. At room temperature Leucite is tetragonal with a relatively high thermal expansion around 20 - 25 x 10^{-6}/K (Rouf et al., 1978) and cubic at high temperature with low thermal expansion 11.7 - 12.8 x 10^{-6}/K (Hermansson and Carlsson, 1976). Both tetragonal and cubic leucite contain 16 ($KAlSi_2O_6$) in the unit cell. At low temperature the potassium ions in the leucite structure are too small to fill the large cavities in the cubic structure, and the potassium cavities are then compressed (Mazzi et al., 1976), resulting in the distortion of the (Si, Al)-O framework. During heating, the *c*-axis of leucite crystal decreases whilst *a*-axis increases, until they become equal, resulting in cubic symmetry. The cubic to tetragonal phase transformation occurs at around 605 - 625ºC (Mackert, 1988) and leads to a reversible 1.2% volume change (Mackert and Evans, 1993) and crystal twinning (Palmer et al., 1988).

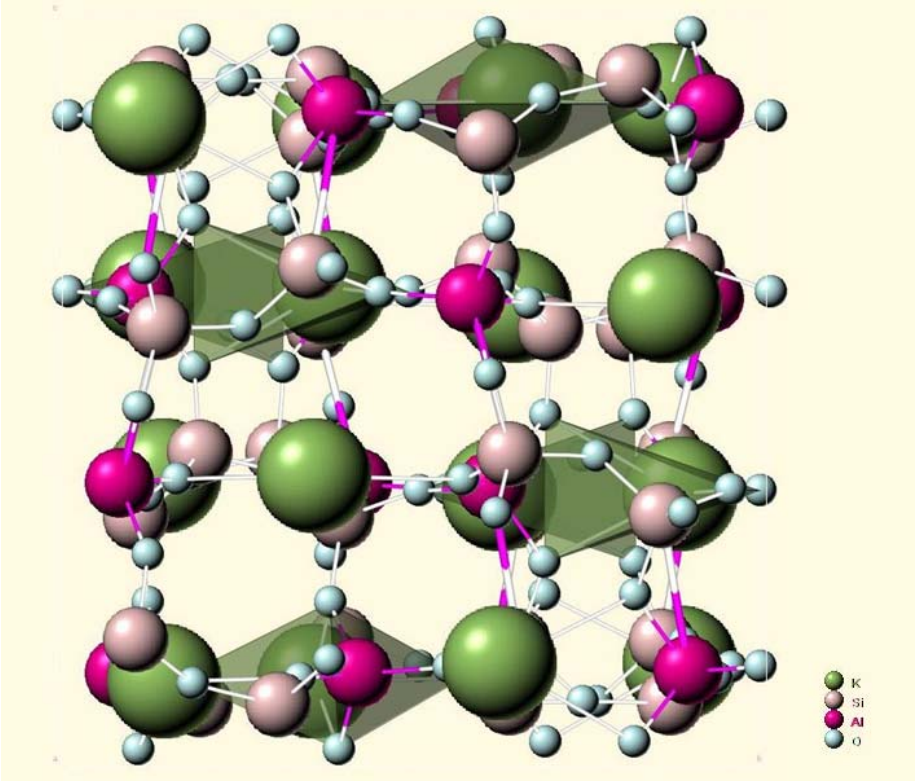

Fig. 2.11: Schematic showing the structure of tetragonal leucite (http://www.webmineral.com/data/Leucite.shtml).

Leucite glass-ceramics are widely used in dental applications for porcelain fused to metal restorations to achieve thermal compatibility with metallic substructures and in all ceramic restorations. They have been successfully produced by nucleation and crystallisation control of selected aluminosilicate glass (Weinstein et al., 1962, Schweiger, 2003, Cattell et al., 2005). The mismatch of thermal expansion between tetragonal leucite and the glass matrix (8 - 10 x 10^{-6}/K) (Vergano et al., 1967) leads to the development of tangential compressive stresses around leucite crystals, which was considered associating to the strengthening in feldspathic dental porcelain (Denry et al., 1996). The compressive stress around large non uniform leucite crystals and clusters, results in the formation of microcracking around leucite crystals and clusters (Mackert and Williams, 1996). The latter microcracking has been linked to the reduction in strength of the glass-ceramics (Cattell et al., 1999). Stabilisation of cubic leucite to room temperature has been achieved by the introduction of Cs_2O and pollucite, which results in a lower thermal expansion coefficient, hardness, toughness (Rasmussen et al., 1998) and flexural strength (Denry et al., 1996). However, an increased fracture

toughness due to transformation toughening was observed when Cs_2O-stabilised leucite core particles were added to a cesium-free matrix porcelain (Rasmussen et al., 2004). Fine cubic leucite (3 - 4 µm) was obtained by ion exchange of the hydrothermal synthesised cubic analcime ($Na[AlSi_2O_6]\cdot H_2O$) using saturated potassium chloride (KCl) solution below 200ºC in hydrothermal condition (Balandis and Sinkyavichene, 2005, Novotna et al., 2004). The fine cubic leucite was suggested as a source material to produce dental composite ceramics which are thermally compactable with metals (Balandis and Sinkyavichene, 2005).

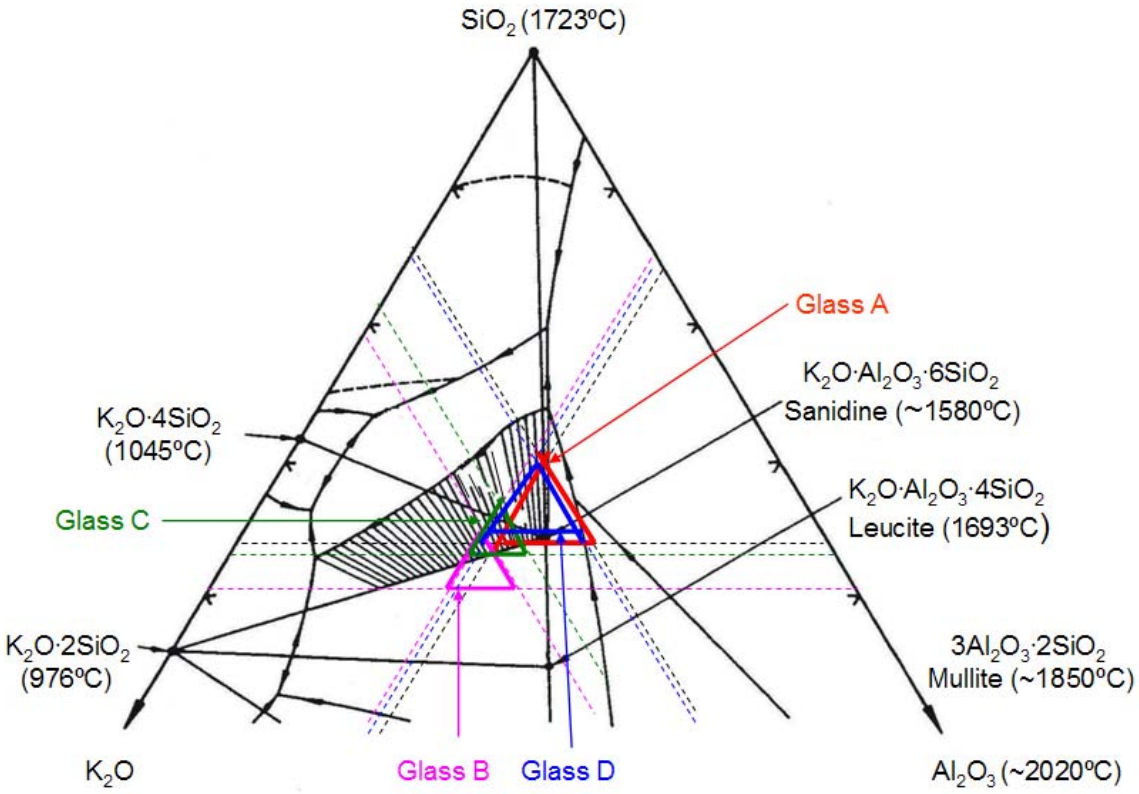

Fig. 2.12: K_2O-SiO_2-Al_2O_3 phase diagram (Schairer and Bowen, 1955). Experimental glasses are marked in coloured triangles according to the K_2O, Al_2O_3 and SiO_2 content (in wt%), where Na_2O was considered as K_2O and other minor components are not factored in.

Increased K_2O compositions increase the leucite content and contribute to an increase in the compressive strength according to literature (Zhang et al., 2002). Schairer and Bowen (1955) compared a K_2O-SiO_2-Al_2O_3 phase diagram, and suggested the compositions within

the shadowed area of the phase diagram (Fig. 2.12) precipitate leucite as a first crystalline phase and sanidine as a second one. Complete re-adsorption of leucite can result in sanidine ($K_2O{\cdot}Al_2O_3{\cdot}6SiO_2$, monoclinic), quartz and potassium tetrasilicate precipitation (Barreiro et al., 1989). In practice, the glass become so viscous that sufficient time is not available to for the adsorption of leucite. It is possible that these porcelains might produce two crystalline phases in the glassy phase. Quantitative X-ray diffraction analysis of multi-fired dental porcelains revealed a leucite concentration change (Fairhurst et al., 1980, Mackert and Evans, 1991). Evidence of the appearance of sanidine after multiple firings was also observed (Tsetsekou et al., 2002). Leucite crystallisation has been mainly achieved by surface nucleation (Höland et al., 1995), however, size and compositional dependent bulk nucleation of leucite was also possible (Tošić et al., 2000, Tošić et al., 2002, Rouf et al., 1978).

2.5 Mechanical Milling

Mechanical milling is a conventional method widely used in the glass and glass-ceramic industry to achieve particle size reduction. During mechanical milling, powder particles are trapped between colliding balls or between ball and container walls. Due to compression, impact or shear forces, the powders experience mechanical stresses at their contact points (Suryanarayana, 2001, Rahaman, 2003, Suryanarayana, 2004, Carter and Norton, 2007). If the stress exceeds the ultimate strength of the particle, then particle fracture occurs and leads to decrease in the particle size and increase in surface area. With prolonged milling and the particle size reduction, the probability of particles with a given flaw size decreases, and the particle becomes stronger (Rahaman, 1995). However, the tendency of particle agglomeration increases with decreasing particle size. Therefore, there is a practical grinding limit where the agglomeration and powder size reduction reaches equilibrium (Garcia et al., 2002).

Mechanical milling with liquid media is termed wet milling, and when no liquid is involved, it is classified as dry milling. During wet milling, the molecules of the liquid media are

absorbed on the newly formed particle surface, and lower the surface energy. It is suggested that wet milling provides less agglomerated conditions and is more suitable for fine ground powder production compared to dry milling (Suryanarayana, 2001, Suryanarayana, 2004). However, wet milling may lead to increased contamination of the grinding powder introduced by the wear of the grinding media (Puclin et al., 1995, Suryanarayana, 2001, Okada et al., 2007).

Mechanical milling used in metallurgy involves repeated welding, fracturing and rewelding of the metal powder or powder mixture and results in material transfer (Gilman and Benjamin, 1983). This type of milling was designated as mechanical alloying. Studies showed that mechanical alloying and mechanical milling of single-composition powders could lead to amorphous alloys (Koch, 1989), metastable phases, solid solutions and nanocrystalline materials (Koch, 1991). Tulyaganov et al., (2002) found that finer calcium-magnesium-aluminosilicate glass powder produced a glass-ceramic with a finer and highly homogeneous microstructure. Mechanical milling is also used in dentistry to achieve the required dental porcelain powder size which is consequently beneficial for the desired porcelain porosity (Klaus et al., 1986). Holland et al., (2001) suggested leucite crystals within current dental leucite glass-ceramics were formed by a surface nucleation mechanism. Reduction in glass powder size which introduces larger surface area could therefore be beneficial for fine leucite glass-ceramic synthesis. Hashimoto and Yamaguchi (2002) investigated the effect of the starting SiO_2 particle size on the size of leucite crystals. Different size of quartz particles were mixed with K_2SO_4 and $Al_2(SO_4)_3$ at a ratio of 5.9:1.0:1.1 (molar ratio), heated at 1000ºC for 3 hours and then treated with hot HCl. The size of the resulting spherical leucite crystals decreased with a decrease in starting SiO_2 particle size. Milling (Attritor milling) of a designed glass composition, followed by various nucleation and crystallisation studies were carried out by Cattell et al., (2003, 2006), and a relationship between the glass powder size and the leucite crystal size was proven.

Different types of mills including high compression roller mills, jet mills, shaker mills, high speed mixer mills, planetary ball mills and Attritor mills are used for research or commercial

purposes. They have different shape design, capacity, and milling efficiency. Several types of mill were used for this study.

2.5.1 Ball Mills

Ball milling is the most common laboratory method for powder reduction and is suitable for both wet and dry milling. As illustrated in Fig. 2.13, a ball mill is a barrel filled with grinding media and the powder to be ground which rotates on its axis. The grinding balls rotate towards the top of the mill and fall onto the particles at the bottom of the mill. If the rotation speed is fast enough, the grinding balls will travel to the top of the mill (Fig. 2.13), where the centrifugal force balances the force of gravity (Rahaman, 1995). This speed was defined as the critical speed of rotation. Powder size reduction is achieved by the compression, impact or shear with the milling media or other particles. The final powder size depends on the type of milling vial and grinding media, ball-to-powder ratio, milling speed, milling time and the properties of the powder.

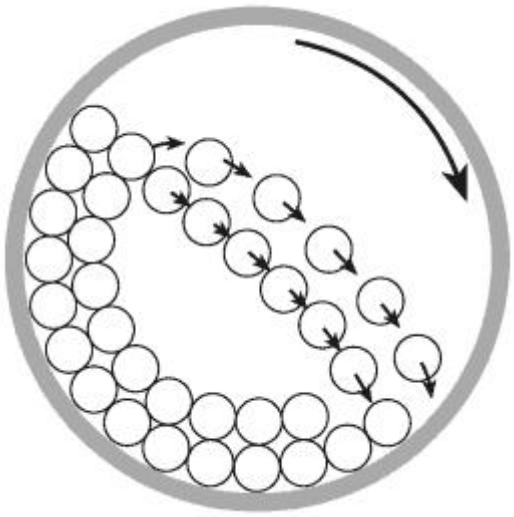

Fig. 2.13: Cross section of a ball mill in rotating motion (black arrow points the rotation direction of ball mill (Rahaman, 2003).

2.5.1.1 Milling Media

Milling media normally have a high density (Carter and Norton, 2007) such as alumina, zirconia, stainless steel etc. This is because the kinetic energy E of the milling media during milling is proportional to mass of the milling media ($E = \frac{1}{2}mv^2$, where m is the mass of the grinding media, v is the relative velocity of the grinding media). Therefore, the higher the density of the milling media, the higher the energy could be generated during the milling. The milling media and milling pot are usually made from the same type of material in order to reduce the material wear.

It was reported that the size of the grinding media has an influence on the milling efficiency, and the final constitution of the powder (McLaughlin, 1999, Guo et al., 1994, Padella et al., 1991). Riffel and Schilz (1998) investigated the effects of grinding ball size on the synthesis of Mg_2Si. They found that larger grinding balls led to a significant increase in contamination, however, small grinding balls could not provide the required kinetic energy. Therefore, a combination of smaller and larger balls might be beneficial.

The weight ratio of the balls to the powder (BPR) has an obvious effect on the milling time: the higher the BPR, the shorter time is required. A higher BPR ratio reduces the mean free path of the grinding ball, and increases the number of collision per unit time, which contributes to higher energy generation. Ideally, 50% filling of the milling pot with suitable BPR ratio gives the best milling efficiency (Suryanarayana, 2001).

2.5.1.2 Milling Speed

The kinetics of the grinding media can be expressed as $E = \frac{1}{2}mv^2$. A higher milling speed leads to a higher energy input into the powder. However, if the milling speed exceeds the critical speed of rotation, the grinding balls will be pinned to the wall of the barrel and do not fall down to exert any impact force. Therefore, the maximum speed should be just below the critical speed, where the grinding balls travel and fall from the maximal height to produce the

maximum collision energy. The mill temperature increases with increase in milling speed. The increased temperature may be beneficial for diffusion, however it might also result in the decomposition of supersaturated solid solutions or a metastable phase formation (Suryanarayana, 2001).

2.5.1.3 Milling Time

The ideal milling time is dependent on a combination of the parameters, such as the type of mill, intensity of milling, and ball to powder weight ratio etc. An “L” shape relationship between the powder size reduction and the milling has been suggested (McLaughlin, 1999). Dramatic powder size reduction occurs at the beginning of the milling, and with further reduction, there is a tendency for agglomeration and contamination to increase.

2.5.2 Attritor Mills

Attritor mills are specially designed for large quantities of powder. Different types of Attritor mills were reviewed by Szegyari and Yang (1984). An Attritor mill consists of a vertical barrel containing a series of impellers. A powerful motor rotates the impellers which in turn agitate the grinding balls. The shear and impact force generated by the grinding balls are applied to the materials to be ground. Powder reduction is achieved by interparticle collisions, ball sliding and collisions between balls, container walls, agitator shaft and impellers. Materials are fed at the top and removed from the lower side of the milling tank. Constant powder withdrawal and reloading of the oversize particles leads to a narrow size particle distribution. It is suggested that Attritor milling produces more spherical particles and smaller particle size powder than a ball mill (Suryanarayana, 2001).

2.6 Glass/Glass-Ceramic Processing

2.6.1 Powder Condensation

Synthesised glasses and glass-ceramics after relevant milling have loose packed particles with a continuous distribution. The powder packing fraction is defined as packing density (Rahaman, 1995). It is influenced by the particle size, shape and distribution, and increases with the increasing spread of the particles size distribution.

Mechanical compaction of powder is a widely used forming operation to attain powder compacts with reduced voids and highest the possible density, since higher packing density reduces the firing shrinkage and facilitates sintering (Hlaváč, 1983). Powder compaction is suitable for a flat shape with a low height to diameter ratio. The whole process consists of the filling of die, powder compaction and powder compact ejection.

The formation of a dental porcelain restoration using powder frit material involves mixing the powder with sufficient liquid binder. The binder removal using a brush or tissue and the subsequent compaction is termed condensation (Binns, 1983). Condensation relies on the surface tension of the liquid, which brings the particle closer (Skinner and Phillips, 1982). Vibration helps to reorient and displace particles for maximum packing and brings the binder to the surface. Condensation of gap graded powder can limit the volume firing shrinkage to 30 - 38% (Hodson, 1959).

2.6.2 Sintering

After condensation, the powder frit is fused and the porosity is eliminated by firing in a furnace under partial vacuum. The process of fusing the particles of powder together is named sintering (Skinner and Phillips, 1982). The firing of dental porcelain involves the bridging between the adjacent particles and the subsequent viscous flow (Kuczynski, 1949). Therefore, viscosity plays an important role in sintering.

2.6.2.1 Sintering Stages

Dental porcelain sintering has been classified in three different stages: low, medium and high bisque (Skinner and Phillips, 1982). In the low bisque stage, the porcelain surface is porous and bridges are formed between adjacent particles. The bridging results in reduced surface energy, however, no perceivable reduction in volume occurs in this stage. In the medium bisque stage, the porcelain surface is still porous, the grains start to melt, and the entrapped air becomes spherical in shape. Shrinkage is evident at this stage. In the high bisque stage, the porcelain is relatively pore free. The surface appears shiny and smooth and no more shrinkage occurs after this point.

2.6.2.2 Driving Force for Sintering

Sintering is a process which reduces the surface area of powder particles. Mackenzi and Shuttleworth (1949) pronounced that the driving force for sintering is the excess free energy of the powder surface over the solid material. Sintering involves the changes in volume, grain boundaries and the surface area of grains. The actual driving force should therefore be the total free energy change for the whole system:

$$\Delta G_T = \Delta G_V + \Delta G_B + \Delta G_S \tag{2.31}$$

Where ΔG_V, ΔG_B and ΔG_S represent the change in free energy associated with volume, boundaries and the surfaces of the grains respectively, where the major driving force is the free surface energy change (Reed, 1995). Rahaman (1995) summarised the possible sources for the energy change: surface curvature, applied pressure, and chemical reaction. He suggested that the driving force of sintering provided by these three sources increase in sequence.

2.6.2.3 Porosity

Pores are the space between solid particles. They scatter the light, which could therefore reduce the material translucency. They can also act as crack initiators in some instances, lowering strength in tension and shear. The ratio of pore volume V_P to the total (bulk) volume of pores and solid (V_s) was defined as porosity (Haynes, 1986):

$$\varepsilon = V_P / (V_p + V_S) \tag{2.32}$$

The sintering of ceramic materials depends importantly on the distribution of pore sizes and the homogeneity of the porosity within the compact (Lange, 1984). The porosity of sintered materials also has an important effect on the strength and the fracture toughness of dental materials (Cattell et al., 1999, Guazzato et al., 2004b).

2.6.2.4 Vacuum Firing

Vacuum firing is widely used in dentistry. The vacuum applied removes the air or atmosphere from the interstitial spaces of the powder compact before sealing of the surface (Vines and Semmelman, 1957). Vacuum firing can not however remove all the air, which becomes spherical under the influence of surface tension and increased firing temperature. At the end of a vacuum firing, a strong compression is generated by the introduced atmospheric pressure applied on the low pressure bubbles. Therefore, vacuum firing results in a denser and less porous final product. Enhanced optical (Binns, 1983) and mechanical properties have been reported by vacuum firing (Kulp et al., 1961, Ferracane, 2001).

2.6.2.5 Firing Temperature and Time

The mechanical strength and the appearance of ceramics are influence by the firing temperature and time. Cheung and Darvell (2002) investigated the effect of time and temperature on the appearance and porosity of sintered dental porcelain. They found that

the reduction in dental porcelain porosity is more sensitive to temperature than sintering time. The influence of the predrying time, heating rate, holding time, and cooling time on the sintering kinetics and porcelain structure have also been discussed (Claus, 1989). Slow cooling is normally applied to dental ceramics after firing to avoid thermal shock (Ferracane, 2001).

2.6.3 Heat Extrusion

Heat extrusion is a method used together with the lost wax technique to produce complex shaped dental restorations (Cattell et al., 1999). It was first utilised for all ceramic restoration production with the introduction of the IPS Empress system (Beham, 1990). A refractory ring containing the target restoration shape is invested, burned out and transferred to a pneumatic heat press furnace. The pre-cerammed ingots can next be extruded via a thermal resistant alumina plunger under pressure from the press furnace. Heat extrusion directly applies the pressure on the ceramic grain boundaries and eliminates the possibility of coarsening during densification (Chiang et al., 1996). After refractory removal, the restoration may be completed on a colour matched die by the application of stains and glazes or alternatively cut back and veneered with the thermally compatible porcelains prior to glazing (Wohlwend and Schairer, 1990). Compared with a conventional sintering process, heat extrusion gives excellent marginal fit, reduces the overall porosity, increases Weibull modulus and flexural strength (Gorman et al., 2000). More uniform crystal distributions within a glass matrix after heat extrusion are well documented in literature (Dong et al., 1992, Oh et al., 2000). Crystal structure alignment of lithium disilicate glass-ceramics after heat extrusion can lead to a higher fracture toughness (Albakry et al., 2004b).

2.7 X-ray Diffraction Analysis

X-ray diffraction (XRD) is a versatile technique which reveals detailed crystallographic information on the structure of natural and manufactured materials. Amorphous glass provides X-ray patterns with broad humps whilst crystals show distinct peaks due to diffraction (Cullity and Stock, 2001, Jenkins and Snyder, 1996). The fundamental law of X-ray crystallography is Bragg's law (Bragg and Bragg, 1924). According to Bragg's Law, parallel X-ray beams incident on a set of crystal planes at a glancing angle θ are reflected on different crystal planes (Fig. 2.14). The path length difference between the parallel incident beams is:

$$MP + PN = 2d \sin\theta \tag{2.33}$$

Where d refers to the interplanar space and can be expressed in terms of the lattice constraints a, b, c, and the miller indices (hkl):

$$\frac{1}{d^2} = \frac{h^2}{a^2} + \frac{k^2}{b^2} + \frac{l^2}{c^2} \tag{2.34}$$

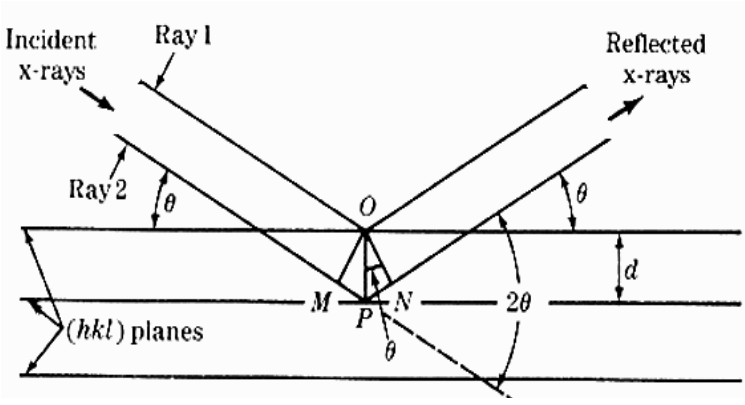

Fig. 2.14: Schematic for Bragg's Equation

These reflected beams will reinforce one another when the path difference is equal to an integral ratio of the incident X-ray beams wavelengths, expressed as:

$$2d \sin\theta = n\lambda \tag{2.35}$$

Where λ is the wavelength of the X-ray, n is an integer. Therefore, for a given incident X-ray with wavelength λ, only specific angles θ satisfy the Bragg Equation. For a simple cubic system, d can be derived as:

$$\frac{1}{d^2} = \frac{h^2}{a^2} + \frac{k^2}{b^2} + \frac{l^2}{c^2} = \frac{h^2 + k^2 + l^2}{a^2} \tag{2.36}$$

When n = 1, all possible Bragg angles at which diffraction occurs on planes (hkl) can be derived:

$$\sin^2\theta = \frac{\lambda^2}{4a^2}(h^2 + k^2 + l^2) \tag{2.37}$$

For tetragonal crystals:

$$\sin^2\theta = \frac{\lambda^2}{4}\left(\frac{h^2 + k^2}{a^2} + \frac{l^2}{c^2}\right) \tag{2.38}$$

A laboratory X-ray diffractometer is schematically illustrated in Fig. 2.15. Fine powder specimens are placed on the support table H, which can be rotated with angle θ. Monochromatic X-rays from source S are incident on the powder specimen, and the reflected X-rays are detected by the detector F. Based on diffracted intensity and 2θ, characteristic diffraction patterns are plotted and then compared with diffraction standards for phase identification (Cullity and Stock, 2001). Internal standard quantitative XRD analysis has been used to investigate the leucite content of dental glass-ceramics (Ong et al., 2000). Glass-ceramic powders were mixed with a selected standard substance at different weight fraction respectively for X-ray diffraction analysis. A calibration curve demonstrated a linear relationship of the intensity ratio of the diffraction of leucite and the standard was established. The leucite concentration can then be obtained easily (Cullity and Stock, 2001). Maximum peak height and the peak areas were used for the calculation of

intensity ratio, and calculation based on peak area showed higher accuracy compared to the one using maximum peak heights (Piché et al., 1994, Assmann et al., 2000, Ong et al., 2000). Natural leucite (Rasmussen et al., 1998) or leucite-containing frits (Assmann et al., 2000, Mackert and Evans, 1991) were used as standards for quantitative analysis. Due to the impurities in natural leucite and the variations in leucite-containing frits, it is hard to duplicate this process. The high purity of hydrothermally synthesised leucite has proven to be more reliable as an standard and gives higher accuracy (Zhang et al., 2007b). However, due to the glass composition and the stoichiometry change during crystallisation, the leucite crystals crystallised in this study have a slightly distorted structure, which is different from these hydrothermally synthesised leucite. Therefore, an internal standard quantitative analysis for the leucite content for this study may not be accurate and reliable.

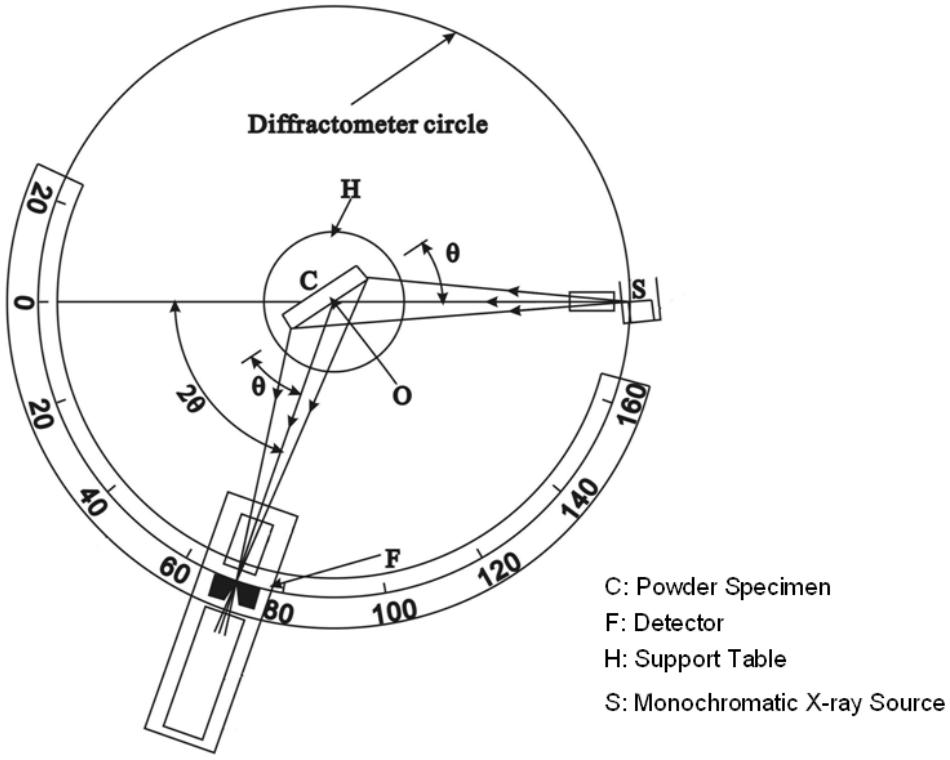

Fig. 2.15: Schematic of an X-ray diffractometer (Cullity and Stock, 2001).

2.8 Secondary Electron Microscopy

Secondary Electron Microscopy (SEM) allows the microstructure and topographic analysis of a given solid specimen (McMillan, 1979). Glass and glass-ceramic specimens can be polished to remove contaminants and expose the microstructure prior to etching. The specimens are coated with gold or carbon to reduce charging and increase secondary electron emission.

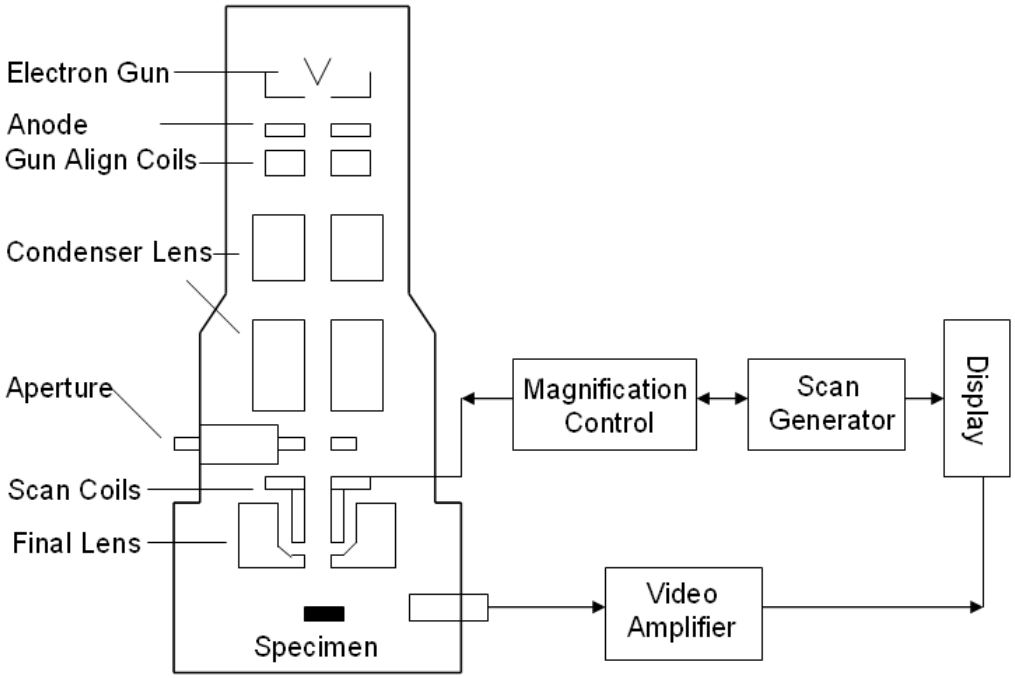

Fig. 2.16: Schematic drawing of a scanning electron microscope.

As illustrated in Fig. 2.16, the electron gun emits electrons which are accelerated towards an anode and emitted as a high energy beam of monochromatic electrons. The condenser lens in conjunction with selected accelerating voltage focus the electron beam via an aperture, which is used to control the depth of field and brightness. Two sets of coils are used to work as an electromagnetic lens to control the helical path of the electron beams, which are focused on the specimen by the final lens. When the continuous electron beam hits the specimen surface, weakly bound electrons are ejected and produce secondary electrons.

The secondary electrons are collected and amplified, then converted to an electronic signal which can be portrayed on a cathode ray tube (CRT). A short specifically oriented, single crystal tungsten wire which is electrolytically etched to a very sharp point is present in the field emission secondary electron microscope (FESEM). This generates a finer electron source (within 5 nm in diameter) and results in improvement in spatial resolution and minimises sample charging and damage (Postek, 1980, Goldstein et al., 1992).

2.9 Energy Dispersive X-ray Spectroscopy

Energy dispersive X-ray spectroscopy (EDS) is a chemical microanalysis technique performed in conjunction with a scanning electron microscope (SEM). When a specimen surface is bombarded by incident electrons in the SEM, electrons ejected from the atoms comprising the sample surface, results in electron vacancies. The electron vacancies are filled by electrons from a higher shell and X-rays emitted to balance the energy differences between electrons. The energy of these X-rays is collected by the X-ray detector containing a silicon semiconductor with a thin layer of gold on both surfaces. When the X-ray strikes the silicon crystal, a number of electrons in the silicon detector are excited and the energy of X-ray is therefore converted into an electronic signal which is amplified by a preamplifier. The resulting electronic pulse is processed by a computer multichannel analyser system, and plotted as a spectrum of the energy versus relative counts of the detected X-rays (Postek et al., 1980). Qualitative and quantitative analysis of the elements present in the sample can be achieved via an X-ray analysis program. Nonetheless, EDS is inefficient for high energy X-rays and light elements detection. This is due to the tendency of semiconductor penetration, the small possibility of X-ray generation and the tendency of low energy X-ray absorption by the coating (Postek et al., 1980, Goldstein et al., 1992). In this study specimens were carbon coated and characteristic X-rays were acquired using a Pentafet detector and a beryllium window to give quantitative analysis, which were used in conjunction with Appen Factors for glass prediction.

2.10 Thermal Analysis

Differential Thermal Analysis (DTA) is a thermoanalytical technique by which the temperature difference between a substance and a reference material is measured as a function of temperature, while both the substance and the reference materials are subjected to a controlled heating program. It has been widely used to characterise the kinetics of chemical reactions and the nucleation and crystallisation kinetics of glass (Kissinger, 1956, Zdaniewski, 1975). The mechanism of the crystallisation in a glass were studied by DTA using different size powders (Barker and James, 1988, Xu et al., 1991, Tošić et al., 2000, Tošić et al., 2002, Ray et al., 1996). Surface nucleation demonstrates a broad crystallisation peak, whereas bulk crystallisation shows a sharp peak (Marotta et al., 1980). Studies on the nucleation temperature range, nucleation rate (Ray and Day, 1990) and the maximum nucleation temperature (Xu et al., 1991, Ray et al., 2000) of glass were carried out using DTA techniques, which are faster than methods using heat treated nucleation and crystallisation controls (Ray et al., 2000).

Differential Scanning Calorimetry (DSC) is a technique by which the difference in the amount of heat required to increase the temperature of a substance and a reference material is measured as a function of temperature. It is based on a power-compensated design. In a DSC apparatus, the sample crucible with weighed sample powder and a reference crucible are placed on holders which are connected to different thermocouples. During heating, different heat was applied to the sample substance and reference material in order to maintain them at an identical temperature. A DSC trace is plotted based on the difference in heat flow between the substance and the reference material against the furnace temperature (T). This trace demonstrates the glass transition temperature (T_g), crystallisation range, crystallisation temperature (T_p) and the melting temperature of the crystalline phase. The exothermic or endothermic peaks deviating from the base line ($\Delta T = 0$) reveals the chemical reactions of the glass upon cooling or heating. The area under the peak is directly proportional to the heat evolved or absorbed by the reacting

sample, and the height of the curve is directly proportional to the rate of reaction. Both DTA and DSC traces are influenced by the sample size, furnace atmosphere, reference material, heating rate, thermocouples and the packing density (Smykatz-Kloss, 1974).

2.10.1 Determination of Activation Energy

The theoretical basis for interpreting DTA/DSC results for isothermal glass crystallisation can be expressed by the Johnson-Mehl-Avrami kinetic equation, which describes the relationship between the evolutions of crystallisation with time t:

$$x = 1 - \exp[-(kt)^n] \tag{2.39}$$

Where x is the volume fraction crystallised after time t, n is the Avrami exponent which indicates the crystallisation mechanism. A value of n close to 1 indicates surface nucleation and $n = 3$ implies bulk nucleation. High values of n corresponds to narrow DTA/DSC peaks (Xu et al., 1991). k represents the reaction rate constant, which is temperature dependant and given by the Arrhenius Equation:

$$k = k_0 \exp(\frac{E}{RT}) \tag{2.40}$$

Where k_0 is the frequency factor, E is the activation energy, R is the universal gas constant and T is the temperature in Kelvin. Taking the logarithm of Equation (2.40) and the Arrhenius Equation into account:

$$\ln[-\ln(1-x)] = -\frac{E}{RT} nk_0 + n \ln t \tag{2.41}$$

Hence, the activation energy can be determined from a single DTA/DSC peak, which equals the slope of $\ln[-\ln(1-x)]$ versus $1/T$. The volume fraction crystallised (x) at any time t can be determined from the ratio of the partial area to the total area of a single crystallisation exotherm (Matusita et al., 1975, Xu et al., 1991, Ray et al., 1996).

A different approach for the activation energy determination was suggested by Kissinger (1956) based on the temperature dependence of the crystallisation. The position of the exothermic peak in the DTA/DSC curve varies according to the heating rate, according to the Kissinger Equation (1956):

$$\ln(\frac{\phi}{T_p^2}) = -\frac{E}{RT_p} + \text{constant} \tag{2.42}$$

Where ϕ is the DTA heating rate, T_p is the peak crystallisation temperature. Matusita and co-workers (1975, 1979, 1980) criticised the invalidity of the Kissinger equation when the majority of nuclei are formed during the DTA/DSC measurement and a modified Kissinger Equation was proposed:

$$\ln(\frac{\phi^n}{T_p^2}) = -m\frac{E_C}{RT_p} + \text{constant} \tag{2.43}$$

Where n is the Avrami exponent as described before, E_c represents the correct activation energy for crystallisation, and m is a numerical factor which depends on the crystallisation mechanism (Table 9.3 in Appendix) and relates to the Avrami exponent n. If the number of nuclei stays constant during the DTA/DSC runs, the value of m equals n, and when the nucleation occurs during DTA/DSC runs, $m = n - 1$. Therefore, the activation energy for crystallisation can be determined by the plot of $\ln(\phi^n / T_p^2)$ versus $1/T_p$. The above modified Kissinger Equation takes the crystallisation mechanism into account, and gives relatively high accuracy compared to the Kissinger Equation. This may not be entirely adequate if the crystallisation mechanism varies with heating rate. The Kissinger Equation was used for the activation energy calculation for this thesis, as the crystallisation mechanism was not confirmed.

2.10.2 Determination of the Nucleation Rate and the Range

The relationship between the number of nuclei per unit volume N and the DTA/DSC peak crystallisation temperature T_p is given by Weinberg (1991):

$$\ln N = \ln \phi + \frac{E_c}{RT_p} + \text{constant} \qquad (2.44)$$

Therefore, the number of nuclei N is proportional to $1/T_p$, for a constant DTA/DSC heating rate ϕ. Glasses are nucleated at different lower temperature T_n for a duration of t_n, then heated with a different rate until crystallisation. The nucleation rate and the range can be determined by plotting the height of the DTA/DSC peak $(\delta T)_p$ or the $1/T_p$ versus T_n and has proven to correlate well with those determined by the classical optical technique of nucleation followed by isothermal crystallisation. There are potential errors when the nucleation and growth curve of the glasses are overlapped (Ray et al., 1991).

2.11 Mechanical Strength Testing

Mechanical strength is an important factor which controls the clinical behaviour of dental restorations. In vivo, complex stress distributions are present. Dental materials are strong under compression, however, they are brittle and weak in tension (Anusavice and Hojjatie, 1987, Cattell et al., 1997b). Different methods were used in dentistry for the strength testing including diametral tensile test (Williams and Smith, 1971, Baharav et al., 1997), three-point bending (Seghi et al., 1995, Cattell et al., 1997a), four-point bending (Ban and Anusavice, 1990, Giordano et al., 1995) and biaxial flexural strength testing.

The diametral tensile test provides a simple experimental method for brittle materials testing, involving loading a cylinder of material across its diameter. Shear force initiates at the point of contact and tensile stresses are generated in the diametric plane of the cylinder. However,

the stress distribution developed within the loaded specimen is complex and could lead to different modes of failure (Ban and Anusavice, 1990, Darvell, 1990). This method is not suitable for materials which deform significantly before fracture (Zidan et al., 1980).

Compared with the diametral tensile test, both three-point and four-point bending tests establish a state of pure tension on lower surface of the tested specimen (Berenbaum and Brodie, 1959). Therefore, the tests provide a tensile stress on the lower surface. However, the method is sensitive to flaws and defects near specimen edges. Undesirable edge fracture can occurs (Wagner and Chu, 1996) and results in large variation in the strength data. These test specimens are normally large in size, 18 - 42 mm in length according to the International Standard ISO 6782 (2008). The defects introduced by the large specimen size may not be representative of those that present in the clinical situation.

2.11.1 Biaxial Flexural Strength Test

Biaxial flexural strength (BFS) test is a more reliable method for the strength measurement of brittle materials (Ban and Anusavice, 1990). Disc-shaped specimens are supported by a ring, several ball bearings. The load is applied centrally to the disc specimen via a flat or ball ended piston. Discs with a diameter of 12.0 - 16.0 mm and a thickness of 1.0 - 1.4 mm were used for the test according to the International Standard ISO 6782 (2008). These smaller size discs result in an improved representation of the volume and dimension of clinical restorations (Palin et al., 2003). The BFS test has greater tolerance for specimen thickness and crosshead speed compared with three-point bending test. The maximum tensile stresses occur within the central loading area, eliminating spurious edge failures associated with three-point and four-point flexure test (Ban and Anusavice, 1990). The strength is calculated using formulae derived by Timoshenko and Woinowsky-Krieger (1959). The calculation of biaxial flexural strength takes the specimen elastic modulus and the Poisson's ratio into account, which attributes to more accurate results. For dental ceramic, a Poisson's of 0.25 (the lateral strain to the axial strain within the elastic range) is used. The reliability or probability of fracture of the test material can be characterised by means of a Weibull

statistical treatment (Ritter, 1986).

2.11.1.1 Loading Geometry

Different test fixtures including ring on ring (Zeng et al., 1998), piston on three balls (Cattell et al., 1999) and piston on ring (Fleming et al., 1999, Palin et al., 2003) were used in literature.

The ring on ring test assumes the specimen disc is thin compared with its diameter, and gives zero friction at the load contact (Morrell, 1999). However, a tendency of stress concentration opposite the loading ring was suggested by finite elemental analysis, which resulted in the failure originated from the loading ring position (Morrell et al., 1999). It is also pronounced that the eccentricity of the loading ring relative to the support ring and the friction play an important role on the test strength. The piston on three balls test was developed primarily to overcome warped test specimens (Morrell, 1999). However, the stress distribution might be complicated under the loading piston (Shetty et al., 1980, Zeng et al., 1996). Damage to the piston tip may also occur during fracture (Morrell, 1999). The ball on three-ball test fixture shows tolerance in specimen warpedness and the supporting balls can be seen as a continuous knife-edge support, since the maximum tensile stress in the centre of the disc is approximately independent from the number of support points (Kirstein and Woolley, 1967). Shetty et al., (1983) criticised the ball loading fixture due to the generation of the steep gradients parallel to the specimen surface and small stressed area associated with the loading ball. However, finite elemental analysis by Börger et al., (2004) showed that in a purely biaxial stress state the maximum tensile stress occurs in the centre of the disc underneath the loading ball. The stress field does not depend on the deformation of loading and supporting balls. A continuous knife-edge (ring) support however, gives better support for the test disc and has been used for bilayer material strength testing (Fleming et al., 2000, Fleming et al., 2004, Addison et al., 2007). The ball on knife-edge (ring) is therefore selected for this study. A plastic sheet can be used between the loading ball and the support balls/ring to evenly distribute the load and reduce the friction (Morrell, 1999).

2.11.1.2 Test Specimen Preparation

The valid use of the linear elastic equation to determine centre stress suggests that the deflection of the disc at its centre shall not exceed one half the specimen thickness according to the Ban and Anusavice (1990). Clinical ceramic crowns fabricated from a monolithic material or be a layered ceramic structure were typically 1.5 to 2.0 mm thick (Rekow and Thompson, 2007). It was suggested that the test specimen should be subjected to appropriate firings, finishing and glazing to mimic the clinical dental restoration (Binns, 1983). Specimen thickness of 2.0 mm (Wagner and Chu, 1996, Cattell et al., 1999, Palin et al., 2003) and 1.2 mm (Ohyama et al., 1999, Yilmaz et al., 2007) were widely used in the literature. Dorsch et al., (1993) performed biaxial flexural strength testing using different loading speed and specimen thickness and found very small difference in the biaxial flexural strength values. No relationship was found between the biaxial flexural strength and specimen thickness variation introduced by specimen lapping (Cattell et al., 1997b, Cheng et al., 2003). Studies on the effects of surface finishing showed smoother surfaces resulted in an increase in biaxial flexural strength (Williamson et al., 1996, Jager et al., 2000). However, specimen lapping in order to achieve a flat uniform surface was carried out to standardise surface flaws for this study.

2.12 Summary

Leucite glass-ceramic are widely used in dentistry for dental restorations to replace missing tooth structure. These materials when not fused to a metal substrate can be used as all-ceramic adhesively bonded restorations. Current leucite glass-ceramics however, have low flexural strengths (Cattell et al., 1999, Wagner and Chu, 1996, Gorman et al., 2000) and fracture toughness (Kelly, 1997, Gorman et al., 2000, Guazzato et al., 2004a) and may be more susceptible to brittle failure (Kelly et al., 1996). This has been associated with the leucite microstructure and thermal compatibility with the glassy phase. The thermal expansion difference between the glass matrix and the leucite crystals led to the development of tangential compressive stresses around the crystals which was considered responsible for the significant strengthening in leucite glass-ceramics (Denry et al., 1996). Glass-ceramic theory indicates controlled nucleation and growth heat treatments and controlled powder processing may improve the glass-ceramic microstructure (Cattell et al., 2005) leading to mechanical and wear property improvements (McMillan, 1979). This is predominantly via a surface crystallisation phenomenon in the leucite glass-ceramic system and with a nucleation heat treatment to produce copious amounts of nuclei (Cattell et al., 2006). Glasses with compositions around leucite stoichiometry should facilitate leucite crystallisation according to Schairer and Bowen phase diagram. Glass compositional modification using Appen Factors could produce glasses with different thermal expansions, which could put compressive stresses around leucite crystals after the cubic to tetragonal leucite transformation. This project therefore aims to produce a range of glasses with predicted thermal properties, and control the leucite crystallisation using two-step controlled crystallisation heat treatments. Control of the glass powder size was attempted in this project to take advantage of the surface crystallisation effect, in order to produce evenly distributed fine leucite microstructures and lead to higher flexural strength and reliable leucite glass-ceramics for Dentistry.

3 MATERIALS AND METHODS

3.1 The Programme of Work

1. To design and synthesise novel aluminosilicate glasses with tailored properties including density, thermal expansion coefficient, refractive index and fusion temperature using Appen Factors.

2. To explore the crystallisation kinetics of experimental aluminosilicate glass formulations and control the leucite crystal size, morphology and volume fraction.

3. To investigate selected commercial glass-ceramics as control materials.

4. To test the biaxial flexural strength of the experimental leucite glass-ceramics and control materials.

3.2 Commercial Materials

Three commercial leucite glass-ceramics (Table 3.1) were selected as control materials.

Table 3.1: The commercial glass-ceramics

Glass-Ceramics	Manufacturer	Batch No
Ceramco 3 (Dentine D2)	Dentsply, Ceramco, Burlington, USA	02111576
IPS Empress Esthetic (ETC2)	Ivoclar-Vivadent, Schaan, Liechtenstein	H22624
Optimal (Dentine A2)	Jeneric Pentron, Wallington, USA	E0766E1796

3.2.1 Specimen Preparation of Commercial Glass-Ceramics

Weighed Ceramco 3 dentine powder (0.96 gram) was mixed with 0.3 ml of modelling liquid (CH.B.24066, Vita, Germany). The powder slurry was transferred to a steel disc die (16 mm diameter x 50 mm depth) and vibrated for 30 seconds. Excess moisture was removed by a tissue for 30 seconds. The powder slurry was left under the weight of an inserted plunger under 1 x 10^5 Pa pressure for 60 seconds. After removal, the powder compacts were transferred and sintered in a dental porcelain furnace (Multimat MCII, Dentsply, Weybridge, UK) according to the manufacturers' instructions and firing cycles (Table 3.2).

Table 3.2: Firing cycles for Ceramco 3 glass-ceramic.

Firing Program	Dentine Firing	Glaze Firing
Firing Temperature (ºC)	930	920
Heating Rate (ºC/min)	45	45
Standby Temperature (ºC)	650	650
Holding Time (min)	1.0	0.5
Drying Time (min)	5	3
Preheat (min)	5	3
Vacuum (hPa)	50	Nil
Vacuum Release Temperature (ºC)	930	Nil

3.2.2 Fabrication of the Commercial Heat Extruded Specimens

Perspex discs (14 mm diameter x 2 mm thickness) were sprued onto muffle bases with 3.0 mm diameter spruing wax and surrounded by paper cylinders. Two hundred grams of IPS Empress Esthetic speed investment material (Lot: GL3038, Ivoclar-Vivadent, Schaan, Liechtenstein) was mixed with 32 ml of IPS Empress Esthetic investment liquid (Lot: GL3034, Ivoclar-Vivadent) and 22 ml of distilled water under vacuum for 90 seconds. The investment was then vibrated into the cylinder, and a muffle gauge was placed on the top of the cylinder to ensure a flat top surface for the refractory.

Commercial IPS Empress Esthetic glass-ceramic (ETC2) ingots and alumina plungers were placed in a room temperature burnout furnace (5365, Kavo, Ewl, Germany) and heated up to 850°C at a rate of 3ºC/minute. The refractory muffles were given 45 minutes to set, and then transferred to the preheated burnout furnace, set at 850°C and held for 45 minutes.

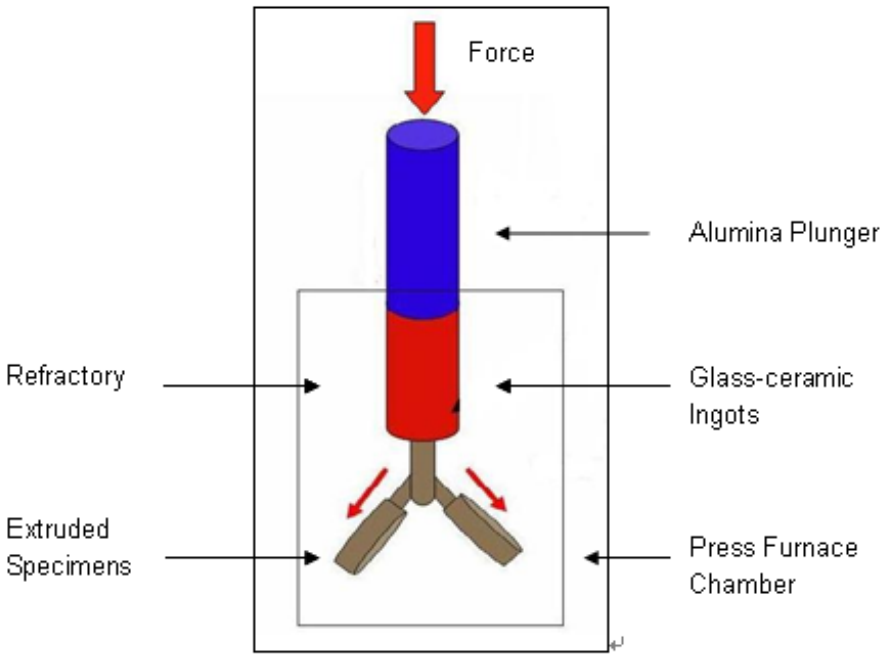

Fig. 3.1: Schematic of the heat extrusion within press furnace chamber.

Preheated Empress Esthetic glass-ceramic ingots or room temperature Optimal glass-ceramic ingots were placed into the refractory muffles followed by a preheated alumina plunger (Fig. 3.1), and heat extruded into the refractory using a preheated (700ºC) Optimal automatic press furnace (Jeneric Pentron, Wallington, USA) according to manufacturers' instructions (Table 3.3). The pressure was delivered via a pneumatic rod integral in the press furnace during the heat extrusion cycle.

Table 3.3: Heat extrusion cycles for the commercial glass-ceramics.

Heat Pressing Parameters	IPS Empress Esthetic (ETC2) Glass-ceramic	Optimal (A2) Glass-ceramic
Start Temperature (ºC)	700	700
Pressing Temperature (ºC)	1075	1165
Heating Rate (ºC/min)	60	40
Vacuum (%)	101	101
Holding Time Before Pressing (min)	20	20
Pressing Time (min)	15	15
Pressing Pressure (Pa)	5×10^5	5×10^5

After cooling, investments were removed from the sample discs with a sandblasting unit (Basic Quattro IS No: 29550000, Renfert, Germany) using 50 micron glass beads (SG4017 Bracon Ltd, Etchingham, East Sussex, UK) at 1.5×10^5 Pa pressure. A diamond disc (006, Bracon Ltd., UK) and a diamond bur (9907, Bracon Ltd., UK) was used to remove the sprue areas. All disc specimens were wet ground with P600, P800 and P1000 grade silicon carbide grinding papers in sequence on the compressive surface only, and the tensile surface was left as sandblasted. The specimens were cleaned using an ultrasonic bath with detergent for 10 minutes, followed by water rinsing for 3 minutes. The disc specimens were fired in a porcelain furnace (Multimatt MCII, Dentsply, Germany) according to the manufacturers' recommended firing cycles (Table 3.4). Firing schedules in Table 3.5 were chosen to mimic that used in realistic restoration construction.

Table 3.4: Firing cycles for the commercial glass-ceramics.

Firing	Standby Temp (ºC)	Drying Time (min)	Preheat (min)	Heating Rate (ºC/min)	Firing Temp (ºC)	Vacuum Release Temp (ºC)	Holding Time (min)
Stain Firing (E)	403	2.0	2.0	60	770	769	1.0
Glaze Firing (E)	403	3.0	3.0	60	770	769	1.0
Incisal Firing (O)	648	2.0	3.0	55	968	968	0.3
Stain Firing (O)	648	2.0	3.0	55	910	910	0.3
Glaze Firing (O)	648	2.0	3.0	55	938	0	0

E = IPS Empress Esthetic ETC2 glass-ceramic, O = Optimal A2 glass-ceramic

(the second incisal bake was fired at 949ºC).

Table 3.5: Firing schedules for the commercial heat extruded glass-ceramics.

Glass-Ceramics	Incisal Firing	Stain Firing	Glaze Firing	Total Firing
IPS Empress Esthetic (ETC2)	0	2	2	4
Optimal (A2)	2	1	1	4

3.3 Experimental Materials

3.3.1 Glass Prediction

Glass compositions (Table 3.6 and marked in Fig. 2.12) were designed using Appen Factors to achieve the required properties including density, thermal expansion coefficient (TEC) and refractive index (R.I.). Property prediction was carried out using the following equation:

$$X = \alpha_1 p_1 + \alpha_2 p_2 + \cdots + \alpha_n p_n = \sum_{i=1}^{n} \alpha_i p_i \qquad (3.1)$$

where X represents the properties of glass, α_i is the corresponding Appen Factors (empiristic factors) that each oxide contributes towards the glass properties, and p_i represents the concentration of the individual oxide in mole percentage. The Appen Factors used are listed in Table 9.1 in Appendix. The fusion temperature contribution (Winkelmann and Schott, 1894) of the each oxide was also used to estimate the experimental glass fusion temperature.

Glass A was used as a starting point in terms of its composition as previous work indicated that its crystallisation behaviour produced favourable mechanical and microstructural properties (Cattell et al., 2005). Glasses were designed by modifying the compositions around leucite stoichiometry, and to get a range of glass thermal expansions to encourage tangential compression of the leucite phase following crystallisation. Zirconia and niobium oxide was also introduced to study their efficiency as nucleating agents. The glass design shows an increase in TiO_2 and a decrease in Na_2O from glass A to D. An increase in K_2O and a decrease in SiO_2 are clear from glass A, D, C and B in sequence.

Table 3.6: Glass composition (in mole %) of the experimental glass batches.

	SiO_2	Al_2O_3	K_2O	CaO	TiO_2	Na_2O	Li_2O	MgO	ZrO_2	Nb_2O_5
Glass A	74.6	10.7	7.9	2.1	0.3	4.7	1.1	0.5	N/A	
Glass B	69.3	10.1	12.5	2.1	0.5	3.9	1.1	0.5	N/A	
Glass C	70.9	10.0	10.9	2.1	0.5	3.9	1.1	0.5	N/A	
Glass D	71.9	10.1	9.5	2.1	2.2	2.6	1.1	0.5	N/A	
Glass E	71.7	10.3	8.1	2.2	0.2	4.3	1.1	1.2	0.7	
Glass NB	69.3	10.1	12.5	2.1	N/A	3.9	1.1	0.5	N/A	0.5

3.3.2 Glass Synthesis

A range of glasses batches were prepared based on the compositions listed in Table 3.6, and the reagents used are listed in Table 9.2 in Appendix. Glass A was prepared by placing the components (Table 3.6) into a baffle jar and agitating on a jar roll for 2 hours. The well mixed batch was transferred to an alumina lined cordierite sagger, and heated in an electric kiln (Fredrickson Kiln Co., New York, USA) at a rate of 10ºC/min to 1316ºC and held for 7 hours. The glass melt was cooled down to room temperature within the kiln. The glass surfaces were removed by sandblasting. The glass frit was then crushed and wet ground with 5 mm diameter yttria stabilised zirconia (YTZ) media, and subsequently screened through a 125 μm nylon screen. The resultant powder was designated as starting glass A.

Glass B, C and D with compositions listed in Table 3.6 were weighed and mixed respectively. The glass batches were placed in a one litre ball mill pot (Pascall Engineering ltd, UK) and agitated on the ball mill for 2 hours to achieve homogeneous glass batches. The well mixed glass batches were transferred to an alumina crucible (CC68, Almath Crucibles Ltd, UK), and heated in an electrical chamber furnace (UAF1600 furnace, Lenton, UK) at a rate of 10ºC/min to 1550ºC and held for 5 hours. The molten glass was immediately transferred to a preheated furnace (Tris Burnout furnace, Dentalfarm, Italy) and annealed at 500ºC for 2 hours, followed by furnace cooling. After cooling, the glass frit was crushed and ball milled for 2 hours with a mixture of 19.0 mm and 26.4 mm diameter alumina grinding media. The resultant glass powder was screened using a 125 μm sieve.

Glass B was remelted in a platinum crucible at 1400ºC for 2 hours, followed by 2 hours annealing at 500ºC, and then furnace cooled. The same milling process described previously was then applied. The glass powder was screened to 125 μm and designated as homogenised glass B (HB).

Glass NB batches were mixed as described previously, and then placed on a platinum/rhodium (90/10) crucible, heated in an electrical chamber furnace (UAF1600 furnace, Lenton, UK) at a rate of 10ºC/min to 1550ºC and held for 5 hours, followed by 2 hours annealing at 500ºC and then furnace cooled. After cooling, the glass frits were smashed and milled for 2 hours. The ground glass powders were remelted in the same crucible at 1550ºC for 2 hours, followed by 2 hours annealing at 500ºC, and furnace cooled. The same milling process described previously was applied to get glass NB powders.

3.3.2.1 Attritor Milling of Glass A

The relationship of the glass particle size with the milling and its effect on the glass crystallisation was investigated. Starting glass A powder prepared in section 3.2.2 was wet ground with distilled water in an Attritor Mill (Model 1-S Lab Attritor, Union Process, USA) with 5 mm yttrium toughened zirconium oxide (YTZ) grinding media (Tosoh Inc., USA) at a rate of 400 rpm. The glass slurry was withdrawn quickly from the milling chamber after 15, 30, 45, 60, 90 and 120 minutes of milling. External cooling was not employed at any point during the milling run. The sample taken at 120 minutes was then further milled with 2 mm YTZ grinding media for another 120 minutes, and designated as 4hr A (Fig. 3.2).

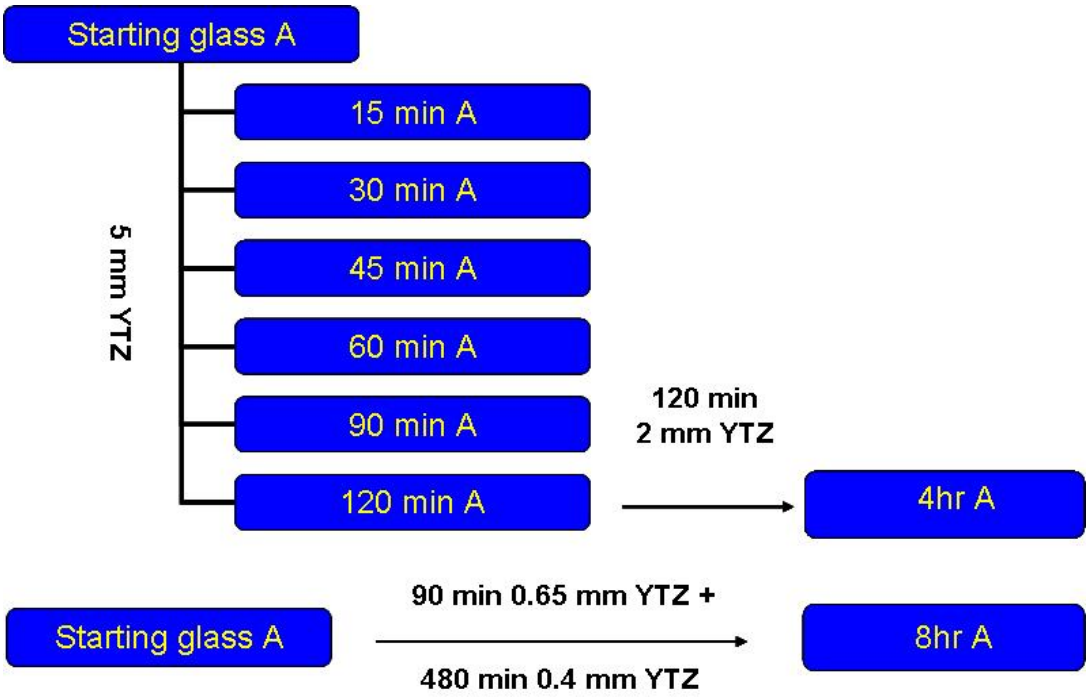

Fig. 3.2: Attritor mill process for glass A.

In order to further reduce the glass powder size, a separate milling regime was carried out and a rate of 400 rpm was used. The starting glass A was first Attritor milled with 0.65 mm YTZ grinding media (Tosoh Inc., USA) for 90 minutes, and then further milled with 0.40 mm YTZ grinding media (Tosoh Inc., USA) for 480 minutes. The consequent glass was designated as 8hr A (Fig. 3.2).

3.3.2.2 Inductively Coupled Plasma - Mass Spectrometer Elemental Analysis

Starting glass A and Attritor milled A glasses were sent for elemental analysis (ALS Chemex, ALS Laboratory, Canada) in order to investigate the elements introduced during milling. A small portion of the glass samples (0.2 gram) were first mixed with 0.9 gram lithium metaborate and then fused at 1000ºC in a graphite crucible. After fusion, the lithium metaborate bead was dissolved in 100 ml of aqueous acid solution containing 4% (w/w) HNO_3 and 2% (w/w) HCl. The specimen were then analysed using an inductively coupled plasma - mass spectrometer (ICP-MS, Elan 9000, PerkinElmer) for quantitative elemental analysis.

3.3.2.3 Experimental Glass Design with Additional Zirconia

Zirconia has been suggested in the literature as a nucleating agent for different glass-ceramics (Yu et al., 2002, Jambi et al., 2007, Wang et al., 2009), however, its effect on the crystallisation of leucite glass-ceramics has not been well established. In order to explore and establish the effect of milling introduced zirconia on the glass crystallisation, a new glass E was designed by adding zirconia to the 4 hours Attritor milled glass A (4hr A), and then agitated on the ball mill for 2 hours to achieve homogeneity. The zirconia content in glass E was therefore triple that found in the milled 4hr A glass by ICP-MS analysis.

3.3.3 Particle Size Analysis

The particle size and distribution of the experimental glass（A, B, C, D, E and HB）powders were analysed using a Mastersizer/E particle analyzer (Malvern Instruments, UK). The powders were added to a circulating water bath at room temperature that circulated through a cell and was exposed to a laser. The particle size was measured by spherical volume in the range 0.5 μm to 180 μm by a 100 mm lens or 0.1 μm to 100 μm by a 45 mm lens according to the actual powder particle size range. The particle size distribution was evaluated with the span value defined as:

$$Span = \frac{D[v,0.9] - D[v,0.1]}{D[v,0.5]} \tag{3.2}$$

Where $D[v,0.9]$, $D[v,0.5]$, $D[v,0.1]$ indicate that the volume percentage of the particle with diameter of $D[v,0.9]$, $D[v,0.5]$, $D[v,0.1]$ is 90%, 50% and 10%.

3.3.4 Differential Scanning Calorimetry Analysis

In order to investigate the crystallisation kinetics, experimental glasses (A, B, HB, C, D and NB) were characterised by differential scanning calorimetry using a Stanton Redcroft DSC 1500 (Rheometric Scientific, Epsom, UK) with matched pairs of platinum-rhodium alloy crucibles. Glass powders were sieved through 300, 125 and 45 μm sieves to give three different powder grades (125 < PS < 300 μm, 45 < PS < 125 μm and PS < 45 μm, where PS is the powder size). DSC runs using different powder sizes at a rate of 20ºC/min within in the temperature range of 25 to 1200ºC were carried out to evaluate the mechanism of glass nucleation. In order to investigate the activation energy for leucite crystallisation, DSC runs with different heating rates including 5, 10, 20, 25 and 40ºC/min were applied for glass powders (A, B, HB, C and NB, 45 < PS < 125 μm) respectively. The Kissinger Equation was applied for the activation energy calculation. Fifty milligrams of glass powder was weighed and used for all DSC runs. Alumina was applied as reference materials.

3.3.5 Crystallisation

3.3.5.1 Effect of Powder Size on Nucleation

Glass A was selected to investigate the effect of glass powder size on the crystallisation kinetics. Glass A (starting) and Attitor milled glasses: 30 min A, 45 min A, 60 min A, 90 min A, 120 min A, 4hr A and 8hr A (Fig. 3.2) were studied. Weighed glass powders (3.0 gram) were mixed with 0.9 ml of modelling liquid (VITA, CH B: 24066, Germany) respectively. The powder slurry was transferred to a rectangular steel mould (plunger cross section 27 x 6 mm^2) and the excess moisture was removed using a tissue for 30 seconds. The powder slurry was then compacted using the steel plunger under 3 x 10^5 Pa pressure for 1 minute. After removal, the glass compacts were placed on to platinum foils and heated in an electric furnace (RHF 1600, Carbolite, UK) from room temperature at a rate of 10ºC/min to 650ºC, held for 1 hour, and then ramped to 1120ºC and held for 1 hour, according to a previous protocol (Cattell, 2003). After the two-step heat treatment, the crystallised glass-ceramic

was air quenched.

3.3.5.2 Nucleation of Glass A (4hr A)

Powder compacts of glass A (4hr A) were prepared as described in section 3.3.5.1. In order to establish the optimum nucleation temperature, the glass compacts were heated from 25ºC at a rate of 10ºC/min to 600, 610, 620, 630, 640, 650, 660, 670, 680, 690 and 700ºC respectively and held for 1 hour, and further ramped at the rate 10ºC/min up to 1120ºC, and then held for 1 hour before air quenching.

Once the optimum nucleation temperature was established, experiments were carried out to investigate the effects of nucleation holds. Glass A (4hr A) compacts were heated from 25ºC at a rate of 10ºC/min to the optimal nucleation temperature for 0.5, 1, 2, 3, 4, and 5 hour holds respectively, and then ramped at 10ºC/min up to 1120ºC and held for 1 hour before air quenching.

3.3.5.3 Crystal Growth of Glass A (4hr A)

Once the nucleation temperature and optimum holding time were established, experiments were carried out to assess the crystal growth temperatures. The glass A (4hr A) compacts were heated from 25ºC at a rate of 10ºC/min to the nucleation temperature and held for 1 hour, then ramped at the rate 10ºC/min up to 1000, 1050, 1100 and 1120ºC respectively, and held for 1 hour before air quenching.

In order to evaluate the effects of the holding time on crystal growth, powder compacts were heated from 25ºC at a rate of 10ºC/min to 610ºC (1 hour hold), then ramped up to the optimum crystal growth temperature at a rate of 10ºC/min, followed by various crystallisation holds (0.5, 1, 2, 3, and 4 hours).

Glass E (4hr A with ZrO_2 additive) was compacted and crystallised at the optimised condition as established in 3.3.5.2 and 3.3.5.3.

3.3.5.4 Sanidine Crystallisation

In order to explore the sanidine crystallisation found in glass A (4hr A), glass A (4hr A) powder compacts were heated from 25ºC at a rate of 10ºC/min to the nucleation temperature, held for 1 hour, and then ramped at 10ºC/min up to 850ºC. Crystallisation holds of 1, 2 and 3 hours were next carried out before air quenching.

3.3.5.5 Crystallisation Study of Glass B, HB, C and D

Glasses B, HB, C and D and were compacted as described in section 3.3.5.1. The powder compacts were nucleated at 30ºC above their glass transition temperature (T_g) for one hour. Crystallisation was successively carried out at different temperatures with different hold times to establish the optimum crystallisation condition.

3.3.5.6 Crystallisation Study of Glass NB

Glass NB compact prepared as described in section 3.3.5.1 was placed on platinum foil. It was nucleated at 30ºC above glass transition temperature (T_g) for 1 hour, and successively ramped up to the DSC peak crystallisation temperature for 1 hour and then air quenching. A heating rate of 20ºC/min was used for the study.

3.3.6 Experimental Glass-Ceramic Specimen Preparation

3.3.6.1 Sintered Glass-Ceramic Fabrication

Weighed glass A (starting / 4hr A / 8hr A), B, HB, C, D and E (50.0 grams) were placed on custom-made refractory trays (made from IPS Empress Esthetic investment materials as described in 3.2.2). They were then heated using a two-step heat treatment with the parameters established in section 3.3.5 (Table 3.7) respectively. After the heat treatment, the glass-ceramics were withdrawn and air quenched. Sandblasting with 50 micron glass beads (SG4017 Bracon Ltd, Etchingham, UK) was carried out to remove any investment sitting on the glass-ceramic surfaces. Glass-ceramic frits (starting A, 4hr A, 8hr A, B, HB, C,

D and E) were crushed and ground in a ball mill (Pascall Engineering ltd, UK) for 2 hours with a mixture of 19.0 mm and 26.4 mm diameter zirconia grinding media, and then screened using a 125 μm sieve.

Glass-ceramic powder (1.0 gram) was moistened with 0.3 ml of modelling liquid (VITA, CH B: 24066, Germany), and then transferred to a hardened steel die (16 mm diameter x 50 mm depth). Thirty seconds of vibration was applied to bring excess moisture to the surface and then excess moisture was removed using a tissue for 30 seconds. The glass-ceramic slurry was then pressed under 3 x 10^5 Pa pressure in a hydraulic press. After removal, the disc specimens were sintered in a porcelain furnace (Multimatt MCII, Dentsply, Germany) according to firing cycles in Table 3.8. Thirty specimens from each group were prepared. All disc specimens were wet ground on both surfaces with P320, P600, P800 and P1000 grade silicon carbide grinding papers in sequence to achieve a disc specimen thickness of 2.0 mm. The specimens were cleaned using an ultrasonic bath with detergent for 10 minutes, followed by water rinsing. One stain and one glaze firing (Table 3.9) was applied to glass-ceramic A (starting, 4hr A and 8hr A) specimens to mimic the realistic firings necessary for dental restorations.

Table 3.7: Two-step heat treatment schedule for experimental glasses.

Experimental Glasses	Nucleation Temperature (ºC)	Nucleation Hold (hours)	Crystallisation Temperature (ºC)	Crystallisation Hold (hours)	Heating Rate (ºC/min)
Glass A (starting)	650	1	1120	1	10
Glass A (4hr A)$_1$	650	1	1120	1	10
Glass A (4hr A)	610	1	1050	1	10
Glass A (8hr A)	650	1	1120	1	10
Glass B	610	1	870	1	10
Glass HB	620	1	795	1	20
Glass C	620	1	920	1	10
Glass D	670	1	1000	1	10
Glass E	610	1	1050	1	10

Table 3.8: Firing cycles for experimental glass-ceramics.

Firing Programme	Glass-Ceramics					
	A (starting / 4hr A / 8hr A)	B	HB	C	D	E
Standby Temperature (ºC)	538	538	538	538	538	538
Drying Time (min)	5	5	2	2	2	5
Preheat (min)	5	5	2	2	2	5
Heating Rate (ºC/min)	38	38	38	38	40	38
Vacuum (Pa)	55	55	55	55	55	55
Vacuum Release Temperature (ºC)	1025	1179	1099	1179	1119	1025
Firing Temperature (ºC)	1040	1180	1100	1180	1120	1040
Holding Time (min)	2.0	6.0	2.0	2.0	4.0	2.0
Cooling Time (min)	3.0	3.0	3.0	3.0	3.0	3.0

Table 3.9: Stain, glaze and ingot firing cycles.

Firing Programme	Starting / 4hr A / 8hr A Glass-ceramics			HB Glass-ceramic Ingot Firing
	Ingot Firing	Stain Firing	Glaze Firing	
Standby Temperature (ºC)	538	538	500	538
Drying Time (min)	5	1	5	2
Preheat (min)	5	2	2	2
Heating Rate (ºC/min)	38	55	55	38
Vacuum (hPa)	55	Nil	Nil	55
Vacuum Release Temperature (ºC)	1025	Nil	Nil	1099
Firing Temperature (ºC)	1040	780	860	1100
Holding Time (min)	2.0	0	0.3	2.0
Cooling Time (min)	3.0	3.0	3.0	3.0

3.3.6.2 Experimental Ingot Fabrication

Weighed glass-ceramic powders (1.6 gram, glass-ceramic A (4hr A) and glass-ceramic HB) were transferred to a specially made steel die (punch diameter 13.0 mm, Specac Ltd, UK). The die punch was loaded with a hydraulic pressure of 0.5 x10^5 Pa and held for 30 seconds. After removal, the powder ingots were sintered in a dental porcelain furnace (Multimat MCII, Dentsply, UK) using the ingot firing cycles listed in Table 3.9.

3.3.6.3 Experimental Glass-Ceramic Heat Extrusion

Thirty perspex discs were sprued onto muffle bases with 3.0 mm diameter spruing wax and surrounded by rubber cylinders. These discs were then invested using 200 grams of IPS Empress Esthetic speed investment material (Lot: GL3038, Ivoclar-Vivadent, Schaan, Liechtenstein), mixed with 32 ml of IPS Empress Esthetic investment liquid (Lot: GL3034, Ivoclar-Vivadent) and 22 ml distilled water. Mixing was carried out under vacuum for 90 seconds, and muffle gauges were placed on the top of the refractory cylinders to ensure a flat top surface. After 45 minutes, the investment were transferring to an 850°C preheated burnout furnace (5365, Kavo, Germany) and held for 45 minutes.

Room temperature glass-ceramic A (4hr A) ingots were placed into the refractory muffles followed by a preheated alumina plunger, and then transferred to a preheated (700ºC) Optimal automatic press furnace (Jeneric Pentron, Wallington, USA). A set of experiments were carried out to establish the heat extrusion parameters for the experimental glass-ceramics. Heat extrusion was performed according to the parameters in Table 3.10. The pressure was delivered via a pneumatic rod integral in the press furnace during the heat extrusion. The heat extrusion for the glass-ceramic HB was carried out using a pressing furnace (EP 3000, Ivoclar Vivident, Schann, Liechtenstein). The extrusion parameters were finalised and listed in Table 3.10.

Table 3.10: Heat Extrusion cycles for the experimental glass-ceramics A (4hr A) and HB.

	Glass-ceramics A (4hr A)	Glass-ceramics HB
Start Temperature (ºC)	700	700
Pressing Temperature (ºC)	1040	1150
Heating Rate (ºC/min)	40	60
Vacuum (%)	101	N/A
Holding Time (min)	15	15
Pressing Time (min)	10	#
Pressing Pressure (Pa)	5×10^5	#
Absorb Speed (E, micron/min)	N/A	300
Ring Size (g)	200	200

#Pressing time and pressure was delivered automatically by the press furnace (approx 8 mins).

After cooling, investment was removed from the sample discs with a sandblasting unit (29550000, Renfert, Germany) using 50 micron glass beads (SG4017 Bracon Ltd, Etchingham, UK) at 1.5×10^5 Pa pressure. A diamond disc (006, Bracon Ltd., UK) and a sintered diamond bur (9907, Bracon Ltd., UK) were used to remove the sprue areas. All disc specimens were wet ground to P1000 silicon carbide grinding paper on the compressive test surface only. Subsequently, the specimens were ultrasonically cleaned for 10 minutes, followed by 3 minutes water rinsing. Heat extruded glass-ceramic A (4hr A) specimens were fired in a porcelain furnace (Multimatt MCII, Dentsply, Germany) using one stain and one glaze firings (Table 3.9) to mimic the realistic firings required for dental restorations.

3.4 Differential Thermal Expansion Analysis

Glass frits (A, B, C, D and NB) were cut into blocks ($6 \times 6 \times 16$ mm^3) using a diamond saw. The glass blocks were polished on both sides against P600 silicon carbide grinding paper to achieve flat surfaces. After grinding, the glass specimens were cleaned using an ultrasonic bath for 3 minutes.

Three grams of glass-ceramic powder (Ceramco 3 Dentine, glass-ceramic A - E) were moistened using 0.9 ml of modelling liquid (VITA, CH B: 24066, Germany) and transferred to

a split steel mould (27 x 6 mm^2 cross section). The compacts were then pressed under 3 x 10^5 Pa pressure in a hydraulic press. After removal, the bar specimen were sintered in a dental porcelain furnace (Multimatt MCII, Dentsply, Germany) according to the dentine firing cycle in Table 3.2 (section 3.2.1) and firing cycles in Table 3.8 (section 3.3.6.1).

Wax cylinders (8 mm in diameter and 20 mm in length) were invested, burnt out and heat extruded using glass-ceramic A (4hr A), IPS Empress Esthetic glass-ceramic (ETC2, H22624 Ivoclar-Vivadent, Schaan, Liechtenstein) and Optimal glass-ceramic (Dentine A2, E0766E1796, Jeneric Pentron, Wallington, USA). The heat extrusion procedures are described in section 3.3.6.3 and 3.2.2 respectively.

The thermal expansion coefficient (TEC) of the glass and glass-ceramic samples were measured using a differential dilatometer (DIL 402PC, Netzsch Instrument, Germany) in a temperature range between 25ºC and 1200ºC, at a heating rate of 3ºC/min. Softening point protection was employed during measurement. A calibration run using a standard alumina rod was carried out between 25ºC to 1200ºC at 3ºC/min prior to the experimental measurements. The plot of the change in length against temperature was corrected against the calibration plot. The glass transition temperature (T_g) and dilatometer softening point (D_{sp}) of the specimens were evaluated from the corrected plot. The thermal expansion (α) was calculated using the following formula:

$$\alpha(T_0 - T) = \frac{1}{L_0}\frac{\Delta L}{\Delta T} = \frac{1}{L_0}\frac{L_T - L_0}{T - T_0} \qquad (3.3)$$

Where ΔL is the change in length, L_T is specimen length at temperature T, L_0 is the original length, ΔT is the change in temperature, and T_0 is the original temperature.

3.5 X-ray Diffraction Analysis

3.5.1 High Temperature X-ray Diffraction (HTXRD)

High temperature X-ray diffraction (HTXRD) analysis was performed on glasses (A (4hr A), B, C, D and HB) to study the phase crystallisation at temperature. An X'Pert Pro X-ray diffractometer (Panalytical, the Netherlands) with flat plate $\theta/2\theta$ geometry and Ni-filtered Cu-Kα radiation (λ_1 = 1.540598 Å and λ_2 = 1.5444260 Å) was used for the HTXRD. Glass frits were selected randomly and placed separately in a 25 ml zirconia grinding jar and ground for 3 minutes using a vibratory mill (MM200, Glen Creston Ltd, UK). The glass powders were screened to 38 μm and placed on a Pt strip in a high temperature furnace (Anton Parr HTK 16, Anton Parr, Austria) which was mounted on the X'Pert Pro X-ray diffractometer. Room temperature X-ray diffraction data was continuously collected from 10º to 80º (2θ range) with a step size of 0.0167º (2θ) and a step time of 26.67 seconds. The glass was subsequently heated at a rate of 1ºC/second. The furnace temperature was monitored using an Anton Parr TCU 2000 temperature controller. High temperature X-ray diffraction measurements were taken at 20ºC temperature intervals from 500ºC to 1100ºC using a standard 15 minutes short scan (2θ range: 10º to 80º, step size: 0.0167º, step time 26.67 seconds). All measurements were made 5 minutes after the temperature was stabilised to allow the domain structure to equilibrate. Calibration was carried out with a NIST standard reference material (SRM) 660a (LaB6, lanthanum hexaboride). The limit of detection for the XRD analysis was 1 wt%.

In order to explore the relationship of phase crystallisation and the crystallisation time, glass A (4hr A) was heated at 1ºC/second to the peak crystallisation temperature according to DSC. High temperature X-ray diffraction patterns at the crystallisation temperature were obtained using standard 15 minutes short scan. 12 continuous x-ray patterns were recorded.

3.5.2 Room Temperature X-ray Diffraction

Room temperature X-ray diffraction analysis was performed on all experimental glasses and the crystallised glass-ceramics, in order to determine their phase composition. Glass and glass-ceramic powders were prepared as described in 3.5.1. Powders were placed in the X'Pert Pro X-ray diffractometer (Panalytical, the Netherlands) using Silicon zero background substrate holders with flat plate geometry. Ni-filtered Cu Kα radiation (λ_1 = 1.540598 Å and λ_2 = 1.5444260 Å) was used. Data were collected from 5 to 120º 2θ, with a step size: 0.0334º, step time 200.03 seconds. Calibration was also carried out with a NIST standard reference material (SRM) 660a (LaB6, lanthanum hexaboride).

3.5.3 Structural Refinement

XRD data were refined using General Structure Analysis Software (Larsen and Von Dreele, 2004) in conjunction with the ICDD database. The model of tetragonal leucite was based on the structure suggested by Mazzi *et al.* (1976), with a space group I41/a with lattice parameters of a = 13.0654 Å, and c = 13.7554 Å (1 Å = 10^{-10} m). The model ICDD number was 00-038-1423. Cubic Leucite (ICDD, 01-076-2298), which has a space group of Ia-3d was used with starting lattice parameters of a = 13.4300 Å (Dove et al., 1993). The sanidine model used was a space group of C2/m with lattice parameters of a = 8.604 Å , b = 13.0350 Å , c = 7.1750 Å and beta = 116º angle (Weitz, 1972). It has an ICDD entry number of 00-025-0618. Sixteen background parameters were used, and the mean unit cell dimensions were calculated.

3.6 Secondary Electron Imaging

The morphology of the experimental glasses and heat treated glass-ceramics was investigated using Secondary Electron Microscopy (SEM). Glass-ceramic samples were embedded in epoxy resin, polished down to 0.3 μm alumina micropolisher (Buehler, USA), cleaned in ethanol for 30 seconds, and subsequently ultrasonically cleaned for 10 minutes. The specimen stubs were then etched with 0.1% hydrofluoric acid (HF) for 60 seconds, followed by water rinsing. The specimen stubs were gold coated using an automatic sputter coater (Agar Scientific Ltd, England) prior to SEM examination. Photomicrographs were taken using a field emission scanning electron microscope (FEI Inspect F, Oxford Instruments, UK or JSM 6300F, Joel Ltd., Japan) at an accelerating voltage of 10 KV and using secondary scanning electron imaging. Photomicrographs were quantitatively assessed using a light pen (270SD + INT-40, Trackballs, US) in conjunction with software (Sigma Scan Pro 5.0, Systat Software, Inc, USA). Leucite crystal size, content and morphology were evaluated by manually drawing around every single crystal. Biaxial fracture test fragments were attached to alumina specimen stubs using carbon cement. Specimens were gold coated and the fracture surfaces were studied.

Environmental scanning electron microscopy (FEI Quanta 3D DualBeam ESEM^{TM}, Oxford Instruments, UK) was used to provide 3D slice and view of the glass-ceramic B morphology.

3.7 Energy Dispersive X-ray Analysis

Energy dispersive X-ray analysis (EDS) was utilised to study the possibility of phase separation in the experimental glasses, and the relationship between the elemental composition of the commercial and experimental glass-ceramics and their thermal properties. EDS analysis was performed using a scanning electron microscope (JSM 6300, Joel Ltd., Japan) with 20 or 10 KV accelerating voltage. Glass and glass-ceramic specimens were embedded in epoxy resin and polished down to 0.3 μm alumina micropolish (Buehler, USA). Specimens were next cleaned in ethanol for 30 seconds, followed by 10 minutes of

ultrasonic cleaning and then 30 seconds of water rinsing. The specimen stubs were etched with 0.1% hydrofluoric acid for 60 seconds, followed by water rinsing and drying. Etched specimens were then carbon coated using a carbon thread evaporation unit (CED 030, Balzers Union Ltd, Liechtenstein). Characteristic X-rays were acquired using a Pentafet detector and a beryllium window to give quantitative results, via an X-ray analysis programme (Link eXLII, Oxford instruments, High Wycombe, UK). The EDS analyses of particles are limited to elements with atomic weights heavier than boron.

3.8 Density Measurement

Density measurement of the glass and glass-ceramics studied in the project was carried out using an analytical balance (Mettler AE 200, Mettler Instruments Ltd, UK) fitted with a density determination kit (Mettler ME-33360, Mettler Instruments Ltd, UK) based on Archimede's Principle. Distilled water was used as reference liquid. The weight of sample in air and the buoyancy of sample when immersed in distilled water were recorded with an accuracy of 0.1 mg. According to the protocol provided with the density determination kit, the sample density ρ could be calculated using equation:

$$\rho = \frac{A}{P} \cdot \rho_0 \qquad (3.4)$$

Where A is the sample weight in air, ρ is the buoyancy of buoyancy of the sample when immersed in distilled water, and the ρ_0 is the density of the reference material distilled water at measurement temperature.

3.9 Refractive Index Measurement

The Becke Line method (Allen, 1962) was used for the glass and glass-ceramic refractive index investigation. A thin layer of glass / glass-ceramic powder (PS < 125 μm) was placed on the centre of a clear microscope glass slide. Gentle taping was applied to the cover glass

in order to level the glass or glass-ceramic powder. A drop of refractive index liquid (1.500 < R.I. < 1.640, Cargille Laboratories, USA) was dropped at the corner of the glass slide and allowed to flow onto and around the glass / glass-ceramic powder. A cover glass slide was then placed on the top. The specimens were viewed under a transmitted and reflected light microscope (Olympus BX 60, Olympus Optical Co., Ltd, UK). A dark halo appeared around the powder particles (Fig. 3.3 B), when the powder R.I was lower than the surrounding oil and white halos (Fig. 3.3 A) occurred when the powder had higher R.I. Therefore, using a series of refractive index liquid allowed the glass / glass-ceramic to be matched when they were no longer visible (Fig. 3.3 C).

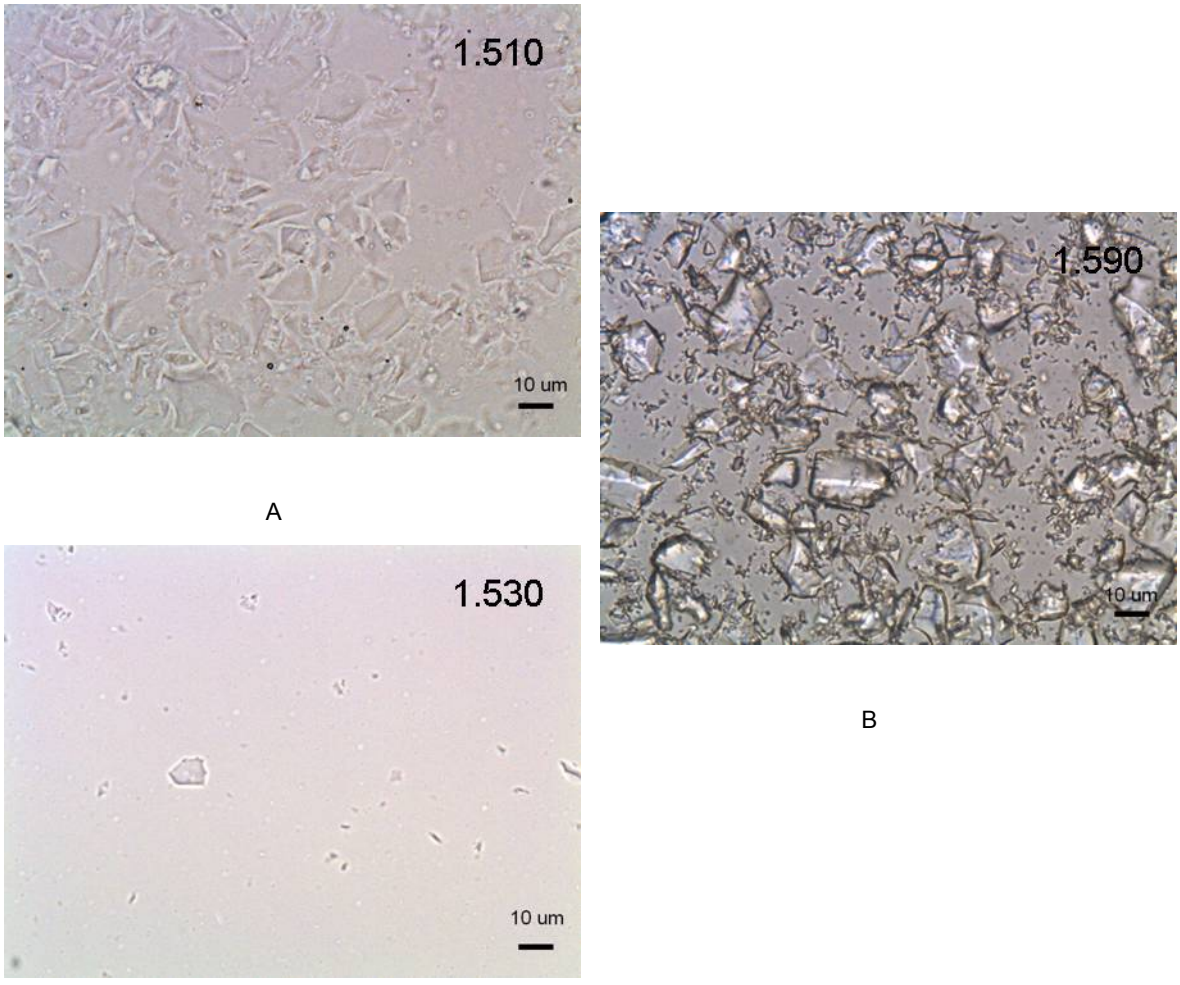

Fig. 3.3: Light microscope images (A, B and C) illustrated the Beck line method.

3.10 Biaxial Flexural Strength Testing

Thirty specimens per groups (sintered glass-ceramics: A (starting, 4hr A, 8hr A), B, HB, C, D, E, and heat extruded groups: 4hr A and IPS Empress Esthetic) were tested using the biaxial flexural strength test. Specimens were centrally loaded on a 10 mm diameter knife-edge support using a 4 mm diameter spherical ball indenter. A thin plastic sheet (0.03 mm) was positioned between the specimen surface and the indenter in order to evenly distribute the load. The load was delivered by an Instron testing machine (5567/H1580, Instron, Buckinghamshire, UK) with a 1 KN load cell via the indenter, at a crosshead speed of 1 mm/min until specimen fracture. The biaxial flexural strength was calculated using the Timoshenko and Woinowsky-Krieger Equation (1959):

$$\sigma_{\max} = \frac{P}{h^2}\left\{(1+\nu)\left[0.485 * \ln\left(\frac{a}{h}\right) + 0.52\right] + 0.48\right\} \qquad (3.5)$$

Where $\sigma_{\max}$ was the biaxial flexural strength of the material (maximum tensile stress), P was the measured load at fracture, h was the specimen thickness, a was the radius of the knife-edge support and ν was a Poisson's ratio of 0.25.

3.10.1 Statistics Analysis

The strength data was analysed using a one way ANOVA (Sigma Stat, version 2.03, SPSS Inc, Chicago, USA). The difference between groups were compared using Tukey's multiple comparison test ($p<0.05$).

3.10.2 Weibull Statistics

Weibull analysis of the test groups was also performed by the Weibull programme (Weibullsmith, Fulton Findings, USA). The biaxial flexural strength test values were ranked ascending. The double logarithm of 1/(1-median rank) was plotted vertically versus the

logarithm of the actual data values and a straight line fitted through the points using the median rank regression methods (determined by least squares regression curve fitting). Strength levels at the 1% and 10% probability of failure were calculated using the cumulative Weibull plots. The equation of Weibull two parameter distribution function used was:

$$P_f = 1 - \exp[-(\frac{\sigma}{\sigma_0})^m] \quad (3.6)$$

Where P_f is the probability of failure and the σ is the strength at a given P_f. The parameter σ_0 is the characteristic strength and m is the Weibull modulus. Goodness of fit to the straight line was calculated using the 90% critical correlation coefficient (CCC), which employed Monte Carlo simulation to approximate the distribution of the correlation coefficient from ideal Weibull's with median rank plotting positions. A good fit was indicated if the correlation coefficient was larger than the CCC and vice versa (Abernethey, 1996). Data sets were compared for the overlap of their double-sided confidence intervals at the 95% level to determine if data sets were different.

4 RESULTS

4.1 Results of the Glass Prediction

The density, thermal expansion coefficient and refractive index values predicted by Appen Factors (Table 9.1 in Appendix) and the fusion temperature predicted by Winkelmann and Schott Factors (Table 9.1 in Appendix) are listed in Table 4.1.

Table 4.1: Glass properties predicted by Appen and Winkelmann and Schott Factors.

	Density (g/cm^3)	Thermal Expansion Coefficient (TEC, $x10^{-6}/K$)	Refractive Index (R.I.)	Fusing Temperature (ºC)
Glass A (4hr A)	2.381	8.599	1.503	865.7
Glass B	2.410	10.345	1.510	840.0
Glass C	2.397	9.679	1.507	855.3
Glass D	2.408	8.690	1.515	873.7

4.2 Particle Size Analysis Results

The particle size analysis was carried out to measure the glass powder size and evaluate the relationship between the glass powder size and milling duration. The glass powder sizes are presented in volume median diameter D [v, 0.5], D [v, 0.1] and D [v, 0.9] (Table 4.2), and the particle size distribution was evaluated using span values.

The experimental glasses (A, B, HB, C and D, through 125 μm sieve) had a similar bimodal size distribution, and the size distribution span ranges from 3.68 to 4.65 (Table 4.2). Glass D showed a bigger span value than glasses A, B, HB and C. A D [v, 0.9] value of 70.39 μm was also reported for glass D which indicated the existence of larger glass size powder. Glass E had a single peak particle distribution with smaller D [v, 0.5], D [v, 0.1] and D [v, 0.9] values and a higher distribution span value when compared with the other glasses.

Table 4.2: Glass powder size of the experimental glasses.

Glasses Powders	Volume Median Diameter (SD, μm)			Span
	D [v, 0.5]	D[v, 0.1]	D [v, 0.9]	
Glass A (starting)	10.57 (0.17)	1.41 (0.03)	48.40 (0.42)	4.45 (0.04)
Glass B	12.44 (0.09)	1.75 (0.04)	47.80 (0.43)	3.70 (0.05)
Glass HB	10.29 (0.09)	1.53 (0.01)	41.66 (0.41)	3.90 (0.01)
Glass C	12.95 (0.14)	1.74 (0.04)	49.44 (0.43)	3.68 (0.03)
Glass D	14.72 (0.11)	1.97 (0.00)	70.39 (0.63)	4.65 (0.08)
Glass E	1.59 (0.01)	0.49 (0.00)	17.48 (0.12)	10.66 (0.05)

The particle size analysis results of glass A with different Attritor milling time are shown in Table 4.3. The glass powder size D [v, 0.5] was plotted against the milling duration and illustrated in Fig. 4.1. The glass A (starting) powder showed a bimodal powder distribution and a wide powder size range (Table 4.3). After 30 minutes milling with 5 mm yttrium toughened zirconium oxide (YTZ) grinding media, the glass powder distribution changed from bimodal to a single peak distribution. A remarkable reduction in the powder size (Fig. 4.1) and span value were noticed (Table 4.3). Further milling up to 90 minutes progressively reduced the glass powder size and gradually increased the span value. The glass powder size and distribution span values did not change significantly between the 90 min A and the 120 min A samples. Given two extra hours milling with 2 mm YTZ balls, the resultant glass A (4hr A) demonstrated a bimodal particle distribution, and a dramatic reduction in D [v, 0.5] and D [v, 0.1] values. However, an increase in D [v, 0.9] and span value were reported. Compared to 4hr A, the 90 minutes milling with 0.65 mm YTZ balls followed by 480 minutes milling with 0.4 mm YTZ balls on glass A (starting) powder resulted in further reduction in powder size and range (Table 4.3).

Table 4.3: Particle size analysis results for Attritor milled glass A series.

Glass Powders	Milling Process	Volume Median Diameter (SD, µm)			Span
		D [v, 0.5]	D [v, 0.1]	D [v, 0.9]	
Glass A	Starting Powder	10.57(0.17)	1.41 (0.03)	48.40 (0.42)	4.45 (0.04)
30 min A	Attritor milled with 5 mm YTZ	4.72 (0.02)	1.21 (0.01)	13.63 (0.06)	2.63 (0.02)
45 min A		3.49 (0.05)	0.99 (0.13)	11.33 (0.63)	2.96 (0.24)
60 min A		3.08 (0.04)	0.93 (0.07)	10.56 (0.22)	3.13 (0.02)
90 min A		2.95 (0.05)	0.85 (0.05)	10.45 (0.63)	3.25 (0.26)
120 min A		2.99 (0.15)	0.91 (0.03)	10.21 (0.58)	3.12 (0.05)
4hr A	120 min with 5 mm YTZ and 120 min with 2 mm YTZ	1.79 (0.05)	0.47(0.02)	15.51 (0.38)	8.39 (0.42)
8hr A	90 min with 0.65 mm YTZ and 480 min with 0.4 mm YTZ	1.14 (0.01)	0.27 (0.00)	7.74 (0.03)	6.53 (0.08)

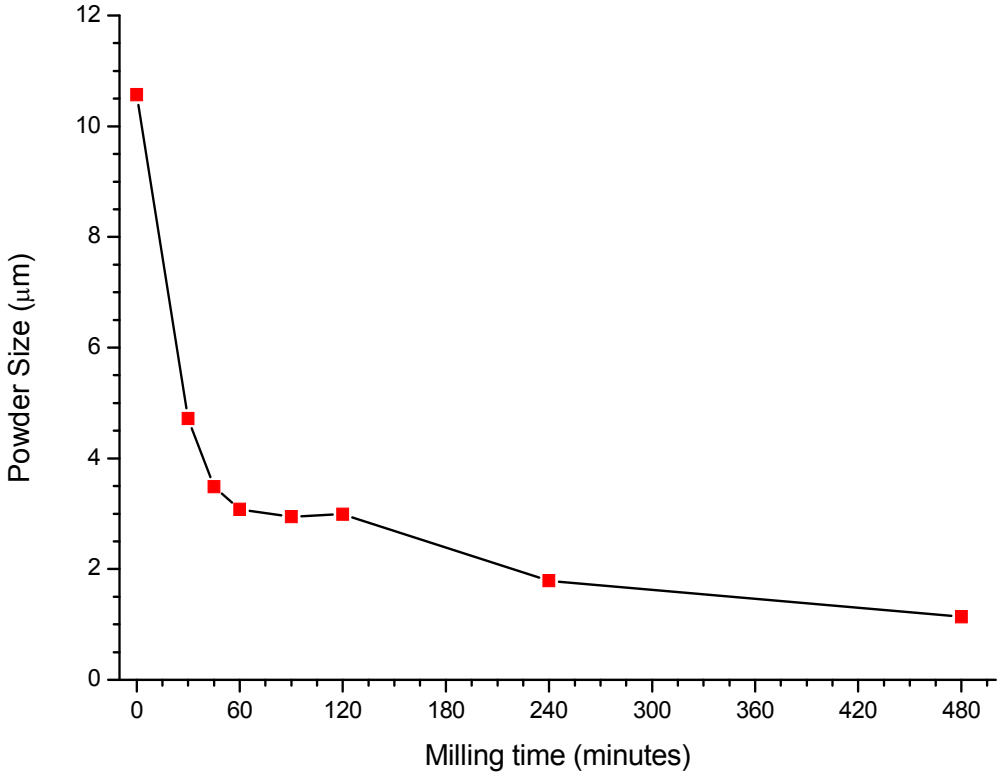

Fig. 4.1: Plot showing the relationship between milling time and powder size of glass A.

4.3 Results of the Coupled Plasma - Mass Spectrometer (ICP-MS) Analyses

Quantitative elemental analysis of the Attritor milled glass A series using ICP-MS is listed in Table 4.4. The amount of zirconium (Zr), yttrium (Y) and hafnium (Hf) increased gradually with the milling time. A relationship between the milling time and the zirconium, yttrium and hafnium content was illustrated in Fig. 4.2 and Fig. 4.3.

Table 4.4: Elemental composition of Attritor milled glass A by ICP-MS.

Glasses	Composition (wt %)							(ppm)		
	SiO_2	Al_2O_3	K_2O	CaO	TiO_2	Na_2O	MgO	Zr	Y	Hf
A (starting)	64.6	16.15	11.55	1.87	0.20	4.12	0.73	270	2.3	6.5
30 min A	62.9	15.58	11.3	1.82	0.19	4.03	0.71	698	23.6	16.4
45 min A	62.6	15.80	11.3	1.80	0.19	4.05	0.71	880	37.8	20.4
60 min A	61.3	15.45	10.75	1.78	0.19	3.87	0.70	948	39.4	22.7
90 min A	64.1	16.15	11.35	1.86	0.20	4.01	0.73	1170	59.4	28.5
120 min A	61.5	15.05	10.6	1.73	0.18	3.76	0.68	1480	77.7	36.0
4hr A	61.1	15.55	11.05	1.78	0.19	3.96	0.70	2430	139	60.1
8hr A	58.9	14.8	10.6	1.70	0.18	3.75	0.67	3930	250	99.6

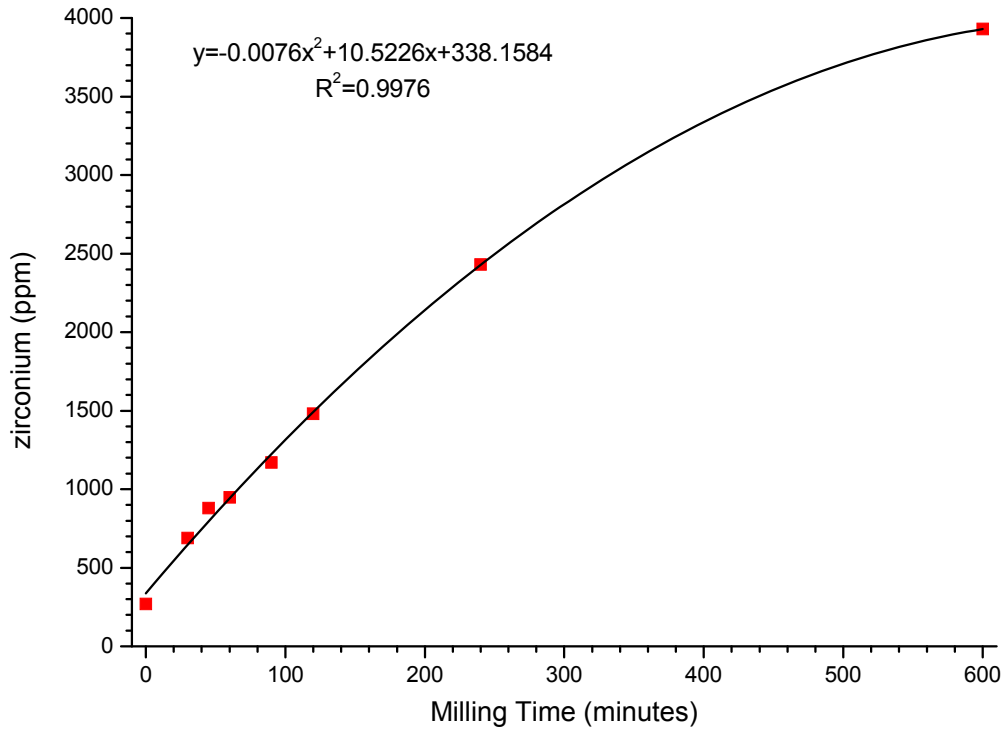

Fig. 4.2: The relationship between the zirconium content and milling time.

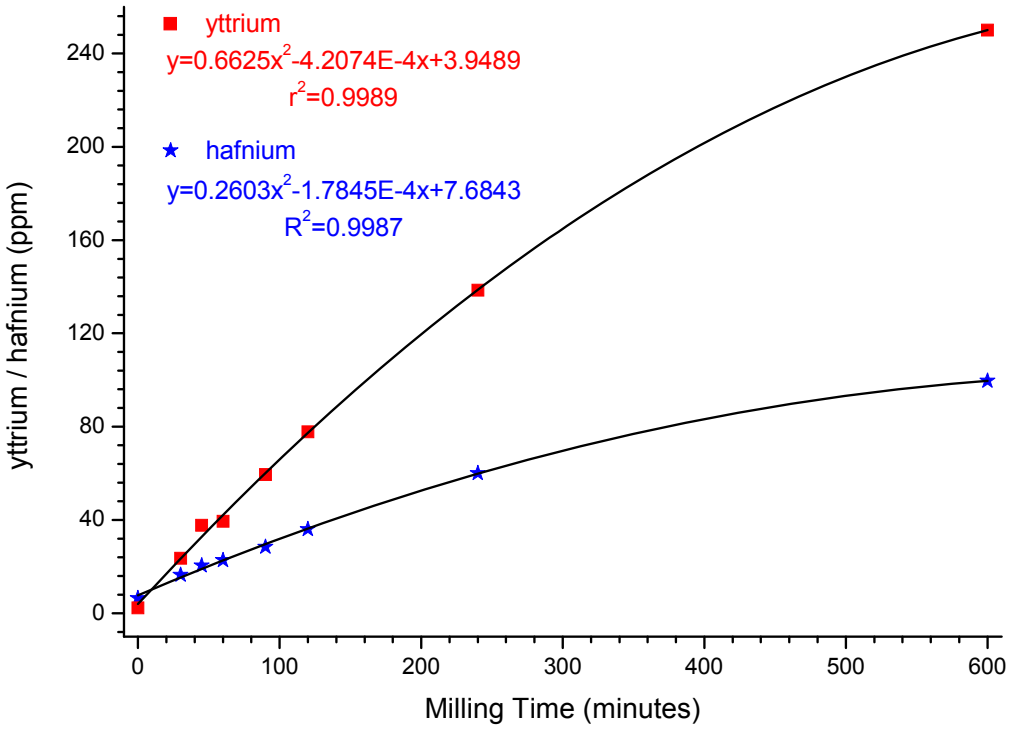

Fig. 4.3: The relationship between the yttrium / hafnium content and milling time.

4.4 Differential Scanning Calorimetry (DSC) Results

4.4.1 DSC Results for Glass A

The differential scanning Calorimetry analysis results of glass A (4hr A) powder heated at rates of 10ºC/min and 20ºC/min within the range 25ºC to 1200ºC are shown in Fig. 4.4. Broad exothermic peaks are presented between 800ºC and 920ºC with a peak temperature of 828.3ºC and 854.8ºC for the 10ºC/min and 20ºC/min run specimens. This data was thought difficult for activation energy calculation due to the broadness of the peaks and the possibility of both leucite and sanidine crystallisation.

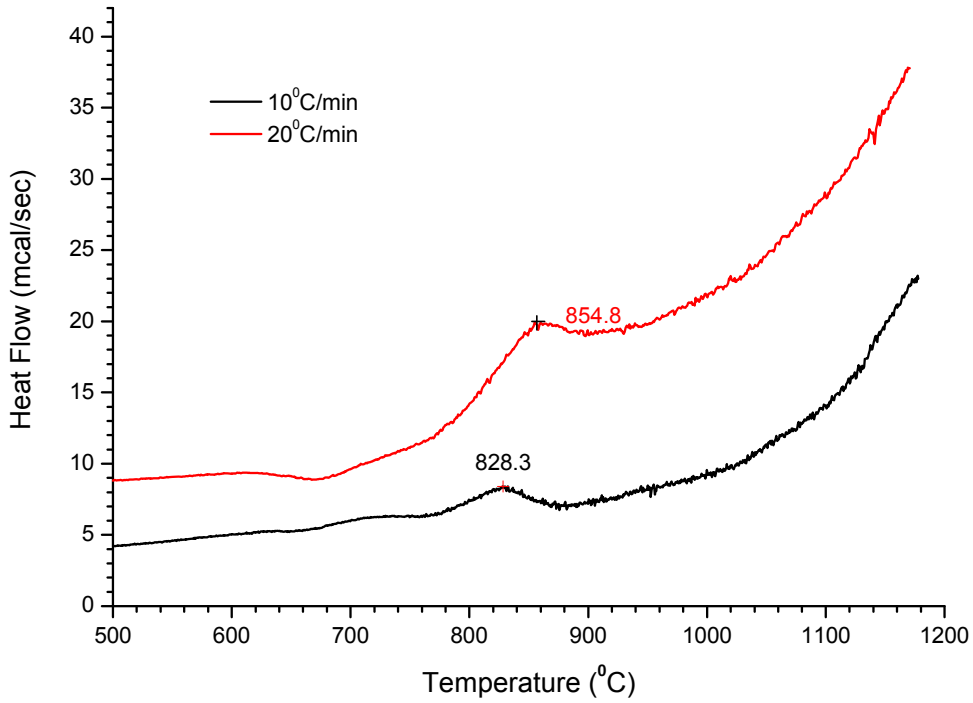

Fig. 4.4: DSC traces of glass A (4hr A) at different rates.

4.4.2 DSC Results for Glass B and HB

4.4.2.1 DSC Results for Glass B

The DSC traces of glass B powder with different powder sizes heated at a rate of 20ºC/min are presented in Fig. 4.5. The characteristic glass transition temperature (T_g) and peak crystallisation temperature (T_p) are given by the DSC traces and listed in Table 4.5. No significant change in both T_g and T_p was found with change in glass powder size.

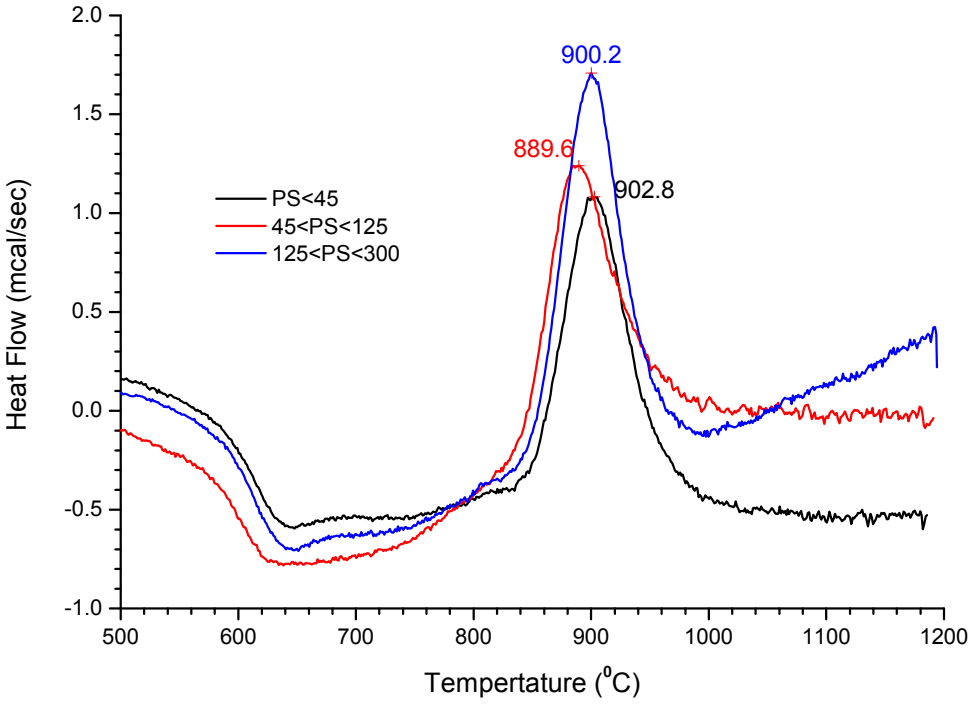

Fig. 4.5: DSC traces for different particle size glass B powders at a rate of 20ºC/min.

The DSC traces of the glass B powder (45<PS<125 μm) determined at different heating rates are given in Fig. 4.6. All traces exhibit distinct crystallisation peaks indicating the peak crystallisation temperature (T_p). It is clear that the peak crystallisation temperature and the crystallisation peak height increase gradually with the increased heating rate. The glass transition temperature (T_g) increases with the increase in heating rate (Table 4.5).

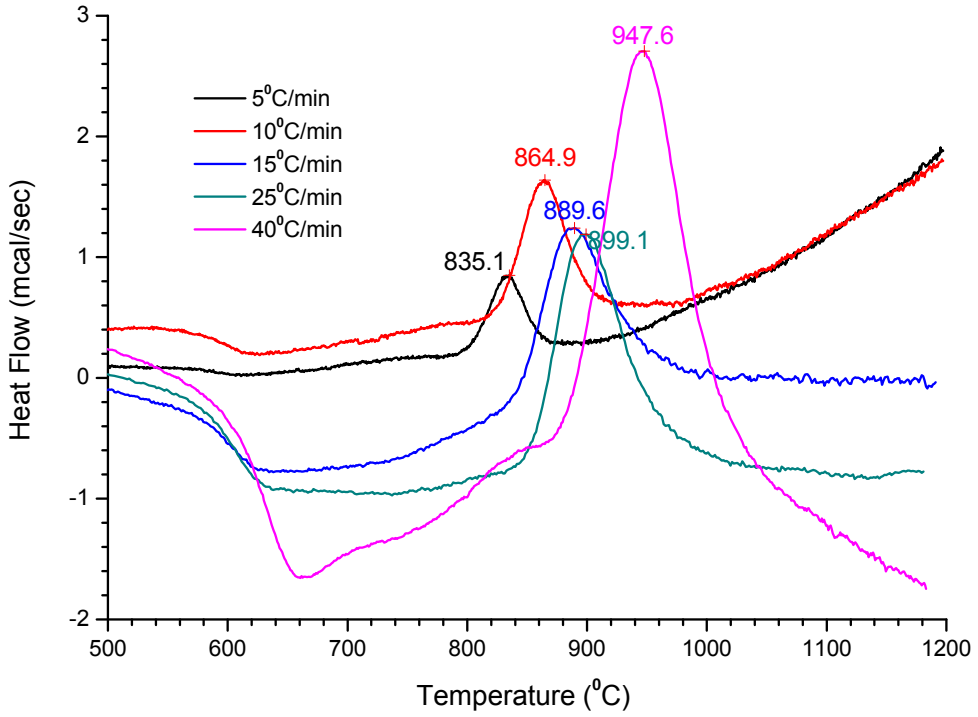

Fig. 4.6: DSC traces of glass B (45<PS<125 μm) at different heating rates.

Table 4.5: DSC results for glass B.

Glass Powder Size Range (μm)	Heating Rate (°C/min)	Glass Transition Temperature T_g (°C)	Peak Crystallisation Temperature T_p (°C)
PS<45	20	593.2	902.8
45<PS<125	5	595.8	835.1
	10	580.2	864.9
	20	587.8	889.6
	25	589.2	899.1
	40	612.8	947.6
125<PS<300	20	588.1	900.2

4.4.2.2 DSC Results for Glass HB (Homogenised Glass B)

Differential Scanning Calorimetry was performed on glass HB (homogenised glass B) with different powder sizes at a heating rate of 20ºC/min. Distinct glass transition and crystallisation peaks are illustrated for all HB glass samples (Fig. 4.7). There is little difference between the crystallisation peak temperature for glass HB with glass powder size 45<PS<125 µm and PS<45 µm. However, the crystallisation peak shifted towards lower temperature when the glass powder size was increased to 125<PS<300 µm. The glass transition temperature (T_g) and peak crystallisation temperatures (T_p) for glass HB with different glass powder sizes are presented in Fig. 4.7 and listed in Table 4.6.

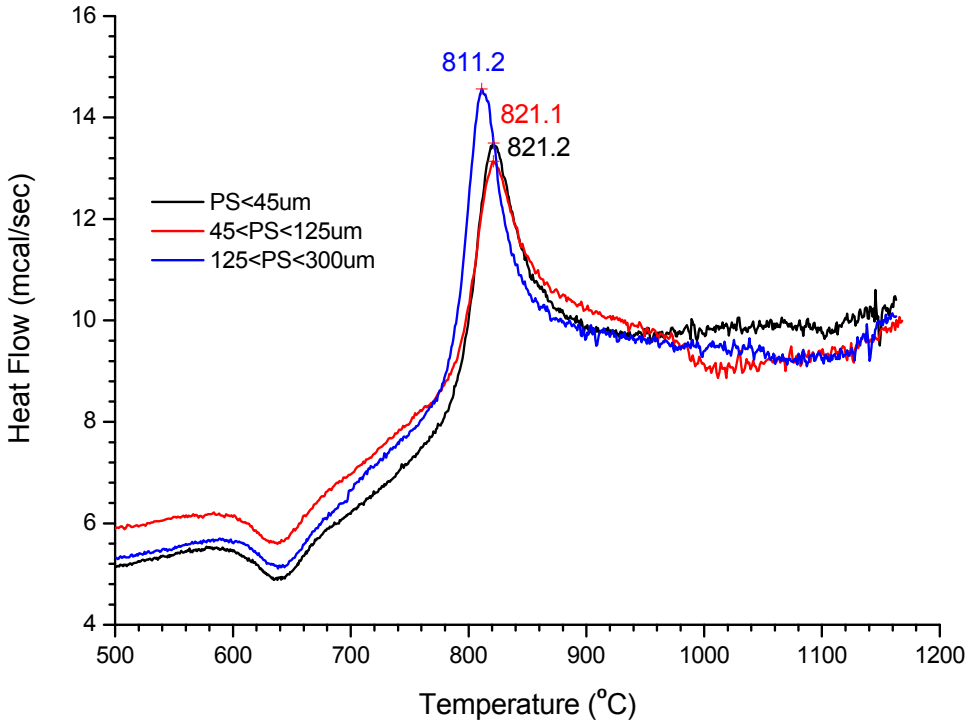

Fig. 4.7: DSC traces for different particle size glass HB powders at a rate of 20ºC/min.

The DSC traces of glass HB powder (45<PS<125 µm) determined at different heating rates are given in Fig. 4.8. The trace for glass HB at a rate of 5ºC/min demonstrates a clear

exothermic peak with a peak temperature of 770.4ºC. However, no glass transition temperature could be extrapolated from the plot. The glass transition became explicit with an increase in heating rates. The crystallisation peak temperature and the peak height increased with an increase in heating rate (Fig. 4.8) and the values are listed in Table 4.6.

Table 4.6: DSC results for glass HB.

Glass Powder Size Range (μm)	Heating Rate (ºC/min)	Glass Transition Temperature T_g (ºC)	Peak Crystallisation Temperature T_p (ºC)
PS<45	20	620.4	812.2
45<PS<125	5	N/A	770.4
	10	603.3	794.2
	20	614.8	821.1
	25	617.8	831.3
	40	618.8	855.4
125<PS<300	20	619.4	811.2

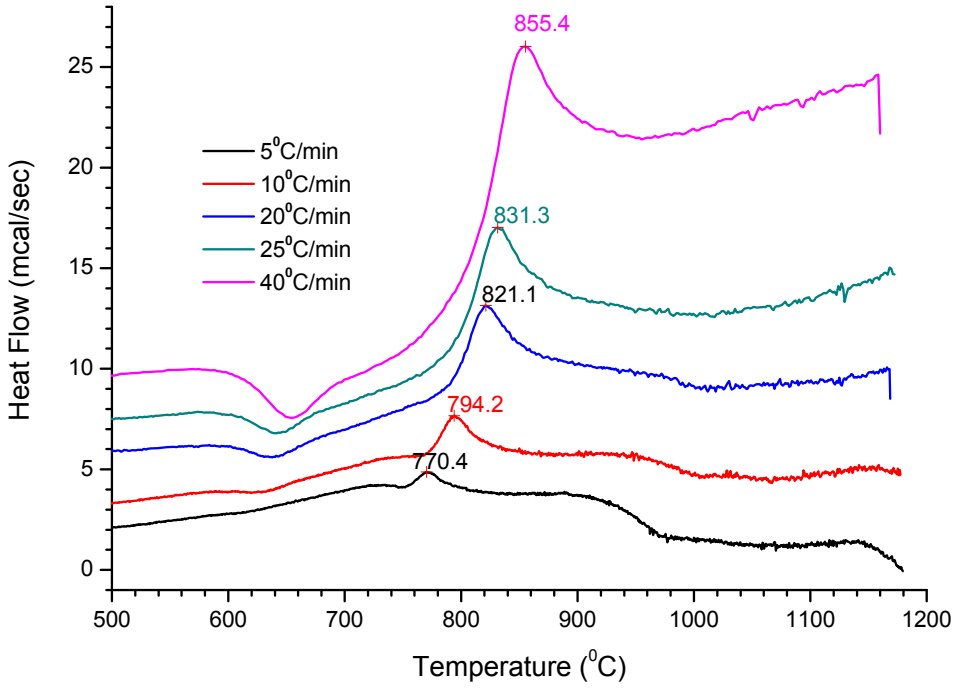

Fig. 4.8: DSC traces for glass HB (45<PS<125 μm) at different heating rates.

4.4.3 DSC Results for Glass NB

Differential Scanning Calorimetry results of glass NB (Nb_2O_5 containing glass) were plotted and illustrated in Fig. 4.9 and Fig. 4.10. The DSC traces of the different particle size glass NB powders at a heating rate of 20ºC/min shows little increase in the peak crystallisation temperature (T_p) and glass transition temperature (T_g) with reduced glass powder size (Fig. 4.9 and Table 4.7). A clear crystallisation peak (883.8ºC) was given by the DSC trace (glass powder size: 45<PS<125 µm) performed at 5ºC/min (Fig. 4.10). However, the glass transition temperature could not be extrapolated from the plot. Increase in glass transition temperature (T_g) and peak crystallisation temperature (T_p) was noticed with increase in heating rate (Fig. 4.10 and Table 4.7).

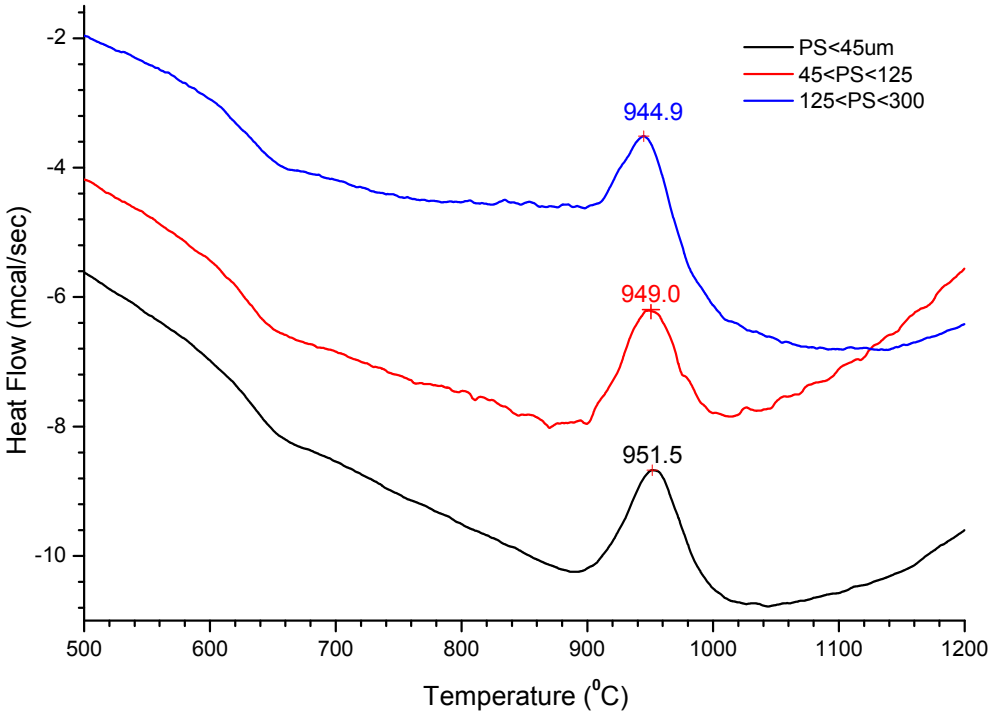

Fig. 4.9: DSC traces for different particle size glass NB powders at a rate of 20ºC/min.

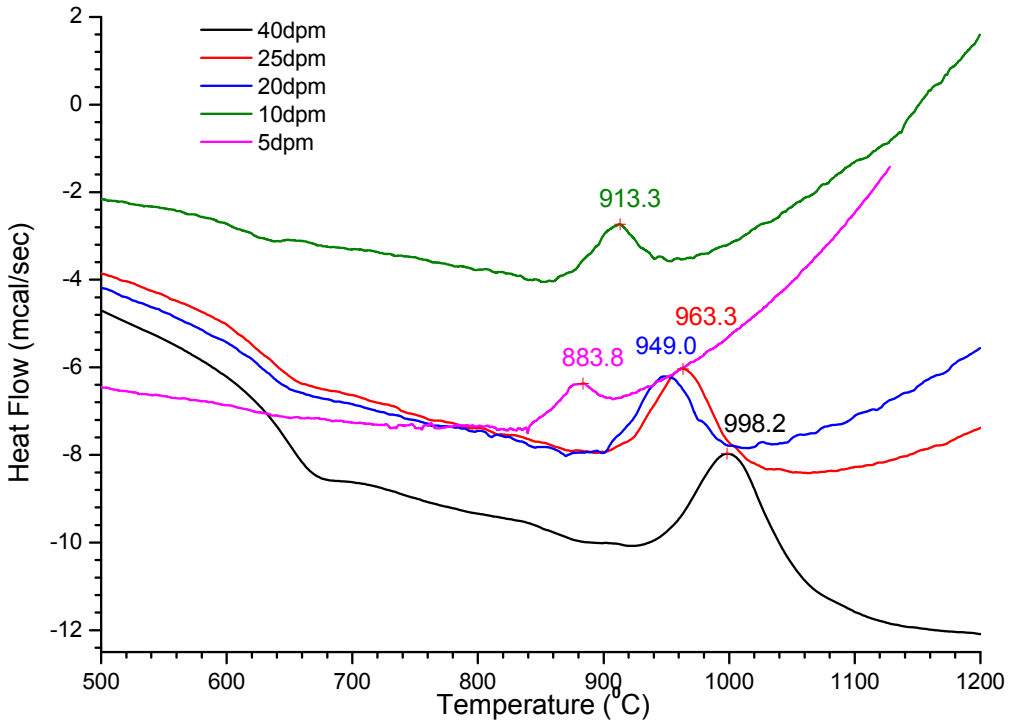

Fig. 4.10: DSC traces for glass NB (45<PS<125 μm) at different heating rates.

Table 4.7: DSC results for glass NB.

Glass Powder Size Range (μm)	Heating Rate (ºC/min)	Glass Transition Temperature T_g (ºC)	Peak Crystallisation Temperature T_p (ºC)
PS<45	20	602.4	951.5
45<PS<125	5	N/A	883.8
	10	598.0	913.3
	20	598.7	949.0
	25	613.6	963.3
	40	618.4	998.2
125<PS<300	20	595.4	944.9

4.4.4 DSC Results for Glass C

The DSC traces of glass C with different powder sizes at a rate of 20ºC/min are presented in Fig. 4.11. The glass transition temperature (T_g) did not change significantly with the powder size (Table 4.8). Exothermic peaks related to the crystallisation were detected for all different size glass C powders and the peak position did not change significantly according to the glass powder size change (Fig. 4.11 and Table 4.8).

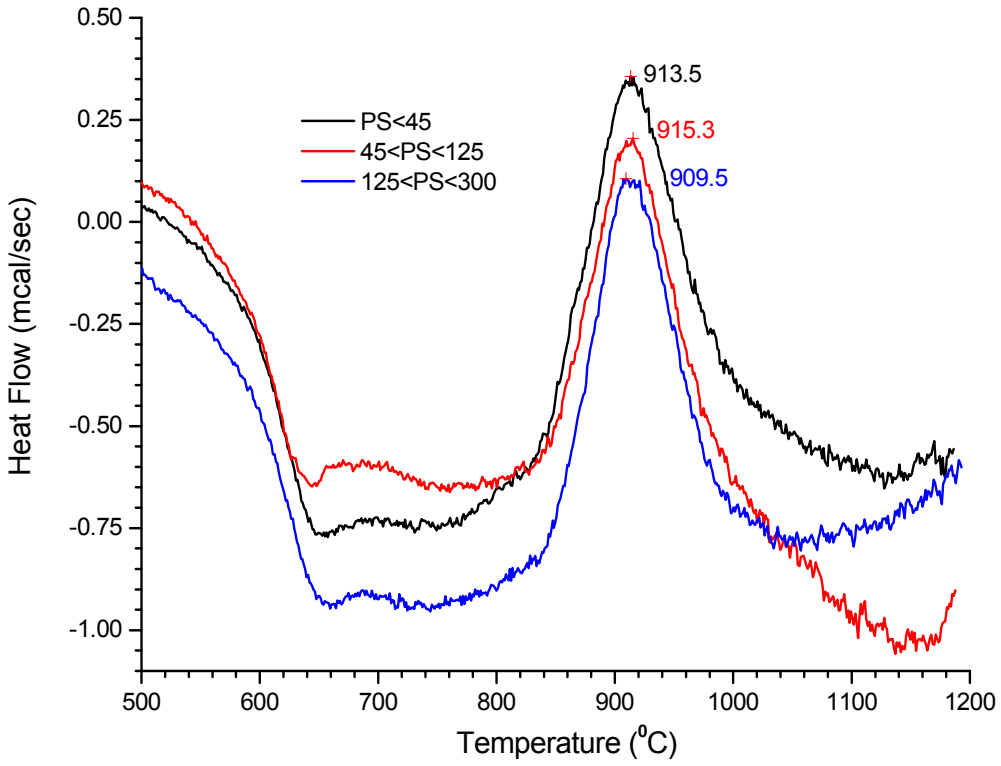

Fig. 4.11: DSC traces for different particle size glass C powders at a rate of 20ºC/min.

The DSC traces of glass C powder (45<PS<125 μm) performed at different heating rates are illustrated in Fig. 4.12. No visible crystallisation peak was detected for the DSC trace for glass C when a heating rate of 5ºC/min was used. Crystallisation peaks shift to higher temperature with an increase in heating rate.

Table 4.8: DSC results for glass C.

Glass Powder Size Range (μm)	Heating Rate (ºC/min)	Glass Transition Temperature T_g (ºC)	Peak Crystallisation Temperature T_p (ºC)
PS<45	20	593.6	913.5
45<PS<125	5	N/A	N/A
	10	589.7	875.7
	20	595.4	915.3
	25	608.3	931.1
	40	612.0	949.7
125<PS<300	20	598.6	909.5

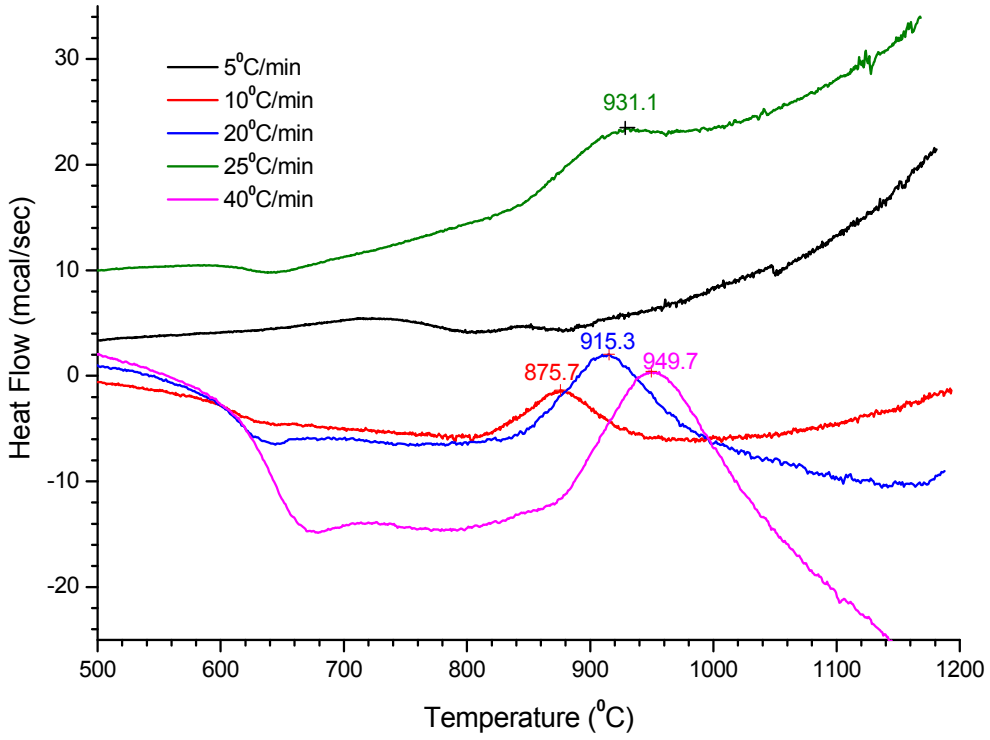

Fig. 4.12: DSC traces for glass C (45<PS<125 μm) at different heating rates.

4.4.5 DSC Results for Glass D

The DSC traces of the different particle size glass D powders at a heating rate of 20ºC/min are presented in Fig. 4.13. The glass transition temperature (T_g) did not change according to the glass powder size. Weak and broad exothermic peaks related to the crystallisation were detected in the temperature range between 850ºC to 1050ºC (Fig. 4.13). Glass D contained a higher TiO_2 content (2.2%, Table 3.6) than the other glasses, which might be influenced by the leucite crystallistaion and its thermal behaviour.

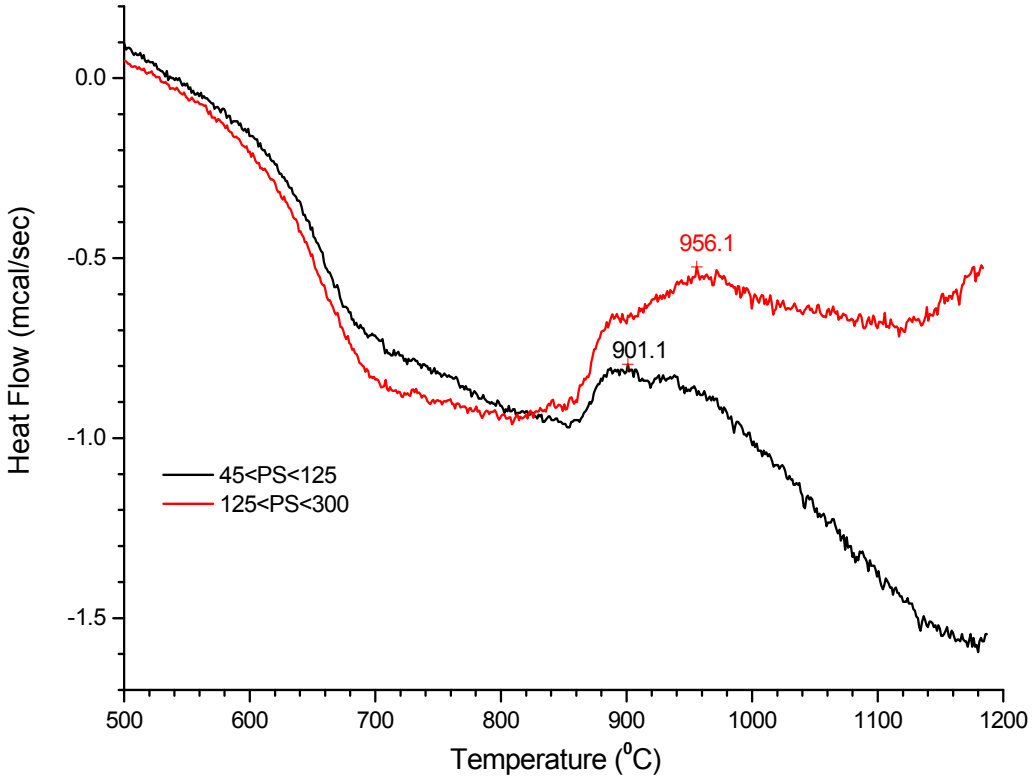

Fig. 4.13: DSC traces for different particle size glass D powders at a rate of 20ºC/min.

4.4.6 Activation Energy of Crystallisation

The Kissinger Equation was used to determine the activation energy.

$$\ln(\phi/T_p^2) = -E/RT_p \quad + \quad \text{constant} \qquad (4.1)$$

Where ϕ is the heating rate, R is the universal gas constant. Plots of $\ln(T_p^2/\phi)$ versus $1000/T_p$ for glass B, HB, C and NB at different heating rates were drawn, and a linear regression was fitted respectively (Fig. 4.14). The activation energy of crystallisation (E_C) for the glasses was deduced from the slope of plots and given in Table 4.9. Due to the broad crystallisation peaks, the activation energy deductions were not carried out for glass A (4hr A) and glass D.

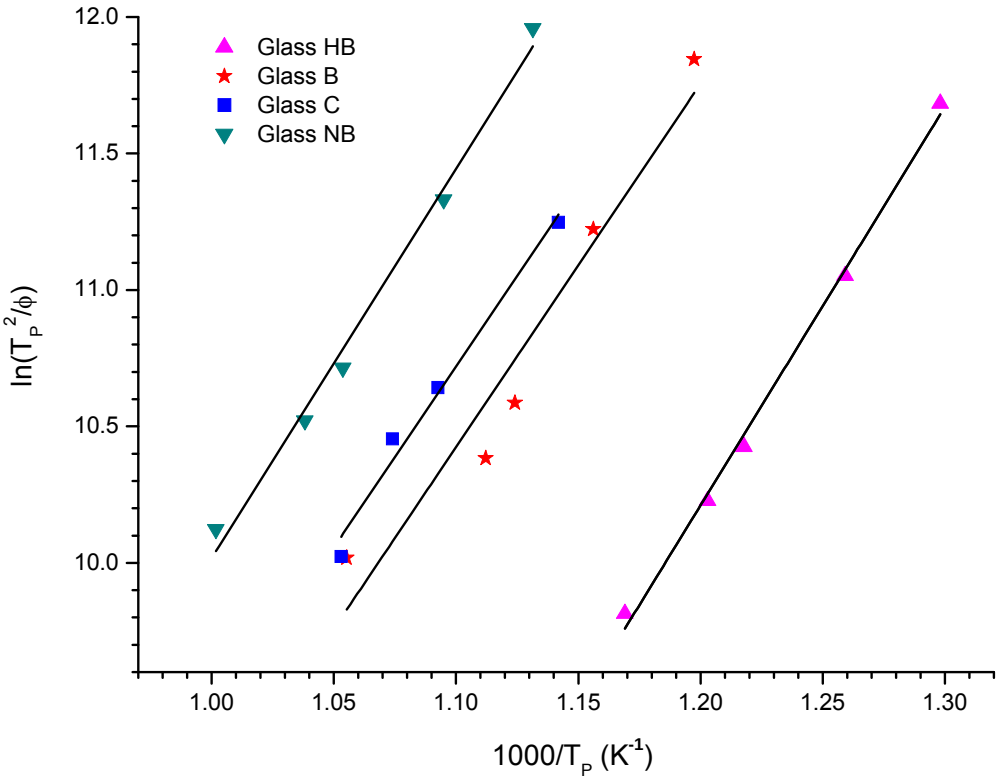

Fig. 4.14: Kissinger plots for glass B, HB, C and NB.

Table 4.9: Glass Activation Energy

Glass	Slope of the Regression Line	r^2	Activation Energy of Crystallisation ($KJ \cdot mol^{-1}$)
Glass B	13.3 (1.9)	0.9951	110.7 (15.8)
Glass HB	14.6 (0.5)	0.9235	116.9 (4.3)
Glass C	13.3 (1.2)	0.9752	110.3 (10.1)
Glass NB	14.3 (0.8)	0.9881	118.6 (6.5)

4.5 Differential Dilatometry Results

4.5.1 Differential Dilatometry Results for the Commercial Glass-Ceramics

The thermal expansion curves of the commercial glass-ceramics (IPS Empress Esthetic, Optimal and Ceramco 3) are shown in Fig. 4.15. The linear thermal expansion coefficient (TEC), glass transition temperature (T_g) and dilatometric softening point (D_{sp}) are given in Table 4.10. Differences between the measured and the predicted TEC values were noticed and may be attributed to the error on the measured residual glass composition introduced by EDS analysis and measurement of leucite content.

Table 4.10: Results of the differential dilatometry for the commercial glass-ceramics.

Glass-Ceramics	TEC (x 10^{-6}/K, 100 - 400ºC)		T_g (ºC)	D_{sp} (ºC)
	Predicted by Appen	Measured		
Ceramco 3	14.2	12.8	521.9	599.5
Optimal	14.4	16.2	608.7	735.2
IPS Empress Esthetic	14.1	16.7	616.3	724.6

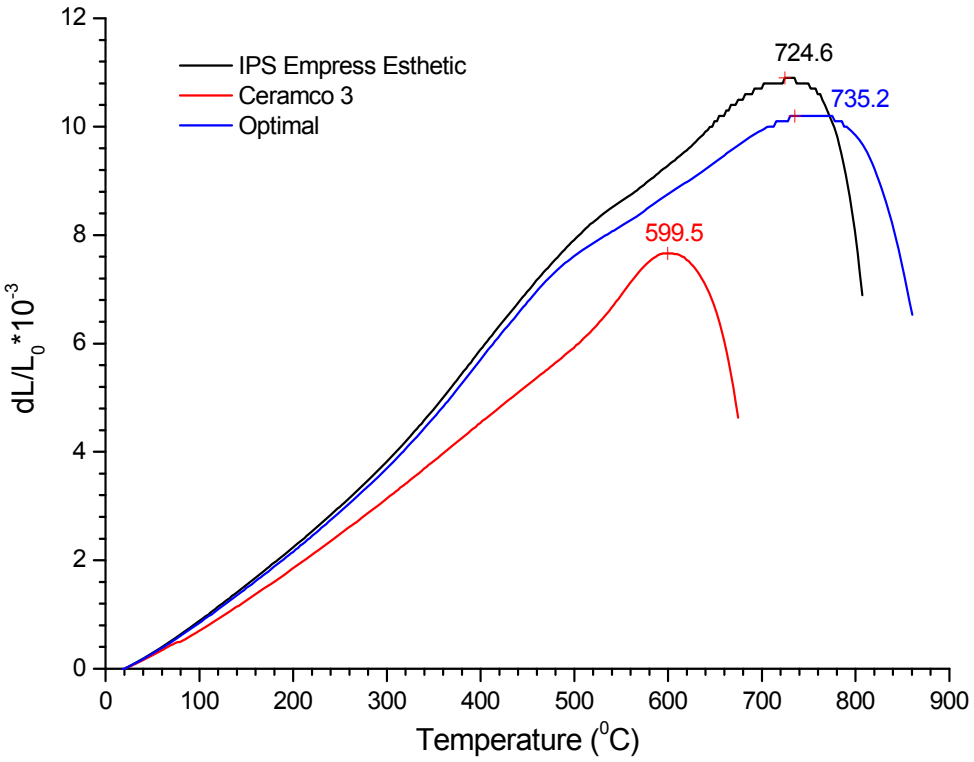

Fig. 4.15: Thermal expansion curves of the commercial glass-ceramics.

4.5.2 Differential Dilatometry Results for the Experimental Glasses

The thermal expansion curves of the designed experimental glasses are plotted in Fig. 4.16. The glass specimens expanded linearly with temperature, where the slope indicated the thermal expansion coefficient of the glass. An increase in thermal expansion coefficient was illustrated at around the glass transition temperature (T_g). The linear thermal expansion coefficient (TEC), glass transition (T_g) and dilatometric softening point (D_{sp}) values were deduced from the curves and given in Table 4.11. The measured thermal expansion coefficient (TEC) values correlated well with those predicted by Appen Factors, and had a deviation less than 0.3 x 10^{-6}/K within the temperature range from 100ºC to 400ºC (Table 4.11). An increase in the glass transition temperature was noticed for glasses from A to D.

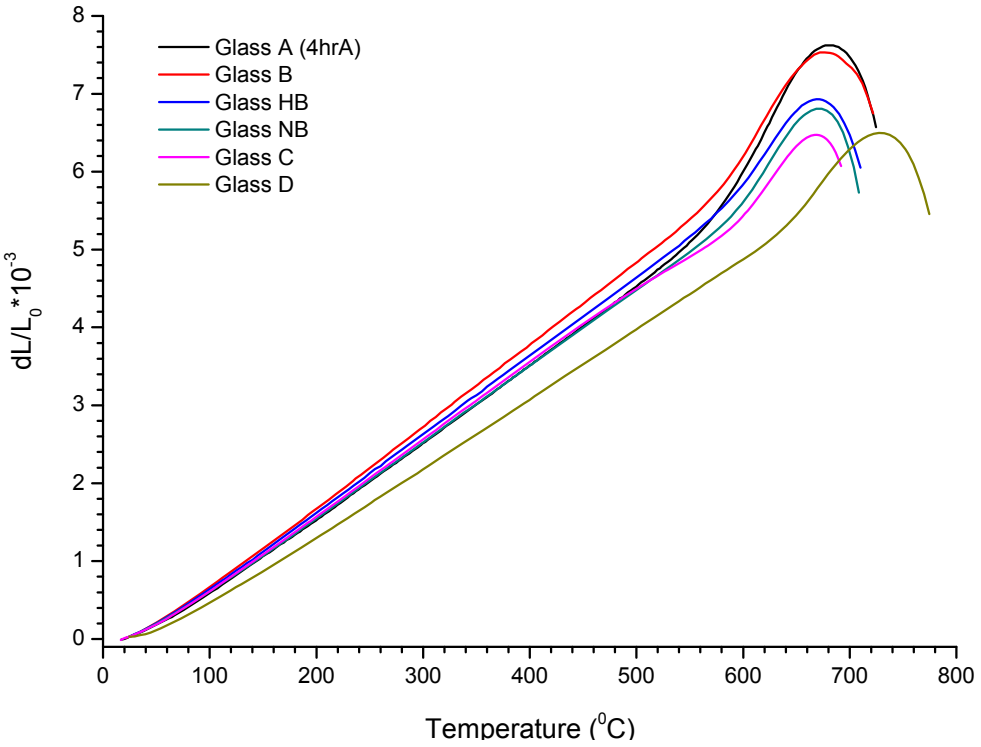

Fig. 4.16: Thermal expansion curves for the experimental glasses.

Table 4.11: Results of the differential dilatometry for the experimental glasses.

Glass	TEC (x 10^{-6}/K, 100 - 400ºC)		T_g (ºC)	D_{sp} (ºC)
	Predicted	Measured		
Glass A (4hr A)	8.6	8.5	581.9	682.7
Glass B	10.3	10.4	581.0	676.2
Glass HB		10.0	589.7	669.9
Glass C	9.7	9.8	590.3	667.9
Glass D	8.7	8.7	639.3	727.1
Glass NB	-	9.7	593.1	671.6

4.5.3 Differential Dilatometry Results for the Experimental Glass-Ceramics

The thermal expansion curves for the experimental glass-ceramics were plotted in Fig. 4.17 - Fig. 4.19. A slight reduction in the slope of the thermal expansion curve indicated a reduction in glass-ceramic TEC. This was thought to be associated with the tetragonal to cubic leucite transformation, where the TEC drops from 20 - 25 x 10^{-6}/K to 11.7 - 12.8 x 10^{-6}/K. The actual TEC of the glass-ceramic was influenced by the tetragonal to cubic leucite transformation, the glass transition temperature (T_g), and leucite content. The linear thermal expansion coefficient (TEC), glass transition temperature (T_g) and dilatometric softening point (D_{sp}) values were deduced from the thermal expansion curves and given in Table 4.12. Glass-ceramics with different parent glass compositions showed different TEC values. An increase in TEC was noticed associated with increased leucite content (Table 4.12).

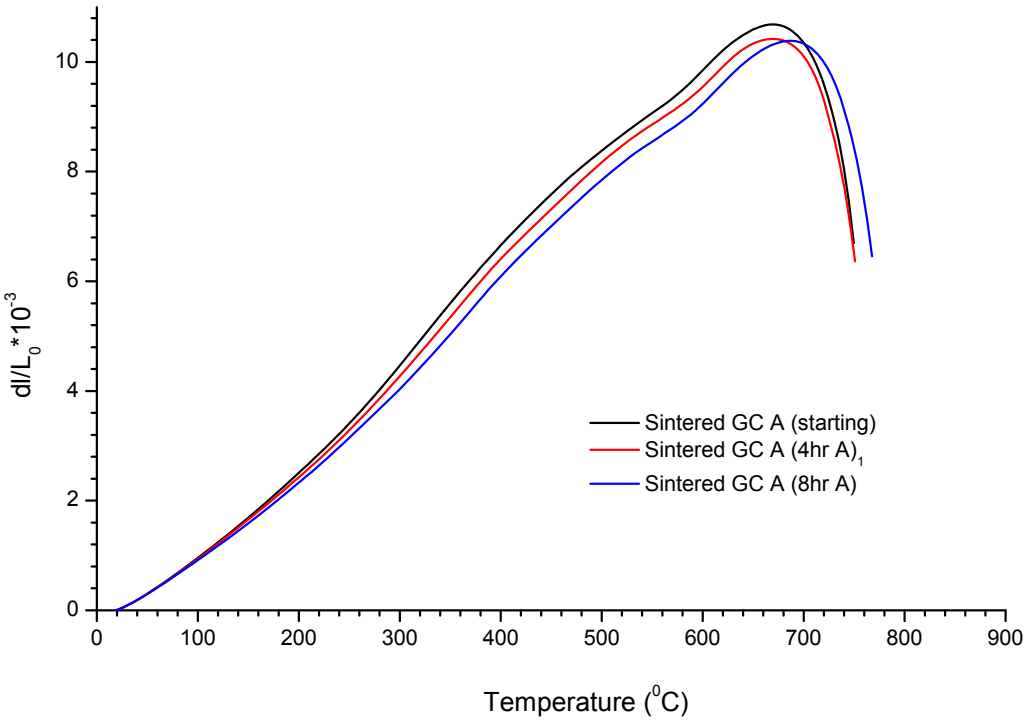

Fig. 4.17: Thermal expansion curves for the heat treated Attritor milled glass-ceramic A groups.

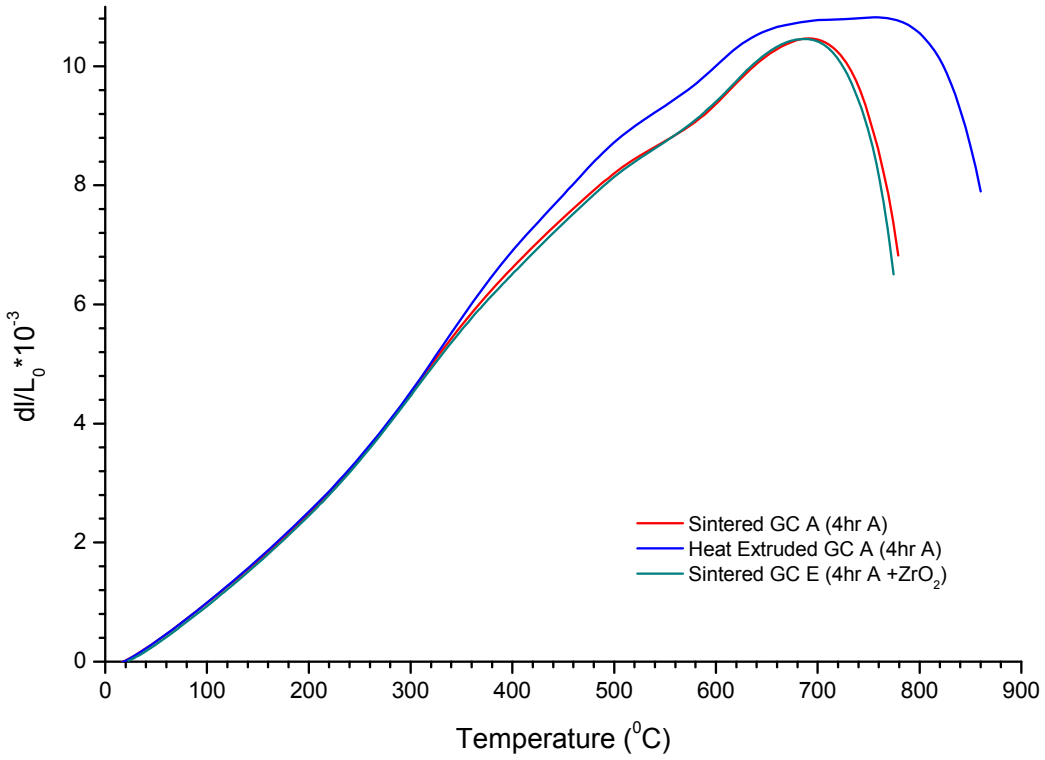

Fig. 4.18: Thermal expansion curves for the optimised of glass-ceramic A groups.

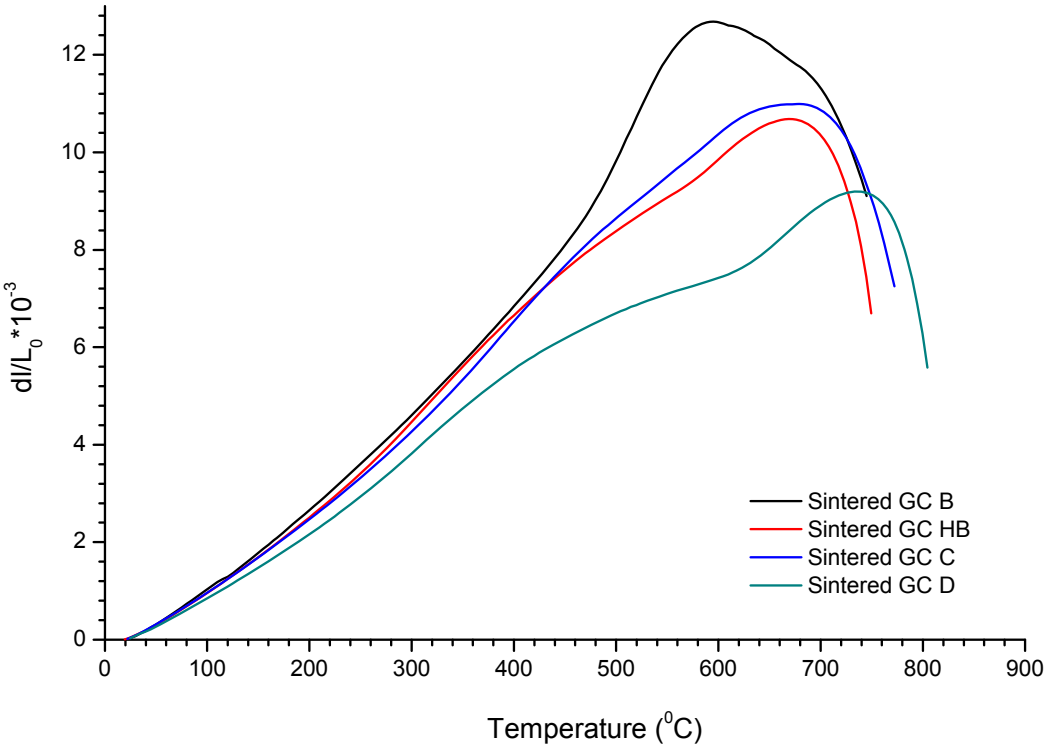

Fig. 4.19: Thermal expansion curves for the experimental glass-ceramics B, HB, C and D.

Table 4.12: Results of the differential dilatometry for the experimental glass-ceramics.

Glass-ceramics (GC)	Two-step Heat Treatments T_N/hold – T_C/hold (ºC/hours)	Measured TEC ($x10^{-6}$/K, 100 - 400ºC	T_g (ºC)	D_{sp} (ºC)
Sintered GC A (starting A)	650/1 – 1120/1	19.0	579.1	668.5
Sintered GC A_1 (4hr A)	650/1 – 1120/1	18.2	589.5	669.2
Sintered GC A (4hr A)	610/1 – 1050/1	18.8	584.7	692.3
Heat Pressed GC A (4hr A)		19.7	580.3	757.8
Sintered GC A (8hr A)	650/1 – 1120/1	17.2	589.3	687.1
Sintered GC B	610/1 – 870/1	19.7	478.3	619.8
Sintered GC HB	610/1 – 795/1	21.0	480.8	608.9
Sintered GC C	620/1 – 920/1	18.6	579.7	675.8
Sintered GC D	670/1 – 1000/1	15.7	627.2	736.5
Sintered GC E	610/1 – 1050/1	18.6	585.0	686.1

4.6 X-ray Diffraction Analysis Results

4.6.1 X-ray Diffraction Results for the Commercial Glass-Ceramics

The X-ray diffraction patterns for the commercial glass-ceramics (Fig. 4.20) showed two phases, an amorphous glass and crystalline tetragonal leucite. Slight displacements were found in the 2θ positions compared to those for tetragonal leucite (ICDD: 00-038-1423). Major reflections indicated (211), (004), (400), (420) and (323) peaks observed at 2θ positions. The unit cell dimensions for tetragonal leucite in the commercial glass-ceramics are listed in Table 4.13.

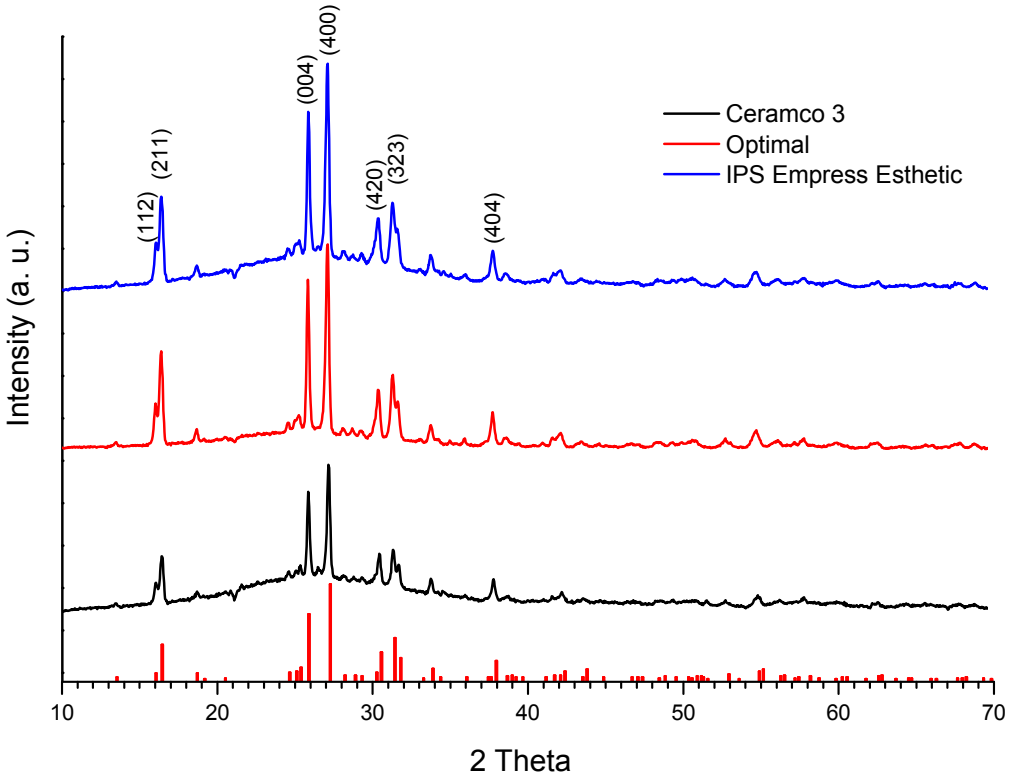

Fig. 4.20: The X-ray diffraction patterns of commercial materials.

Table 4.13: The mean unit cell dimension for commercial glass-ceramics.

Glass-ceramic	Mean *a*-axis Unit Cell Dimension Å (SD)	Mean *c*-axis Unit Cell Dimension Å (SD)	Mean Unit Cell Volume Å (SD)
IPS Empress Esthetic	13.1069 (0.0006)	13.1770 (0.0009)	2263.69 (0.32)
Optimal	13.1006 (0.0005)	13.7311 (0.0007)	2356.61 (0.18)
Ceramco 3	13.0738 (0.0006)	13.7209 (0.0010)	2345.23 (0.36)

4.6.2 X-ray Diffraction Results for Experimental Glasses

The X-ray diffraction patterns of the Attritor milled glass A groups are given in Fig. 4.21. All glasses were largely amorphous. No crystalline peaks were found in glass A (starting, 30min A and 45min A). A small crystalline peak with 2θ position at 26.072º was illustrated in the XRD trace of glass A (60min A). Small crystalline peaks were also found in the glass A (90min A, 120min A and 4hr A, Fig. 4.21) with 2θ position listed in Table 4.14.

Table 4.14: The *2θ* positions for the detectable reflections of Attritor milled glass A groups.

Glasses	Reflections (*2θ*)
60min A	26.072º
90min A	15.928º, 26.085º, 29.438º
120minA	15.906º, 26.080º
4hr A	15.869º, 26.090º
8hr A	15.869º

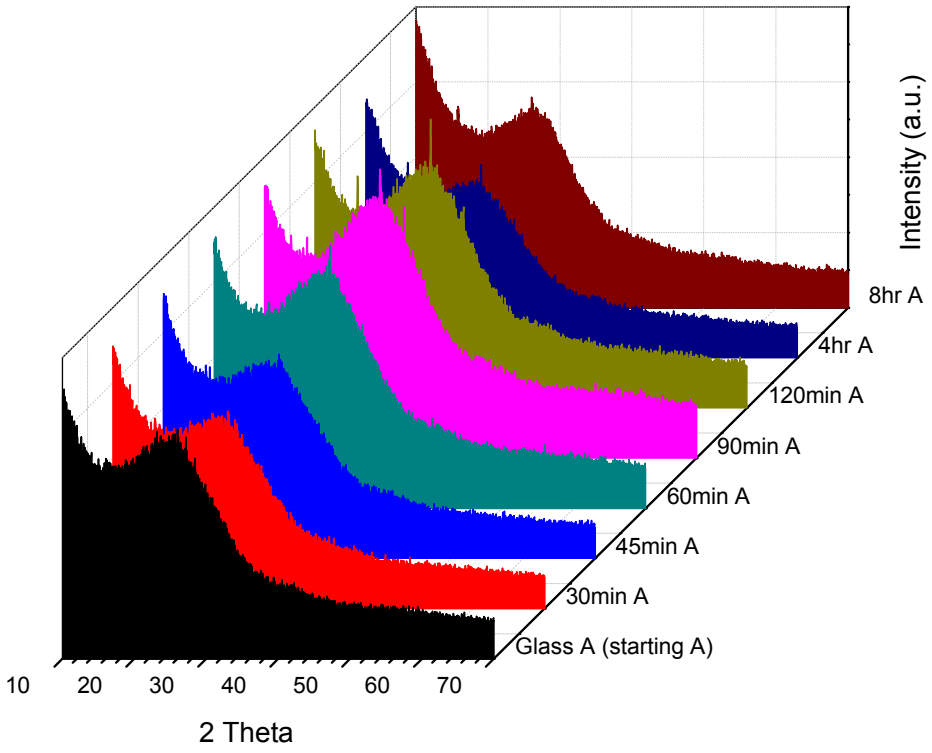

Fig. 4.21: The X-ray diffraction patterns for the Attritor milled glass A groups.

The X-ray diffraction patterns of experimental glasses including B, HB, C, D and NB are illustrated in Fig. 4.22 and Fig. 4.23. Glass B, C, D and NB were amorphous without detected crystalline peaks. However, crystalline peaks for glass HB were observed with *2θ* positions of 16.544º, 26.018º, 27.247º, 30.517º and 31.515º, which correspond to tetragonal leucite (ICDD: 00-038-1423) with miller indices (211), (004), (400), (420) and (323) respectively.

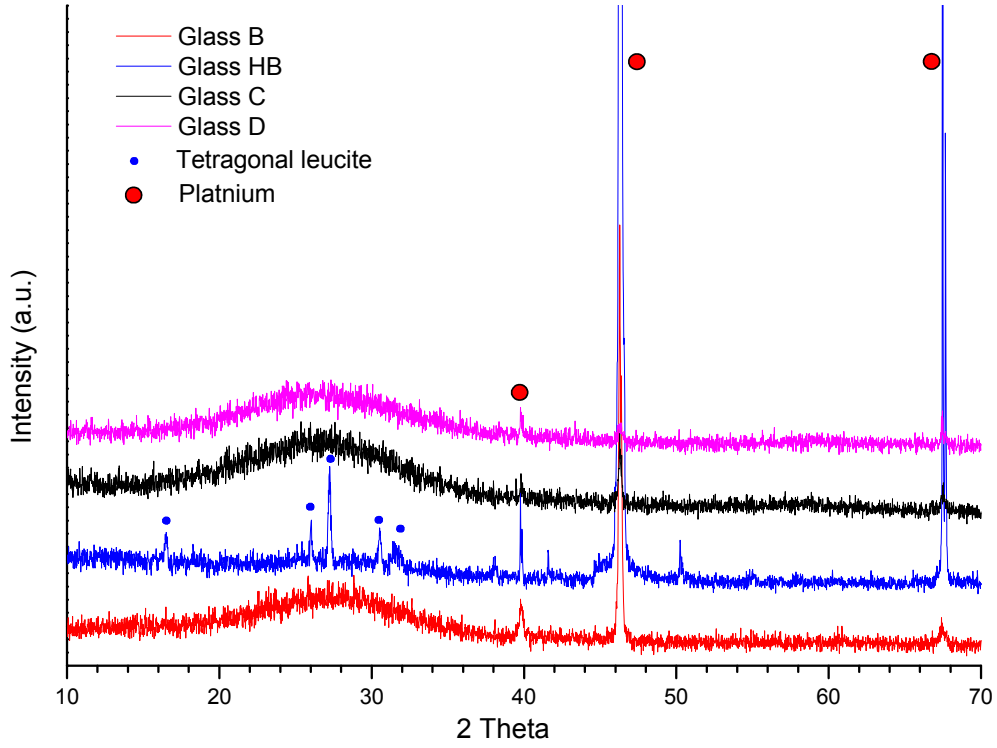

Fig. 4.22: The X-ray diffraction patterns for the experimental B, HB, C and D glasses.

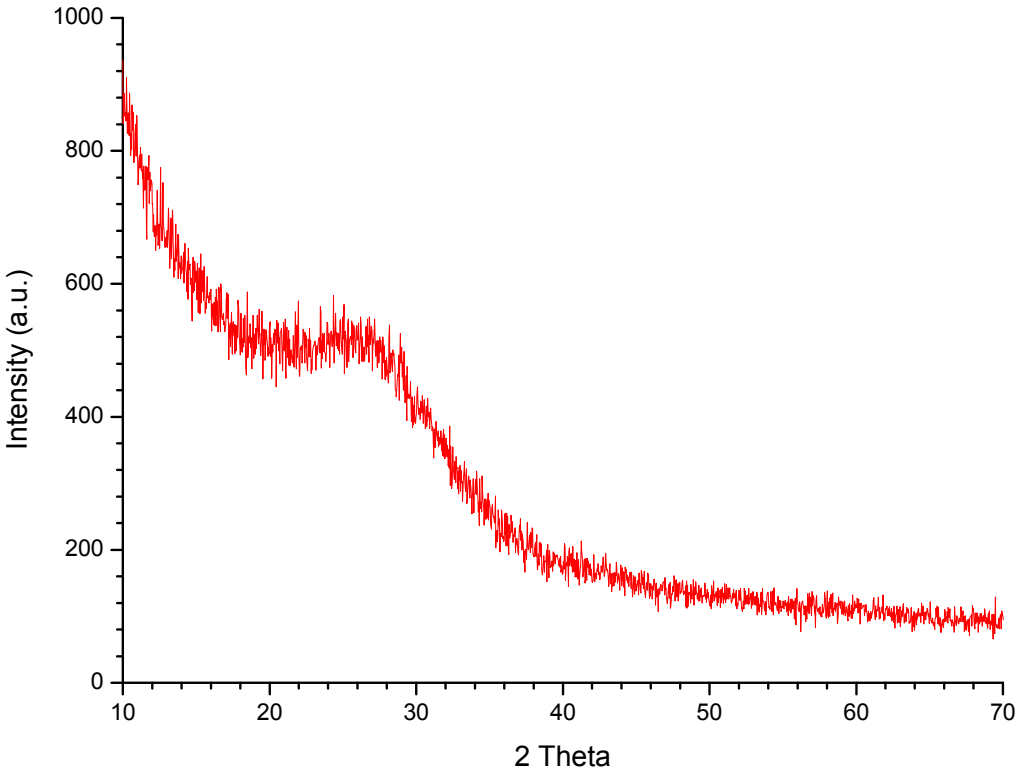

Fig. 4.23: The X-ray diffraction pattern for glass NB.

4.6.3 High Temperature X-ray Diffraction (HTXRD) Results for the Experimental Glasses

4.6.3.1 HTXRD Results for Glass A (4hr A)

The high temperature X-ray diffraction results of glass A (4hr A) recorded at 20ºC intervals are selected and presented in Fig. 4.24. Distinct platinum (Pt) peaks at 2θ positions around 39.716º, 46.163º, 67.544º are presented in the X-ray diffraction patterns for glass A (4hr A) at all temperatures. These peaks were from the Pt specimen strip. Small shifts in the Pt peak positions according to temperature were noticed which are in agreements with the literature.

The glass A (4hr A) was largely amorphous at room temperature and at 680ºC crystalline peaks with peak positions at 16.034º, 26.360º, 31.072º (2θ) were identified (Fig. 4.24 and Fig. 4.25). These peaks were the three major reflections (211), (400) and (332) for cubic leucite (ICDD: 01-076-2298) respectively. However, a minor shift in 2θ positions was observed compared with the database record. The crystalline peak intensity increased with increase in temperature. Secondary peaks indicated a sanidine phase crystallisation was first noticed at 760ºC, and the maximum sanidine crystallisation throughout different temperatures was identified at 860ºC (Fig. 4.24). The sanidine crystallisation peaks reduced with further increase in temperature and no sanidine crystallisation could be identified at 1050ºC (Table 4.15 and Fig. 4.25). The maximum leucite crystallisation was indicated at 1050ºC.

The high temperature X-ray diffraction patterns of glass A (4hr A) at 850ºC were recorded at 15 minutes intervals up to 3 hours. The results suggested major cubic leucite and trace sanidine phase in the glassy matrix when glass A was heated to 850ºC (0 mins hold). Holding at this temperature led to sanidine precipitation and the loss of cubic leucite and glassy liquid (Fig. 4.26).

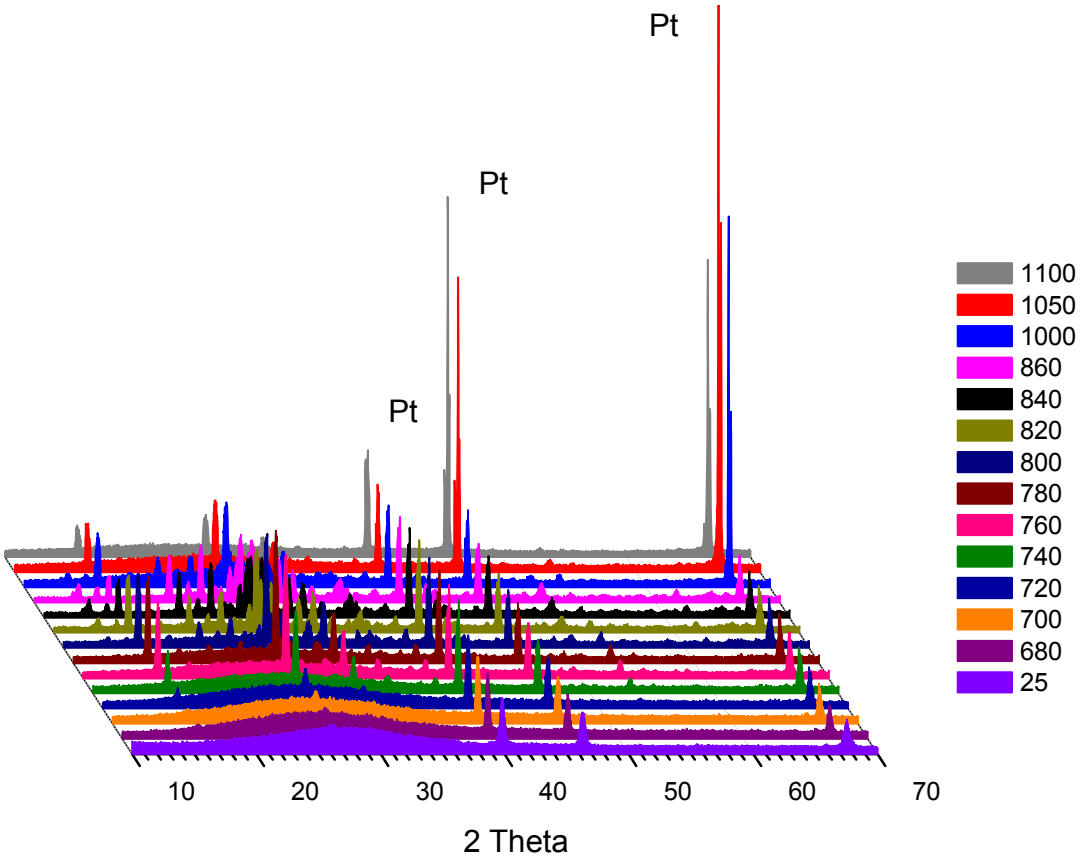

Fig. 4.24: The high temperature X-ray diffraction patterns for glass A (4hr A).

Table 4.15: Phase identification of glass A (4hr A) by high temperature XRD.

Temperature (ºC)	Phase Composition
<680	Amorphous
680	Amorphous*
760	Amorphous + Cubic Leucite (MP) + Sanidine (M)
860	Amorphous + Cubic Leucite (M) + Sanidine (MP)
1000	Amorphous + Cubic Leucite (MP) + Sanidine (M)
1050	Amorphous + Cubic Leucite (M)

* trace amount of cubic leucite, MP (major phase), M (minor Phase)

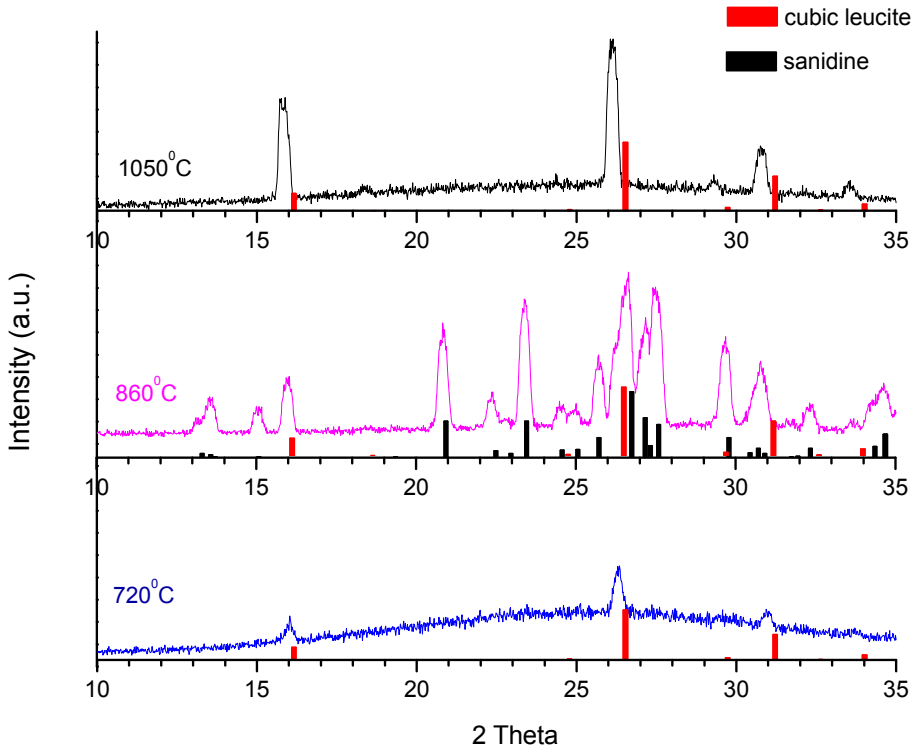

Fig. 4.25: X-ray diffraction patterns for glass A (4hr A) at 720, 860 and 1050ºC.

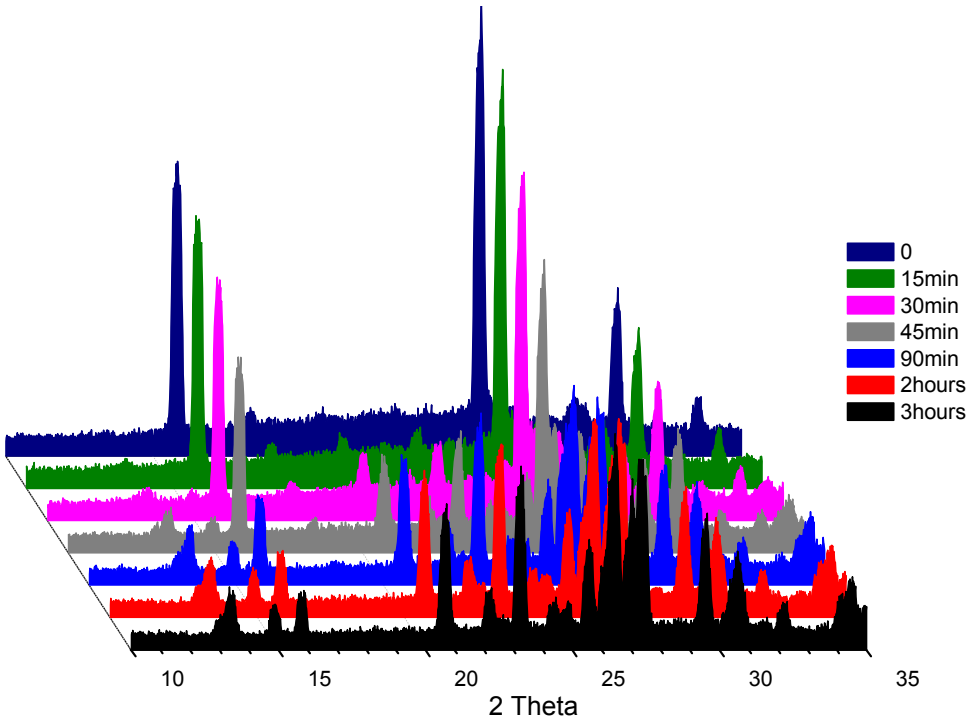

Fig. 4.26: The high temperature X-ray diffraction patterns for glass A (4hr A) at 850ºC.

4.6.3.2 HTXRD Results for Glass B/HB

The high temperature X-ray diffraction patterns of glass B at different temperatures show an amorphous phase with no evidence of crystalline peaks below 680°C (Fig. 4.27). The first crystalline peak with peak positions at 26.296º was noticed at 700°C, and was matched with one of the cubic leucite reflections (ICDD: 01-076-2298). A significant increase in the cubic leucite peak intensity was observed from 700°C to 720°C. Maximum cubic leucite peak intensity was detected at 800°C. Cubic leucite was the only crystalline phase found throughout the temperature range.

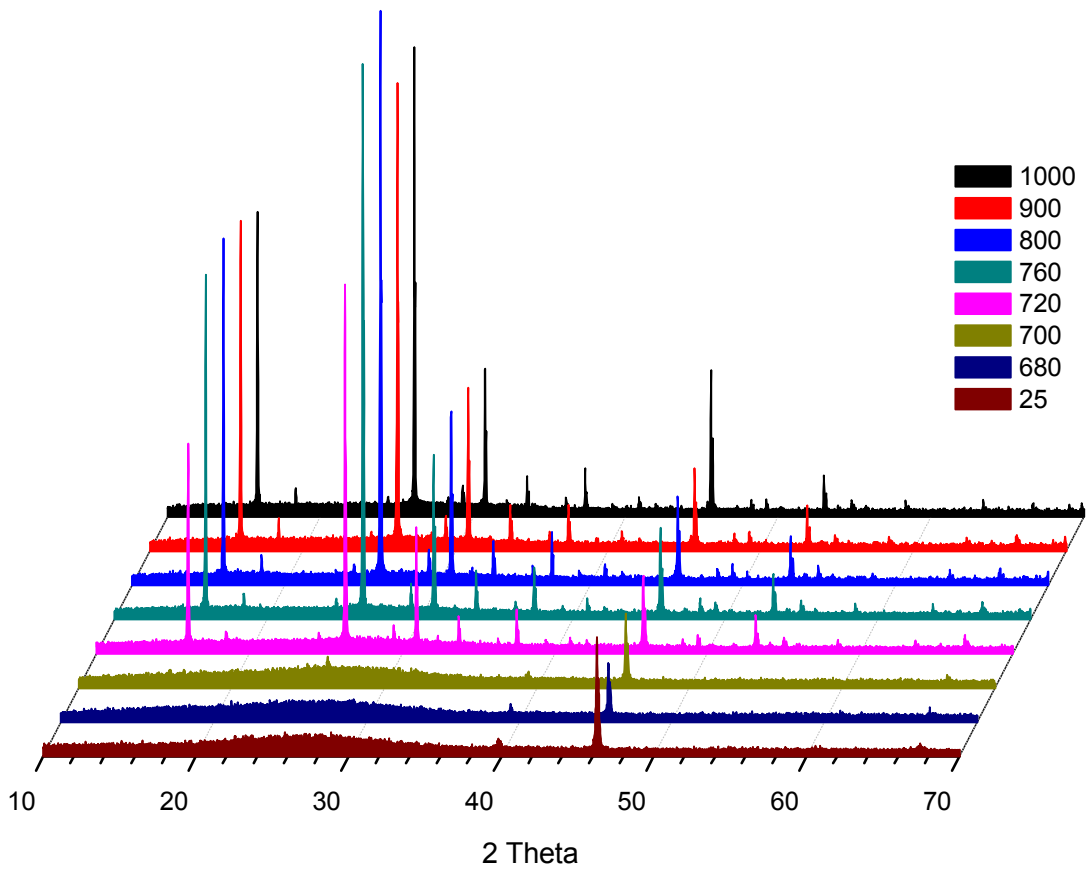

Fig. 4.27: The high temperature X-ray diffraction patterns for glass B.

The high temperature X-ray diffraction results of glass HB are illustrated in Fig. 4.28. The X-ray diffraction pattern at 25ºC shows distinct Pt peaks (2θ position: 46.2º and 67.5º), and a trace amount of tetragonal leucite (ICDD: 00-038-1423) indicated by the (004) and (400) reflections. Cubic leucite (ICDD: 01-076-2298) was first detected at 500°C where a significant reduction in the Pt peak intensity was observed. The crystalline peak intensity associated with cubic leucite increased with an increase in temperature (Fig. 4.28). Cubic leucite was the only crystalline phase found throughout the temperature range.

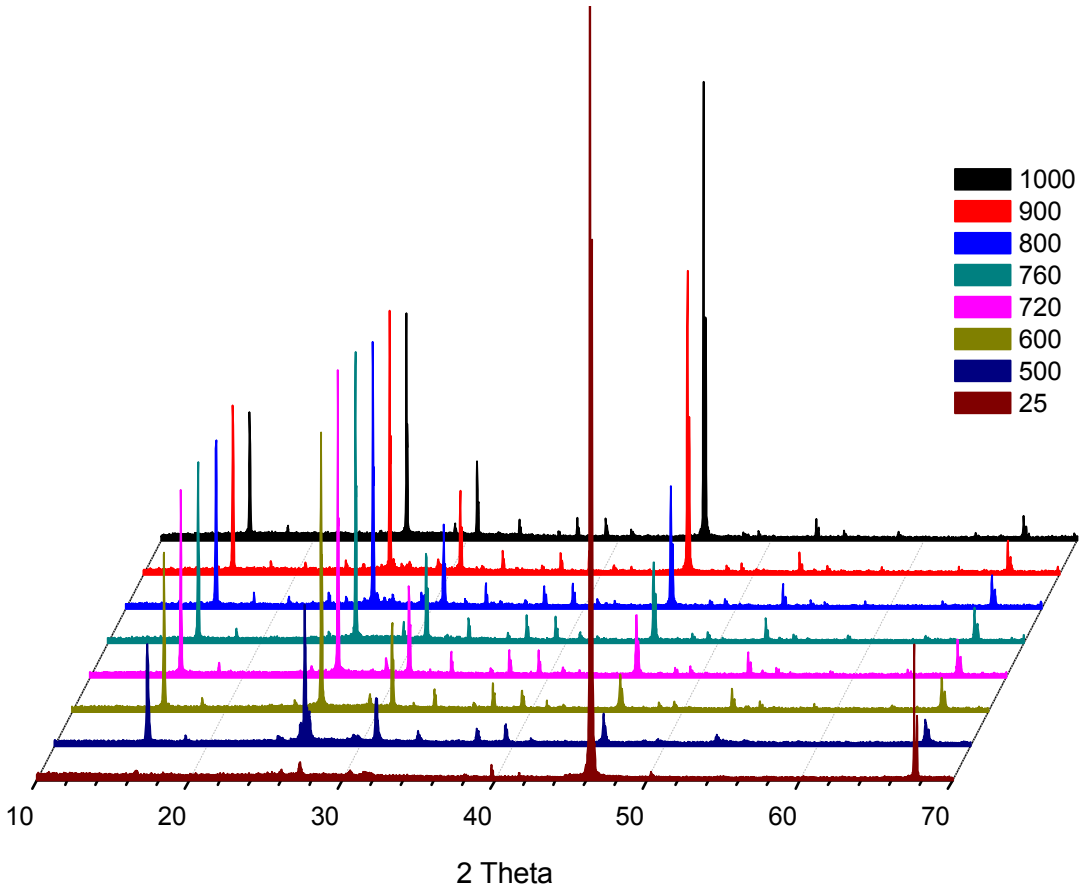

Fig. 4.28: The high temperature X-ray diffraction patterns for glass HB.

4.6.3.3 HTXRD Results for Glass C

The high temperature X-ray diffraction (HTXRD) results of glass C are presented in Fig. 4.29 and Table 4.16. The X-ray diffraction pattern of glass C at room temperature (25ºC) demonstrates an amorphous phase (Fig. 4.29). The relative intensity ratio of the platinum and crystalline phase qualitatively suggests the phase crystallisation trend of the glass.

A small crystallisation peak was first found at 560°C (Fig. 4.29 and Table 4.16), which was identified as one of the peaks for cubic leucite (ICDD: 01-076-2298). The cubic leucite crystallisation progressed slowly with increase in temperature (Table 4.16). Crystalline peaks associated with sanidine (ICDD: 00-025-0618) were noticed at 720°C as well as peaks for cubic leucite. Sanidine crystallisation peak intensity increased with temperature, and the leucite decreased. A major sanidine crystalline phase with a minor cubic leucite phase was present at 780°C. With further increase in temperature, the crystalline sanidine peak intensity reduced and that for cubic leucite increased. A major cubic leucite phase and a trace amount of sanidine were detected at 880°C. No sign of sanidine was found on and after 920°C (Table 4.16).

Table 4.16: Phase identification of glass C by high temperature XRD.

Temperature	Phase
<560	Amorphous
560	Amorphous*
720	Amorphous + Cubic Leucite (MP) + Sanidine (M)
780	Amorphous + Cubic Leucite (M) + Sanidine (MP)
880	Amorphous + Cubic Leucite (MP) + Sanidine (M)
>= 920	Cubic Leucite (MP)

* trace amount of tetragonal leucite, MP (major phase), M (minor Phase).

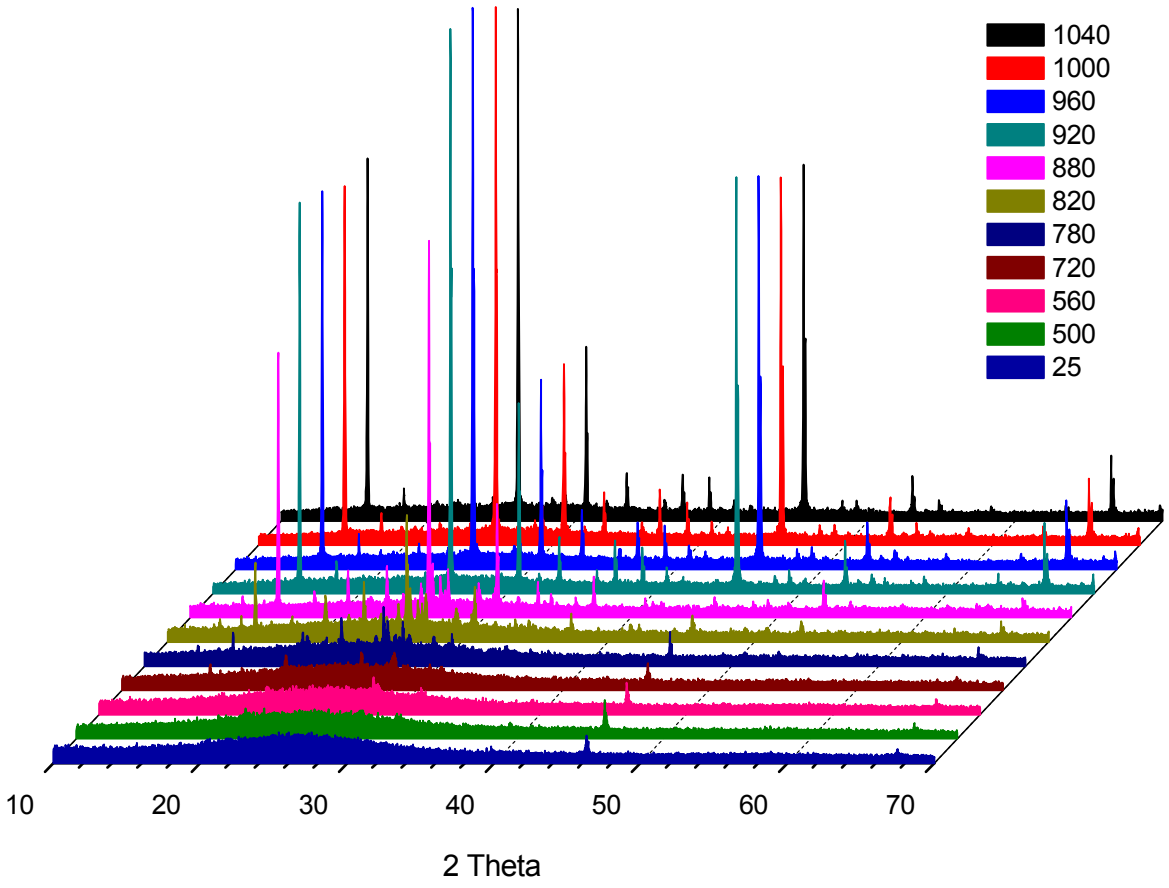

Fig. 4.29: The high temperature X-ray diffraction patterns for glass C.

4.6.3.4 HTXRD Results for Glass D

The high temperature X-ray diffraction (HTXRD) results of glass D shows a broad amorphous hump with detectable Pt peaks (2θ positions: 39.789° and 46.291°, Fig. 4.30) at room temperature. The first sign of crystallisation peaks was noticed at 800°C, and was confirmed to be cubic leucite (ICDD: 01-076-2298). No secondary phase was observed throughout the whole temperature range. Maximum cubic leucite crystallisation occurred between 960°C and 1000°C according to the peak intensity (Fig. 4.30).

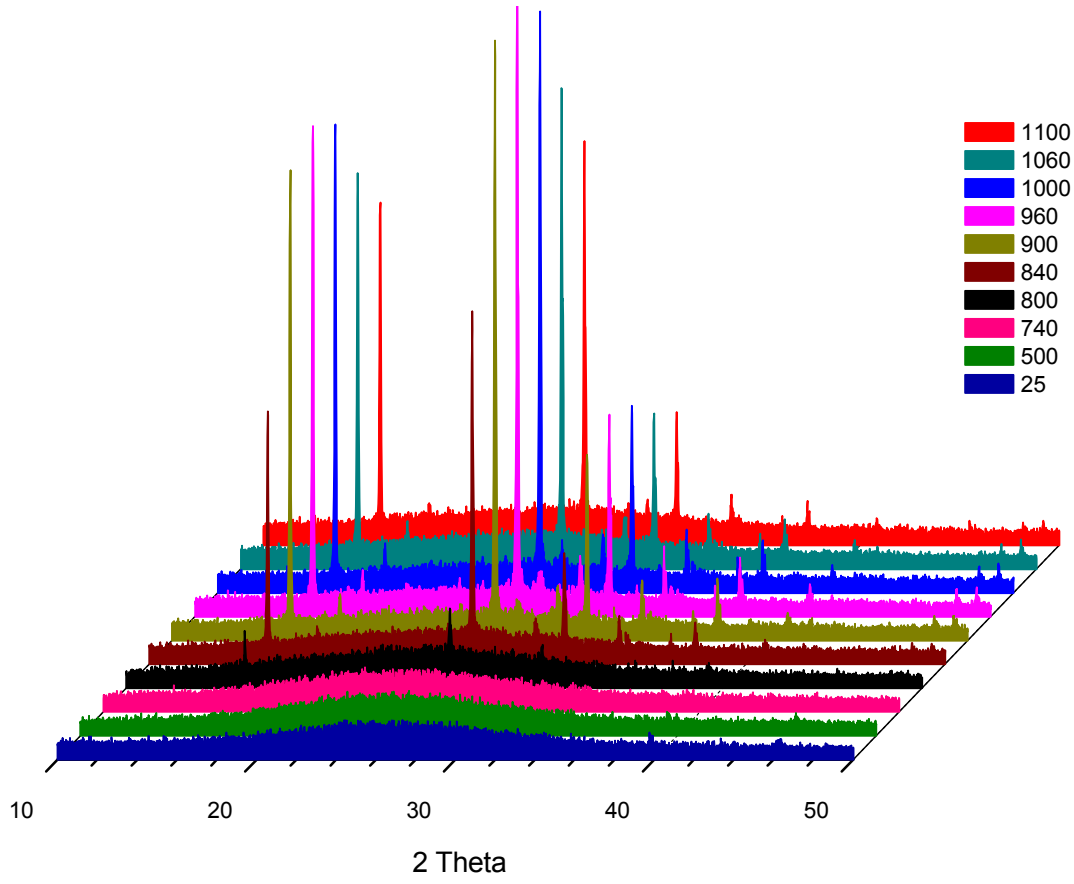

Fig. 4.30: The high temperature X-ray diffraction patterns for glass D.

4.6.4 X-ray Diffraction Results of the Experimental Glass-Ceramics

4.6.4.1 XRD Results for Glass-Ceramics A

The X-ray diffraction patterns of the crystalline glass-ceramics A (Attritor milled groups) after two-step heat treatment (25ºC to 650ºC/1h then to 1120ºC/1h at 10ºC/min) are given in Fig. 4.31. The groups consisted of two major solids phases, an amorphous component and tetragonal leucite (ICDD: 00-038-1423). The mean unit cell dimensions are listed in Table 4.17.

The X-ray diffraction traces of glass A (4hr A) nucleation and growth control groups were plotted and phase identification was carried out. Tetragonal leucite was confirmed to be the major crystalline phase for all glass-ceramic specimens (Table 4.18).

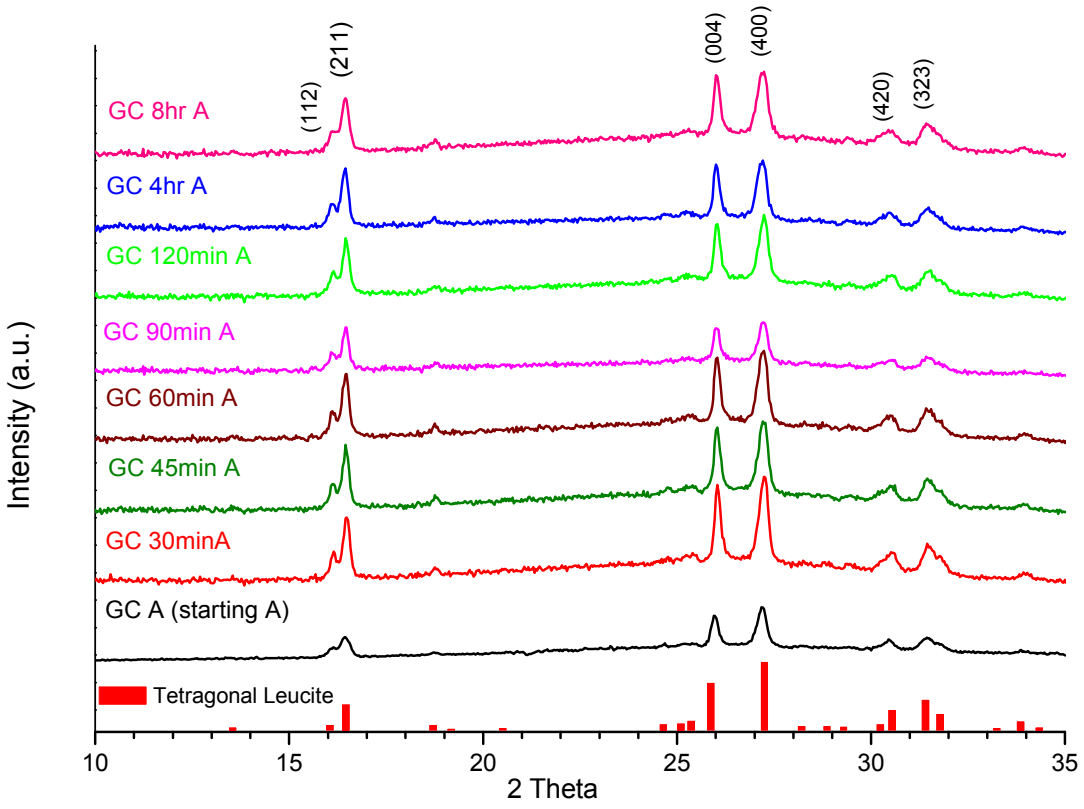

Fig. 4.31: The X-ray diffraction traces for glass-ceramics A (Attitor milled series, 650ºC/1h - 1120ºC/1h at 10ºC/min).

Table 4.17: The mean unit cell dimensions for Attritor milled glass-ceramic A (650ºC/1h - 1120ºC /1h at 10ºC/min).

Glass-ceramics	Mean *a*-axis Unit Cell Dimension Å (SD)	Mean *c*-axis Unit Cell Dimension Å (SD)	Mean Unit Cell Volume Å (SD)
A (starting)	13.1089 (0.0009)	13.7071 (0.0015)	2355.47 (1.22)
30 min A	13.0996 (0.0007)	13.6808 (0.0011)	2347.62 (0.54)
45 min A	13.1072 (0.0008)	13.6884 (0.0013)	2351.16 (0.83)
60 min A	13.1131 (0.0008)	13.6880 (0.0013)	2353.70 (0.83)
90 min A	13.1074 (0.0011)	13.6948 (0.0018)	2352.82 (2.18)
120 min A	13.1024 (0.0009)	13.6880 (0.0014)	2349.89 (1.13)
A (4hr A)	13.1229 (0.0010)	13.6963 (0.0015)	2358.65 (1.50)
A (8hr A)	13.1345 (0.0009)	13.7103 (0.0013)	2365.23 (1.05)

Table 4.18: XRD phase identification of the nucleation and growth groups for the 4hr A glass-ceramics.

Nucleation Temperature (ºC)	Holding Time (hours)	Crystallisation Temperature (ºC) /Time (hours)	Crystalline Phase
600	1	1120/1	Tetragonal leucite
610			
620			
630			
640			
650			
660			
670			
680			
690			
700			
610	0.5		
	2		
	3		
	4		
	5		

All specimens were ramped at 10ºC/min from 25ºC to the nucleation temperature, held for the designated time then ramped up to 1120ºC for a further 1hour hold, follow by air quenching.

Glass-ceramic A (4hr A) heat treated at 610ºC (1 hour hold) followed by different crystallisation temperatures with one hour hold indicated two major solid phases; tetragonal leucite and an amorphous component (Fig. 4.32 and Table 4.19). The crystalline peak intensity of the glass-ceramics A (4hr A) suggests a higher leucite volume fraction at a crystallisation temperature of 1050ºC (Fig. 4.32). The unit cell dimensions are given in Table 4.20. Longer crystallisation hold (4 hours) did not lead to phase changes (Table 4.19).

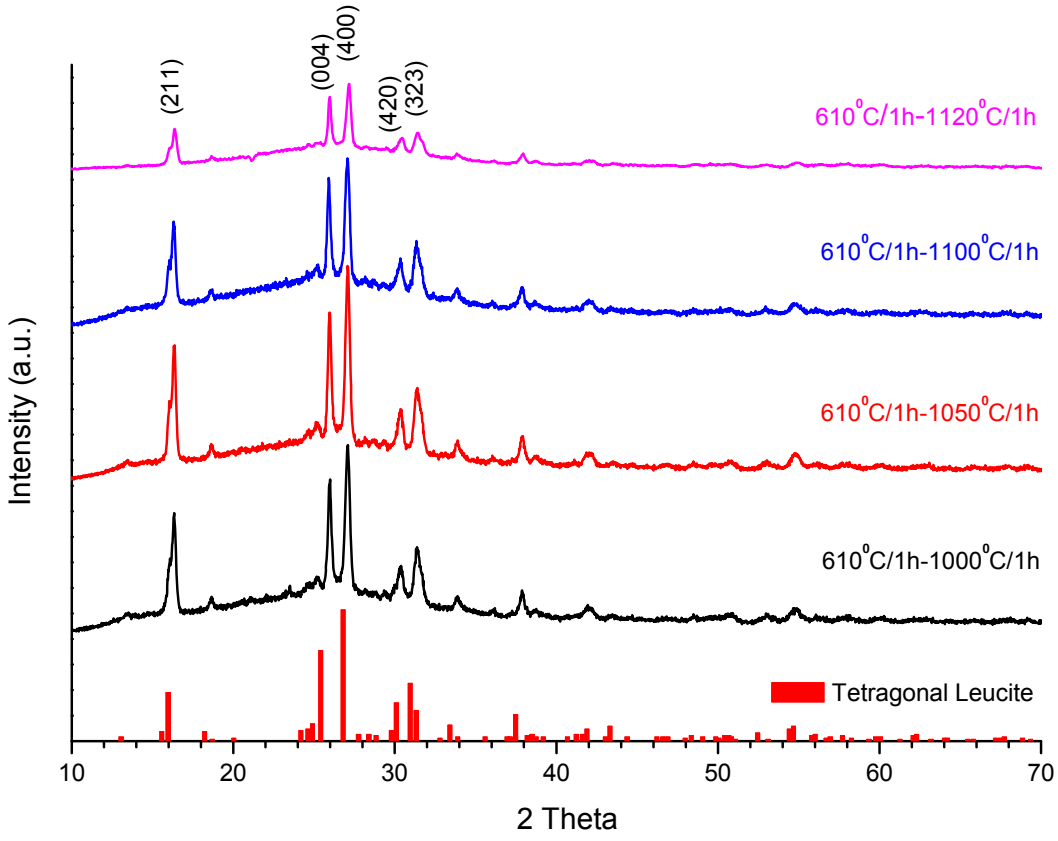

Fig. 4.32: The X-ray diffraction traces for glass A (4hr A) at different crystallisation temperatures (heating rate 10ºC/min).

Table 4.19: XRD phase identification for glass A (4hr A) after crystallisation heat treatments.

Nucleation Temperature (ºC) / Holding Time (hours)	Crystallisation Temperature (ºC) / Holding Time (hours)	Crystalline Phase
610ºC/1h	1000ºC/1h	Tetragonal leucite
	1050ºC/1h	
	1100ºC/1h	
	1120ºC/1h	
610ºC/4h	1050ºC/1h	
610ºC/1h	1050ºC/0.5h	
	1050ºC/1h	
	1050ºC/2h	
	1050ºC/3h	
	1050ºC/4h	

Specimens ramped at 10ºC/min from 25ºC for a designated two-step heat treatment before air quenching.

Table 4.20: The mean unit cell dimensions for glass A (4hr A) after different crystallisation heat treatments

Crystallisation Temperature (ºC)	Mean *a*-axis Unit Cell Dimension Å (SD)	Mean *c*-axis Unit Cell Dimension Å (SD)	Mean Unit Cell Volume Å (SD)
1000	13.1776 (0.0008)	13.7226 (0.0012)	2382.92 (0.77)
1050	13.1343 (0.0007)	13.6989 (0.0012)	2363.19 (0.64)
1100	13.1841 (0.0009)	13.7469 (0.0013)	2389.49 (1.05)
1120	13.1303 (0.0009)	13.7155 (0.0015)	2364.62 (1.22)

Specimens ramped from 25ºC at 10ºC/min to 610ºC held for 1 hour, and then ramped up to the crystallisation temperature for 1 hour hold before air quenching.

4.6.4.2 XRD Results for Sanidine Crystallisation of Glass A (4hr A)

The X-ray diffraction patterns of crystallised glass-ceramic A (4hr A) heat treated at 610ºC for one hour followed by different crystallisation holds at 850ºC showed the coexistent of a sanidine and tetragonal leucite phase within the glass matrix (Fig. 4.33).

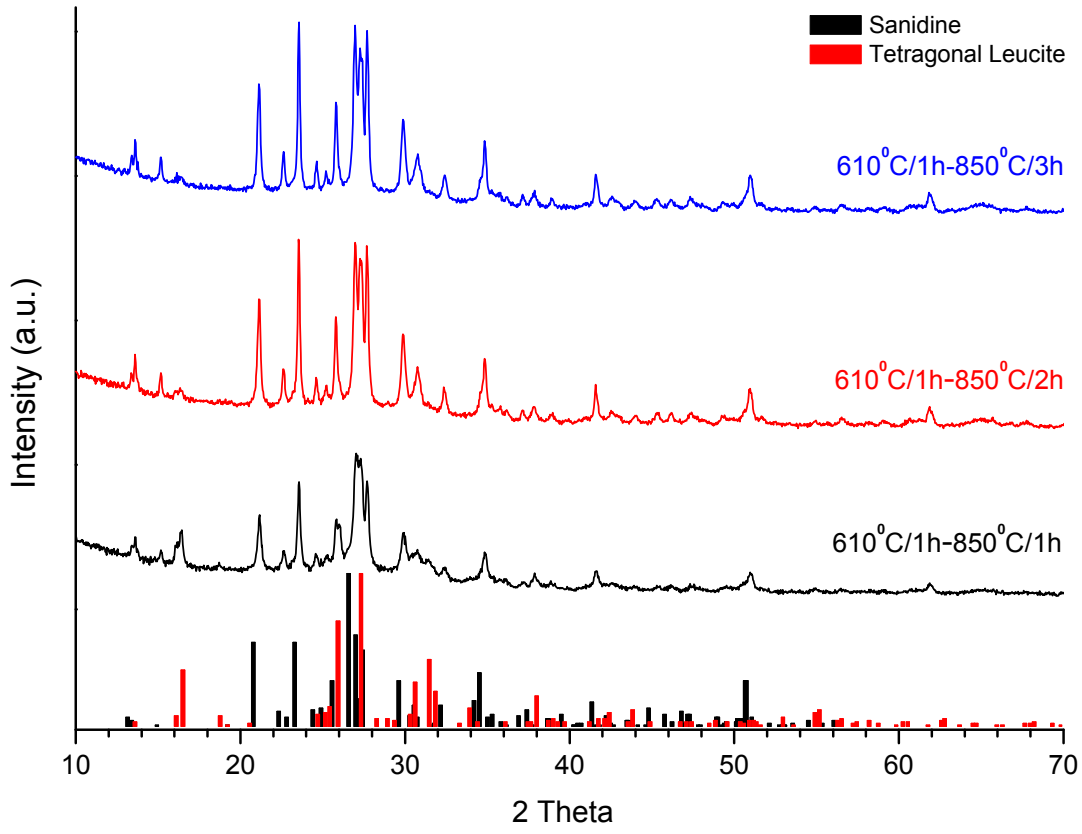

Fig. 4.33: The X-ray diffraction traces of sanidine/leucite crystallisation of glass-ceramic A (4hr A, heating rate 10ºC/min).

4.6.4.3 XRD Results for Glass-Ceramics B, HB and NB

The X-ray diffraction results of crystallised glass-ceramic B, HB and NB with different heat treatments are given in Table 4.21 and Fig. 4.34. Tetragonal leucite is the only detected crystallised phase.

Table 4.21: XRD phase identification of glass-ceramics B.

Glass-Ceramics	Two-step Heat Treatment Temperature (ºC) / Holding Time (hours)		Heating Rate (ºC/min)	Crystalline Phase
	Nucleation	Crystallisation		
Glass-ceramic B	610/1	870/1	10	Tetragonal leucite
		900/1		
		950/1		
	610/2	870/1		
	610/4	870/1		
Glass-ceramic HB	610/1	870/1		
	620/1	870/1		
	620/1	795/1		
	620/1	795/1	20	
Glass-ceramic NB	630/1	949/1	20	

Specimens ramped from 25ºC followed by two-step heat treatments and air quenching.

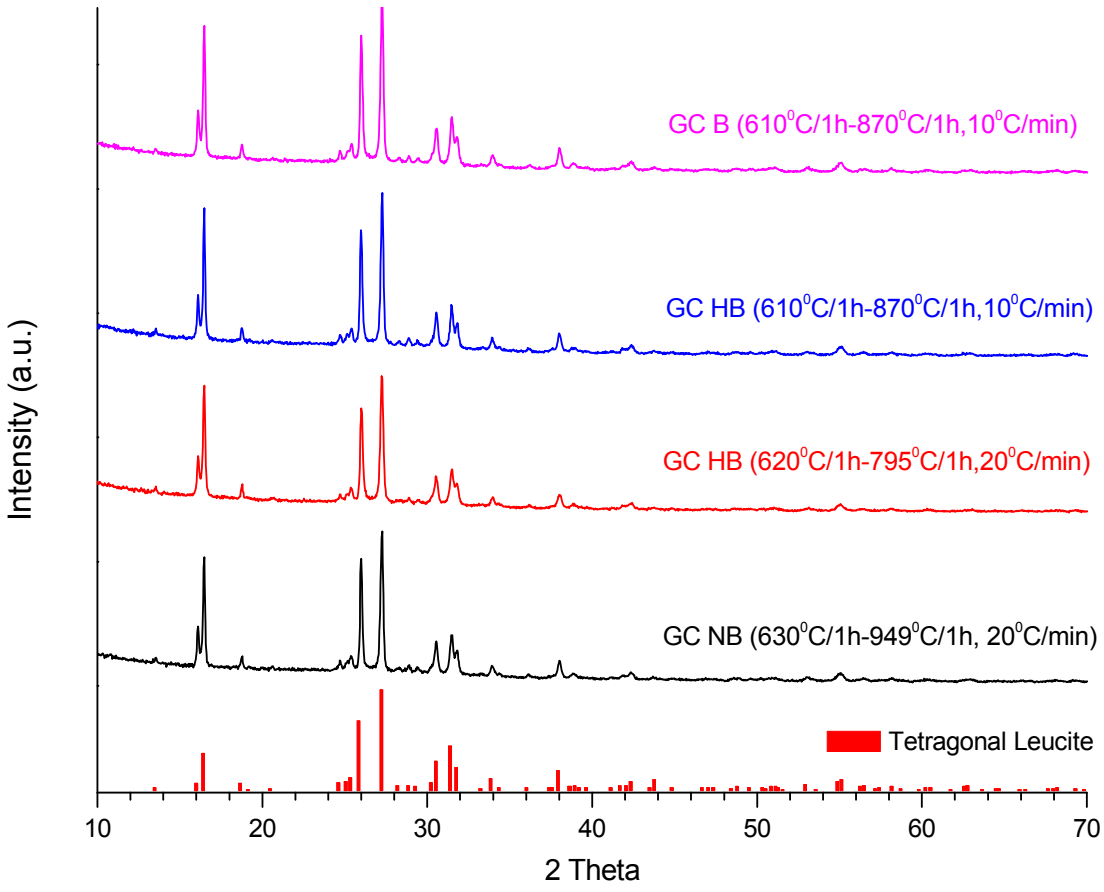

Fig. 4.34: The X-ray diffraction traces of glass-ceramics B, HB and NB

4.6.4.4 XRD Results for Glass-Ceramics C, D and E

The X-ray diffraction patterns of crystallised glass-ceramics C, D and E with different two-step heat treatments are plotted in Fig. 4.35 and Fig. 4.36. Tetragonal leucite was the only detected crystallised phase for all glass-ceramics (Table 4.22 and Table 4.23).

Table 4.22: XRD phase identification of glass-ceramic C.

Two-step Heat Treatments Temperature (ºC) / Holding Time (hours)		Crystalline Phase
Nucleation	Crystallisation	
620/1	920/1	Tetragonal leucite
	960/0.5	
	960/1	
	960/2	
	960/3	
	960/4	
	960/5	
	1000/1	
620/2	920/1	
	960/1	
	1000/1	
620/4	920/1	

Table 4.23: XRD phase identification of glass-ceramics D and E.

Glass-ceramics	Two-step Heat Treatments Temperature (ºC) / Holding Time (hours)		Crystalline Phase
	Nucleation	Crystallisation	
Glass-ceramic D	670/1	1000/0.5	Tetragonal leucite
		1000/1	
		1000/2	
		1000/3	
		1000/4	
		1000/5	
	670/2	1000/1	
	670/4		
Glass-ceramic E	610/1	1050/1	

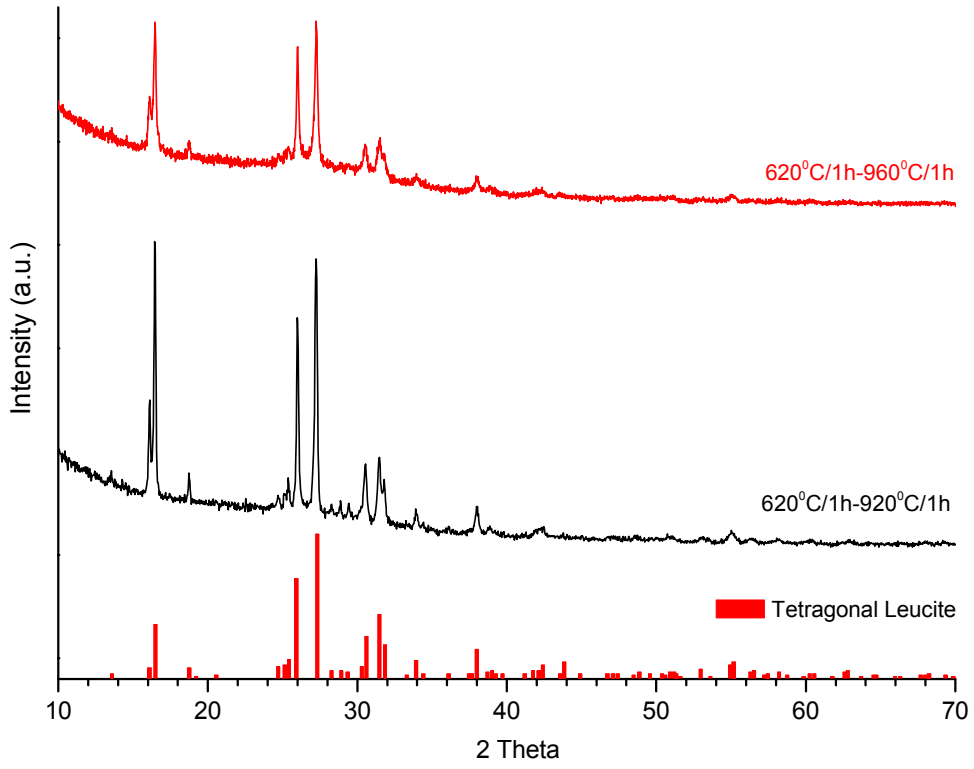

Fig. 4.35: The X-ray diffraction traces of glass-ceramics C (heating rate 10ºC/min).

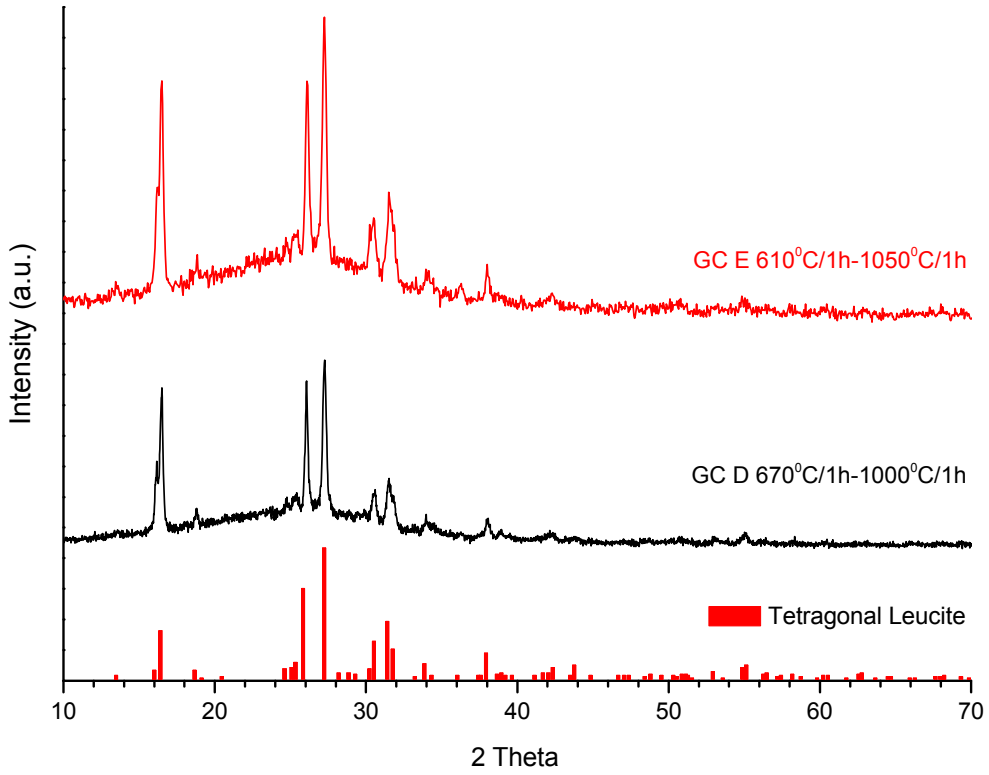

Fig. 4.36: The X-ray diffraction traces of glass-ceramics D and E (heating rate 10ºC/min).

4.7 Density Measurement Results

The density of the experimental glasses/glass-ceramics A, B, C and D measured by Archimede's Principle are given in Table 4.24. Data were analysed using a one way ANOVA (F test, $p<0.001$, Sigma Stat, version 2.03, SPSS Inc, Chicago, USA). The measured density value of glass B was higher than glasses A (4h A), C and D. Glass-ceramics A (4hr A), B and C have higher measured density values than glasses A (4hr A), B and C accordingly ($p<0.05$). However, no statistical difference was found between the glass-ceramic D and glass D ($p>0.05$). Plots showing the mean density of experimental glasses and glass-ceramics are illustrated in Fig. 4.37.

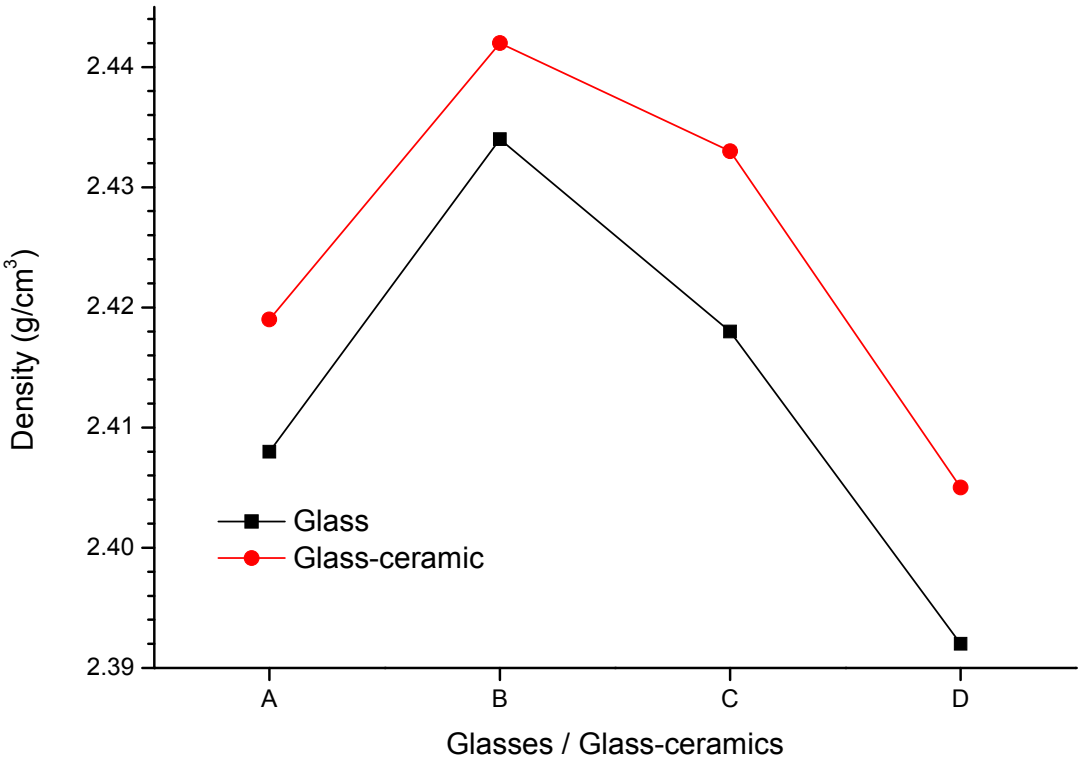

Fig. 4.37: Measured density comparisons of experimental glass and glass-ceramics.

Table 4.24: Density of experimental glasses / glass-ceramics (unit: g/cm^3).

Test Group	Predicted Value (Appen)	Measured Value (Glass)	Measured Value (Glass-ceramic)
Glass A (4hr A)	2.381	2.408^{a} (0.014)	2.419^{cd} (0.011)
Glass B	2.410	2.434^{b} (0.006)	2.442^{c} (0.010)
Glass C	2.397	2.418^{a} (0.006)	2.432^{c} (0.010)
Glass D	2.408	2.392^{ae} (0.013)	2.405^{de} (0.017)

Different superscript letters indicate significant differences between groups ($p<0.05$).

4.8 Refractive Index Measurement Results

Experimental glasses A, B and C were transparent. Glass D frits are transparent but slightly yellowish. The reflective index of glasses A, B, C and D measured by the Becke Line method using refractive index liquids are listed in Table 4.25. The measured reflective index is close to the predicted values by using the Appen Factors.

Glass-ceramics A (4hr A), A (starting A), E (4hr A with additional ZrO_2) were translucent, however the glass-ceramic A (8hr A) was translucent with a yellowish tint. The sintered glass-ceramics (B and HB) showed a high degree of translucency. Glass-ceramic C was translucent, and the glass-ceramic D appeared white and opaque. The refractive index of glass-ceramics A (4hr A), B, C and D were measured and listed in Table 4.25.

Table 4.25: Refractive index of the experimental glasses / glass-ceramics.

Test Group	Predicted Value (Appen)	Measured Value (Glass)	Measured Value (Glass-ceramic)
Glass A (4hr A)	1.503	1.500	1.520
Glass B (HB)	1.510	1.500	1.510
Glass C	1.507	1.510	1.530
Glass D	1.515	1.520	1.560

4.9 Secondary Electron Microscopy (SEM) Results

4.9.1 SEM Results for the Commercial Control Glass-Ceramics

The secondary electron imaging photomicrographs of the sintered or heat extruded commercial glass-ceramics are given in Fig. 4.38 - Fig. 4.40. IPS Empress Esthetic glass-ceramic showed uneven size tetragonal leucite dispersion in the glass matrix. Crystal coalescence, crystal necking and microcracking in leucite crystals and glass matrix was also noticed (Fig. 4.38). The Optimal glass-ceramic had larger and irregular leucite crystals in nature. Characteristic leucite twinning and microcracking present both within the leucite crystals and the glass matrix were clearly visible. Signs of cracks extending from leucite agglomerates were noticed in the glass matrix (Fig. 4.39). The Ceramco 3 glass-ceramic displayed extensive leucite crystal agglomerates interspersed with a few discrete leucite crystals with faceted crystals, irregular in size and shape. Both leucite clusters and discrete crystals showed angular grain boundaries. Extensive microcracking was present in the leucite crystals and surrounding glass matrix (Fig. 4.40). The quantitative analysis results of leucite particle size and the area fraction are presented in Table 4.26. A large standard deviation may be due to non uniform crystal growth. Quantitative elemental analysis results of the glass matrix of all commercial glass-ceramics using energy dispersive X-ray analysis (EDS) are given in Table 4.27.

Table 4.26: Quantitative measurement results of the commercial glass-ceramics.

Glass-ceramics	Leucite Area Fraction (%)	Crystal Size Mean (SD) (μm^2)	Particle Range (μm^2)
IPS Empress Esthetic	31.2	1.7 (2.0)	0.1 - 10.2
Optimal	36.5	5.5 (9.7)	0.2 - 86.1
Ceramco 3	30.4	8.1 (13.2)	0.1 - 178.2

Leucite crystal size and area fraction measurement were carried out based on images with magnification of 2200x.

Table 4.27: Compositional data of the glass matrix of commercial glass-ceramics.

mole%	Si	Al	K	Ca	Na	Mg	Ba	O
IPS Empress Esthetic	22.91	7.82	6.10	0.37	1.37	0	0	61.35
Optimal	25.18	6.38	3.86	0.17	1.48	0	0	62.89
Ceramco 3	25.07	4.35	3.1	1.1	3.72	0.46	0.29	61.92

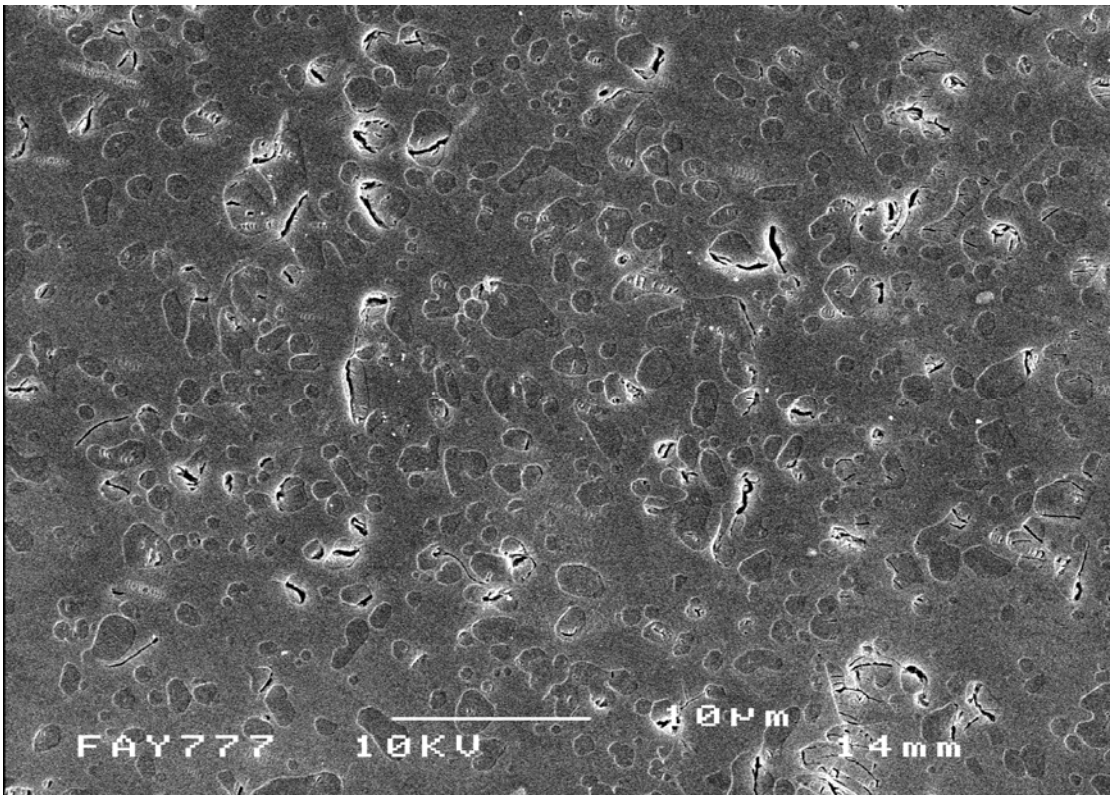

Fig. 4.38: SEM micrograph of the heat extruded IPS Empress Esthetic glass-ceramic showing leucite crystal coalescence, and microcracking within the leucite crystals and glass matrix (2200 x).

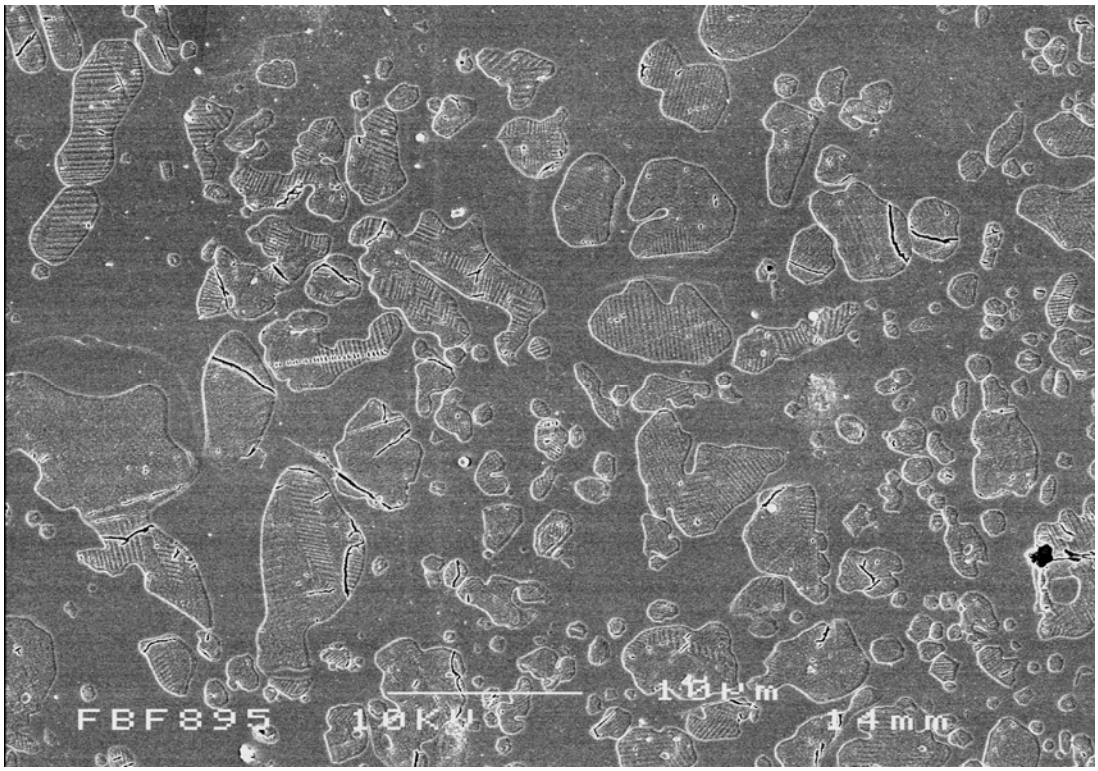

Fig. 4.39: SEM micrograph of the heat extruded Optimal glass-ceramic showing larger and irregular leucite crystals with crystal and matrix microcracking (2200 x).

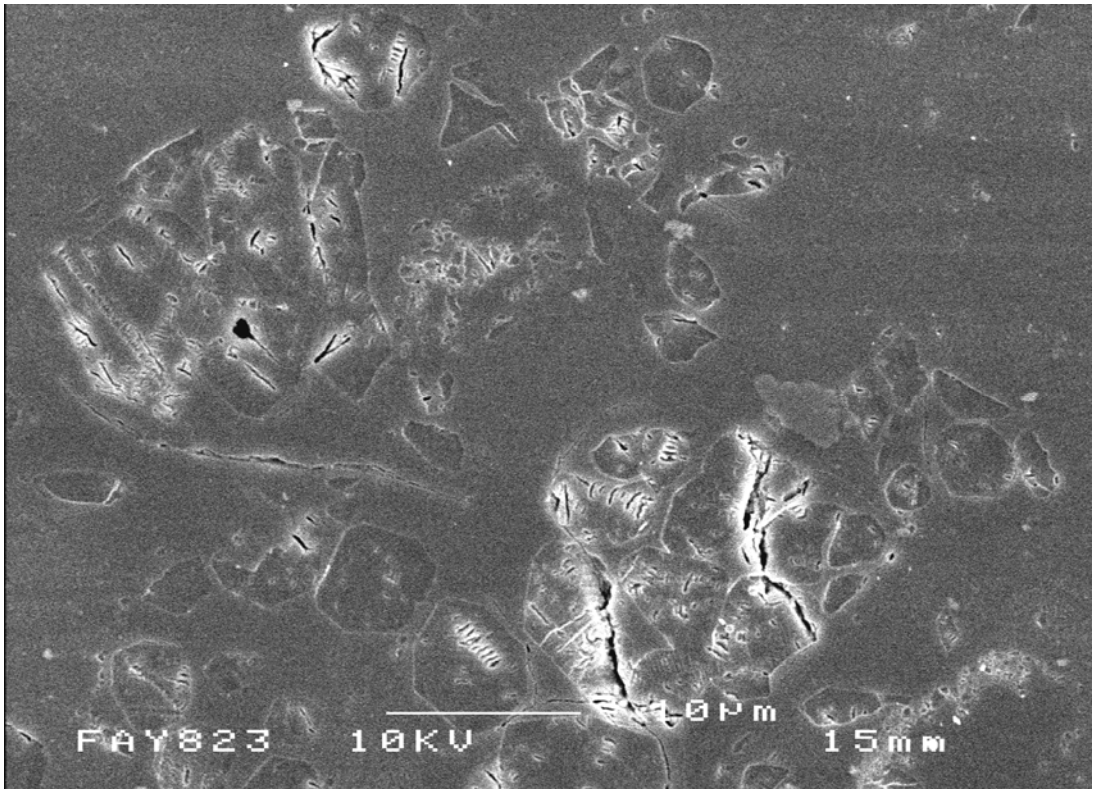

Fig. 4.40: SEM micrograph of the sintered Ceramco 3 glass-ceramic showing extensive leucite crystal agglomerates and extensive microcracking (2200 x).

4.9.2 SEM Results for the Experimental Glasses

Sign of spherical phase separation was observed in glass B (Fig. 4.41), glass C (Fig. 4.42) and glass D (Fig. 4.43). Energy dispersive X-ray analysis (EDS) results (mole %) of the spherical phase separated area and the glass matrix are presented in Table 4.28 - Table 4.30. No clear differences in the elemental composition between the spherical phase separated areas and the glass matrix were observed, which might be attributed to the limitation of the EDS beam width and penetration depth.

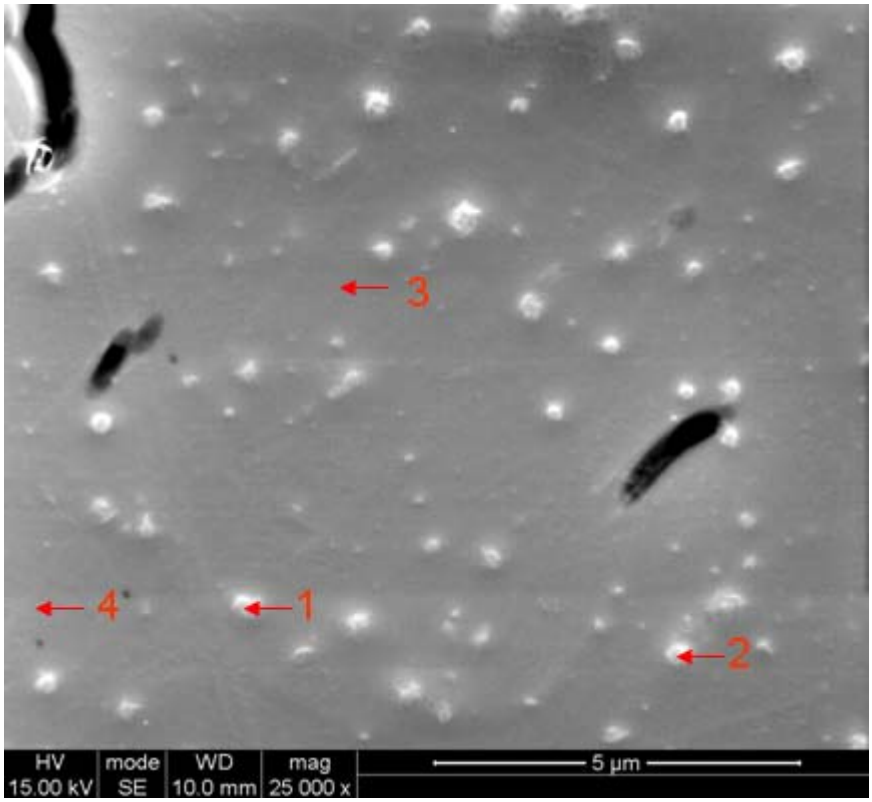

Fig. 4.41: SEM micrograph of the glass B frit showing spherical domains, 1 and 2 are phase separated areas, 3 and 4 are glass matrix.

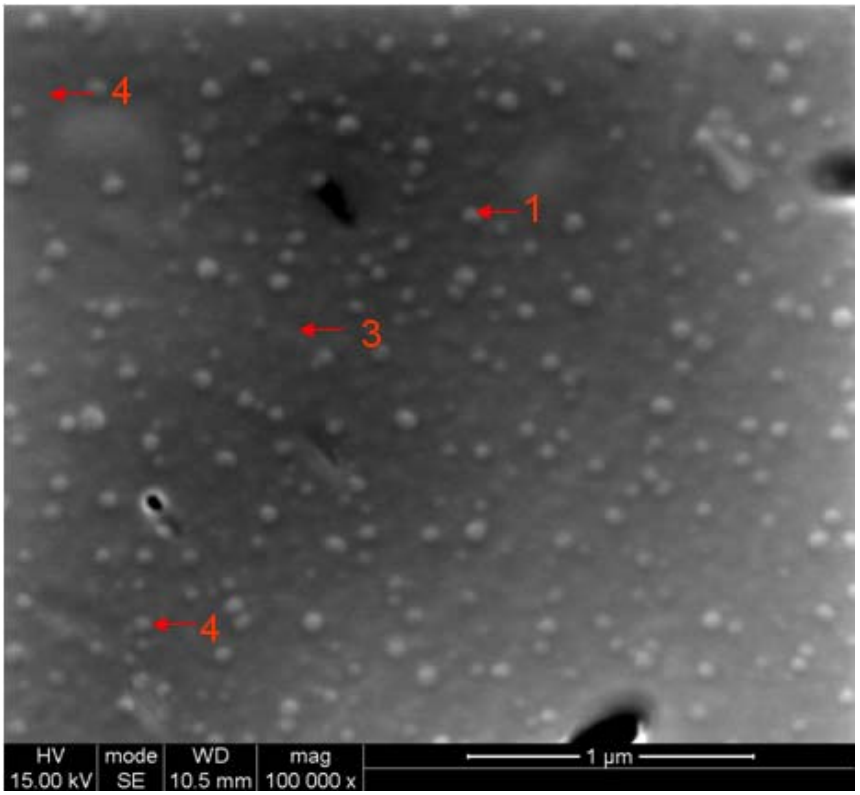

Fig. 4.42: SEM micrograph of the glass C frit showing spherical domains, 1 and 2 are phase separated areas, 3 and 4 are glass matrix.

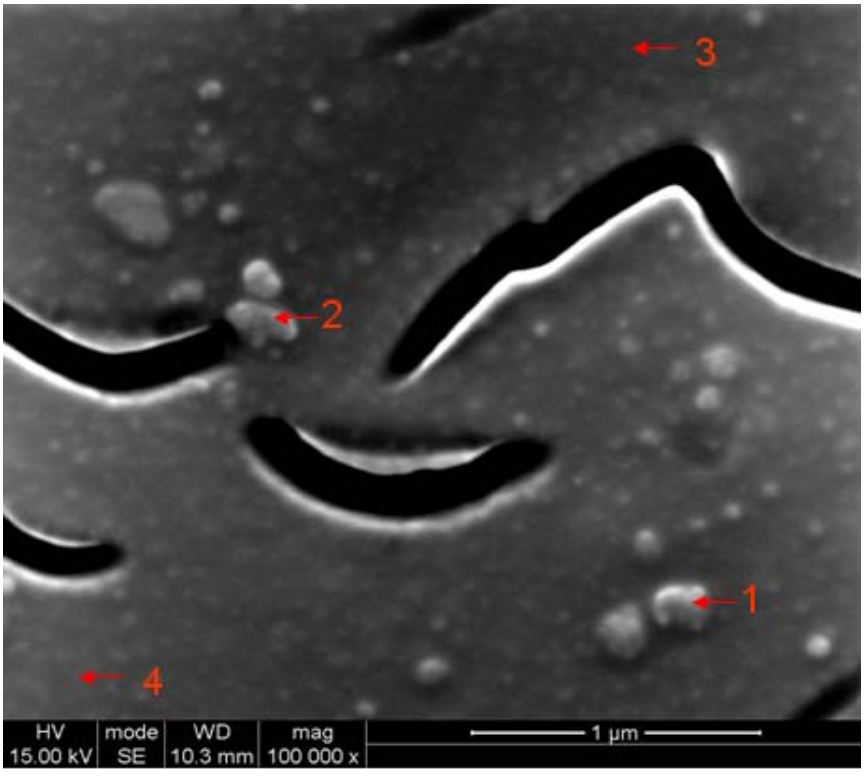

Fig. 4.43: SEM micrograph of the glass D frit showing spherical domains and signs of coarsening, 1 and 2 are phase separated areas, 3 and 4 are glass matrix.

Table 4.28: EDS spot analysis results of glass B frit (elements in mole %).

Elements	Spherical Phase Separated Areas		Glass Matrix	
	Spectrum 1	Spectrum 2	Spectrum 3	Spectrum 4
Na	1.69	1.68	1.69	1.66
Mg	0.14	0.12	0.14	0.15
Al	5.86	5.81	5.86	5.91
Si	24.33	24.39	24.33	24.12
K	5.35	5.31	5.35	5.69
Ca	0.53	0.54	0.53	0.56
Ti	0.15	0.17	0.15	0.14
O	61.95	61.98	61.95	61.77

Table 4.29: EDS spot analysis results of glass C frit (elements in mole %).

Elements	Spherical Phase Separated Areas		Glass Matrix	
	Spectrum 1	Spectrum 2	Spectrum 3	Spectrum 4
Na	1.55	1.64	1.34	1.28
Mg	0.13	0.17	0.15	0.17
Al	6.26	6.28	6.40	6.42
Si	24.32	24.21	24.81	24.82
K	4.82	4.87	3.74	3.75
Ca	0.55	0.55	0.58	0.60
Ti	0.16	0.16	0.17	0.13
O	62.21	62.13	62.82	62.83

Table 4.30: EDS spot analysis results of glass D frit (elements in mole %).

Elements	Spherical Phase Separated Areas		Glass Matrix	
	Spectrum 1	Spectrum 2	Spectrum 3	Spectrum 4
Na	1.04	1.02	1.00	0.97
Mg	0.15	0.12	0.14	0.12
Al	6.03	5.88	6.01	5.86
Si	24.67	24.72	24.74	24.77
K	4.00	4.12	3.88	4.13
Ca	0.60	0.58	0.61	0.61
Ti	0.63	0.68	0.65	0.65
O	62.90	62.88	62.98	62.90

4.9.3 SEM Results for the Experimental Glass-Ceramics

4.9.3.1 SEM Results for the Attritor Milled and Heat Treated Glass-Ceramic A

The results of the scanning secondary electron imaging for the Attritor milled and heat treated glass A are given in Fig. 4.45 - Fig. 4.47. Glass-ceramic A (starting A, Fig. 4.44) shows an even distribution of leucite crystals in the glass matrix with microcracking restricted to leucite crystals (Fig. 4.44). Some crystal twinning was visible. Glass-ceramic A (30 min A) had a smaller leucite crystal size (Table 4.31), and some crystal coalescence was noticed. Glass-ceramic A (45 min A) showed some relatively large leucite clusters (Fig. 4.45). Further milling of the glasses resulted in a reduction in the mean leucite crystal size and an increase in crystal number of the heat treated glass-ceramics (Table 4.31). A remarkable increase in the leucite crystal number and distinct reduction in mean leucite crystal size were observed for glass-ceramic A (4hr A, Fig. 4.46) and glass-ceramic A (8hr A, Fig. 4.47). Although the mean crystal sizes had large standard deviations due to limited crystal coalescence and the presence of a few larger crystals, the mean glass powder size D [v, 0.5] was plotted versus the leucite crystal size or leucite crystal number (Fig. 4.48 and Fig. 4.49). These plots indicated a relationship between the glass powder size and mean leucite crystal size (r^2 = 0.9329) and Leucite crystal number (r^2 = 0.9891).

Table 4.31: Quantitative measurement results of the Attritor milled and heat treated glass-ceramics A.

Glass-ceramics	Leucite Area Fraction (%)	Crystal No	Crystal Size Mean (SD) (μm^2)	Size Range (μm^2)
Glass A	25.0	558	0.99 (0.59)	0.14 - 4.31
30 min A	23.0	640	0.79 (0.60)	0.06 - 6.58
45 min A	22.8	629	0.80 (0.86)	0.10 - 9.43
60 min A	22.2	694	0.71 (0.50)	0.01 - 5.14
90 min A	23.3	905	0.57 (0.45)	0.11 - 8.70
120 min A	25.7	1092	0.52 (0.42)	0.02 - 5.28
4hr A	25.4	1434	0.39 (0.28)	0.03 - 4.90
8hr A	24.9	3378	0.16 (0.10)	0.01 - 1.25

Specimens ramped at 10ºC/min to 650ºC/1h hold, then up to 1120ºC/1h hold. Leucite crystal size and area fraction measurement were carried out based on images with a magnification of 2200 x.

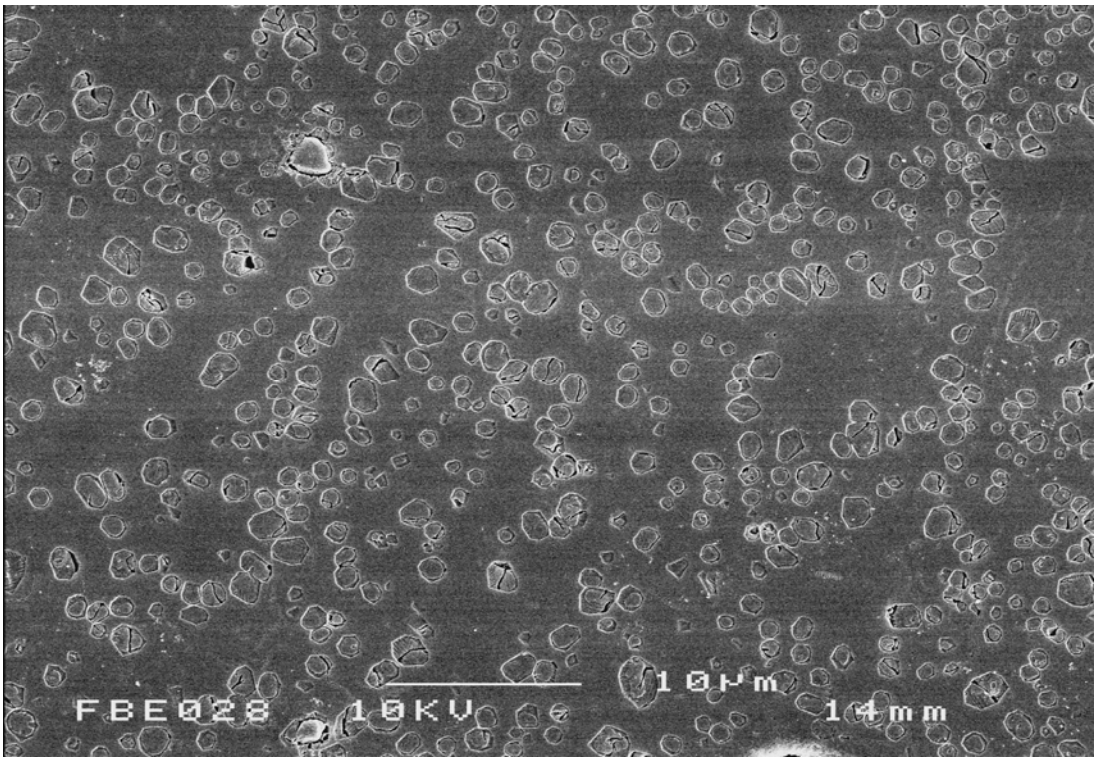

Fig. 4.44: SEM micrograph of two-step heat treated starting glass A showing tetragonal leucite crystals in the glass matrix (2200 x).

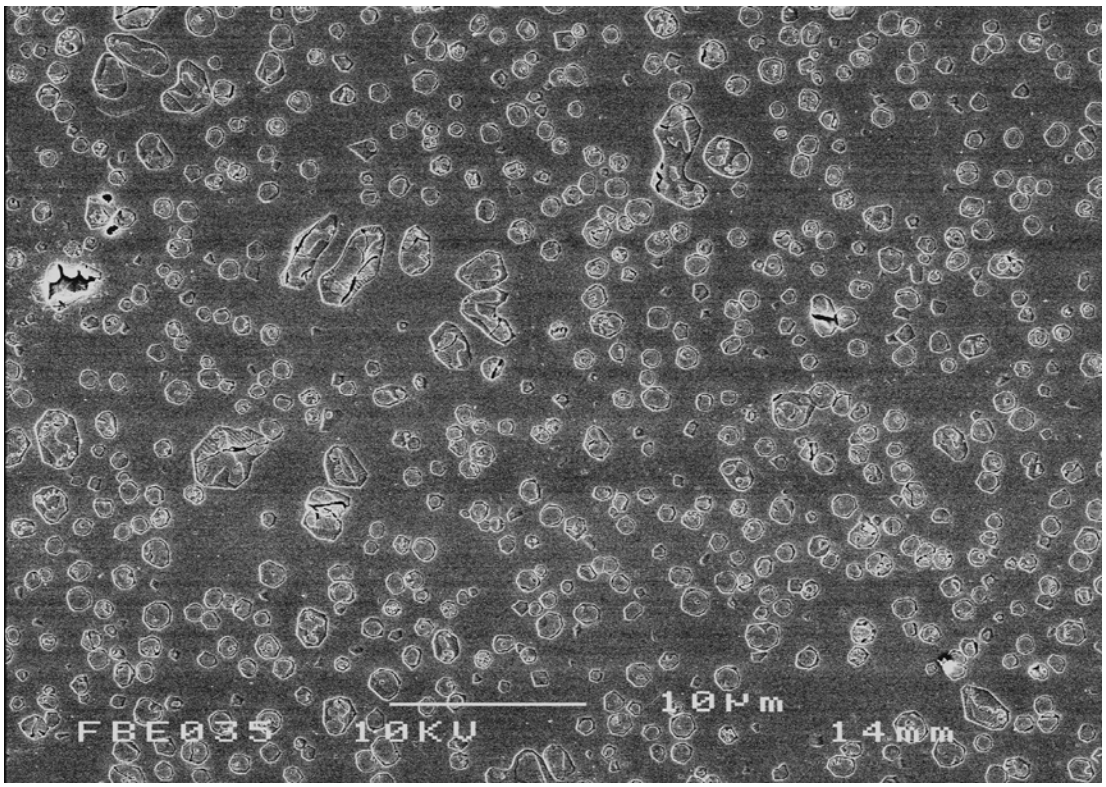

Fig. 4.45: SEM micrograph of two-step heat treated glass A (45 min A) showing evidence of some leucite crystal growth (2200 x).

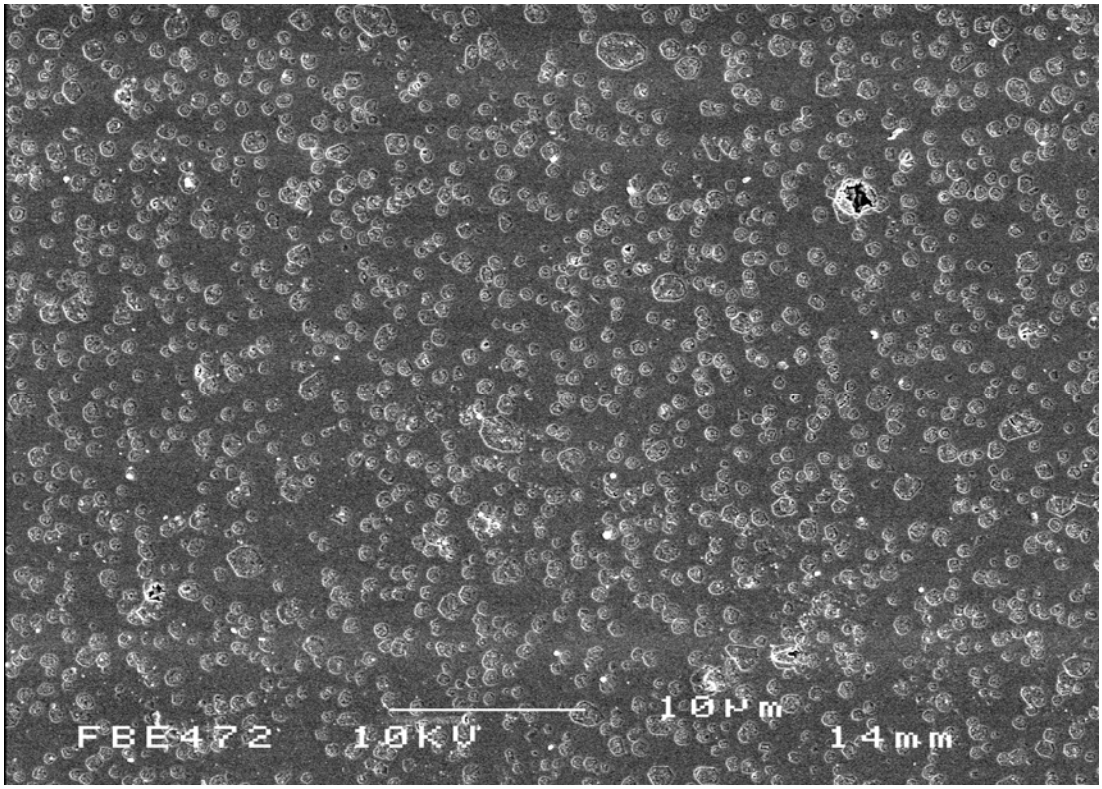

Fig. 4.46: SEM micrograph of two-step heat treated glass A (4hr A) showing a dense dispersal of fine leucite crystallisation in the glass matrix (2200 x).

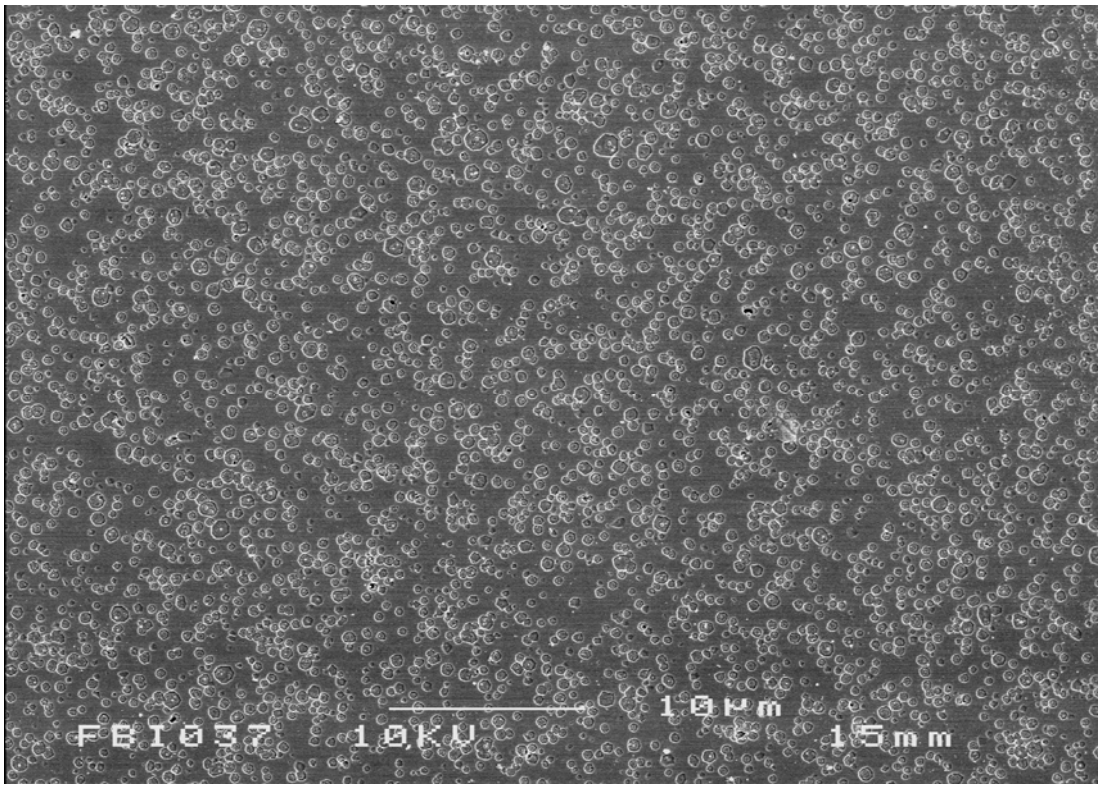

Fig. 4.47: SEM micrograph of two-step heat treated glass A (8hr A) showing an increase of fine leucite crystals in the glass matrix (2200 x).

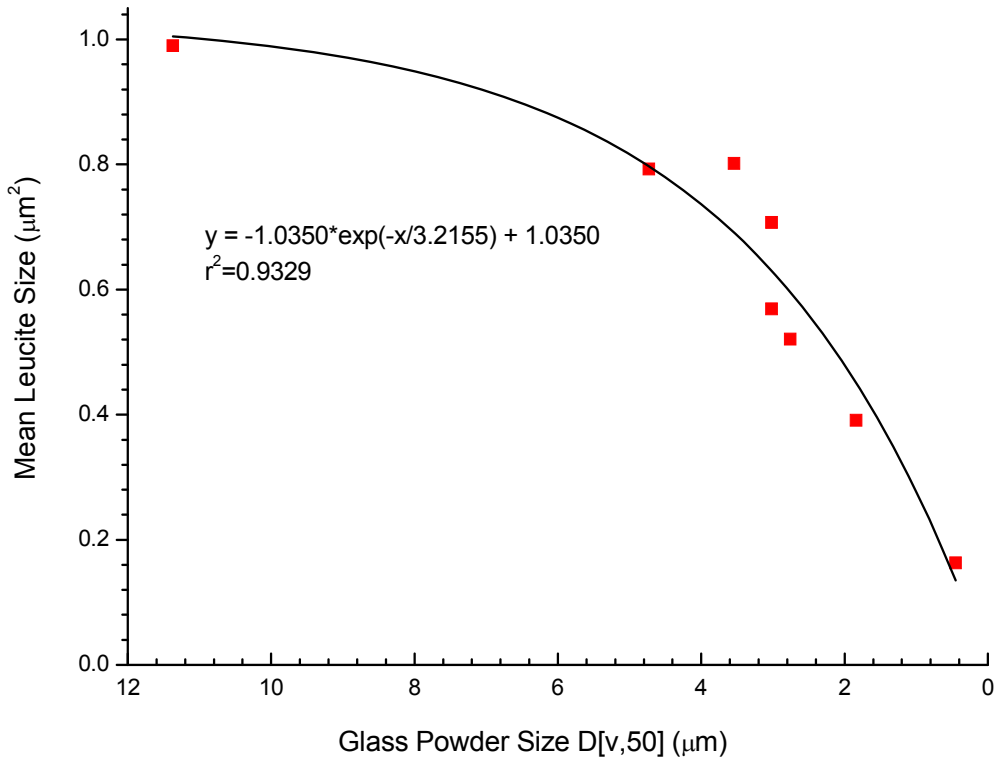

Fig. 4.48: The relationship between the glass powder size and mean leucite crystal size.

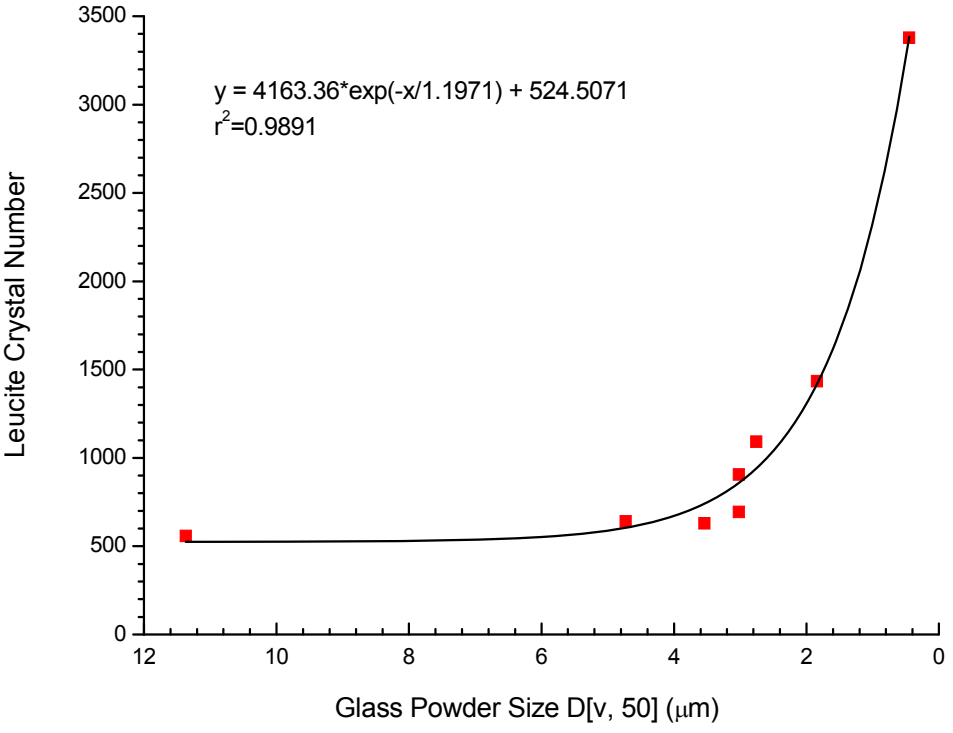

Fig. 4.49: The relationship between the glass powder size and leucite crystal number.

4.9.4 SEM Results of the Glass A (4hr A) Crystallisation

4.9.4.1 Nucleation Temperature Control Results

The leucite crystal size, range and area fraction of glass A (4hr A) compacts after different two-step heat treatments (1 hour nucleation at different nucleation temperatures followed by 1 hour crystallisation at 1120ºC) are illustrated in Table 4.32, Fig. 4.50 and Fig. 4.51. A maximum leucite crystal number of 1751 was observed for glass-ceramic A (4hr A) nucleated at 610ºC, and the leucite crystal number decreases with increase in nucleation temperature. A steady reduction in leucite area fraction was found with increase in nucleation temperature from 650ºC onwards. The maximum leucite area fraction (25.4%) was achieved with a nucleation temperature of 650ºC. Glass-ceramic A (4hr A) nucleated at 610ºC gave the smallest Mean (SD) leucite crystal size 0.30 (0.24) μm^2, maximum leucite crystal number 1751, and a relatively high leucite area fraction (23.4%) (Table 4.32).

Table 4.32: The results of different nucleation treatments on the glass A (4hr A).

Nucleation Temperature (ºC)	Leucite Area Fraction (%)	Crystal No	Crystal size Mean (SD) (μm^2)	Size Range (μm^2)
600	21.2	1383	0.34 (0.28)	0.05 - 4.69
610	23.4	1751	0.30 (0.24)	0.01 - 2.92
620	21.8	1577	0.31 (0.23)	0.02 - 3.12
630	23.4	1439	0.36 (0.25)	0.06 - 2.87
640	18.4	1266	0.32 0.20)	0.04 - 2.00
650	25.4	1434	0.39 (0.28)	0.03 - 4.90
660	24.1	1513	0.35 (0.22)	0.05 - 2.51
670	22.0	1240	0.39 (0.25)	0.05 - 3.27
680	21.6	1281	0.37 (0.26)	0.04 - 2.76
690	20.5	1308	0.35 (0.26)	0.01 - 2.47
700	18.7	963	0.43 (0.24)	0.04 - 2.99

Specimens ramped at 10ºC/min to T_n/1h hold and then 1120ºC/1h hold. Leucite crystal size and area fraction measurement were carried out based on images with a magnification of 2200 x.

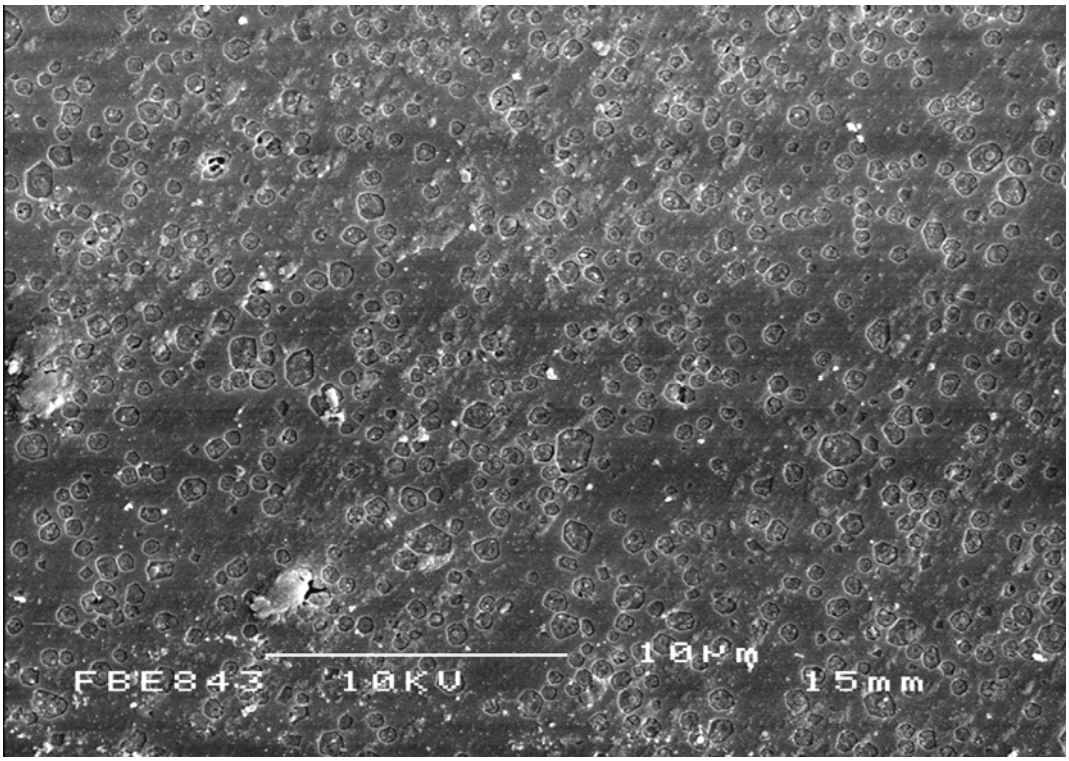

Fig. 4.50: SEM micrograph of glass-ceramic A (4hr A, 610ºC/1h - 1120ºC/1h) showing fine leucite crystals 0.30 (0.24) μm^2 in the glass matrix (3500 x).

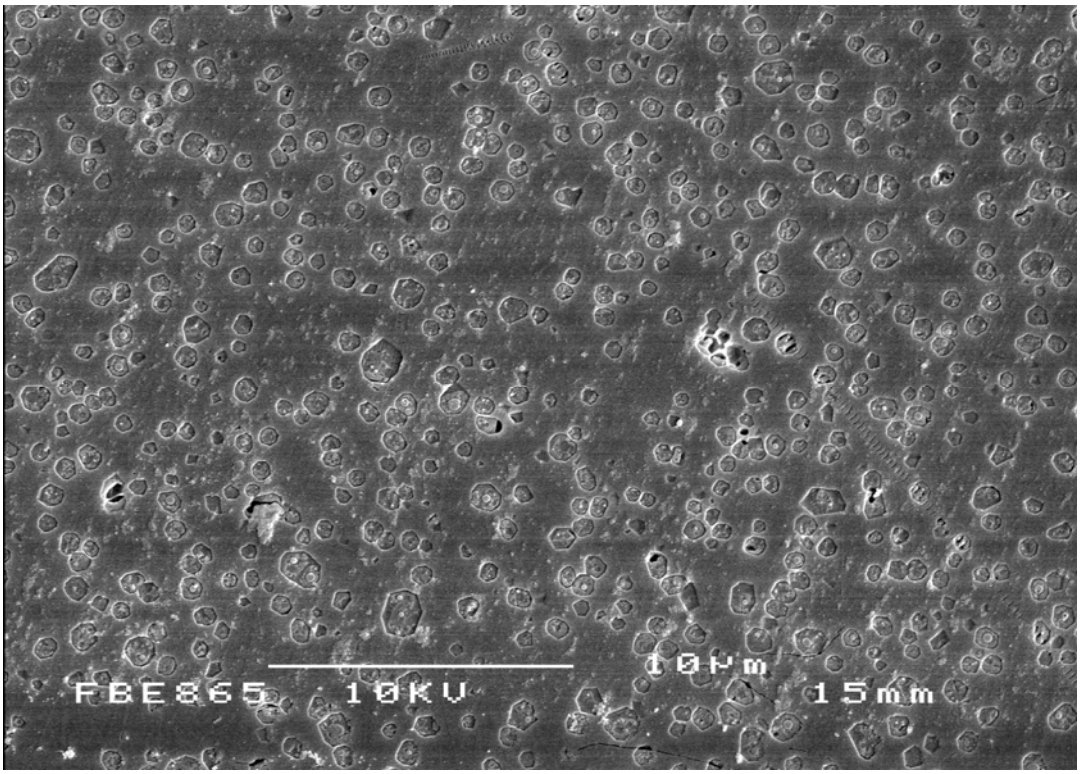

Fig. 4.51: SEM micrograph of glass-ceramic A (4hr A, 700ºC/1h - 1120ºC/1h) showing increased leucite crystal growth in the glass matrix (3500 x).

4.9.4.2 Nucleation Hold Time Results

The quantitative measurement results of leucite crystal size, range and the leucite area fraction of glass A (4hr A) compacts after different nucleation holds at 610ºC, followed by ramping to 1120ºC for 1 hour hold are given in Table 4.33. Leucite area fraction linearly increased with the increased nucleation hold time (Fig. 4.53). Glass-ceramic A (4hr A) with 1 hour nucleation hold gave the smallest Mean (SD) crystal size of 0.30 (0.24) μm^2 (Fig. 4.50 and Table 4.33). The 4 hours nucleation held glass-ceramic A (4hr A) gave the maximum crystal number of 1853 (Table 4.33), however, crystal coalescence was noticed (Fig. 4.52).

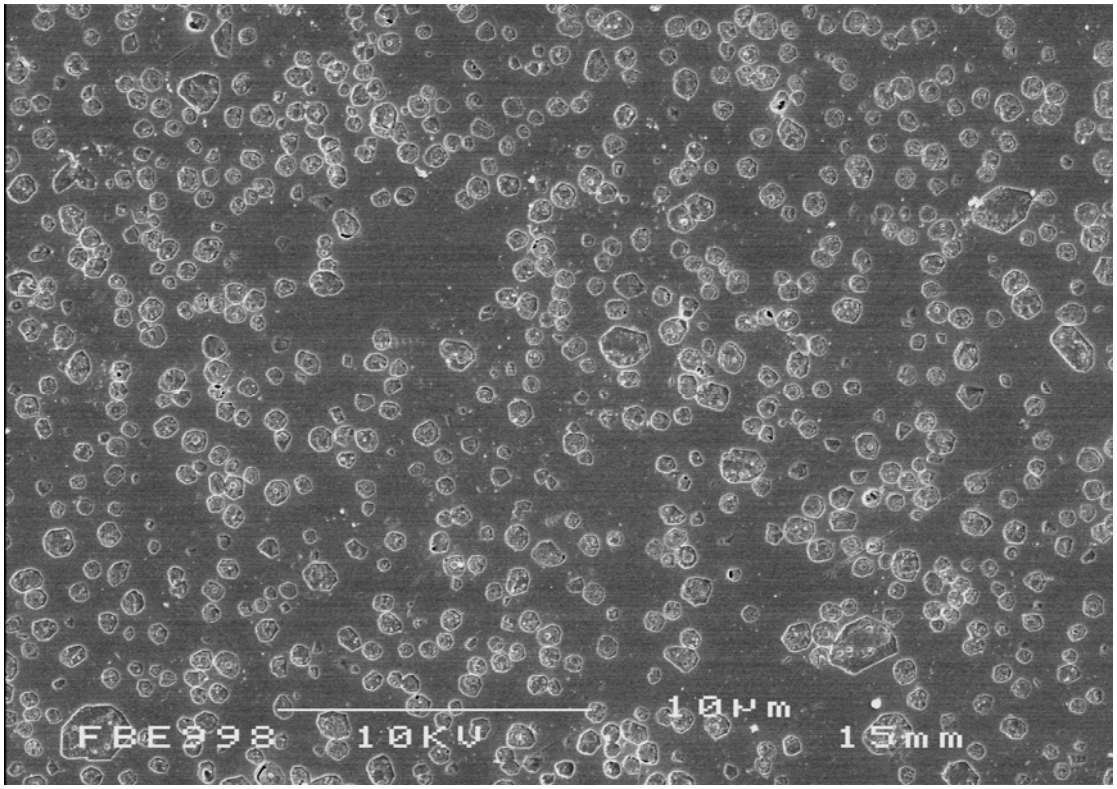

Fig. 4.52: SEM micrograph of glass-ceramic A (4hr A, 610ºC/4h - 1120ºC/1h) showing evidence of crystal coalescence (3500 x).

Table 4.33: Quantitative measurement results of the different nucleation holds at 610ºC on glass A (4hr A).

Holding Time (h)	Leucite Area Fraction (%)	Crystal No	Crystal Size Mean (SD) (μm^2)	Size Range (μm^2)
0.5	22.6	1702	0.30 (0.22)	0.05 - 2.77
1	23.4	1751	0.30 (0.24)	0.01 - 2.92
2	23.5	1610	0.33 (0.25)	0.04 - 3.61
3	25.2	1650	0.34 (0.25)	0.02 - 3.00
4	26.6	1853	0.32 (0.19)	0.02 - 2.07
5	26.7	1754	0.34 (0.24)	0.02 - 3.06

Leucite crystal size and area fraction measurement were carried out based on images with a magnification of 2200 x.

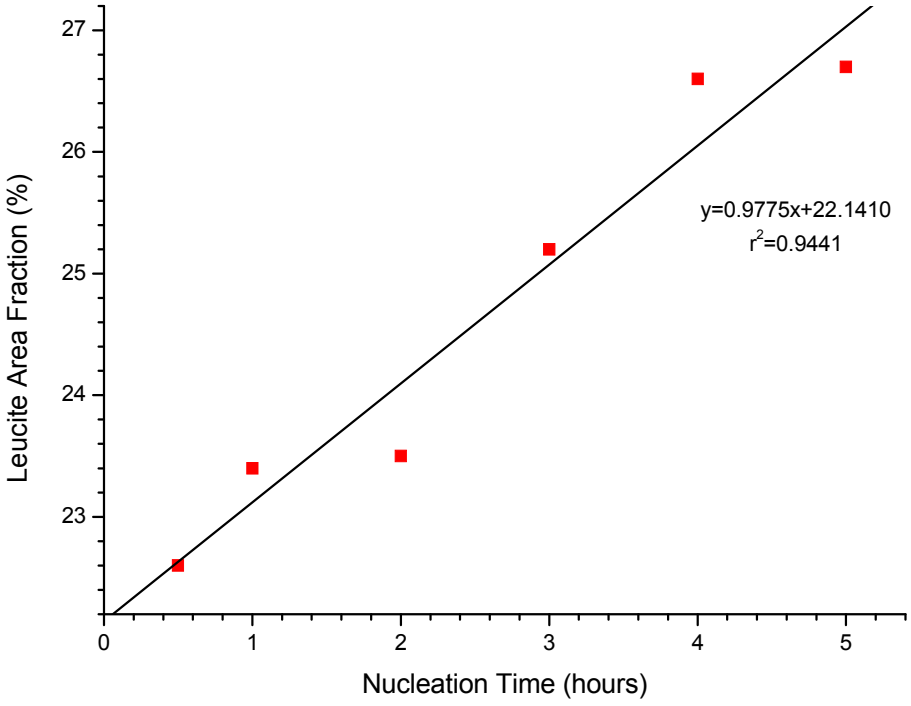

Fig. 4.53: The relationship between the leucite area fraction and nucleation hold.

4.9.4.3 Crystal Growth Temperature Control Results

The secondary electron imaging micrographs of the glass A (4hr A) compacts after different two-step heat treatments (different nucleation holds at 610ºC followed by 1 hour crystal growth at selected temperatures) are given in Fig. 4.54 - Fig. 4.57. The quantitative measurement results of the leucite crystal size, range and leucite area fraction are listed in Table 4.34. Glass-ceramic A (4hr A) nucleated at 610ºC (1 hour) and crystallised at 1000ºC (1 hour) showed the coexistence of extensive leucite crystals and signs of a second phase (lath shaped crystal) in the glass matrix (Fig. 4.54). Glass-ceramic A (4hr A) nucleated at 610ºC for 1 hour and crystallised at 1050ºC for 1 hour (Fig. 4.55) gave the maximum leucite crystal number (4895) and minimum Mean (SD) leucite crystal size 0.15 (0.09) μm^2. A remarkable reduction in the crystal number, area fraction and increase in mean crystal size were detected for higher crystallisation temperatures (Fig. 4.56 and Table 4.34). Prolonged nucleation hold (4 hours) followed by 1 hour crystallisation at 1050ºC resulted in a reduction in leucite crystal number, area fraction and increases in the mean crystal size (Table 4.34 and Fig. 4.57).

Table 4.34: The results of the different crystal growth temperatures on the glass A (4hr A).

Heat Treatments (ºC/hours)	Leucite Area Fraction (%)	Crystal No	Leucite Crystal Size Mean (SD) (μm^2)	Size Range (μm^2)
610/1-1000/1	33.4	3057	0.24 (0.19)	0.01 - 2.76
610/1-1050/1	33.4	4895	0.15 (0.09)	0.01 - 0.91
610/1-1100/1	23.3	1731	0.30 (0.24)	0.18 - 2.91
610/1-1120/1	23.4	1751	0.30 (0.24)	0.01 - 4.00
610/4-1050/1	28.9	3259	0.20 (0.16)	0.01 - 2.48

Leucite crystal size and area fraction measurement were carried out based on images with a magnification of 2200 x.

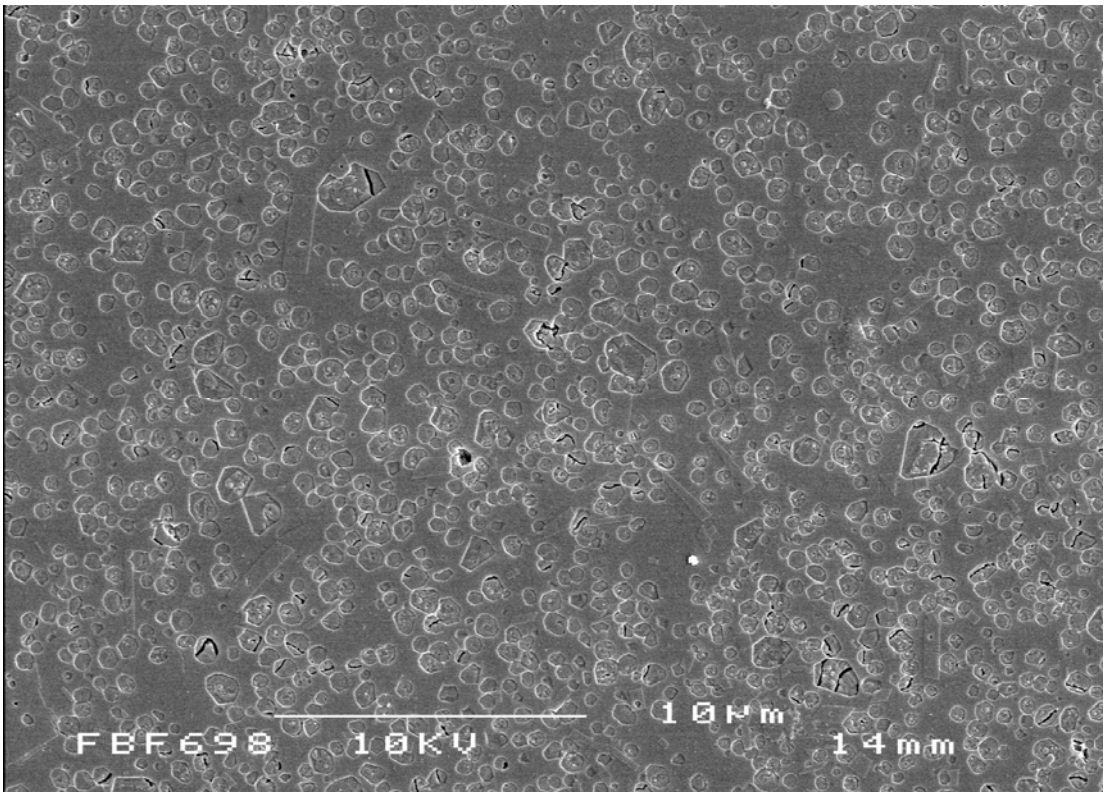

Fig. 4.54: SEM micrograph of glass-ceramic A (4hr A, 610ºC/1h - 1000ºC/1h) showing the coexistence of leucite and lath shaped sanidine crystals (3500 x).

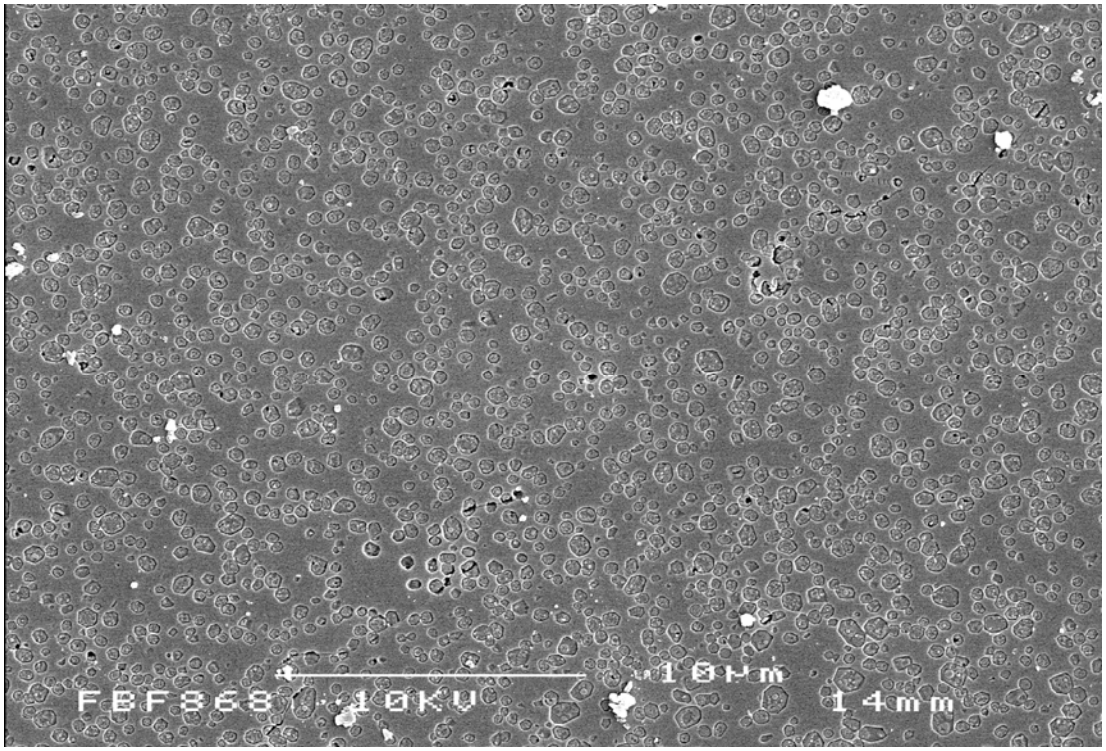

Fig. 4.55: SEM micrograph of glass-ceramic A (4hr A, 610ºC/1h - 1050ºC/1h) showing a uniform distribution of fine leucite crystals (3500 x).

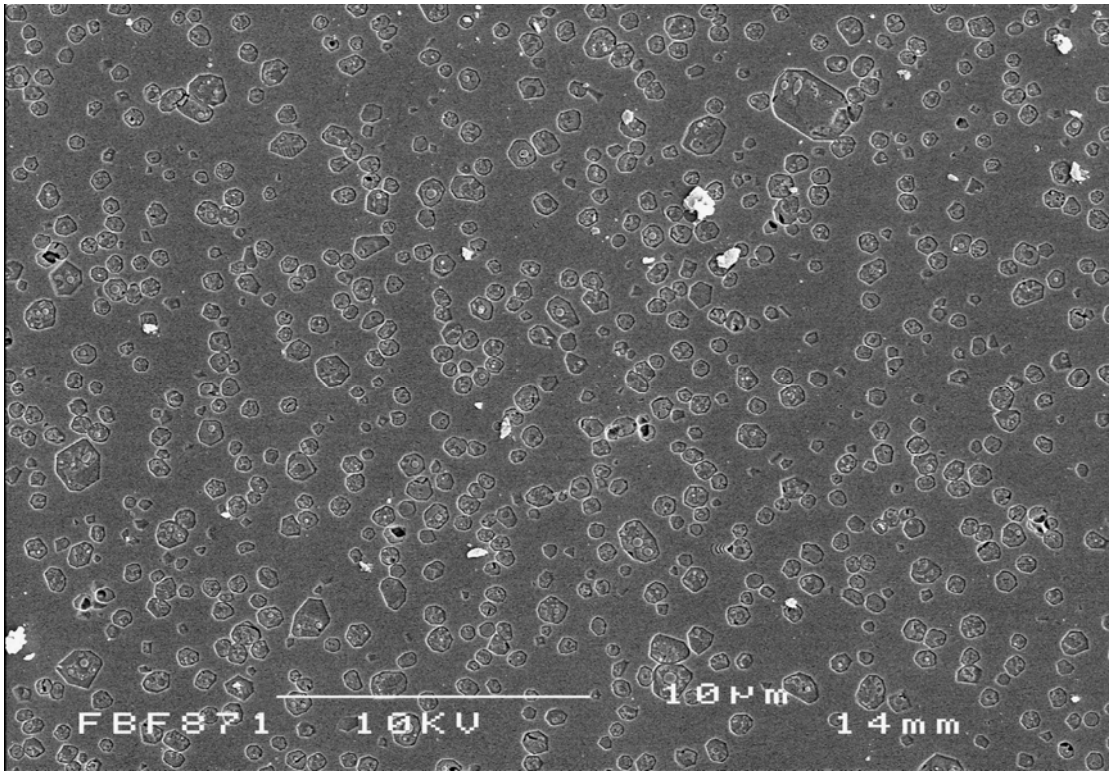

Fig. 4.56: SEM micrograph of glass-ceramic A (4hr A) (610ºC/1h - 1100ºC/1h, showing a reduction in leucite crystal number in glass matrix (3500 x).

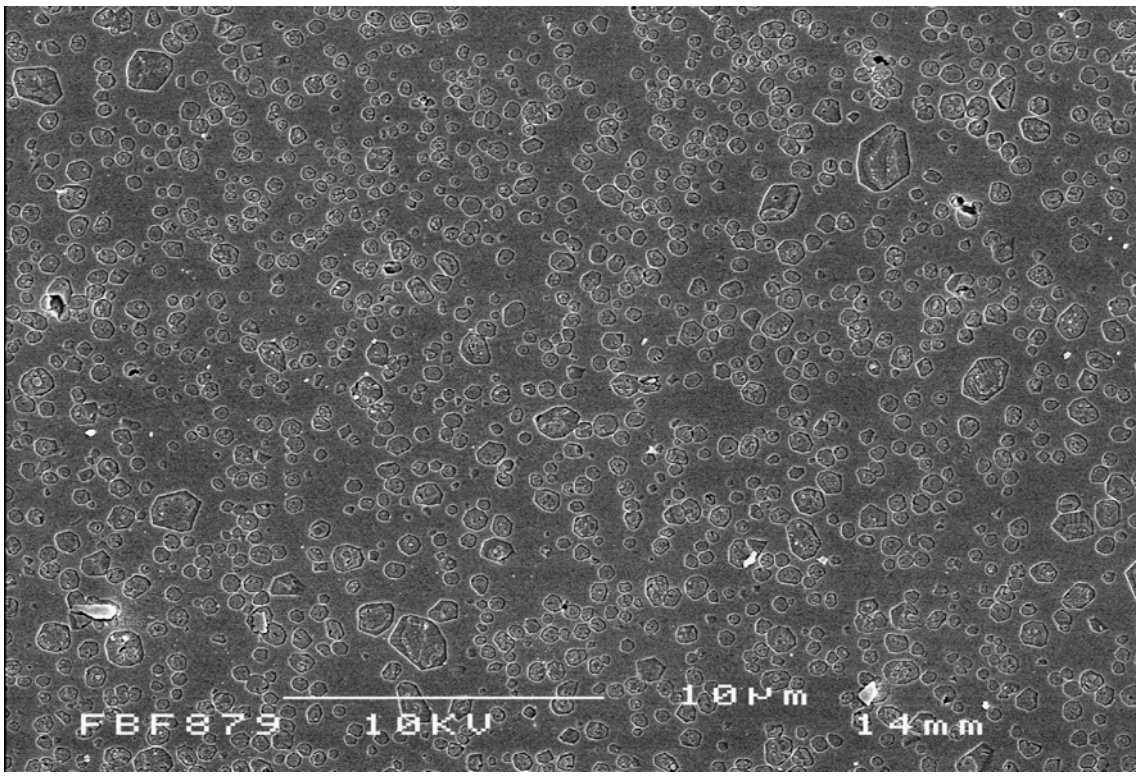

Fig. 4.57: SEM micrograph of glass-ceramic A (4hr A) showing the effect of the 4 hours nucleation at 610ºC and 1 hour crystal growth at 1050ºC (3500 x).

4.9.4.4 Crystal Growth Hold Time Results

The glass A (4hr A) nucleated at 610ºC for 1 hour and followed by different crystal growth holds at 1050ºC produced an even distribution of fine leucite crystals and some larger leucite crystals in the glass matrix (Fig. 4.58). Microcracking was observed only within larger leucite crystals. The mean leucite crystal size, range and area fraction are listed in Table 4.35. Glass-ceramic A (4hr A, Fig. 4.55) with a 1 hour crystallisation hold at 1050ºC gave the maximum leucite crystal number 4895, and the smallest Mean (SD) leucite crystal size 0.15 (0.09) μm^2. A gradual increase in the mean crystal size was recorded with prolonged crystal growth holds (Table 4.35).

Table 4.35: The results of the different crystal growth holds at 1050ºC on the glass A (4hr A).

Heat Treatments 610ºC/1h - 1050ºC	Leucite Area Fraction (%)	Crystal No	Crystal Size Mean (SD) (μm^2)	Size Range (μm^2)
0.5h	29.49	2717	0.24 (0.19)	0.01 - 3.18
1h	33.38	4895	0.15 (0.09)	0.01 - 0.91
2h	27.09	3122	0.19 (0.18)	0.01 - 2.47
3h	29.51	3039	0.22 (0.19)	0.02 - 2.93
4h	28.96	2697	0.24 (0.21)	0.01 - 2.93

Leucite crystal size and area fraction measurement were carried out based on images with a magnification of 2200 x.

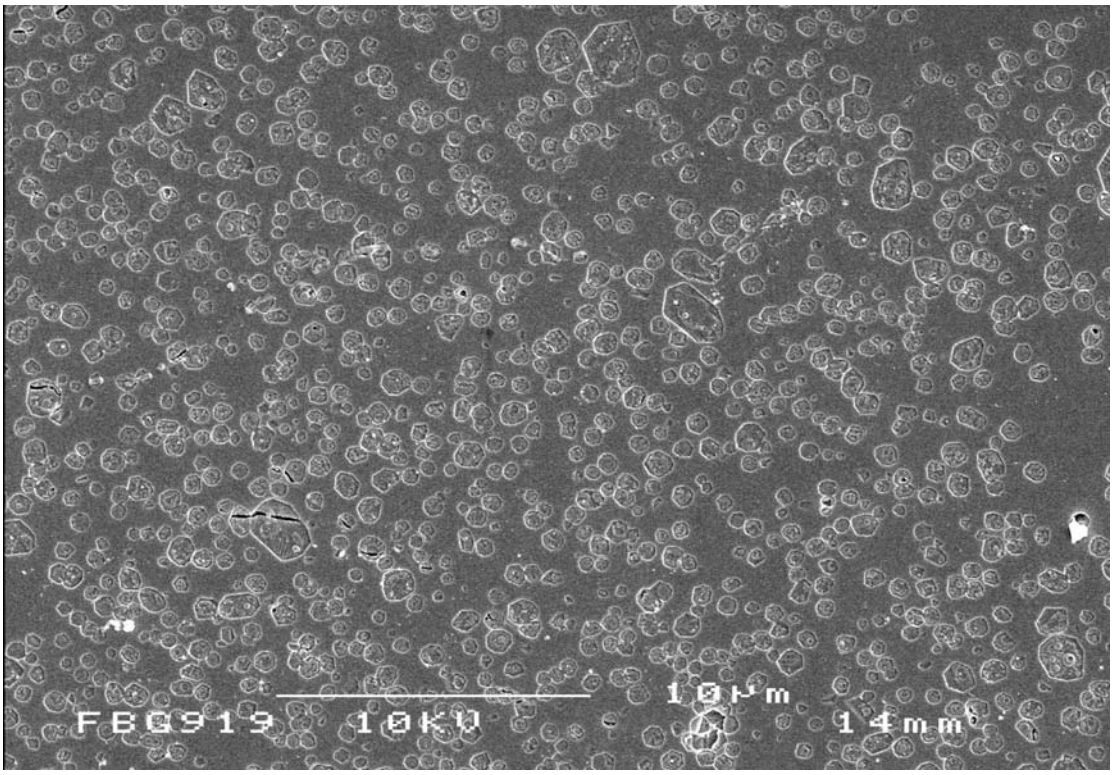

Fig. 4.58: SEM micrograph of glass-ceramic A (4hr A, 610ºC/1h - 1050ºC/4h) showing an increase in leucite crystal size and a few larger crystals after a growth hold of 4 hours (3500 x).

4.9.4.5 Sanidine Crystallisation

Sanidine and leucite crystals were visible in glass-ceramic A (4hr A) with two-step heat treatments (1 hour nucleation at 610ºC, followed by different crystal growth holds at 850ºC). Tetragonal leucite was the major crystalline phase for the 1 hour crystal growth glass-ceramic A (4hr A, Fig. 4.59). The two hour hold specimen showed a reduction in leucite crystal number and size, and sanidine was the major crystalline phase (Fig. 4.60). Very few leucite crystals were found in the 3 hours crystal growth hold specimen (Fig. 4.61). The quantitative measurement results for leucite crystallisation are listed in Table 4.36.

Table 4.36: The quantitative measurement results of sanidine crystallisation on glass-ceramics A (4hr A).

Heat Treatments 610ºC/1h - 860ºC	Leucite Area Fraction (%)	Crystal No	Crystal Size Mean (SD) (μm^2)	Size Range (μm^2)
1h	24.72%	252	0.11 (0.11)	0.01 - 1.00
2h	5.06%	55	0.10 (0.10)	0.01 - 0.34
3h	0.16%	8	0.02 (0.01)	0.01 - 0.03

Leucite crystal size and area fraction measurement were carried out based on images with a magnification of 2200 x.

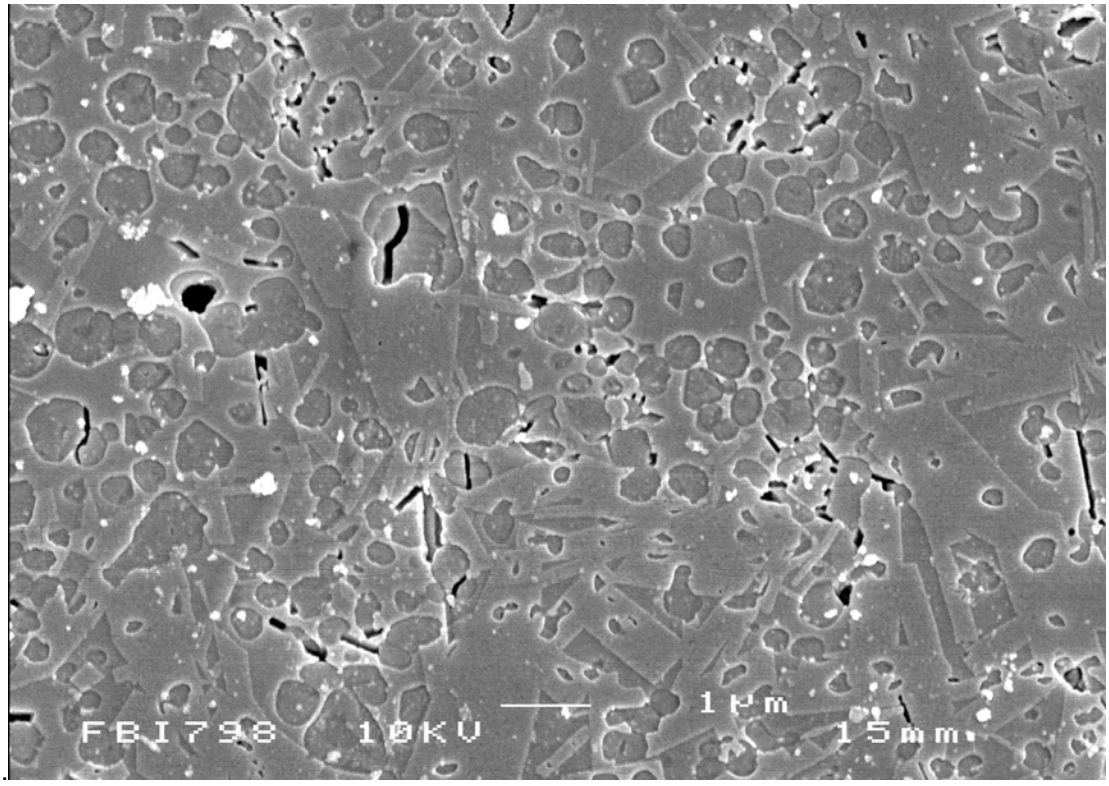

Fig. 4.59: SEM micrograph of glass-ceramic A (4hr A) (610ºC/1h - 850ºC/1h) showing the coexistence of tetragonal leucite and sanidine within the glass matrix (10,000 x).

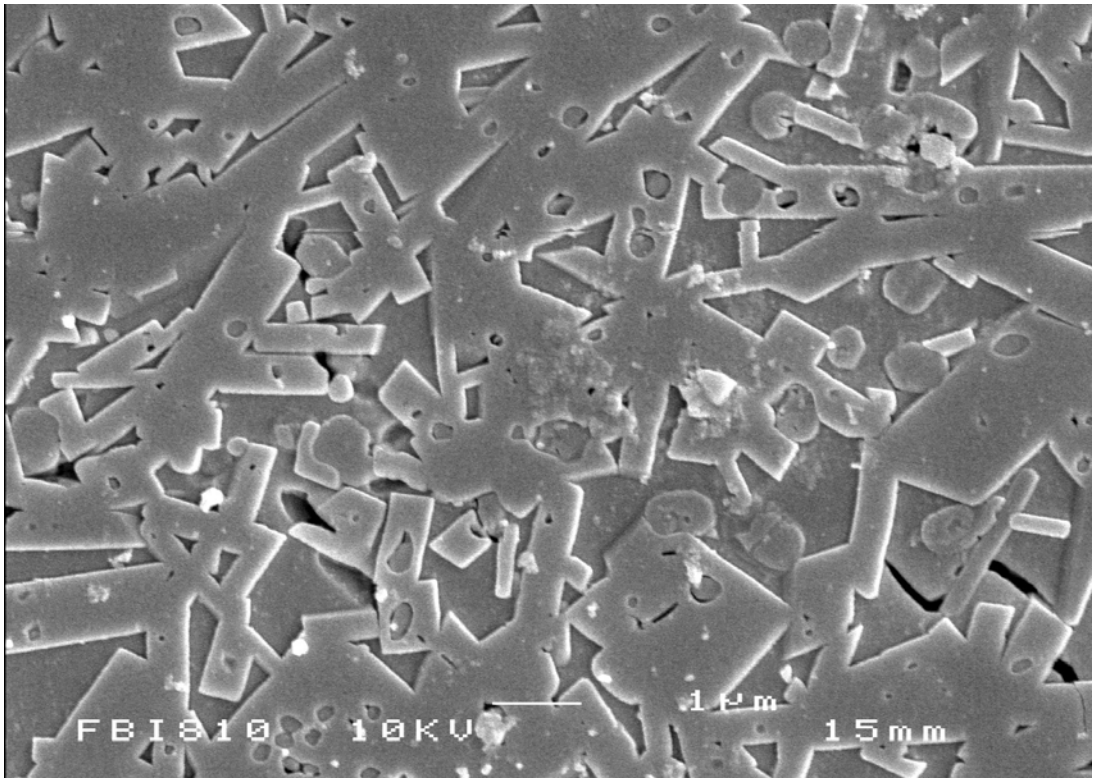

Fig. 4.60: SEM micrograph of glass-ceramic A (4hr A) (610ºC/1h - 850ºC/2h) showing a major sanidine phase and minor leucite phase (10,000 x).

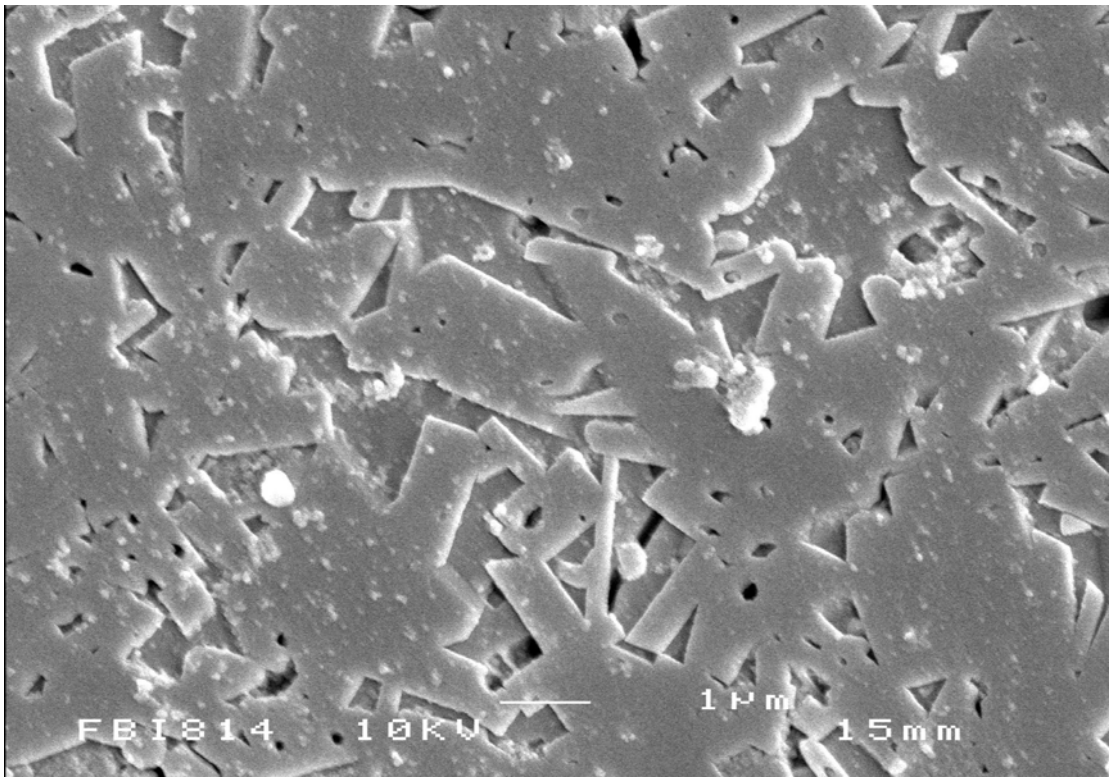

Fig. 4.61: SEM micrograph of glass-ceramic A (4hr A) (610ºC/1h - 850ºC/3h) showing extensive growth of the sanidine phase (10,000 x).

4.9.5 SEM Results for Glass-Ceramic B, HB and NB

Glass-ceramic B nucleated at 610ºC for 1 hour and crystallised at 870ºC for 1 hour showed a highly crystalline structure with high aspect ratio fibre-like leucite crystals, together with a high density of more spherical crystals (Fig. 4.62 and Fig. 4.63). There was evidence of elongated fibre-like leucite crystals growing in preferred orientated domains (Fig. 4.62). However, at higher growth temperatures (960ºC), ripening of these areas was noticed (Fig. 4.64). Glass HB (homogenised glass B) underwent the same two-step heat treatment (610ºC/1h - 870ºC/1h) and yielded rosette shaped domains, orientated fibres and a high density of spherical leucite crystals (Fig. 4.65 - Fig. 4.67). Glass-ceramic HB (620ºC/1h - 795ºC/1h at 20ºC/min) produced a finer microstructure containing spherical leucite crystals and fibres with preferred orientation (Fig. 4.68). Some densely dispersed areas of leucite were highly interconnected (Fig. 4.69). Glass-ceramic NB (630ºC/1h - 949ºC/1h at 20ºC/min) showed a mixture of spherical and interconnected leucite crystals (Fig. 4.70). The leucite crystal size, range and content of glass-ceramics B, HB and NB were quantitatively measured and are listed in Table 4.37.

Table 4.37: The results of different crystallisation heat treatments on the glass B/HB/NB.

Glass-ceramic	Heat Rate (ºC/min)	Leucite Area Fraction (%)	Crystal No	Crystal Size Mean (SD) (μm^2)	Size Range (μm^2)
B (610/1h-870/1h)	10	58.9%	392	1.23 (1.59)	0.02 - 9.35
HB (610/1h-870/1h)	10	65.7%	301	1.79 (2.16)	0.03 - 14.74
HB (620/1h-795/1h)	20	50.0%	569	0.57 (0.55)	0.02 - 4.06
NB (630/1h-949/1h)	20	44.1%	199	1.77 (2.30)	0.05 - 19.24

Leucite crystal size and area fraction measurement were carried out based on images with a magnification of 10,000 x.

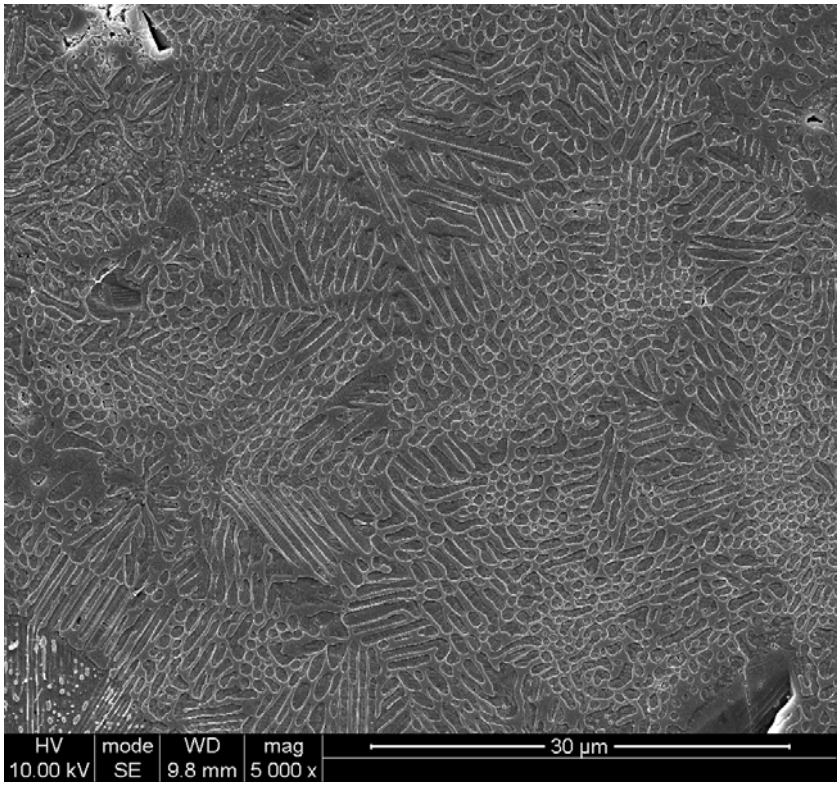

Fig. 4.62: SEM micrograph of glass-ceramic B (610ºC/1h - 870ºC/1h at 10ºC/min) showing preferred orientated leucite domains.

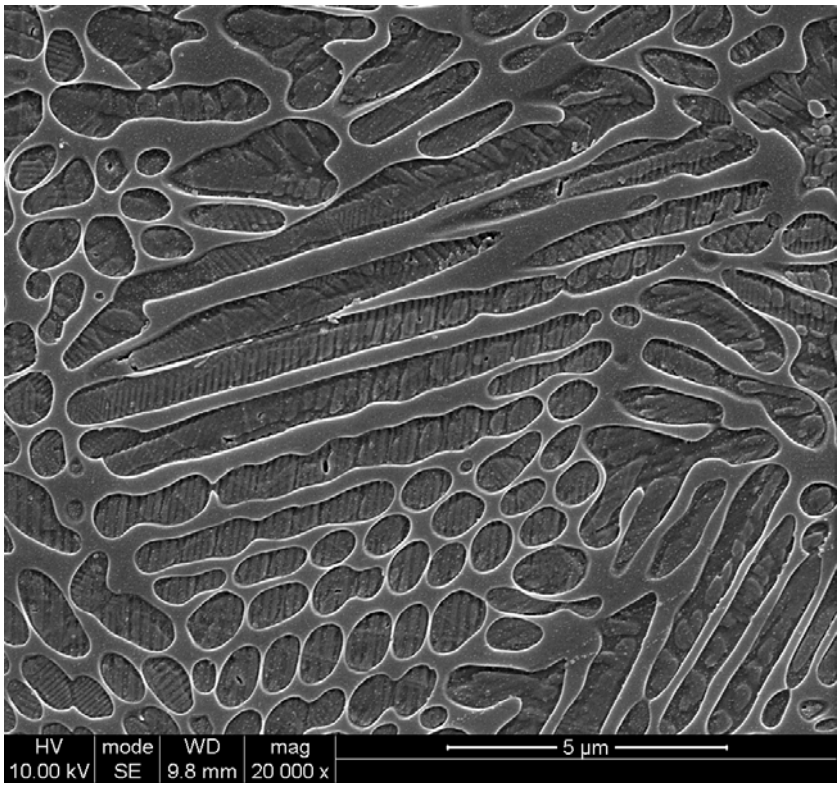

Fig. 4.63: SEM micrograph of glass-ceramic B (610ºC/1h - 870ºC/1h at 10ºC/min) showing high aspect ratio fibre-like leucite crystals and spherical crystals.

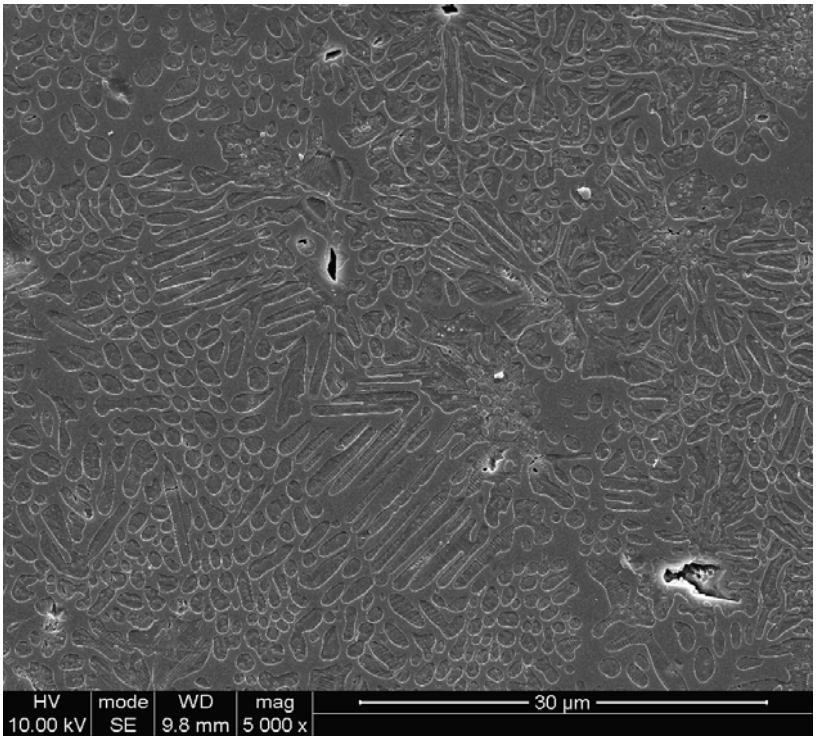

Fig. 4.64: SEM micrograph of glass-ceramic B (610ºC/1h - 960ºC/1h at 10ºC/min) showing a mixture of fine, elongated leucite crystal and signs of crystal coalescence and ripening.

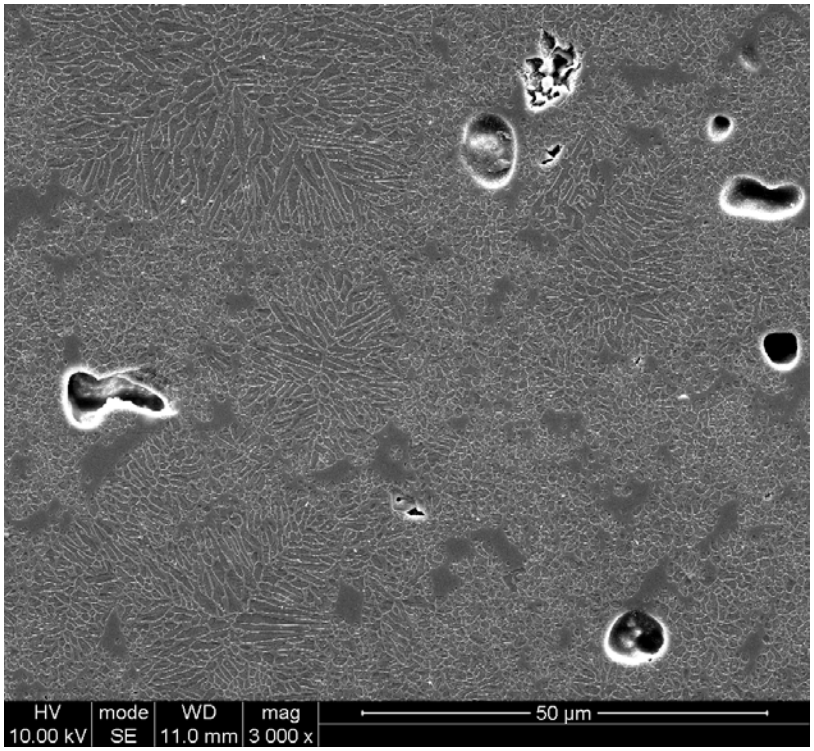

Fig. 4.65: SEM micrograph of glass-ceramic HB (610ºC/1h - 870ºC/1h at 10ºC/min) showing rosette shape leucite domains and fine spherical leucite crystals in the glassy matrix.

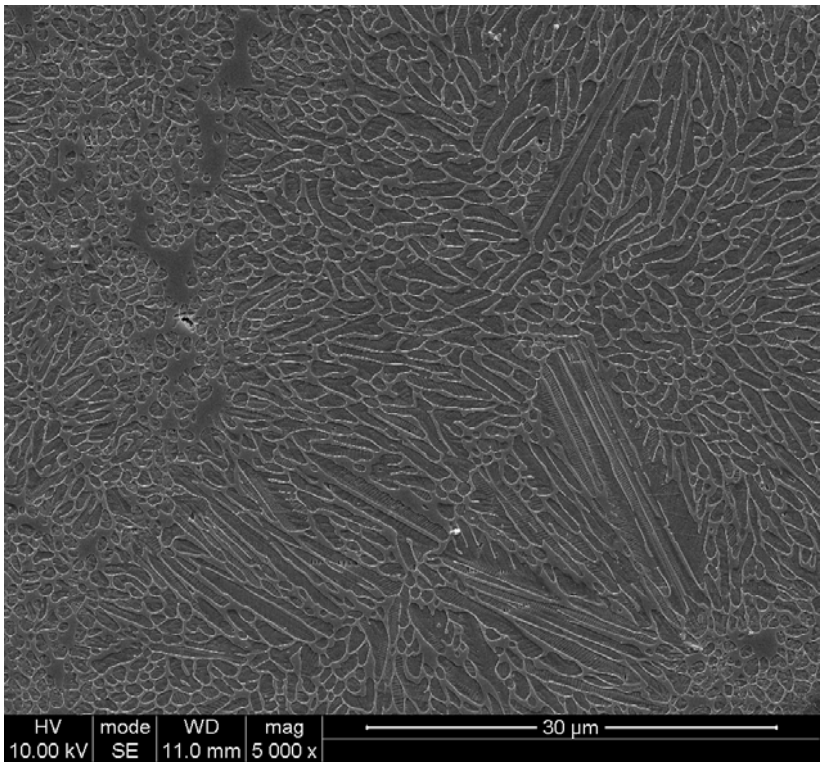

Fig. 4.66: SEM micrograph of glass-ceramic HB (610ºC/1h - 870ºC/1h at 10ºC/min) showing a mixture high aspect ratio orientated fibres-like leucite crystals and fine leucite crystals.

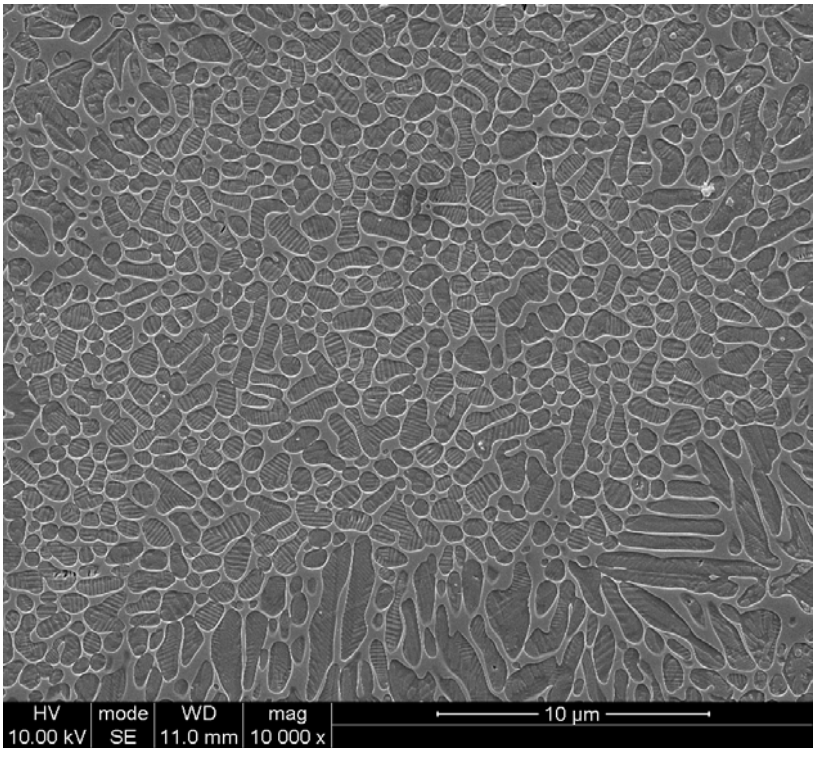

Fig. 4.67: SEM micrograph of glass-ceramic HB (610ºC/1h - 870ºC/1h at 10ºC/min) showing high density of spherical leucite crystals.

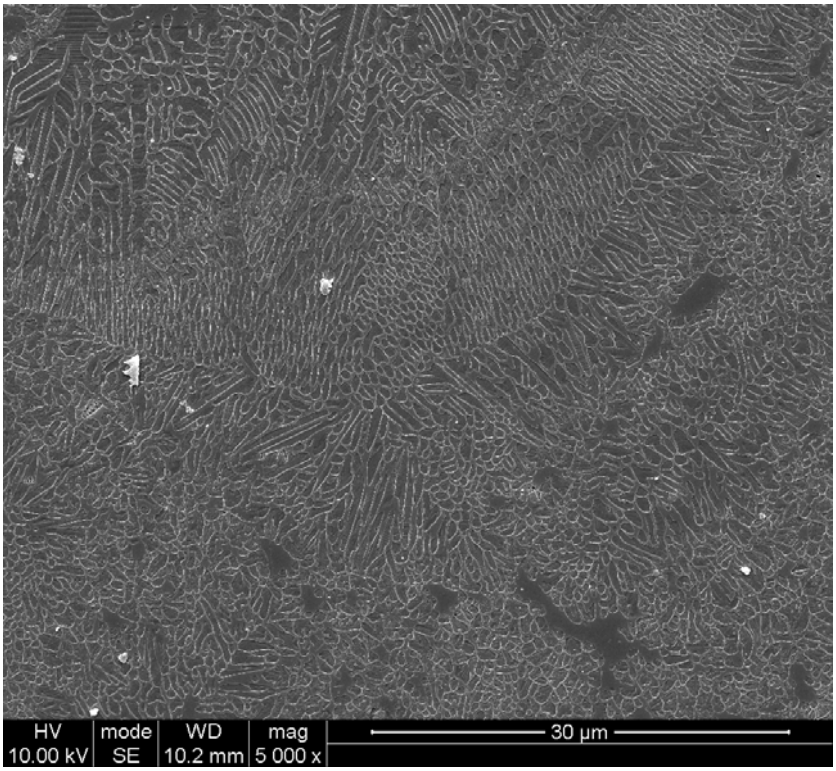

Fig. 4.68: SEM micrograph of glass-ceramic HB (620ºC/1h - 795ºC/1h at 20ºC/min) showing a highly crystalline structure with finer leucite crystals and preferred orientation.

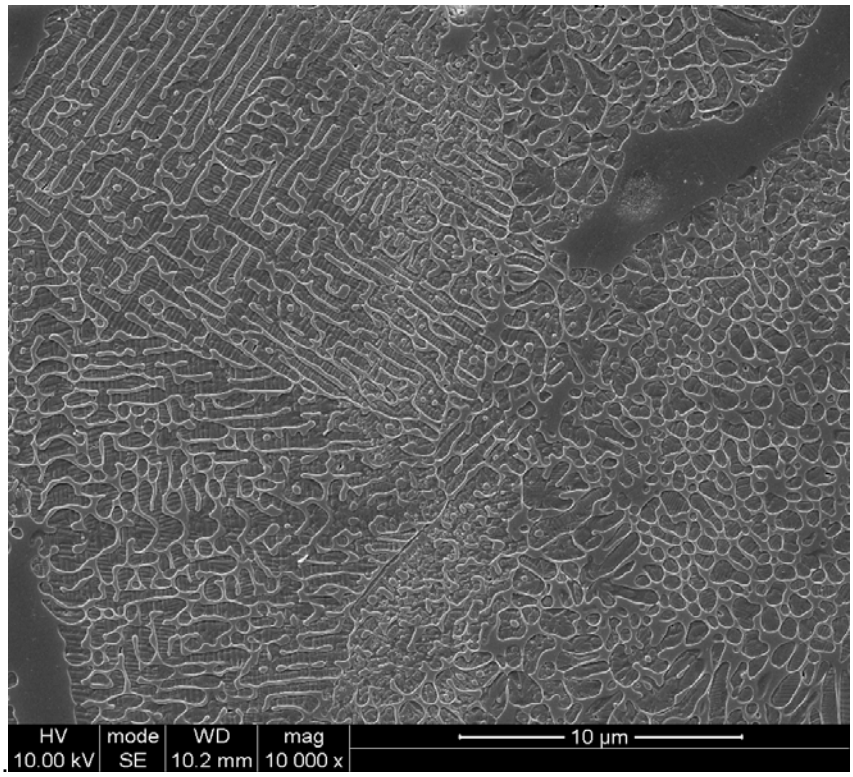

Fig. 4.69: SEM micrograph of glass-ceramic HB (620ºC/1h - 795ºC/1h at 20ºC/min) showing densely dispersed areas of highly interconnected leucite crystals.

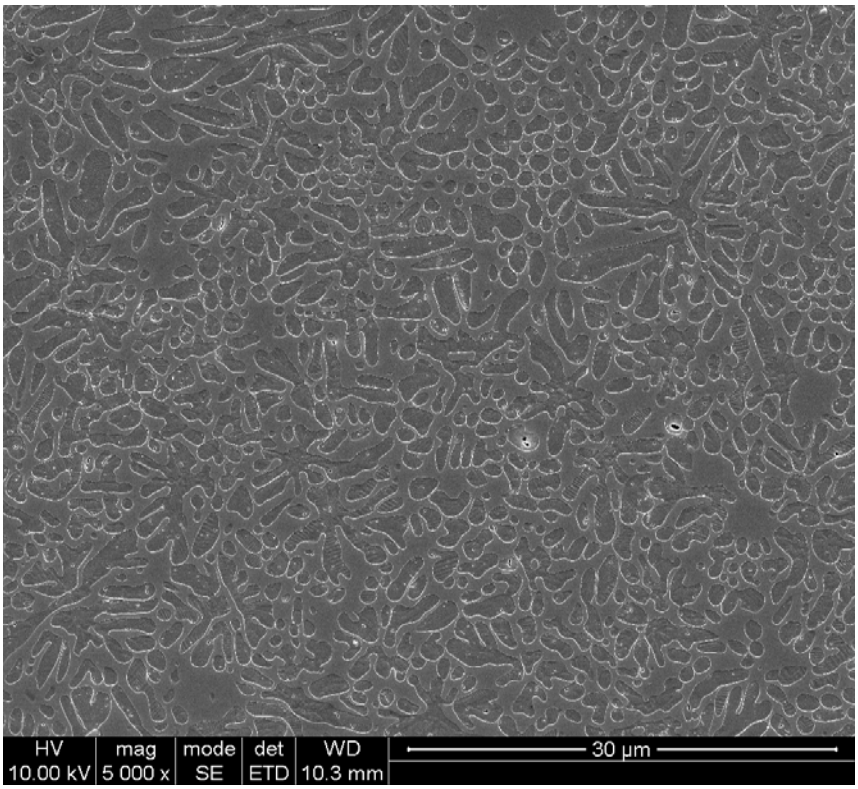

Fig. 4.70: SEM micrograph of glass-ceramic NB (630ºC/1h - 949ºC/1h at 20ºC/min) showing a mixture of spherical and interconnected leucite crystals.

4.9.6 SEM Results for Glass-Ceramic C

Glass-ceramic C nucleated at 620ºC for 1 hour and crystallised at 920ºC for 1 hour at a rate of 10ºC/min shows a mixed morphology of spherical and fibre-like crystals interspersed in the glassy matrix (Fig. 4.71 and Fig. 4.72). Domains of orientated fibres were present (Fig. 4.72). Leucite crystals were unevenly distributed in the glass matrix and large glassy areas were visible. Glass-ceramic C heat treated at a higher crystallisation temperature (960ºC) demonstrated growth of more spherical leucite crystals with some large glassy areas (Fig. 4.73). Some minor areas with a dense dispersal of rod like structures were also found (Fig. 4.74). Glass-ceramic C heat treated at 1000ºC (1 hour) showed severe crystal coalescent and some large glassy areas. The Mean crystal size and leucite fraction are shown in Table 4.38 for glass-ceramic C crystallised at different temperatures.

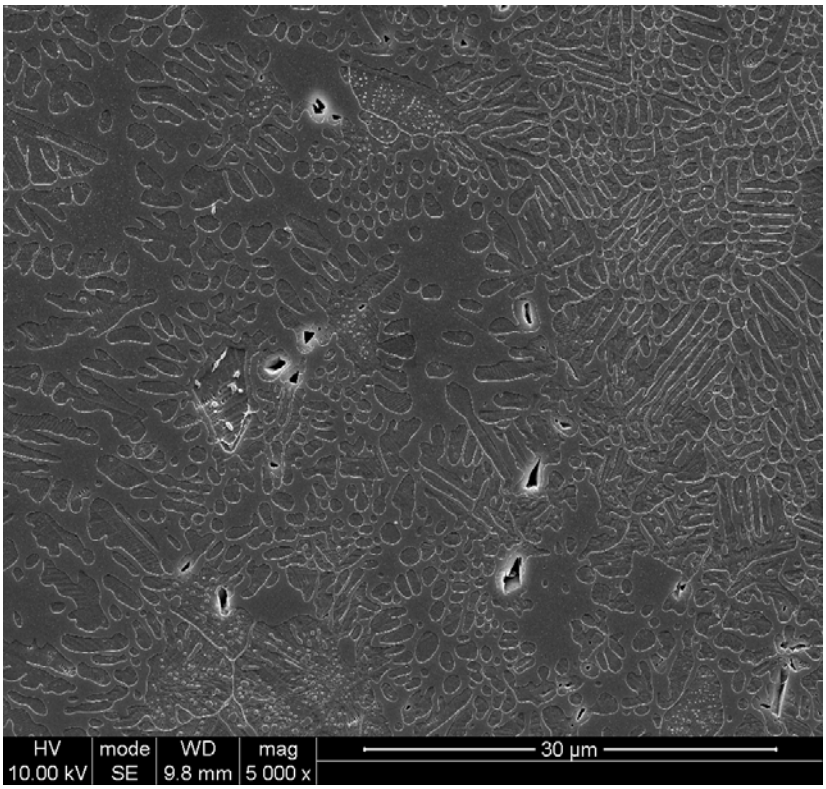

Fig. 4.71: SEM micrograph of glass-ceramic C (620ºC/1h - 920ºC/1h) showing a mixed morphology of spherical and fibre-like leucite crystals.

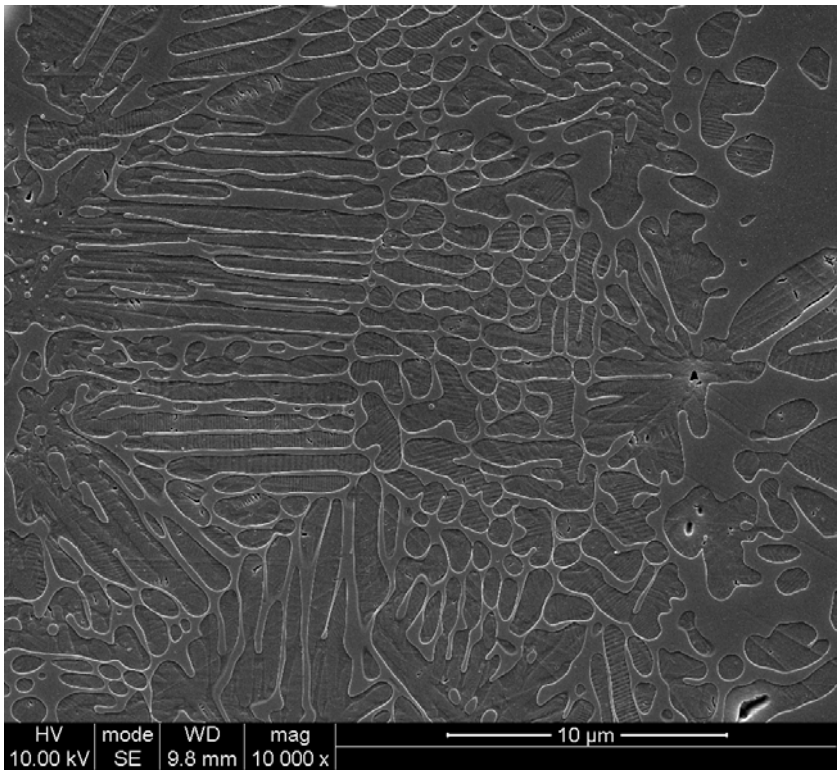

Fig. 4.72: SEM micrograph of glass-ceramic C (620ºC/1h - 920ºC/1h) showing a mixed morphology of spherical and orientated fibre-like crystals.

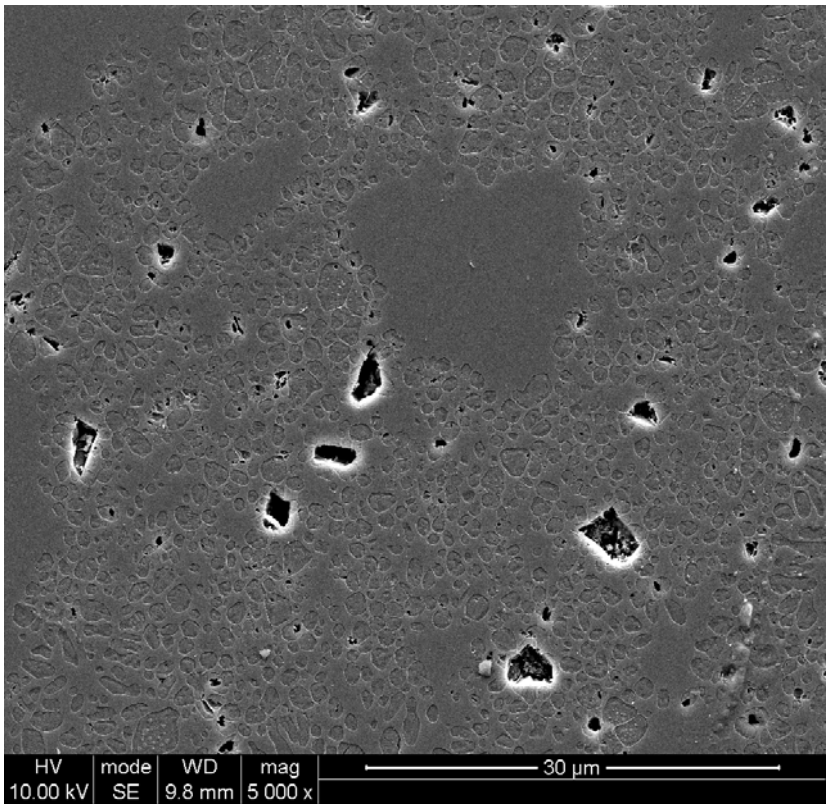

Fig. 4.73: SEM micrograph of glass-ceramic C (620ºC/1h - 960ºC/1h) showing spherical leucite crystals and areas of glass matrix.

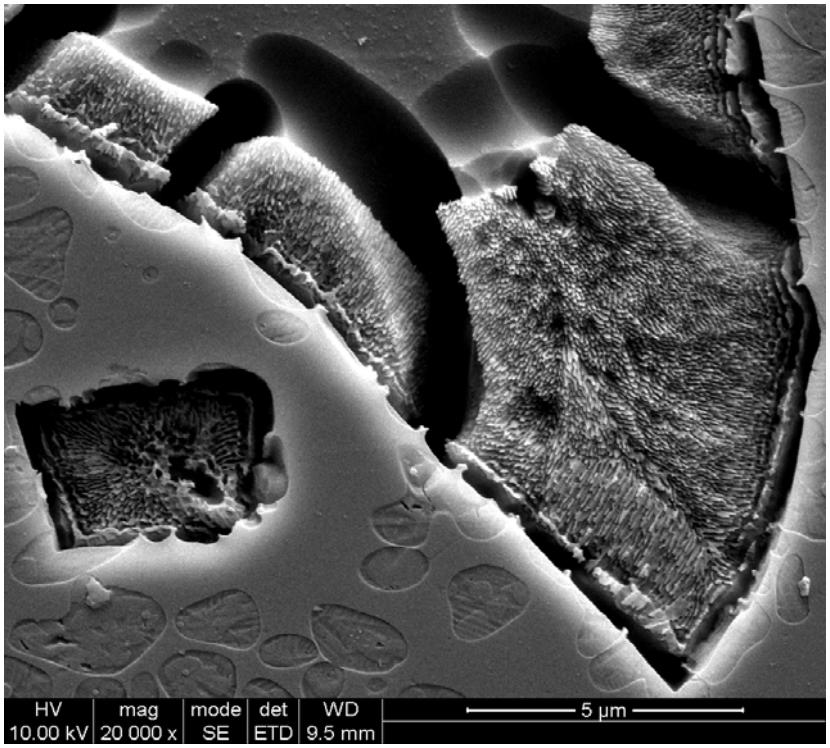

Fig. 4.74: SEM micrograph of glass-ceramic C (620ºC/1h - 960ºC/1h) showing a dense dispersal of rod like structures.

Table 4.38: The results of different crystallisation heat treatments on the glass C.

Glass-ceramic C Heat Treatments	Heat Rate (ºC/min)	Leucite Area Fraction (%)	Crystal No	Crystal Size Mean (SD) (μm^2)	Size Range (μm^2)
620/1h-920/1h	10	54.2%	1315	1.45 (2.22)	0.11 - 13.94
620/1h-960/1h	10	42.1%	1482	0.93 (0.78)	0.07- 6.86

Leucite crystal size and area fraction measurement were carried out based on images with a magnification of 5,000 x.

4.9.7 SEM Results for Glass-Ceramic D

Glass-ceramic D nucleated at 670ºC for 1 hour and crystallised at 1000ºC at 10ºC/min is presented in Fig. 4.75. Leucite crystal clustering and large areas of glass matrix were in evidence compared with glass-ceramics B, HB and C. Signs of crystal and matrix microcracking were also present in the microstructure. Sparse areas of orientated fibre-like structure were observed within the microstructures (Fig. 4.76 and Fig. 4.77). According to Fig. 4.77, this phase had a high aspect ratio. Glass-ceramic D (670ºC/1h - 1000ºC/5h at 10ºC/min) showed further crystal coalescence, a reduction in leucite fraction and extensive matrix microcracking (Fig. 4.78).

Table 4.39: The quantitative measurement results of glass-ceramic D.

Glass-ceramic D Heat Treatments	Heat Rate (ºC/min)	Leucite Area Fraction (%)	Crystal No	Crystal Size Mean (SD) (μm^2)	Size Range (μm^2)
670/1h-1000/1h	10	33.14%	597	1.83 (1.75)	0.05 - 11.11

Leucite crystal size and area fraction measurement were carried out based on images with a magnification of 5,000 x.

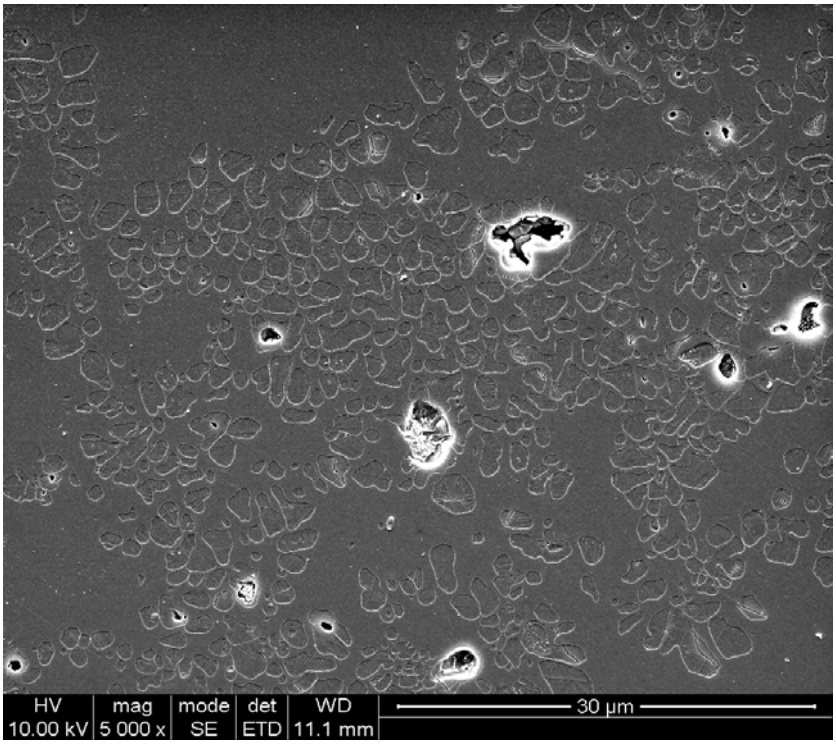

Fig. 4.75: SEM micrograph of glass-ceramic D (670ºC/1h - 1000ºC/1h) showing a dense dispersal of leucite crystals interspersed with large area of glass matrix.

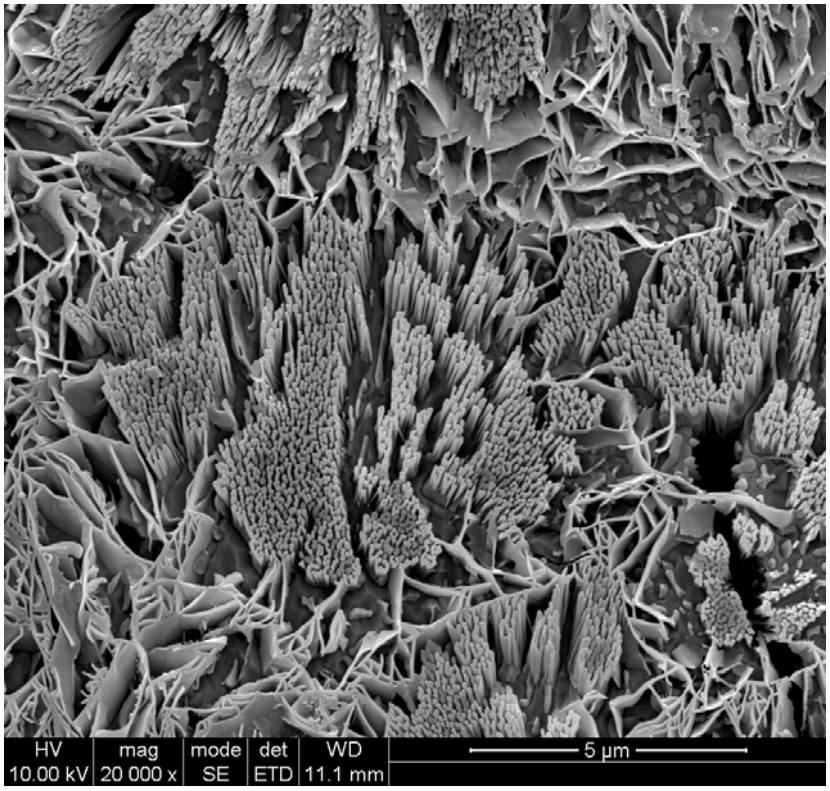

Fig. 4.76: SEM micrograph of glass-ceramic D (670ºC/1h - 1000ºC/1h) showing a dense dispersal of a fibre-like structure.

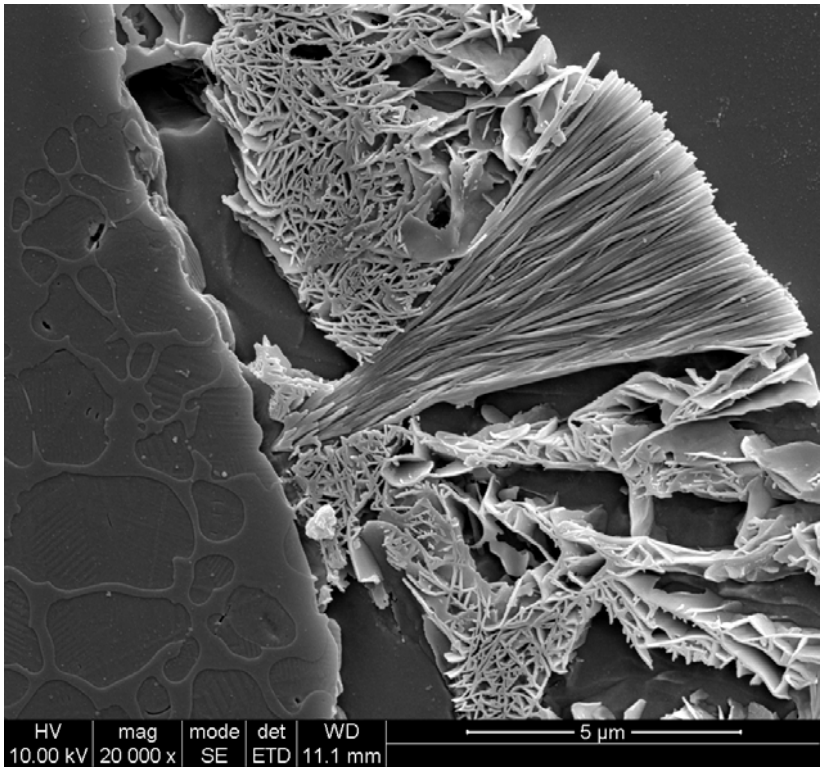

Fig. 4.77: SEM micrograph of glass-ceramic D (670ºC/1h - 1000ºC/1h) showing the high aspect ratio of the fibre phase.

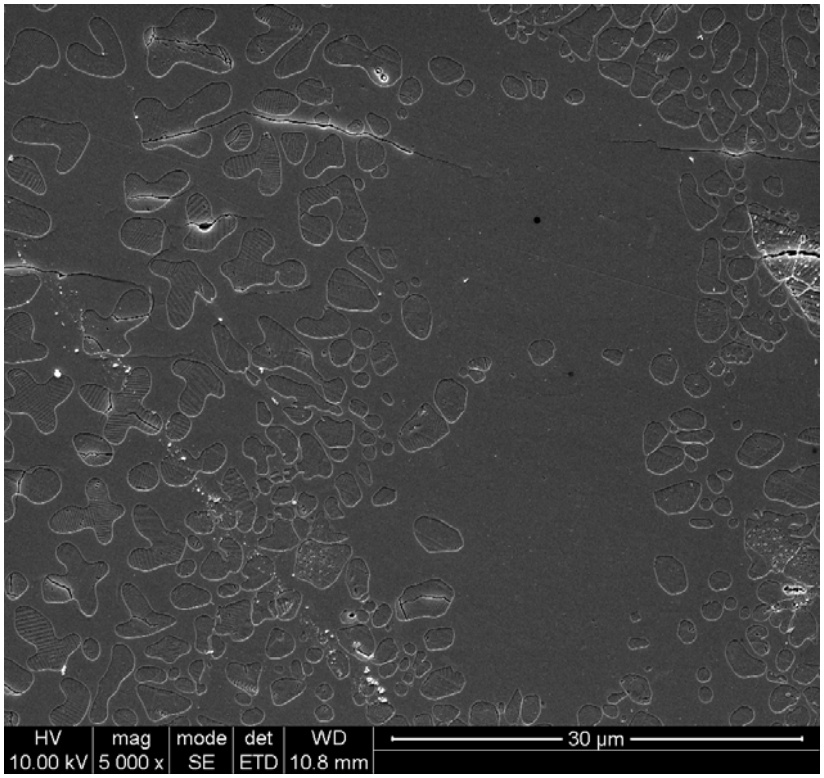

Fig. 4.78: SEM micrograph of glass-ceramic D (670ºC/1h - 1000ºC/5h) showing leucite crystal coalescence, large area of glass matrix and microcracking.

4.9.7.1 EDS Analysis of Glass-Ceramic D

Energy dispersive X-ray analysis (EDS) was carried out on glass-ceramic D to characterise the different areas presented on the micrograph. These areas included the glass matrix, leucite crystals and the fibre area (Fig. 4.79). The results of the EDS analysis are presented in Table 4.40. The fibre areas had a different elemental composition compared to the leucite crystals, which were aluminum and potassium rich.

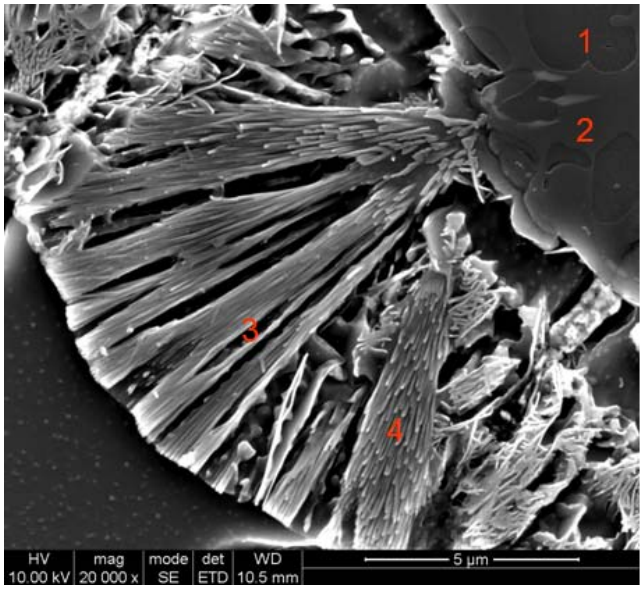

Fig. 4.79: SEM photomicrograph of the glass-ceramic D showing different structures (numbers refers to Table 4.40).

Table 4.40: EDS analysis results of glass-ceramic D (elements in mole %).

Elements	Leucite (1)	Glass Matrix (2)	Fibre Area (3)	Fine Fibre Area (4)
Si	24.50	25.88	16.66	17.25
Al	6.59	5.06	13.77	14.42
K	4.89	3.37	6.49	6.04
Ca	0.28	0.51	0.35	0.07
Ti	0.41	0.58	0.51	0.67
Na	0.40	1.02	2.33	0.57
Mg	0.15	0.18	0.02	0.06
Zr	0	0	0.08	0
O	62.78	63.40	59.87	60.91

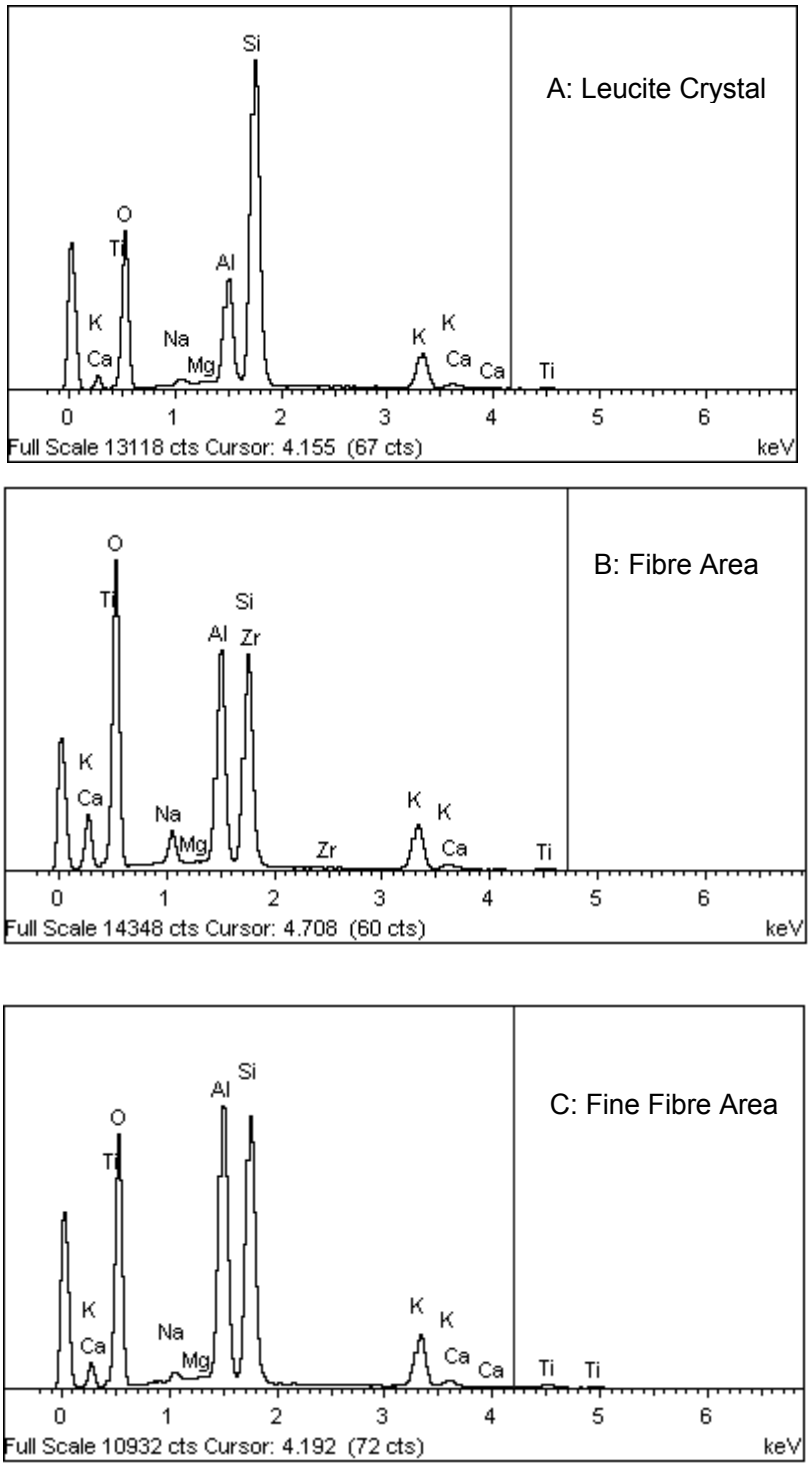

Fig. 4.80: EDS spot analysis of glass-ceramic D showing results for (A) leucite crystal, (B) fibre area and (C) fine fibre area.

4.9.8 SEM Results for Glass-Ceramic E

Glass-ceramic E, two-step heat treated using the optimised crystallisation condition (610ºC/1h - 1050ºC/1h at 10ºC/min) showed an even microstructure with fine leucite crystals and some crystal coalescence (Fig. 4.81 and Table 4.41). Some white spots (Fig. 4.82) and rectangular area were noticed on the fracture surface (as showed in section 4.10.4.1).

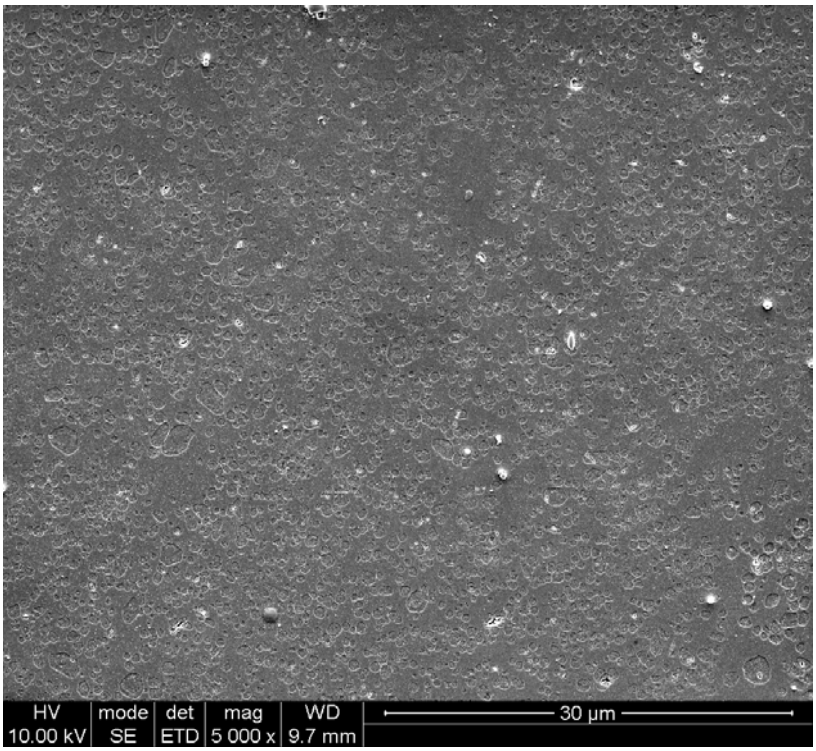

Fig. 4.81: SEM micrograph of glass-ceramic E (610ºC/1h - 1050ºC/h) showing an even microstructure with fine leucite crystals and little crystal coalescence.

Table 4.41: The quantitative measurement results for glass-ceramic E.

Glass-ceramic E (610ºC/1h - 1050ºC/1h, at 10 ºC/min)	Leucite Area Fraction (%)	Crystal No	Crystal Size Mean (SD) (μm^2)	Size Range (μm^2)
	29.62%	872	0.27 (0.28)	0.02 - 4.6

Leucite crystal size and area fraction measurement were carried out based on images with a magnification of 5,000 x.

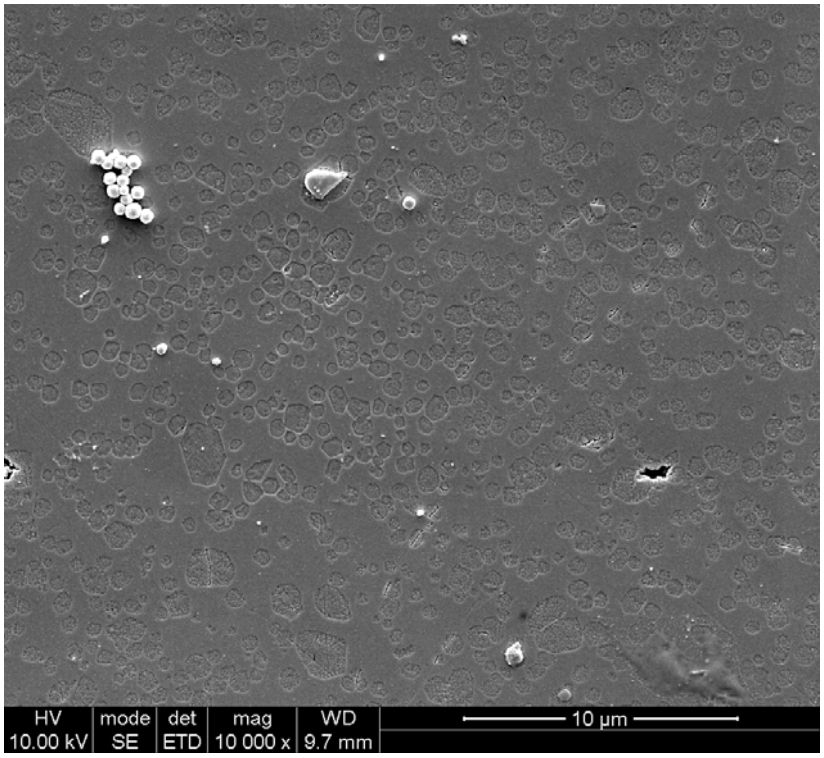

Fig. 4.82: SEM micrograph of glass-ceramic E (610ºC/1h - 1050ºC/1h) showing signs of leucite crystal growth and contamination.

4.9.9 SEM Results of Glass-Ceramic after Sintering/Heat Extrusion

4.9.9.1 SEM Results of Sintered/Heat Extruded Glass-Ceramic A Series

Glass-ceramic A (starting A, 4hr A, 8hr A) and glass-ceramic E frit were milled into powder, compacted, and then sintered or heat extruded according methods described in section 3.3.6. The SEM microstructure of the sintered/heat extruded glass-ceramics are presented in Fig. 4.84 - Fig. 4.90. All glass-ceramics A had evenly distributed leucite crystals with very little microcracking. The crystal size reduction trend of glass-ceramic A (from starting to 4hr A and 8hr A) was in agreement with those as heat treated glass-ceramic presented in sections 4.9.3 and 4.9.4.

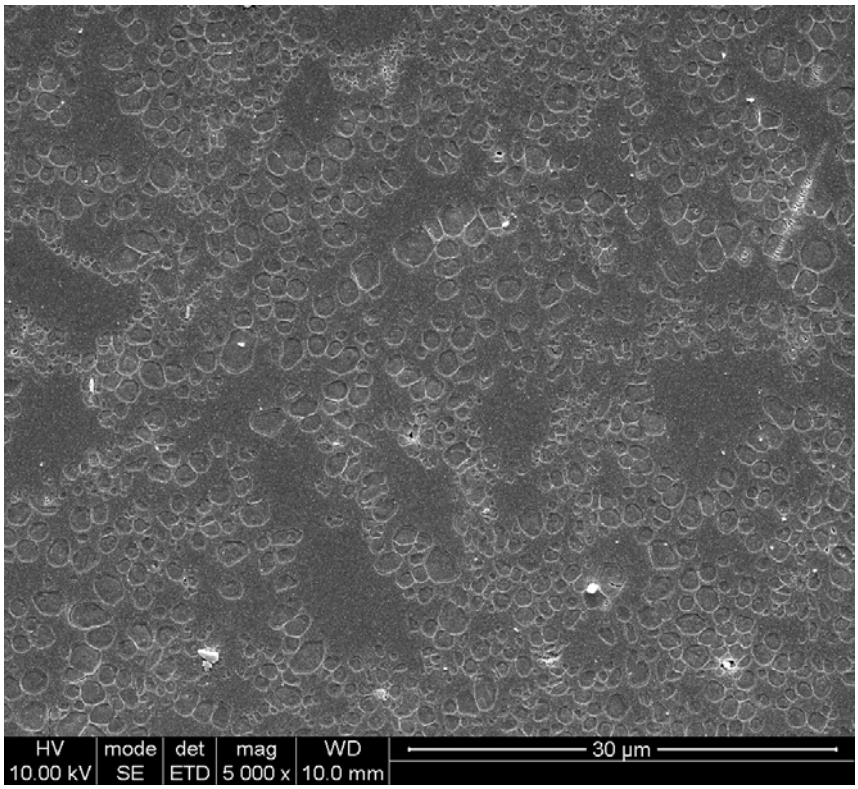

Fig. 4.83: SEM micrograph of sintered glass-ceramic A (starting) showing leucite crystals and areas of glass matrix.

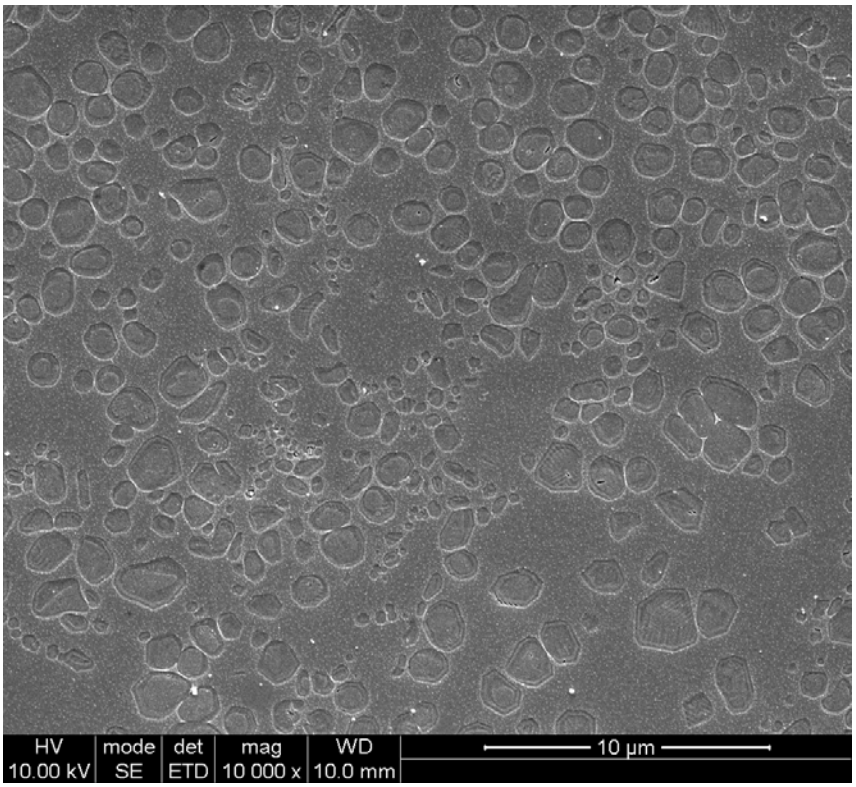

Fig. 4.84: SEM micrograph of sintered glass-ceramic A (starting) showing leucite crystals and a lack of matrix and crystal microcracking.

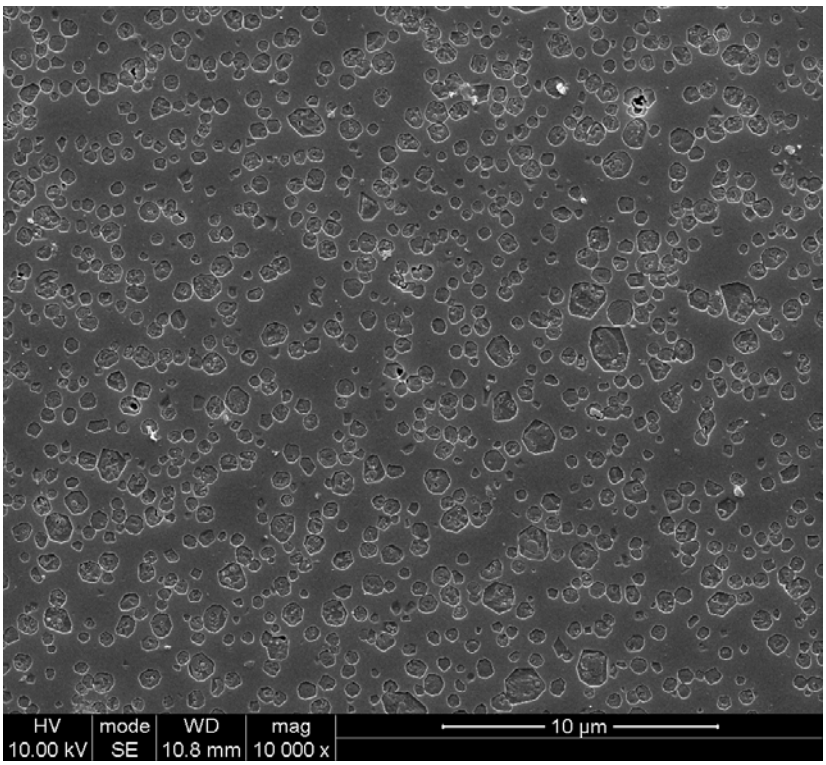

Fig. 4.85: SEM micrograph of sintered glass-ceramic A (4hr A) showing evenly distributed fine leucite crystals without crystal and matrix microcracking.

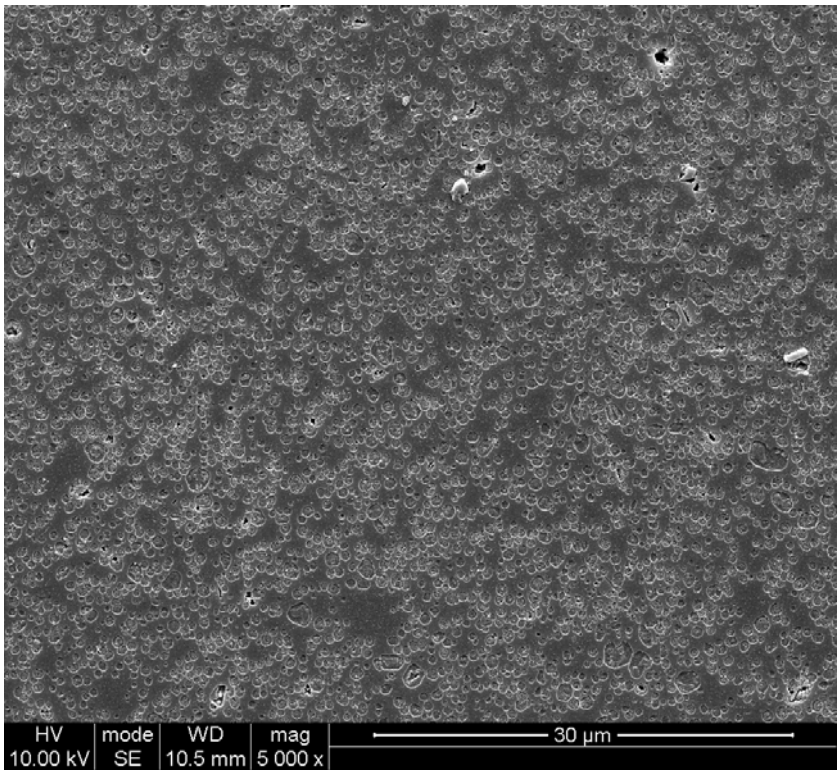

Fig. 4.86: SEM micrograph of sintered glass-ceramic A (4hr A) showing a dense dispersal of fine leucite crystals.

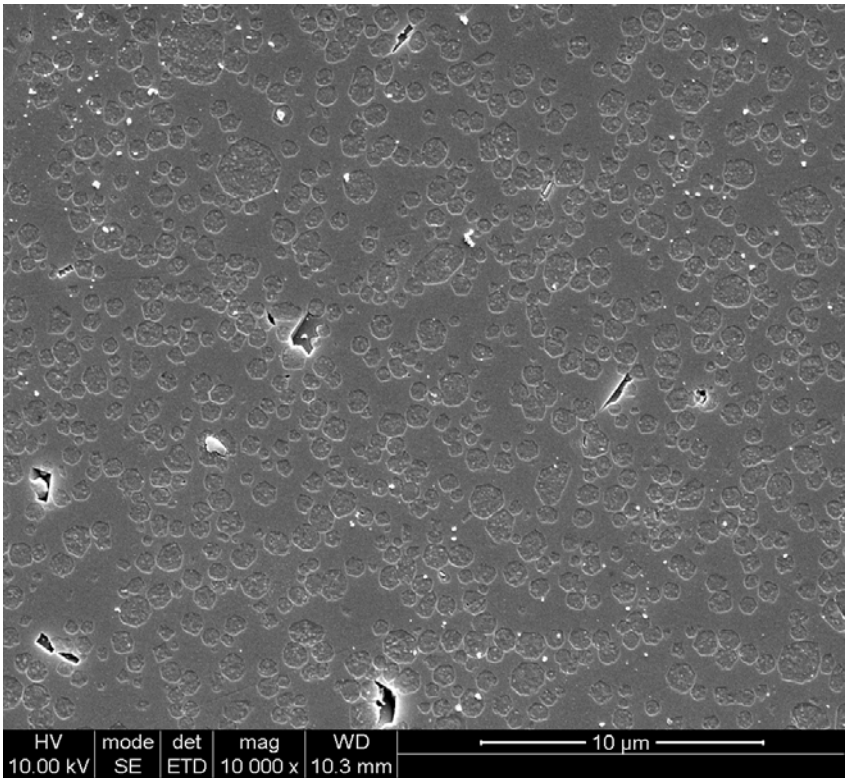

Fig. 4.87: SEM micrograph of heat extruded glass-ceramic A (4hr A) showing evenly distributed fine leucite crystals.

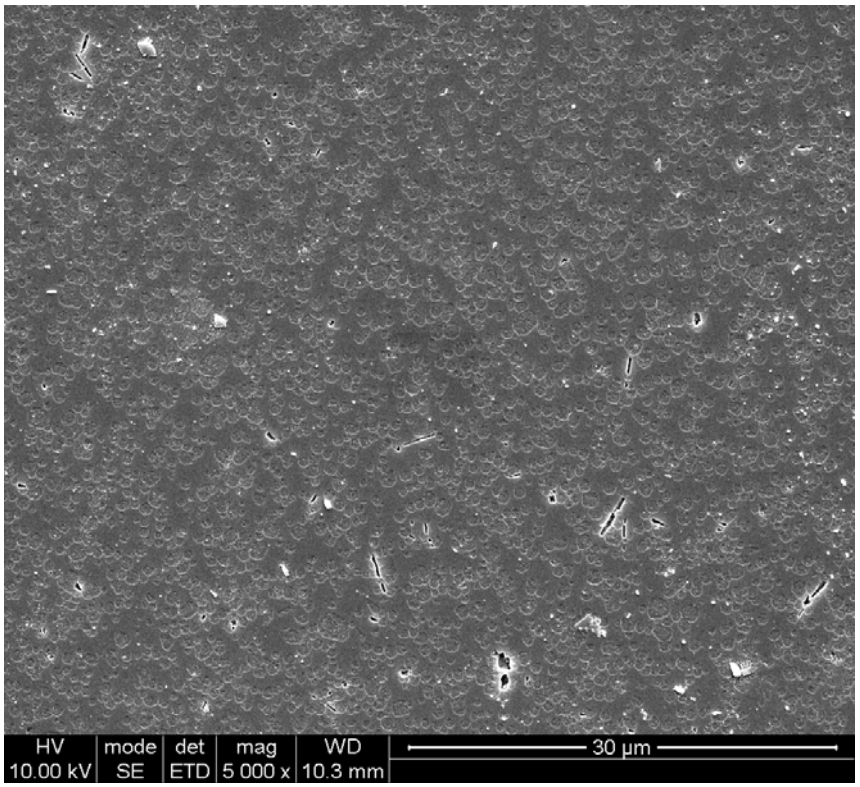

Fig. 4.88: SEM micrograph of heat extruded glass-ceramic A (4hr A) showing an even distribution of fine leucite crystals.

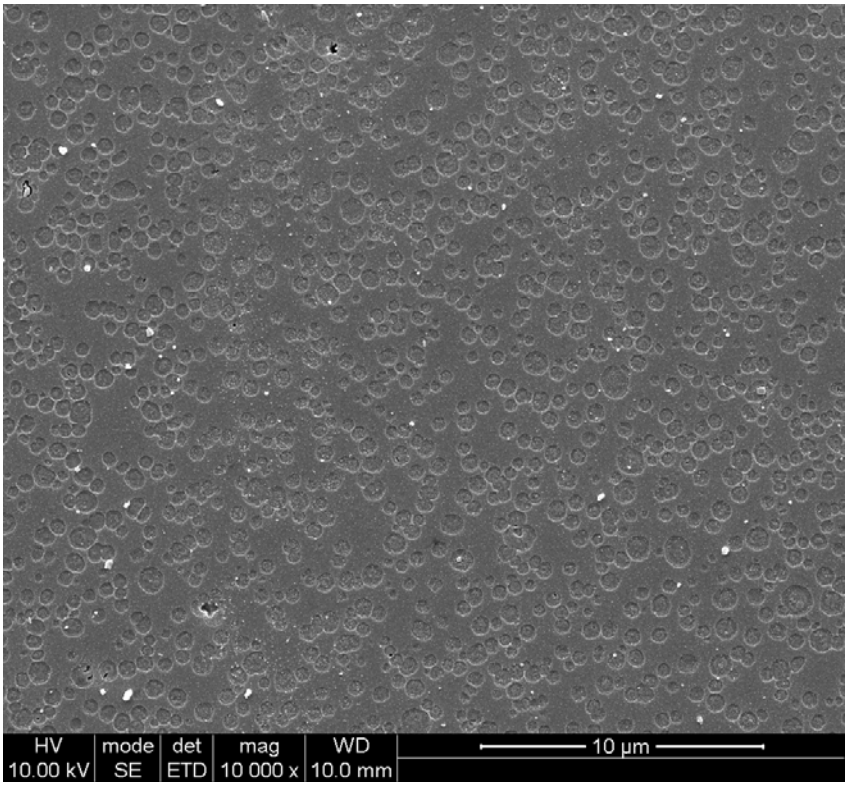

Fig. 4.89: SEM micrograph of sintered glass-ceramic A (8hr A) showing evenly distributed fine leucite crystals and a lack of matrix and crystal microcracking.

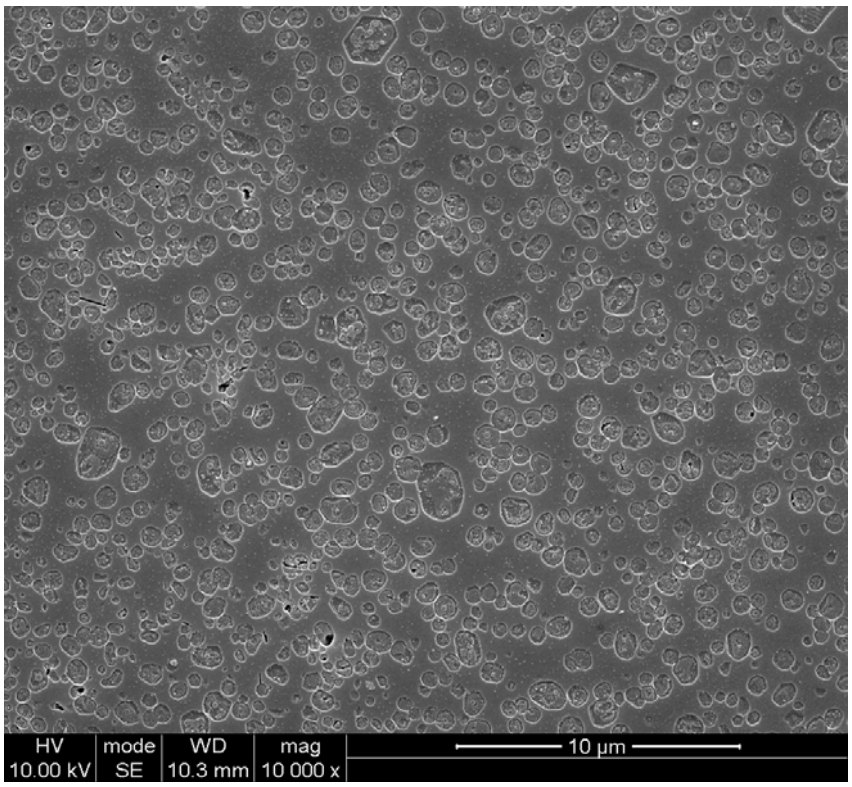

Fig. 4.90: SEM micrograph of sintered glass-ceramic E (4hr A with additional ZrO_2) showing a dense dispersal of fine leucite crystals.

4.9.9.2 SEM Results of Sintered Glass-Ceramic B

SEM analysis of the sintered glass-ceramics (B and HB) showed a dense dispersal of spherical leucite crystals and a ripening of the leucite crystals (Fig. 4.91 and Fig. 4.92). The sintered glass-ceramic B (610ºC/1h - 870ºC/1h, Fig. 4.91) showed some large leucite crystals and areas of glass matrix. The sintered glass-ceramic HB (620ºC/1h - 795ºC/1h at 20ºC/min, Fig. 4.92) demonstrated a much finer leucite microstructure compared to the sintered glass-ceramic B. No microcracking was present in the glass matrix of both sintered glass-ceramics B and HB. The heat extruded glass-ceramic HB showed crystal growth and the elimination of large glass area (Fig. 4.93).

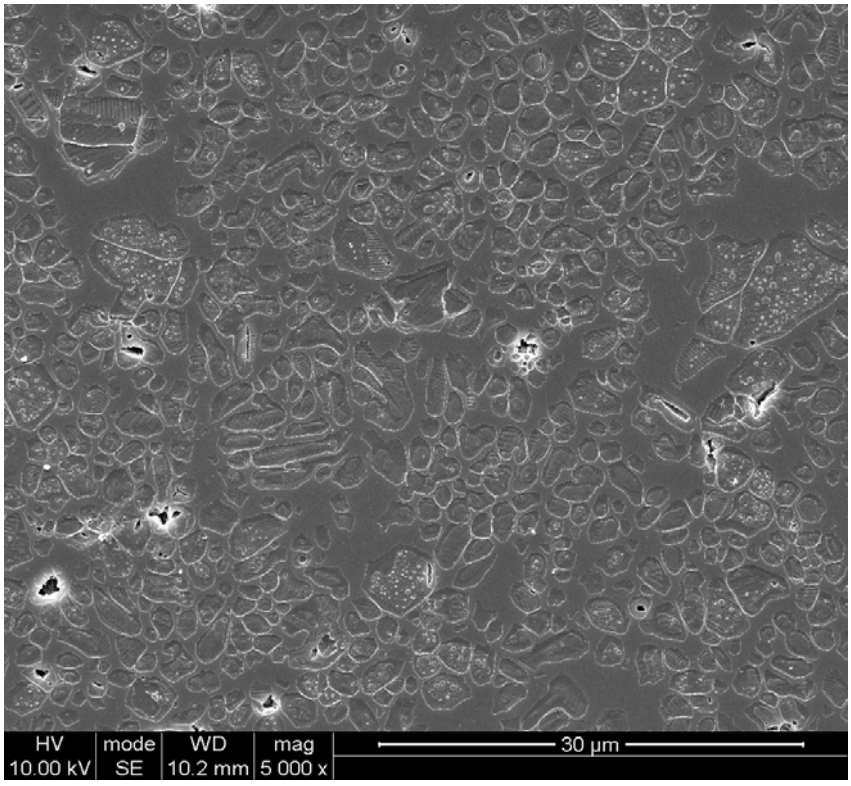

Fig. 4.91: SEM micrograph of sintered glass-ceramic B showing a leucite crystal ripening and areas of glass matrix.

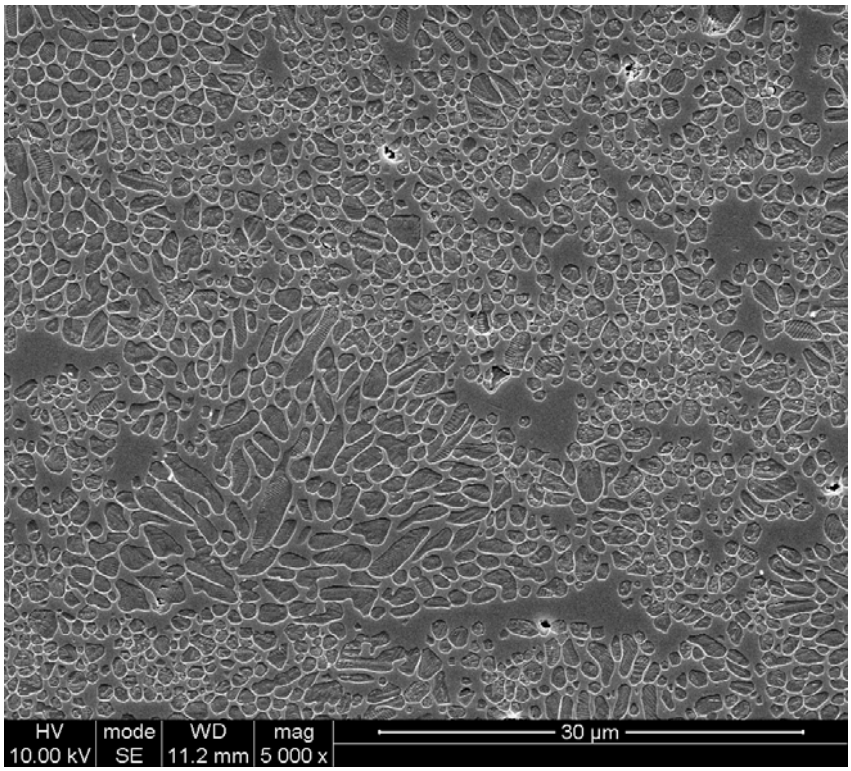

Fig. 4.92: SEM micrograph of sintered glass-ceramic HB showing a densely dispersed leucite microstructure with small area of glass matrix.

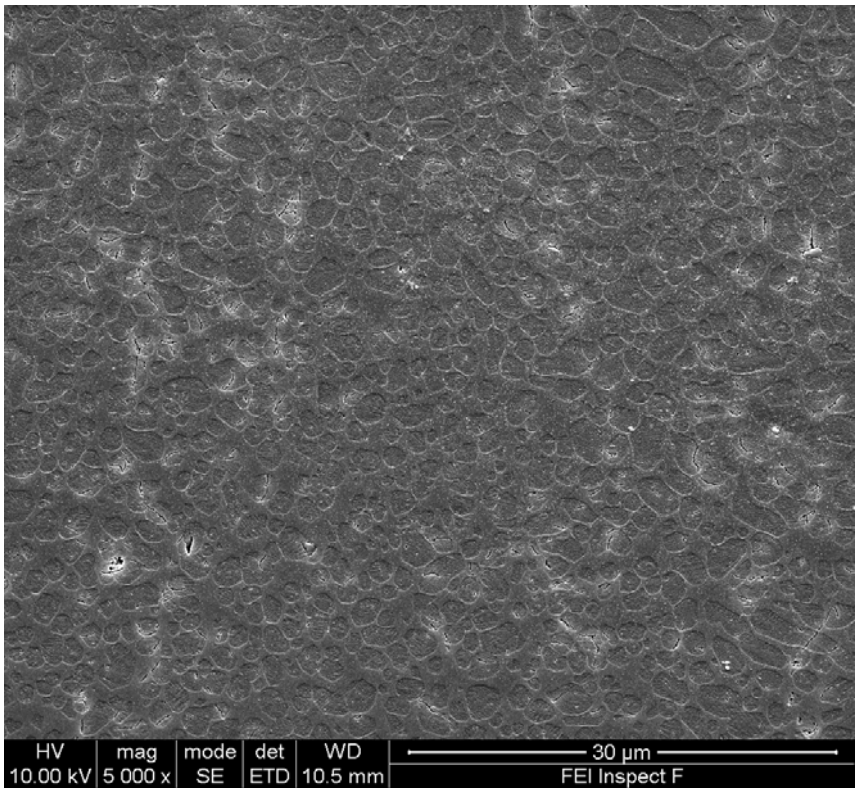

Fig. 4.93: SEM micrograph of heat extruded glass-ceramic HB showing elimination of the glassy areas.

4.9.9.3 SEM Results of Sintered Glass-Ceramic C and D

Spherical leucite crystals, crystal growth and some microcracking were observed in the glass-ceramic C (620ºC/1h - 920ºC/1h at 10ºC/min) after firing in a porcelain furnace (Fig. 4.94). Sintered glass-ceramic D showed leucite crystal growth, and some large leucite clusters were found Fig. 4.95 .

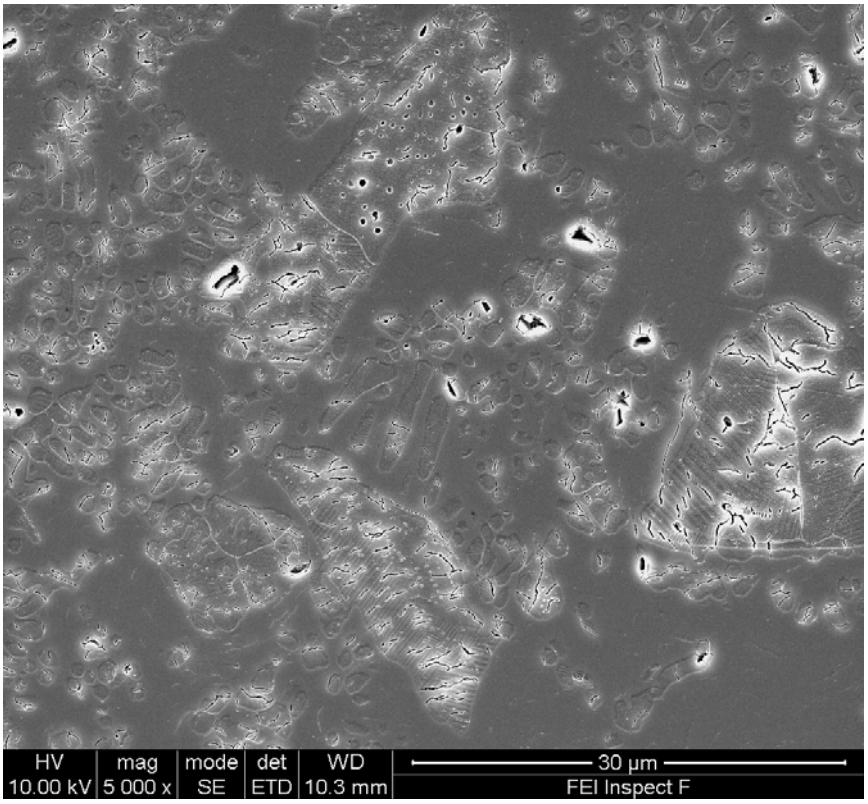

Fig. 4.94: SEM micrograph of sintered glass-ceramic C (620ºC/1h - 920ºC/1h) showing big leucite cluster and areas of glass matrix

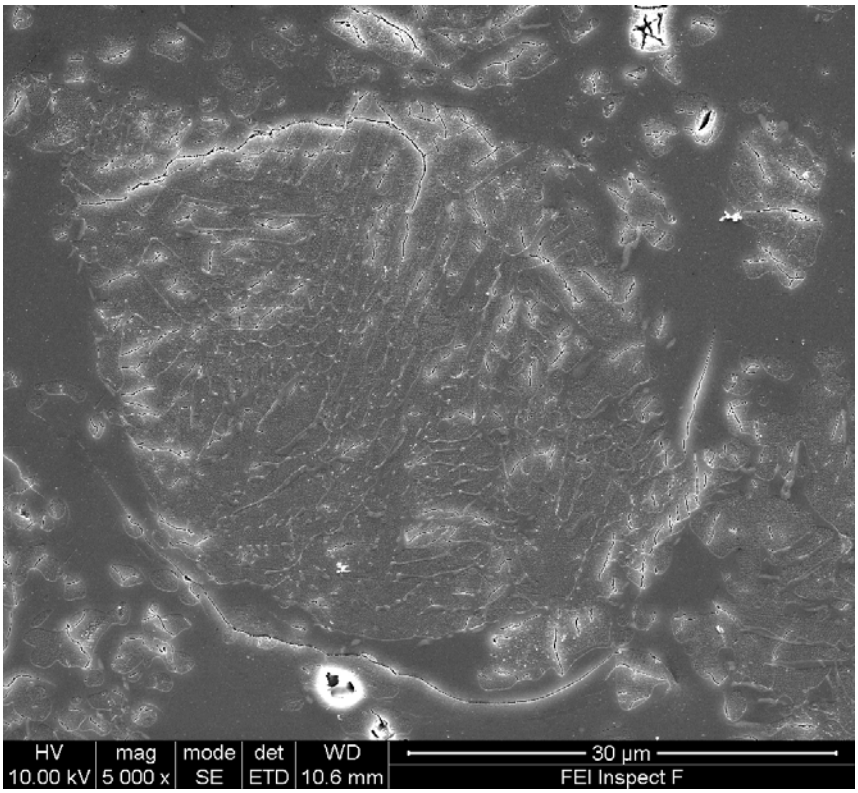

Fig. 4.95: SEM micrograph of sintered glass-ceramic D (670ºC/1h - 1000ºC/1h at 10ºC/min) showing a leucite crystal cluster and extensive microcracking in the glass matrix.

4.10 Biaxial Flexural Strength (BFS) Test Results

4.10.1 BFS Results of the Attritor Milled Glass-ceramic A Group

The results of biaxial flexural strength (BFS) test for the experimental heat treated Attritor milled glass-ceramics A (starting), A (4hr A)$_1$, A (8hr A) and the commercial control IPS Empress Esthetic are presented in Table 4.42. The strength data was analysed using a one way ANOVA (F test, $p<0.001$, Sigma Stat, version 2.03, SPSS Inc, Chicago, USA). The sintered glass-ceramic A (4hr A)$_1$, A (8hr A) had significantly higher BFS values than the IPS Empress Esthetic and the sintered glass-ceramic A (starting A) groups when analysed using Tukey's multiple comparison test ($p<0.001$). The sintered glass-ceramic A (4hr A)$_1$ demonstrated the highest Mean (SD) BFS of 253.8 (53.3) MPa, and this was statistically different from the glass-ceramic A (8hr A) groups were found ($p<0.05$). There was no

statistical difference between the IPS Empress Esthetic and the glass-ceramic A (starting A) ($P>0.05$). The power of the performed test with the significant level at $p<0.05$ was 1.0.

Table 4.42: The biaxial flexural strength results for the (Attritor milled) glass-ceramics A.

Test group	Mean Strength (MPa)	SD (MPa)
Sintered Glass-ceramic A (starting)	153.2[a]	21.7
Sintered Glass-ceramic A (4hr A)$_1$	253.8[b]	53.3
Sintered Glass-ceramic A (8hr A)	219.5[c]	54.1
Heat Extruded IPS Empress Esthetic	165.5[a]	30.6

Experimental glass-ceramics were two-step heat treated (650ºC/1h -1120ºC/1h at 10ºC/min) and then fired in a porcelain furnace. Groups with different superscript letters indicate significant differences ($p<0.05$).

The Weibull analysis of the test groups was performed using a Weibull Programme (WinSmith Weibull, Fulton Findings, USA) and groups were compared by the overlap of their double-sided confidence intervals at the 95% level. The results are presented in Table 4.43. The biaxial flexural strength data of the test groups presented in Fig. 4.96 - Fig. 4.99, using Weibull plots which were generated by plotting the $\ln\ln(1/(1-P_f))$ against ln(biaxial flexural strength), where P_f is the median rank. The Weibull modulus of the sintered glass-ceramic A (starting A) was statistically higher than the sintered glass-ceramic A (4hr A)$_1$ and A (8hr A) groups. However, there was no statistical difference between the control IPS Empress Esthetic and all the experimental groups ($p>0.05$) (Table 4.43).

The characteristic strength (σ_0) values were compared for the overlap of their double-sided confidence intervals at 95% level (Table 4.43) and using a likelihood ratio contour test (Weibullsmith, Fulton Findings, USA) to determine if the data sets were different (Fig. 4.101). Sintered glass-ceramic A (4hr A)$_1$ and A (8hr A) groups show significantly higher characteristic strength values than the IPS Empress Esthetic group and the glass-ceramic A (starting A) groups ($p<0.05$). There was significant differences between characteristic strength values for the A (4hr A)$_1$ group and A (8hr A) group ($p<0.05$).

Table 4.43: Weibull analysis results of the Attritor milled glass-ceramic A groups

Glass-ceramics	m	C.I. for m (95%)	$\sigma_{0.01}$ (MPa)	$\sigma_{0.1}$ (MPa)	σ_0 (MPa)	C.I. for σ_0 (95%)	r^2
Sintered Starting A	8.5^{a}	6.9 - 10.4	94.0	124.1	162.0^{a}	156.0 - 168.2	0.941
Sintered 4hr A_1	5.4^{bc}	4.3 - 6.8	116.5	180.6	274.9^{b}	259.2 - 291.7	0.971
Sintered 8hr A	4.7^{bc}	3.8 - 5.8	89.6	148.0	239.5^{c}	223.8 - 256.3	0.972
Heat Extruded IPS Empress Esthetic	6.3^{ac}	5.0 - 7.9	85.8	111.0	177.5^{d}	168.8 - 186.6	0.977

C.I. = confidence interval, m = Weibull Modulus, $\sigma_{0.01}$ = stress levels at 1% probability of failure, $\sigma_{0.1}$ = stress levels at 10% probability of failure, σ_0 = the characteristic strength. Different superscript letters indicate significant differences ($p<0.05$)

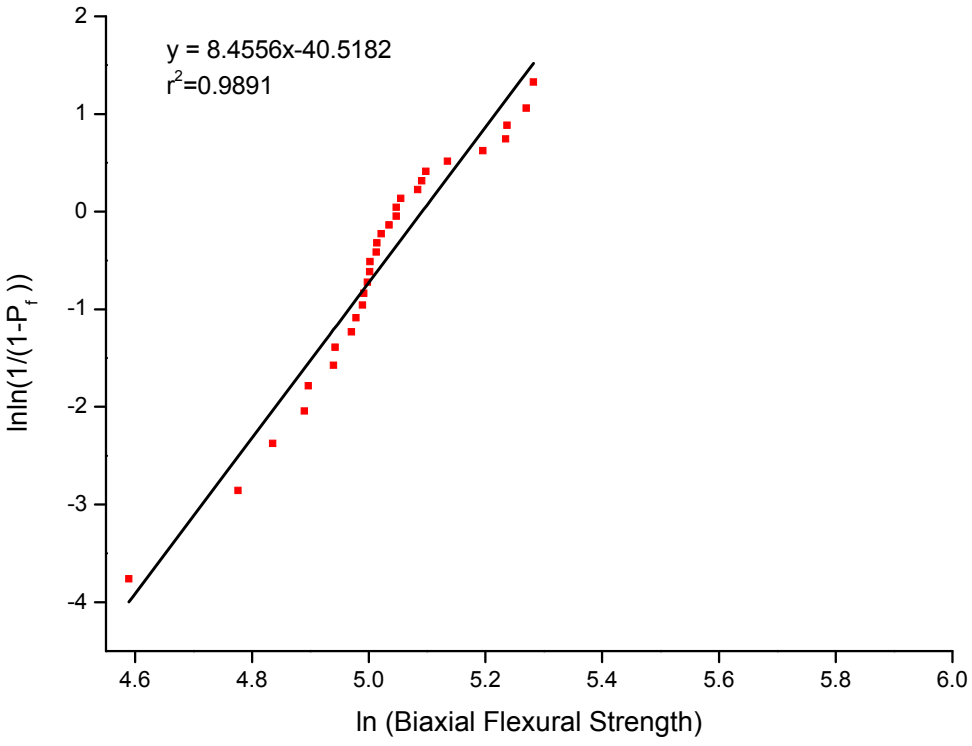

Fig. 4.96: Weibull plot of the sintered glass-ceramic A (starting).

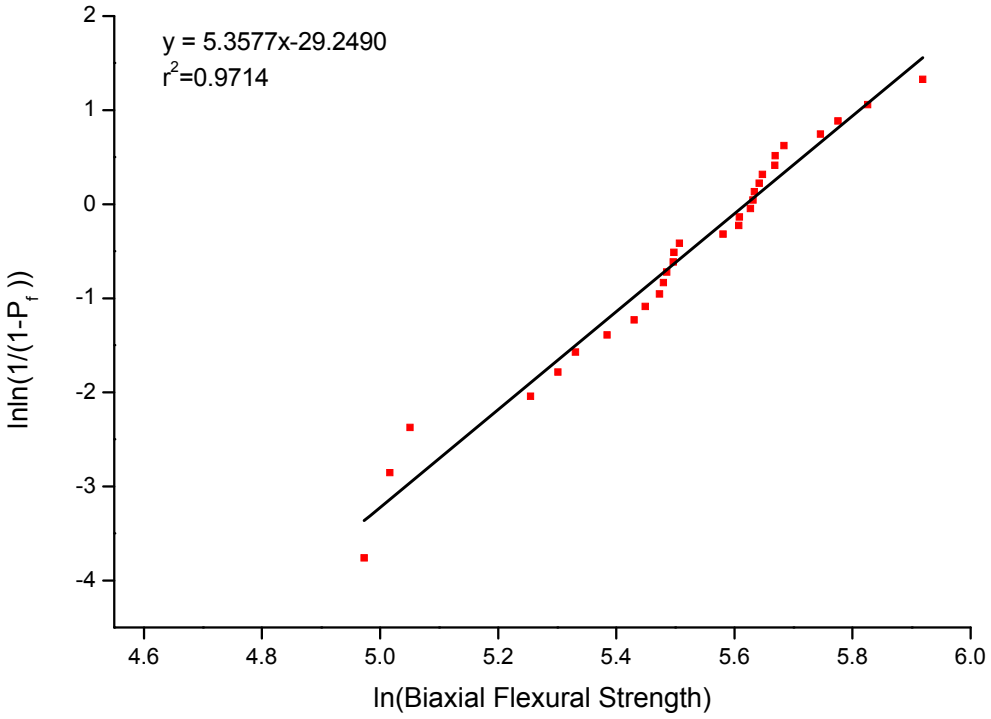

Fig. 4.97: Weibull plot of the sintered glass-ceramic A (4hr A)$_1$.

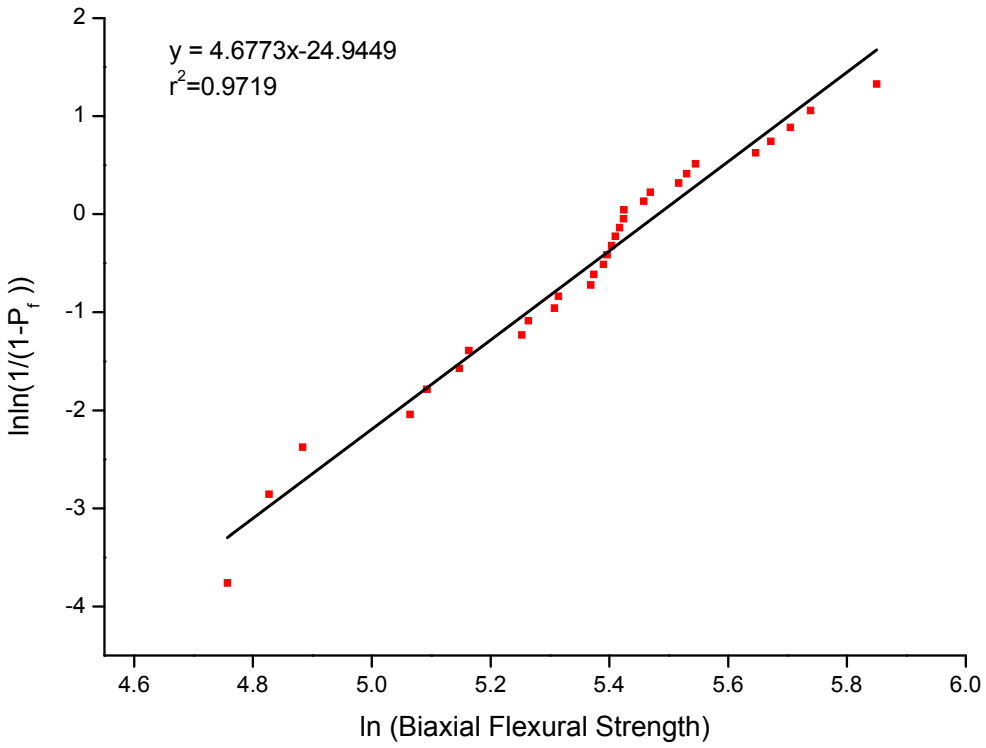

Fig. 4.98: Weibull plot of the sintered glass-ceramic A (8hr A).

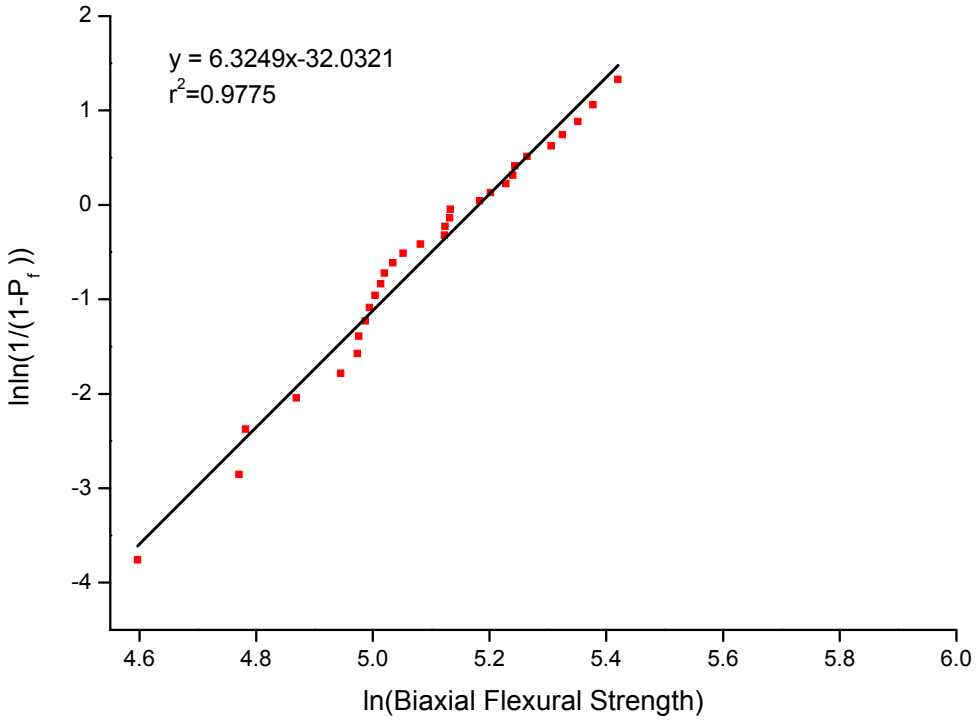

Fig. 4.99: Weibull plot of the heat extruded IPS Empress Esthetic glass-ceramic.

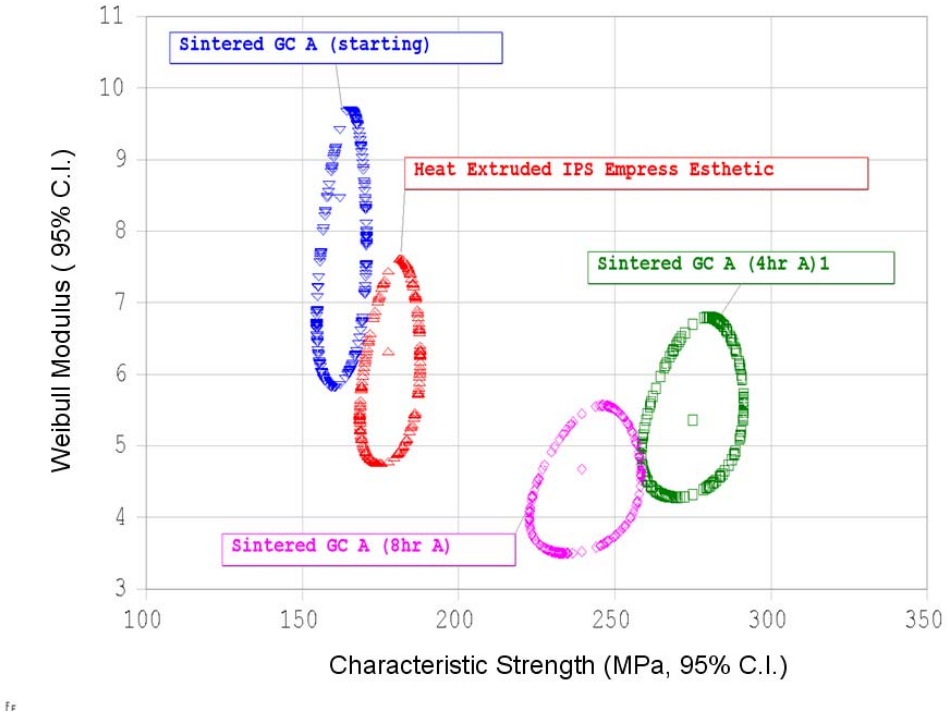

Fig. 4.100: Weibull likelihood ratio contour plots of the heat treated Attritor milled glass-ceramics showing differences according to the overlap of their 95% double-sided confidence intervals.

4.10.2 BFS Results of Glass-Ceramic A (4hr A) Optimisation

The results of biaxial flexural strength (BFS) test for the glass-ceramic A optimisation study groups including; sintered A (4hr A), E (4hr A with additional ZrO_2) and heat extruded A (4hr A) are given in Table 4.44. Glass-ceramics were two-step heat treated (610ºC/1h - 1050ºC/1h), ground and then fired in a dental porcelain furnace or heat extruded (section 3.2.6). The strength data was analysed using a one way ANOVA (F test, $p<0.001$). The sintered glass-ceramic A (4hr A) and heat extruded glass-ceramic A (4hr A) had significantly higher BFS values than the glass-ceramic E group when analysed using the Tukey's multiple comparison test ($p<0.05$). No statistical difference was found between the heat extruded glass-ceramic A (4hr A) group and sintered glass-ceramic A (4hr A) group ($p>0.05$). The power of the performed test with the significance level set at $p<0.05$ was 0.845. All three groups had significantly higher biaxial flexural strength values than the glass-ceramic A (starting A) and the control IPS Empress group. However, no significant difference was found between the sintered A (4hr A) groups, and the sintered glass-ceramic A (4hr A)$_1$, group (Table 4.44).

Table 4.44: The biaxial flexural strength results for the glass-ceramic A (4hr A) optimisation.

Test group	Mean Strength (MPa)	SD (MPa)
Sintered Glass-ceramic A (4hr A)	252.4[a]	38.7
Heat Extruded Glass-ceramic A (4hr A)	245.0[a]	24.3
Sintered Glass-ceramic E	215.4[b]	57.2

Glass-ceramics were two-step heat treated (610ºC/1h -1050ºC/1h at 10ºC/min), and fired in a porcelain furnace or heat extruded. Groups with different superscript letters indicate significant difference ($p<0.05$).

The Weibull analysis of the test groups was performed using WinSmith Weibull and groups were compared by the overlap of their double-sided confidence intervals at the 95% level. The results are presented in Table 4.45. The Weibull plots are illustrated in Fig. 4.101 - Fig. 4.103. There was no statistical difference in Weilbull modulus (m) or characteristic strength (σ_0) between the sintered A (4hr A) or the heat extruded A (4hr A) groups ($p<0.05$). The

glass-ceramic E group had a lower Weibull m value compared to the other test groups in Table 4.45, although there was no statistical difference in characteristic strength (σ_0). The heat extruded A (4hr A) group had a higher Weibull m and characteristic strength compared to the extruded IPS Empress Esthetic control group ($p<0.05$). A cumulative Weibull plot for heat extruded optimised glass-ceramic A (4hr A) and the IPS Empress Esthetic are illustrated in Fig. 4.104, showing the significant improvement in strength compared with the control.

Table 4.45: Weibull analysis results of the glass-ceramic (4hr A) optimisation.

Glass-ceramics	m	C.I. for m (95%)	$\sigma_{0.01}$ (MPa)	$\sigma_{0.1}$ (MPa)	σ_0 (MPa)	C.I. for σ_0 (95%)	r^2
Sintered A (4hr A)	8.7[a]	7.5 - 10.1	156.8	205.4	266.2[a]	256.3 - 276.4	0.881
Heat Extruded A (4hr A)	11.9[a]	9.3 - 15.1	173.3	211.3	255.5[a]	248.8 - 262.4	0.976
Sintered E	4.1[b]	3.2 - 5.2	76.3	136.2	237.3[a]	219.5 - 256.6	0.974

C.I. = confidence interval, m = Weibull Modulus, $\sigma_{0.01}$ = stress levels at 1% probability of failure, $\sigma_{0.1}$ = stress levels at 10% probability of failure, σ_0 = the characteristic strength. Groups with different superscript letters indicate significant difference ($p<0.05$).

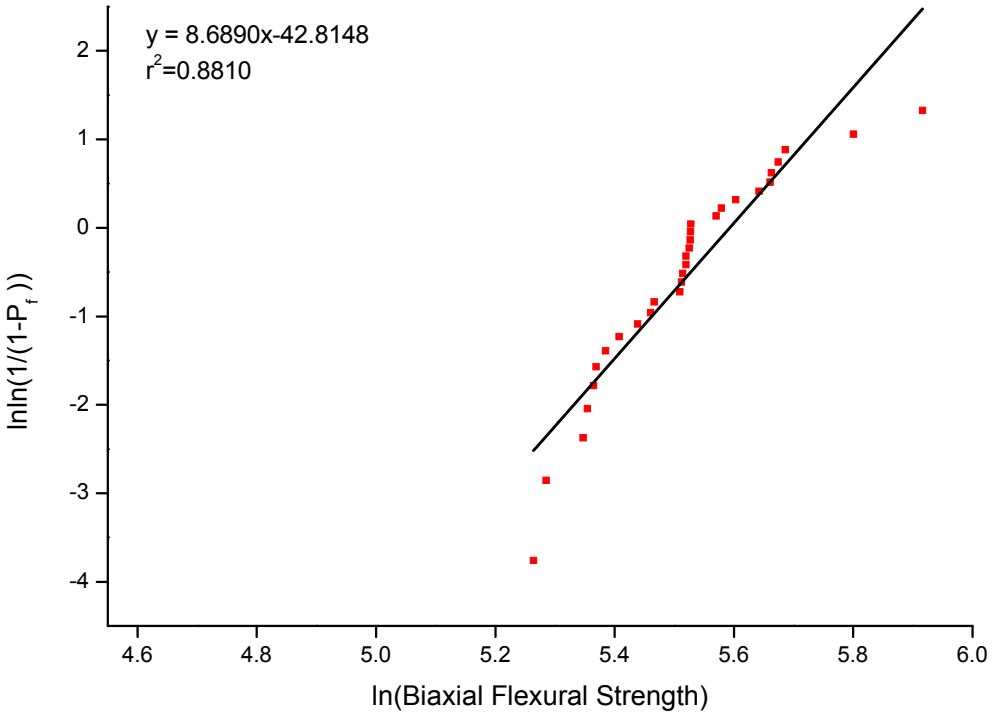

Fig. 4.101: Weibull plot of the sintered glass-ceramic A (4hr A).

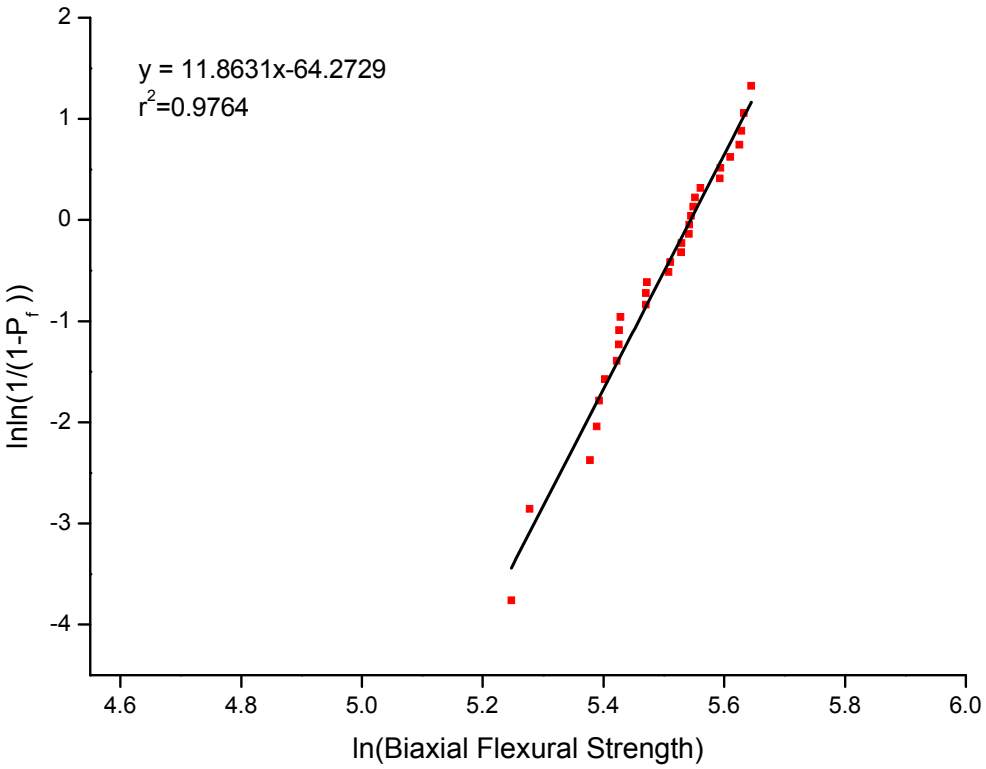

Fig. 4.102: Weibull plot of heat extruded glass-ceramic A (4hr A).

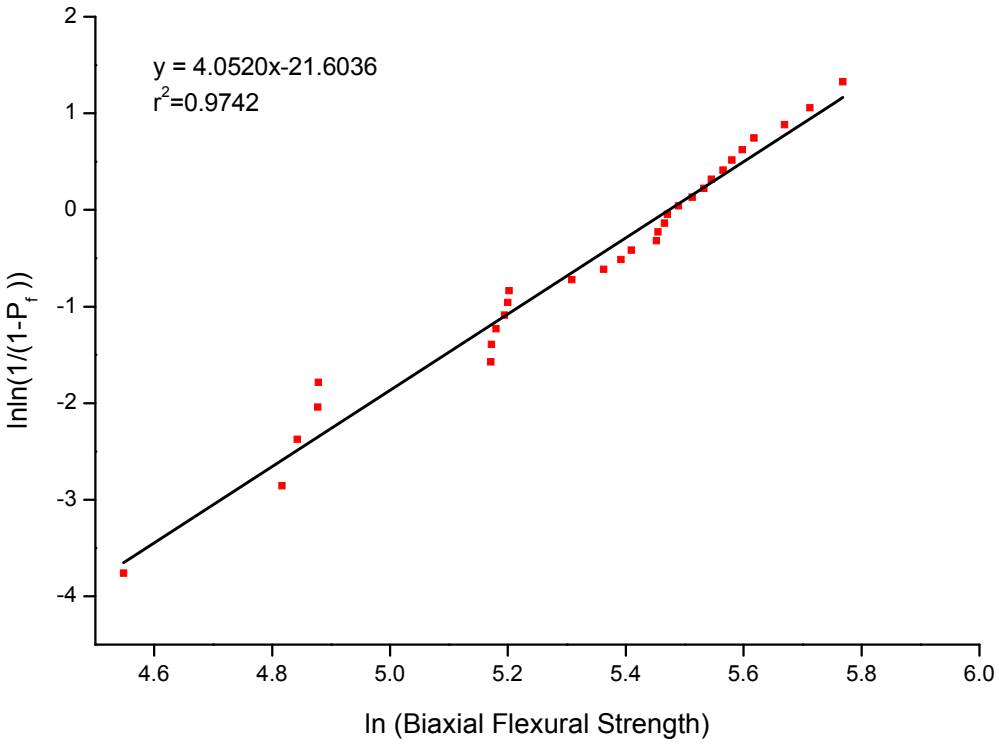

Fig. 4.103: Weibull plot of sintered glass-ceramic E (4hr A with additional ZrO_2).

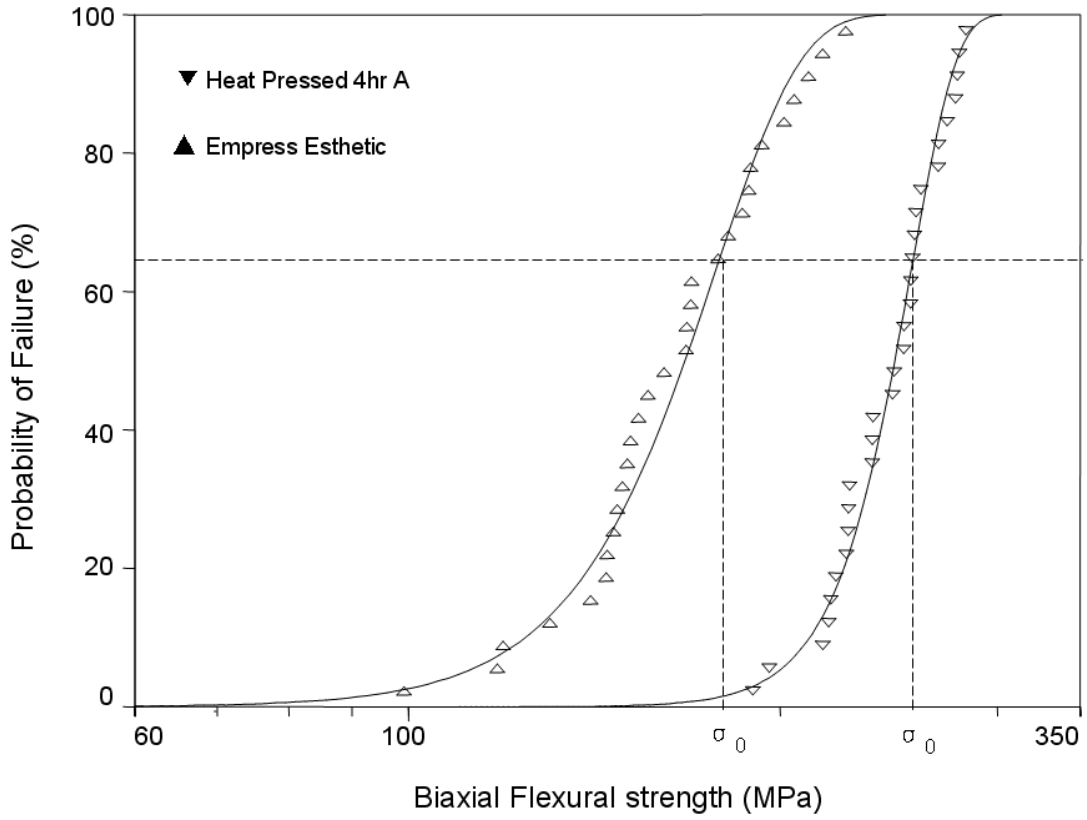

Fig. 4.104: Cumulative Weibull plot of the heat extruded optimised glass-ceramic A (4hr A) and the heat extruded control IPS Empress Esthetic glass-ceramic.

4.10.3 BFS Results of Designed Experimental Glass-Ceramics

The results of the biaxial flexural strength (BFS) testing for the designed experimental glass-ceramic groups: A (4hr A) B, HB, C, D and the commercial control (IPS Empress Esthetic) are illustrated in Table 4.46. The data was analysed using a one way ANOVA (F test, $p<0.001$). The sintered glass-ceramic A (4hr A) had a significantly higher BFS than all the other experimental glass-ceramic groups, and the control IPS Empress Esthetic group when analysed using Tukey's multiple comparison test ($p<0.001$). The BFS values of the sintered glass-ceramics B and HB were significantly higher than the sintered glass-ceramics C, D and the control IPS Empress Esthetic group ($p<0.001$). However, there were no statistical difference between the glass-ceramic B and glass-ceramic HB group ($p>0.05$). Sintered glass-ceramics C and D showed lower BFS values than the all other groups, and a

significant difference was also found between them ($p<0.001$). The power of the performed test with the significant level at $p<0.05$ was 1.0.

Table 4.46: The biaxial flexural strength results for the glass-ceramics A, B, HB, C and D.

Test group	Mean Strength (MPa)	SD (MPa)
Sintered Glass-ceramic A (4hr A)	253.8[a]	53.3
Sintered glass-ceramic B	199.3[b]	20.6
Sintered glass-ceramic HB	212.2[b]	28.2
Sintered glass-ceramic C	131.7[c]	9.0
Sintered glass-ceramic D	115.3 [d]	10.2
Heat Extruded IPS Empress Esthetic	165.5[e]	30.6

Experimental glass-ceramics were two-step heat treated and fired in a dental porcelain furnace according to section 3.3.6. Groups with different superscript letters indicate significant difference ($p<0.05$).

The Weibull analysis of the test groups was performed using WinSmith Weibull and groups were compared by the overlap of their double-sided confidence intervals at the 95% level. The results are presented in Table 4.43. The Weibull plots were are plotted in Fig. 4.105 - Fig. 4.108. The Weibull modulus of glass-ceramic B, HB, C and D groups were statistically higher than the control IPS Empress Esthetic group and glass-ceramic E group. Glass-ceramic C presented the highest Weibull modulus, which was statistically higher than all the other groups apart from glass-ceramic B. However, there was no difference in Weibull modulus values between the sintered glass-ceramic B, HB and A (4hr A) groups according to Table 4.47 and the contour plot Fig. 4.109.

Sintered glass-ceramic A (4hr A) had a significantly higher characteristic strength compared to all test groups (Table 4.47). The characteristic strength of sintered glass-ceramics B and HB were significantly higher than glass-ceramics C, D and the IPS Empress Esthetic group ($p<0.05$). Characteristic strength differences between glass-ceramics B and HB, and between glass-ceramic C and D groups were statistically significant ($p<0.05$).

Table 4.47: Weibull analysis results of the experimental glass-ceramic groups

Glass-ceramics	m	C.I. for m (95%)	$\sigma_{0.01}$ (MPa)	$\sigma_{0.1}$ (MPa)	σ_0 (MPa)	C.I. for σ_0 (95%)	r^2
Sintered 4hr A	8.7^{ad}	7.5 - 10.1	156.8	205.4	266.2^{a}	256.3 - 276.4	0.881
B	11.5^{abc}	9.1 - 14.4	139.2	170.9	208.0^{b}	202.3 - 213.8	0.884
HB	8.5^{ac}	6.7 - 10.9	130.7	172.2	224.4^{c}	216.2 - 232.9	0.985
C	17.6^{b}	14.1 - 21.9	104.4	119.3	135.6^{d}	133.2 - 138.1	0.977
D	13.2^{c}	10.3 - 16.8	84.5	101.0	119.7^{e}	116.9 - 122.7	0.912
Heat Extruded IPS Empress Esthetic	6.3^{d}	5.0 - 7.9	85.8	111.0	177.5^{f}	168.8 - 186.6	0.977

C.I. = confidence interval, m = Weibull Modulus, $\sigma_{0.01}$ = stress levels at 1% probability of failure, $\sigma_{0.1}$ = stress levels at 10% probability of failure, σ_0 = the characteristic strength. Groups with different superscript letters indicate significant difference ($p<0.05$).

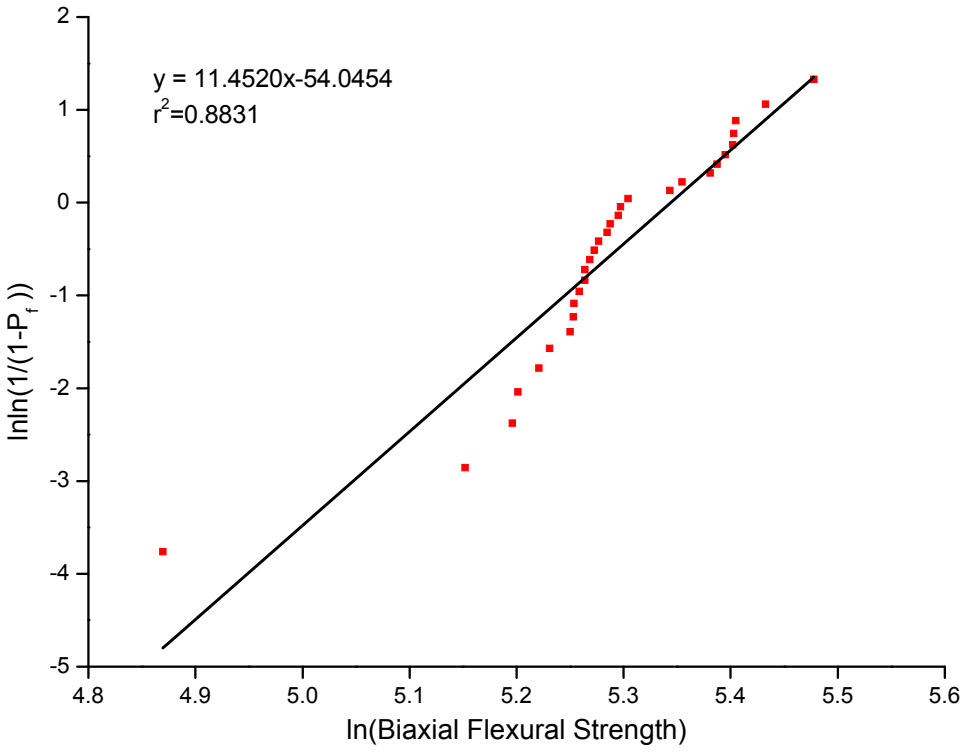

Fig. 4.105: Weibull plot of sintered glass-ceramic B (610ºC/1h - 870ºC/1h at 10ºC/min).

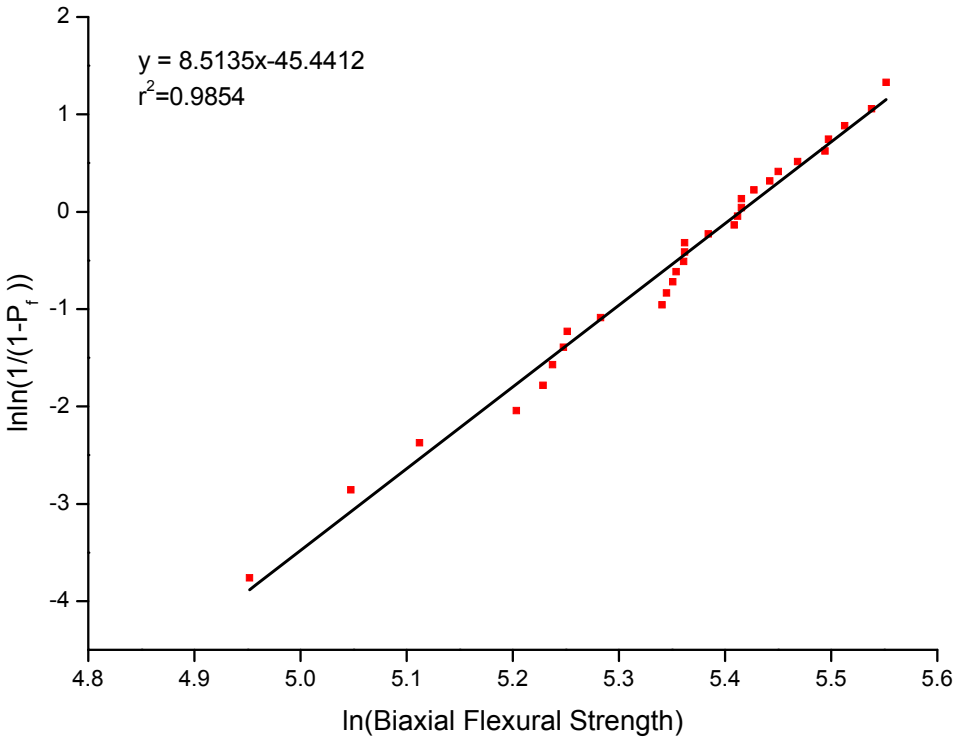

Fig. 4.106: Weibull plot of sintered glass-ceramic HB (620ºC/1h - 795ºC/1h at 20ºC/min).

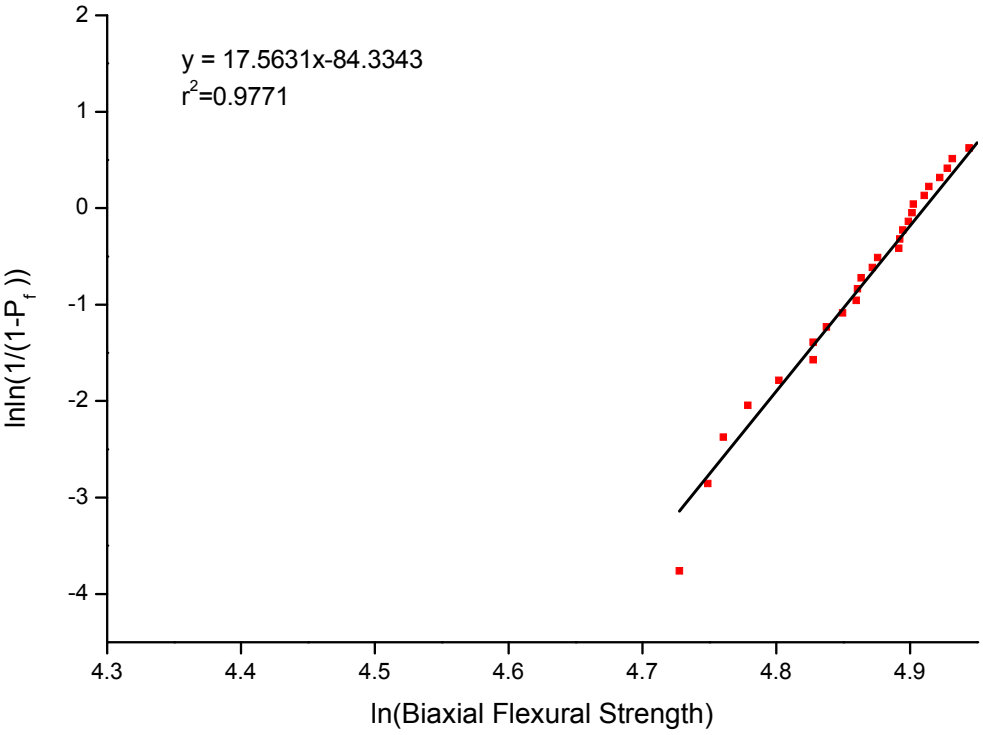

Fig. 4.107: Weibull plot of sintered glass-ceramic C (620ºC/1h - 920ºC/1h at 10ºC/min).

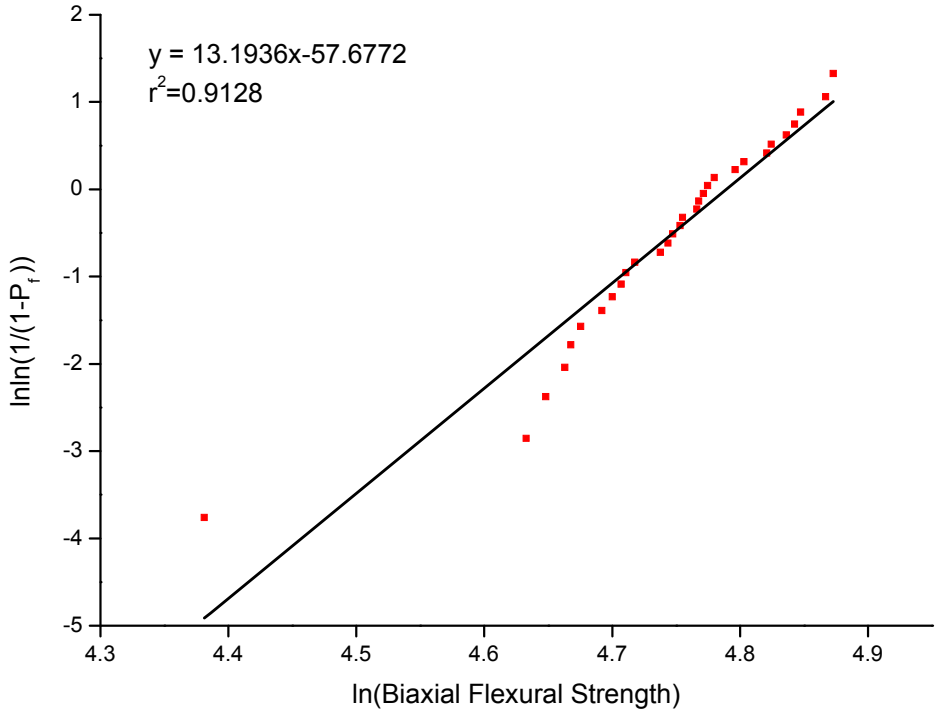

Fig. 4.108: Weibull plot of sintered glass-ceramic D (670ºC/1h - 1000ºC/1h at 10ºC/min).

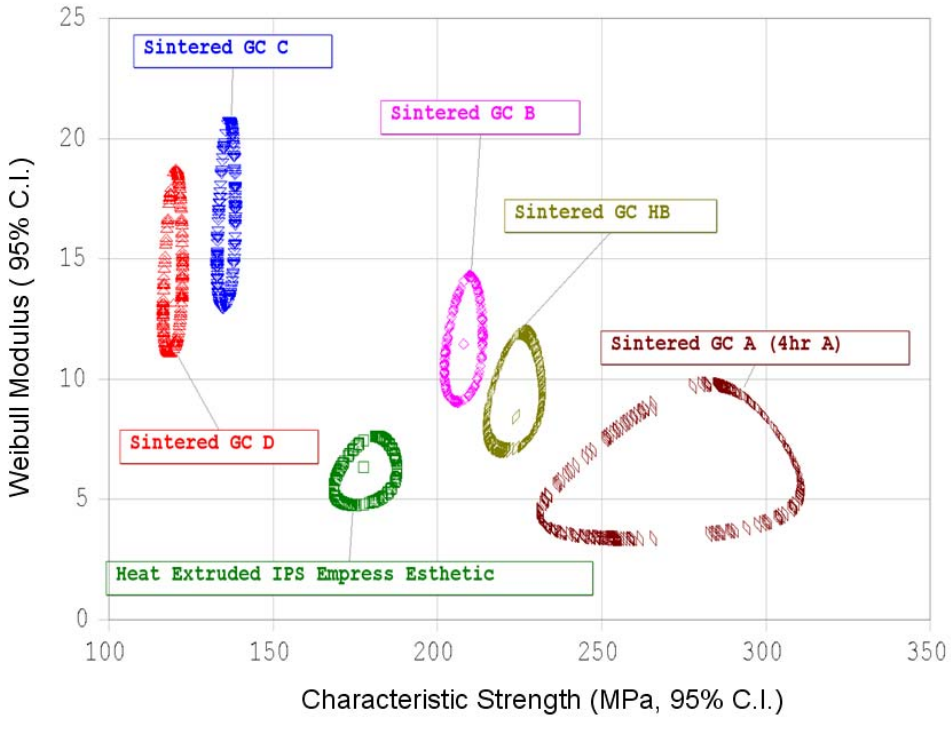

Fig. 4.109: Likelihood ratio contour plots showing the differences according to the overlap of their 95% double-sided confidence intervals.

4.10.4 Fracture Surface of the Biaxial Flexural Strength Test Specimens.

The fracture surfaces of the biaxial flexural strength testing groups were analysed using secondary electron imaging and are given in Fig. 4.121 - Fig. 4.120. Glass-ceramics A (4hr A and 8hr A) and glass-ceramic E demonstrated finer intergranular fracture surfaces than the control IPS Empress Esthetic glass-ceramic and glass-ceramic A (starting). The glass-ceramics C and D illustrated more transgranular fracture surfaces (Fig. 4.119 and Fig. 4.120). Glassy area and a potential secondary phase in glass-ceramic C were indicated by Fig. 4.114. Inclusions were also found for glass-ceramic D (Fig. 4.116).

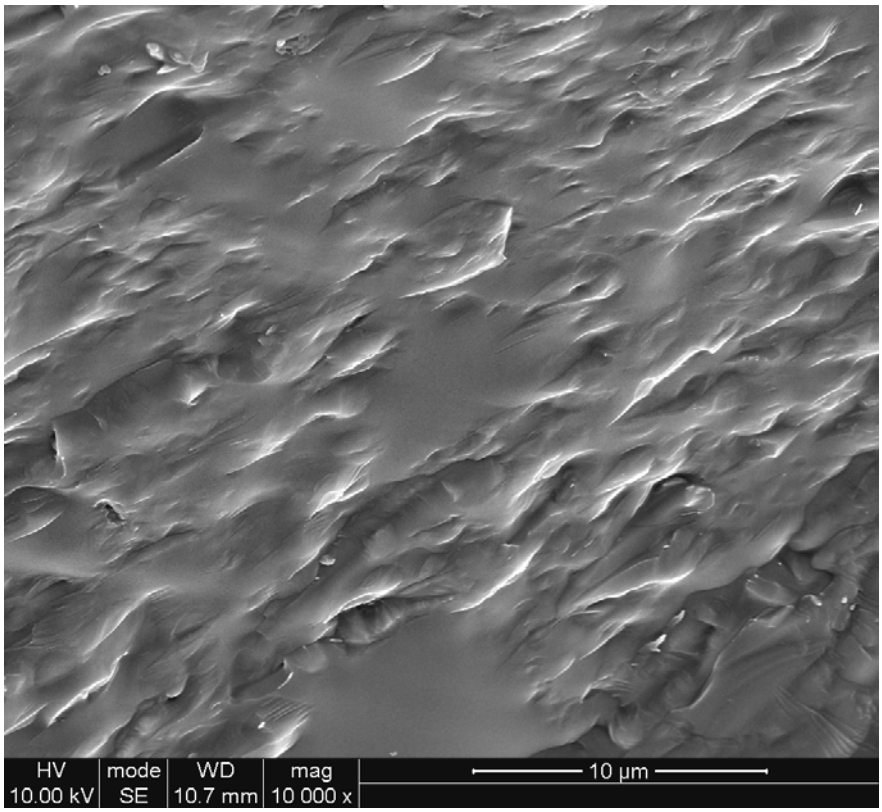

Fig. 4.110: Fracture surface of sintered glass-ceramic A (starting).

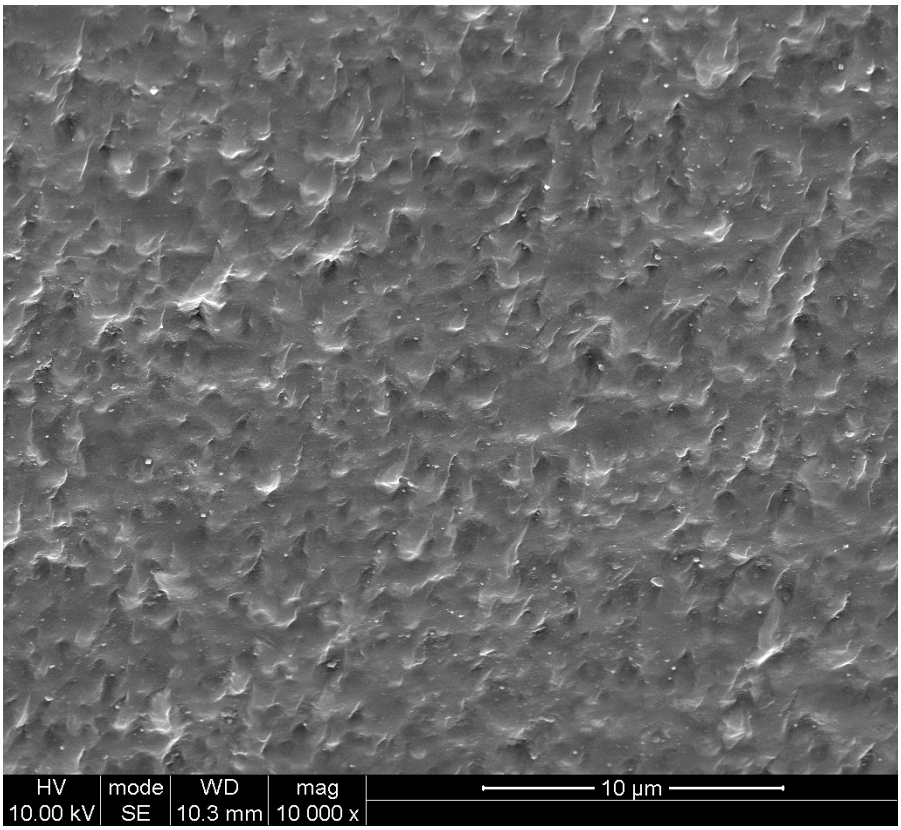

Fig. 4.111: Fracture surface of sintered glass-ceramic A (4hr A).

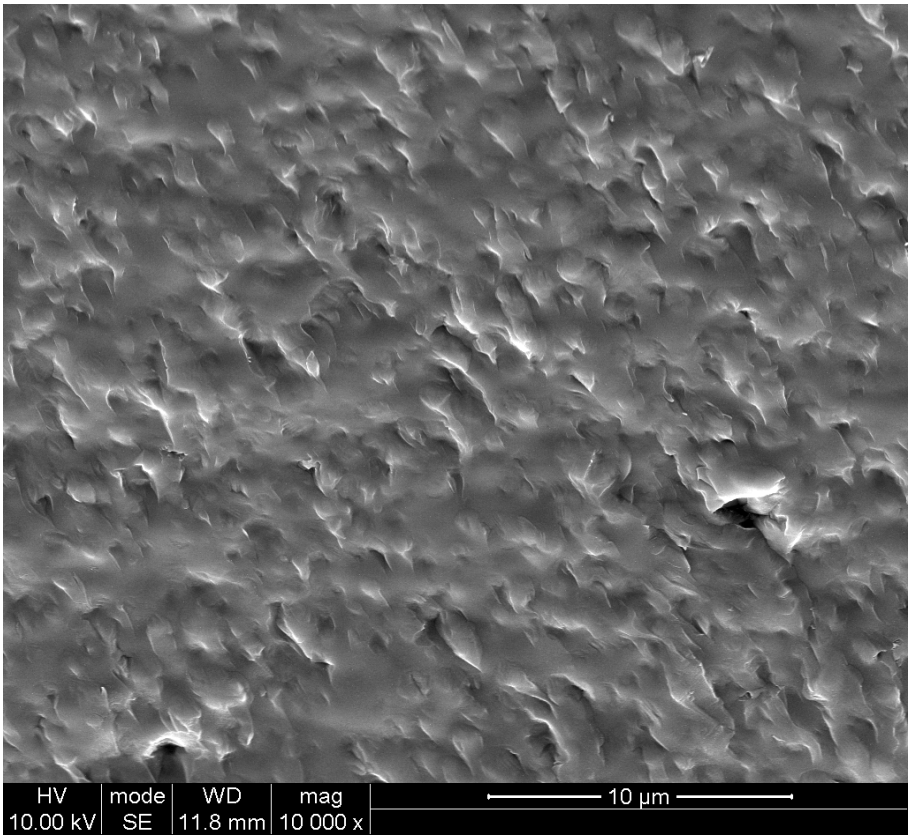

Fig. 4.112: Fracture surface of heat extruded glass-ceramic A (4hr A).

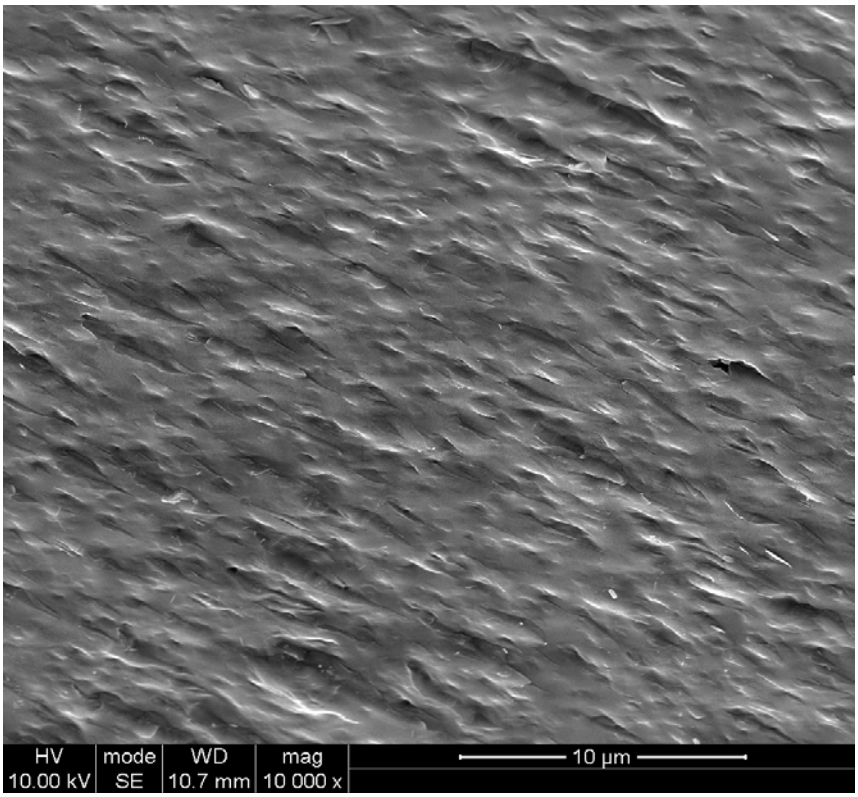

Fig. 4.113: Fracture surface of sintered glass-ceramic A (8hr A).

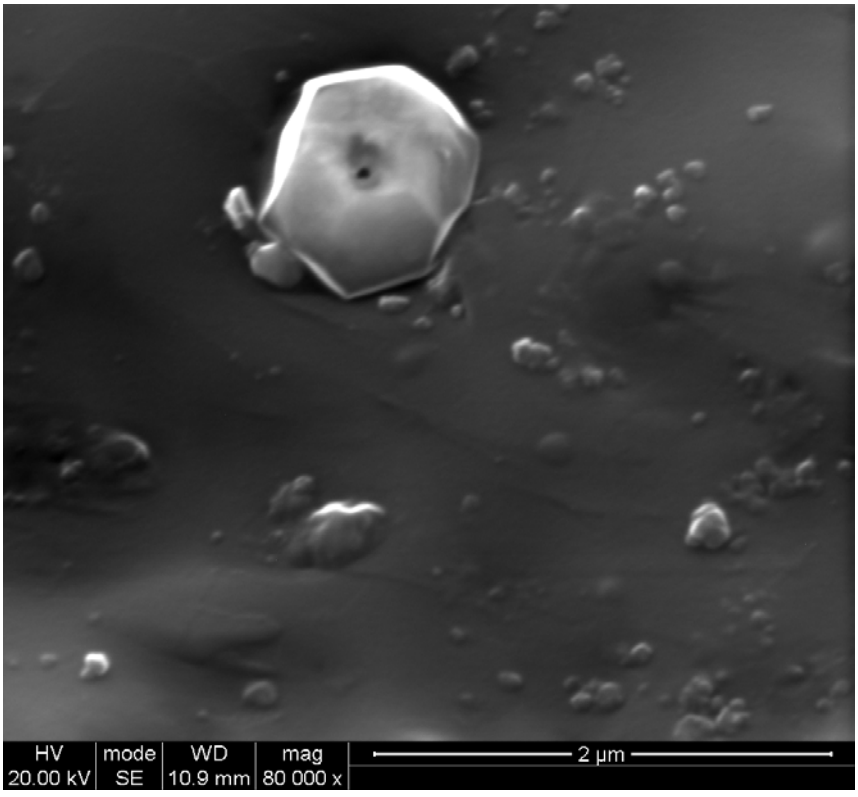

Fig. 4.114: Fracture surface of sintered glass-ceramic A (8hr A) showing a glassy area and signs of a different species.

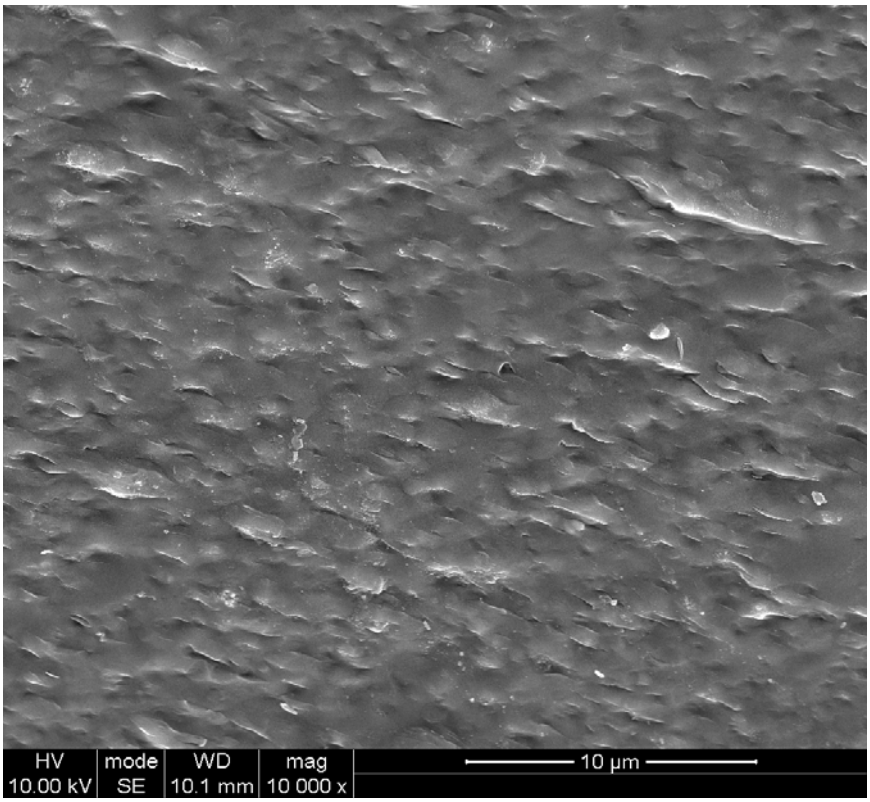

Fig. 4.115: Fracture surface of sintered glass-ceramic E.

Fig. 4.116: Fracture surface of heat extruded glass-ceramic E illustrating inclusions.

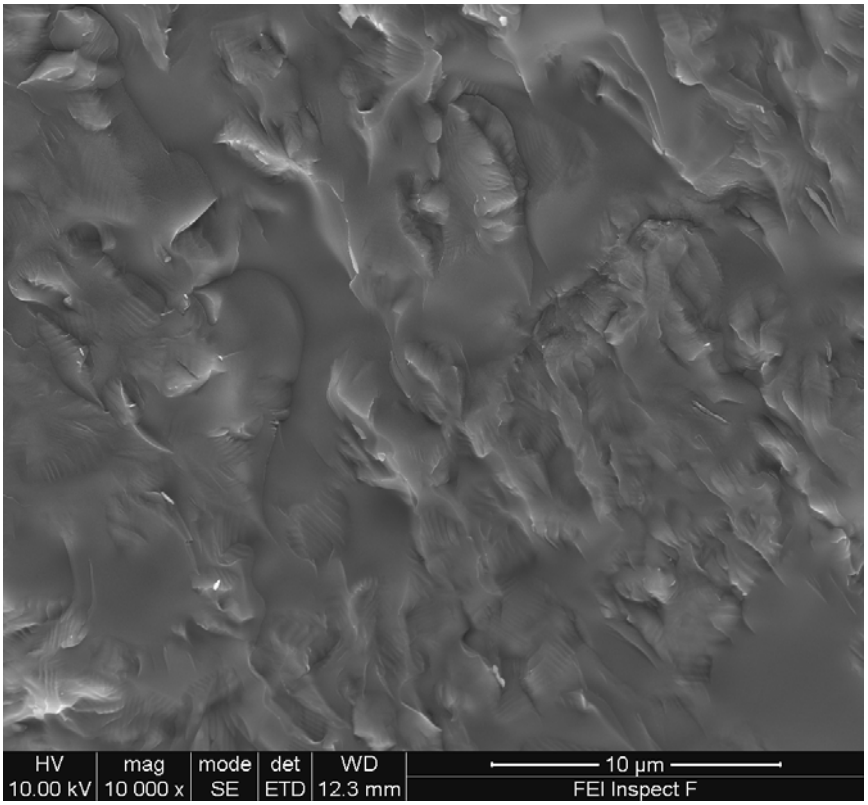

Fig. 4.117: Fracture surface of sintered glass-ceramic B.

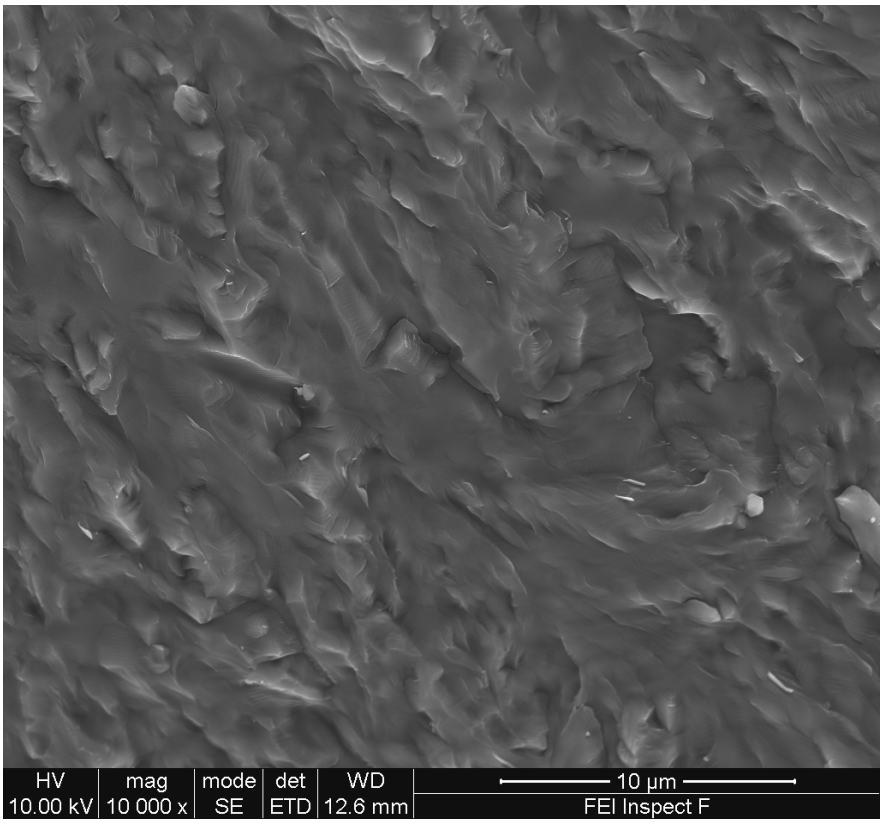

Fig. 4.118: Fracture surface of heat extruded glass-ceramic HB.

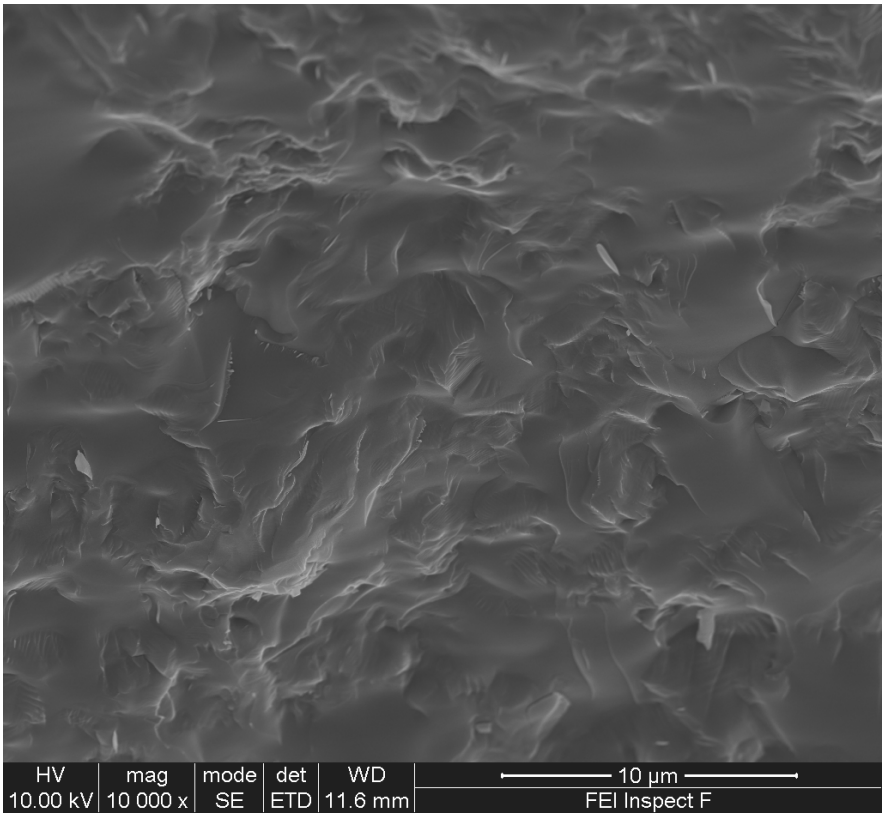

Fig. 4.119: Fracture surface of sintered glass-ceramic C.

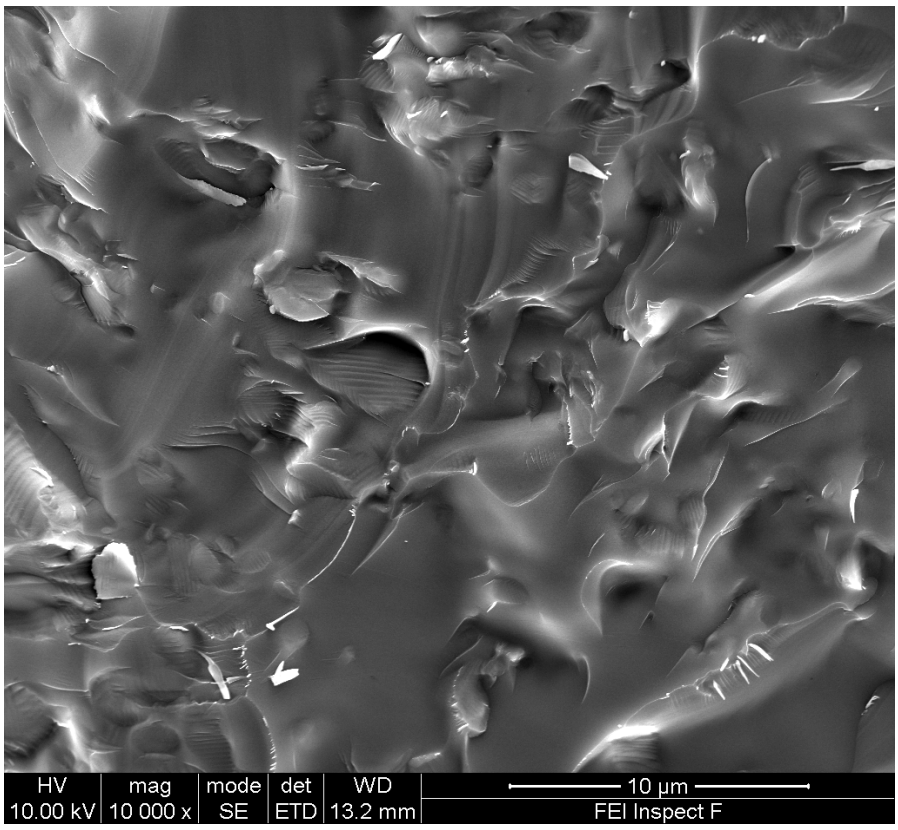

Fig. 4.120: Fracture surface of sintered glass-ceramic D.

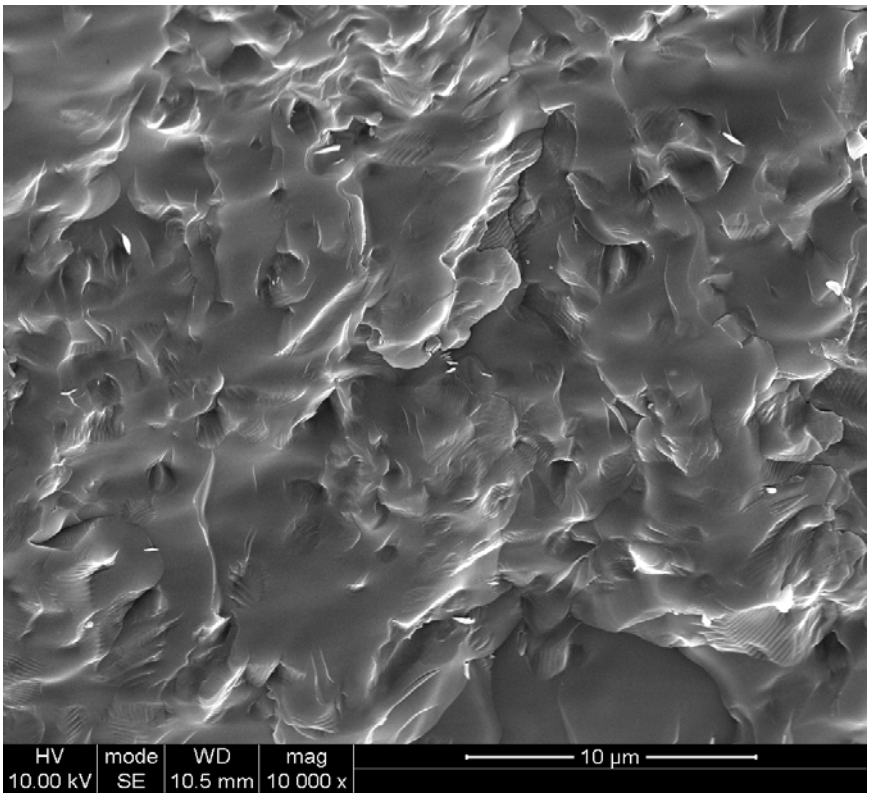

Fig. 4.121: Fracture surface of heat extruded IPS Empress Esthetic glass-ceramic.

4.10.4.1 EDS Analysis of Glass-Ceramic E

The EDS spot analysis of the rectangular area and twinning leucite crystals showed different elemental compositions (Table 4.48: EDS spot analysis results of glass-ceramic E (Table 4.48 and Fig. 4.80). The rectangular area was zirconium rich and where silicon and zirconium are the main components. The twinning leucite areas were aluminium, silicon, and potassium rich.

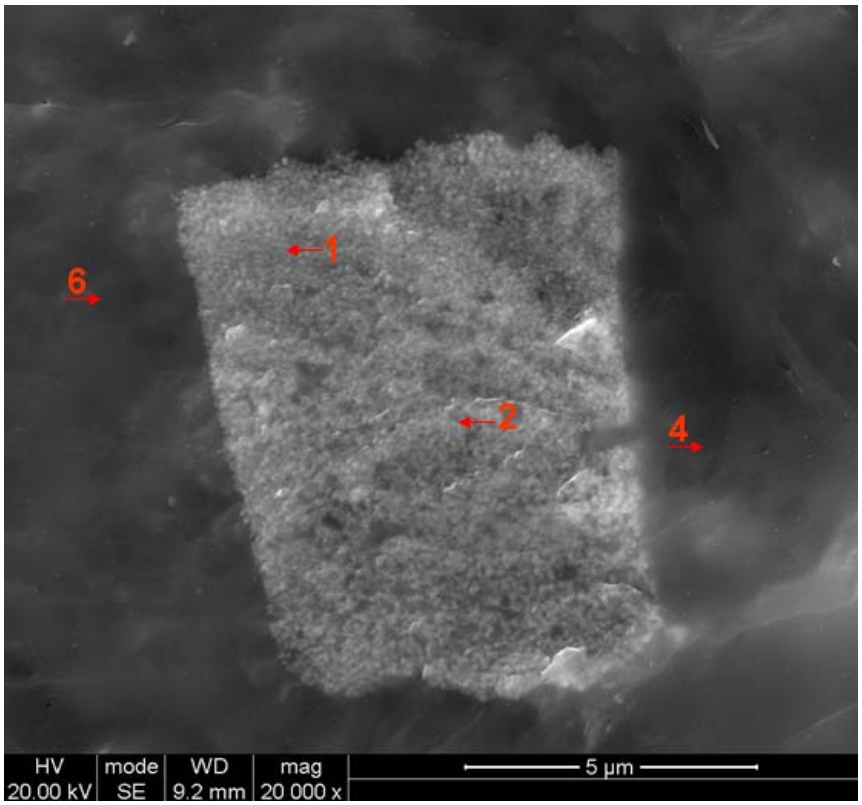

Fig. 4.122: SEM micrograph of glass-ceramic E showing a rectangular phase.

Table 4.48: EDS spot analysis results of glass-ceramic E (elements in mole %).

Elements	Secondary Phase		Twinned Leucite Crystal	
	Spectrum 1	Spectrum 2	Spectrum 4	Spectrum 6
Na	0.89	1.45	1.65	1.79
Mg	0.04	0.16	0.39	0.31
Al	2.28	2.14	5.71	5.83
Si	9.31	8.84	23.82	23.24
K	1.19	1.16	4.59	4.86
Ca	0.67	0.65	0.80	0.95
Ti	0.02	0.12	0.12	0.06
Zr	20.59	20.74	0.72	1.01
O	65.01	67.74	62.20	61.95

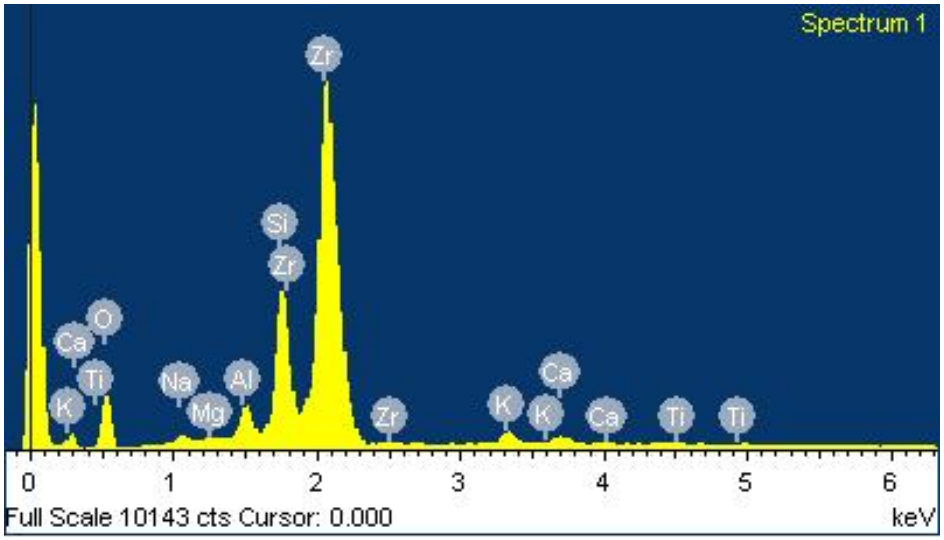

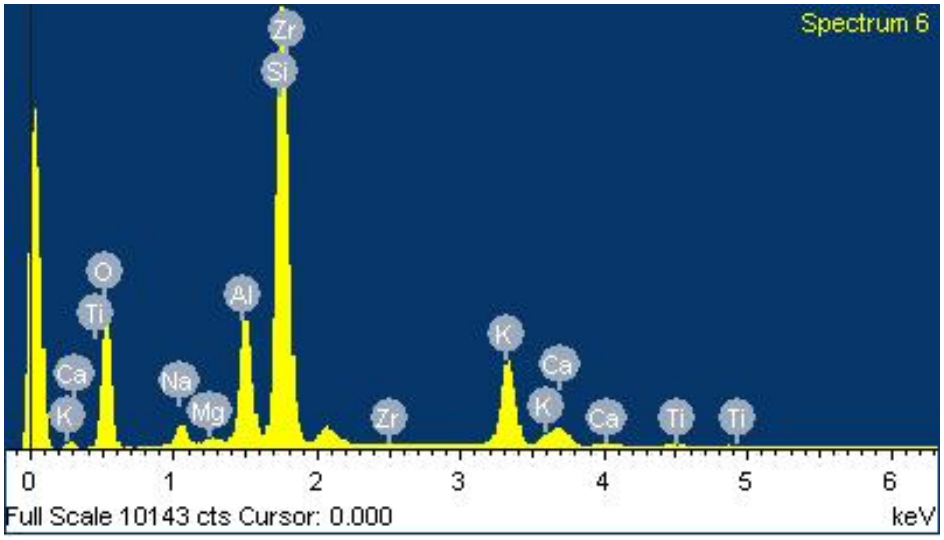

Fig. 4.123: EDS spot analysis of glass-ceramic E (Spectrum 1): rectangular area showing Zr rich and (Spectrum 6): twinned leucite areas showing Si and Al rich.

5 DISCUSSION

5.1 Commercial Materials

Characteristic twinned tetragonal leucite crystals were found in all tested commercial materials (Fig. 4.38 - Fig. 4.40). Crystal twinning is associated with the cubic to tetragonal leucite transformation during glass-ceramic cooling process, where the crystal unit cell expands in the *c*-axis and contracts in the *a*-axis (Mackert, 1988). Laminar and merohedrical twins can be developed (Mazzi et al., 1976, Palmer et al., 1988, Putnis, 1992). Twinning of tetragonal leucite can lead to microcracking within leucite crystals and in the glass matrix (Mackert, 1988). Microcracking was present both in the leucite crystals and the glass matrix around large leucite clusters for Optimal and Ceramco glass-ceramics. Some signs of cracks linking from individual leucite agglomerates were noticed (Fig. 4.39). Similar microcracking was also observed by other researchers (Fairhurst et al., 1992, Mackert and Williams, 1996). This might result in catastrophic failure of the materials. However, less microcracking within the crystals and glass matrix was illustrated in IPS Empress Esthetic glass-ceramic (Fig. 4.38). It was suggested that the microcracking in leucite containing dental porcelain can be miminised by reducing the mean leucite particle diameter to less than 4 μm (Mackert et al., 2001). All glass-ceramics showed a crystal area fraction between 30 - 37% (Table 4.26), which was within the range reported for dental leucite glass-ceramics (Piché et al., 1994).

Tetragonal leucite was confirmed for all commercial glass-ceramics. However, displacements in 2θ positions of the crystal reflections were noticed when compared to the tetragonal leucite (ICDD: 00-038-1423). These changes were thought to be associated with the glass residual stress, structural relaxation of the unit cell and distortion of leucite crystal during processing, which was also suggested by Cattell (2003).

The commercial glass-ceramic TEC values ranged from 12.8 - 16.7 x 10^{-6}/K, 100 - 400ºC and the TEC value for IPS Empress Esthetic glass-ceramic was in the same range as that given by the manufacturer's (17.8 x 10^{-6}/K, 100 - 500ºC). The thermal expansion coefficient

plays an important role for the glass-ceramic. During cooling, the different thermal expansion between the glass matrix and leucite crystals can develop tangential compressive stresses around the leucite crystals. The tangential compressive stress can counteract the crack driving force and act as a crack deflector and strengthen the material (Denry et al., 1996, Lee et al., 1997). However, it can also lead to microcracks along the *c*-axis and around the leucite crystals, and work as a crack initiator or facilitate crack propagation (Denry et al., 1996, Mackert and Williams, 1996).

IPS Empress Esthetic glass-ceramic showed a Mean (SD) biaxial flexural strength of 165.5 (30.6) MPa (Table 4.42), which is higher than the values (120 - 149 MPa) given by other researchers (Cattell et al., 1999, Wagner and Chu, 1996, Gorman et al., 2000). However, this was in agreement with the manufacturer's value. Weibull regression analysis of the strength data revealed a characteristic strength of 177.5 MPa and a low Weibull modulus (m = 6.3) (Table 4.43). The values were in the range documented in the literature (Cattell et al., 2001, Albakry et al., 2004a). Potential failure at lower stress levels was suggested by the 1% and 10% probability of failure. This might be a consequence of the uneven crystal size, distribution and microcracking of the residual glass. Glassy areas within the fracture surface influenced the transgranular fracture surface of IPS Empress Esthetic (Fig. 4.121) and large crystal free glassy areas were visible.

5.2 Experimental Appen Factor Prediction

Glass was considered as a polymer by Stevels (1954) and many other researchers. The glass properties depend on the relationship between the glass network and network modifying ions which contribute to the amount of bridging and non bridging oxygen ions. Appen Factors have been used for the empirical glass property prediction (Appen, 1961). The predicted and measured TEC values in the present study correlated well with each other for the experimental glasses (Table 4.11). A deviation less than 0.3 x 10^{-6}/K within the temperature range from 100 to 400ºC were found. Glass density measured based on the

Archimede's Principle (Table 4.24) and the measured R.I. values (Table 4.25) were also in good agreement with the predicted values. This confirms the claim that calculation using Appen Factors gives high accuracy for the property prediction of silicate glass, whose silica content is more than 50% (Scholze and Lakin, 1991, Priven and Mazurin, 2003).

An increase in TEC was found from glasses A, D, C and B in sequence (Table 4.11). This might be attributed to the increase in K_2O and decrease in SiO_2 content of the glass composition as shown in Table 3.6. The thermal expansion of glass depends on the structure and thermal vibration, which decreases with the increase in stability of the glass network. With the introduction of network modifiers, the glass structural mobility increases due to the increased non-bridging oxygen number and results in increased TEC of the glass. Therefore, the TEC variation is proportional to the amount of the network modifier. Network modifiers like K_2O and Na_2O have high Appen Factors for TEC (Winkelmann and Schott, 1894, Scholze and Lakin, 1991, Bach and Neuroth, 1998), where K_2O has the highest TEC Appen Factor of 46.5/42.0 x 10^{-6}/K (Table 9.1 in Appendix). Substitution of lower thermal expansion contribution oxides of glasses A, D, C and B using K2O, leads to an increase in TEC, although the small reduction in Na_2O content can counteract the TEC increase.

Alumina, potassium and silicon oxide show high Appen Factors for density of 40.4, 34.1/33.5 and 26.1 - 27.25 g/cm^3 respectively (Table 9.1 in Appendix). An increase in the SiO_2 content by replacing Al_2O_3 and K_2O leads to a decrease in density. Glass D frits were transparent but yellowish tinted, and showed the highest refractive index. An explanation for the high refractive index may be the contribution of TiO_2 which had a high Appen Factor for refractive index (2.080 - 2.230, Table 9.1 in Appendix).

Compared with the glasses, the heat treated glass-ceramics gave higher TEC, density and refractive index. During heat treatment, the residual glass composition changed with the depletion of leucite at a stoichiometry of $K_2O{\cdot}Al_2O_3{\cdot}4SiO_2$. Therefore the TEC of the overall glass-ceramic depends on residual glass, leucite crystal and the leucite crystal content. Tetragonal Leucite has a refractive index of 1.510 ± 0.001, density of 2.485 ± 0.015 g/cm^3

(Deer et al., 2004) and high TEC around 20 - 25 x 10^{-6}/K (Rouf et al., 1978). Leucite crystallisation in the parent glass therefore leads to increase in the TEC and density. The increase in glass-ceramic refractive index was thought to be a consequence of the refractive index difference between the glass matrix and leucite. It was suggested increased glass-ceramic translucency could be achieved by a reduction in the crystal size or minimising the refractive index difference between the glass matrix and crystal (Beall and Duke, 1969). All experimental glasses produced translucent glass-ceramics with the exception of glass D. The opacity of glass-ceramic D might be associated with the high refractive index of the glass, larger leucite crystal size and the refractive index difference between glass and leucite (Table 4.25).

Thermal expansion coefficient of the residual glass in the commercial glass-ceramic was predicted using Appen Factors and the glass elemental compositions given by EDS spot analysis. Glass-ceramics are considered as composite materials (Karamanov and Pelino, 1999), and the properties depend on the relative ratio of the crystals and glass matrix (Pisciella and Pelino, 2008). Thermal expansion coefficient of the commercial glass-ceramics predicted using Appen Factors and the TEC of crystalline leucite did not correlate well with the measured TEC values by dilatometry (Table 4.10). The deviation might be associated with the uneven distribution of leucite crystals, which led to an uneven residual glass composition. Elemental compositions given by EDS spot analysis might not be representative for the overall residual glass due to the inability of EDS for lighter elements detection and the variation of the residual glass.

5.3 Effect of Glass Compositions on Crystallisation

High temperature X-ray diffraction analysis on the designed parent glass A, B, C and D showed the possibility of leucite and sanidine crystallisation in glass A (4hr A) and C, in contrast to glass B and D which only facilitate leucite crystallisation (section 4.6.3). According to the K_2O-Al_2O_3-SiO_2 ternary phase diagram (Schairer and Bowen, 1955), the

composition of the parent glass determines the crystal phases upon cooling. Mackert et al., (1986) suggested the Na_2O in the glass composition can be considered as K_2O for glass cooling path determination, as albite ($Na_2O{\cdot}Al_2O_3{\cdot}6SiO_2$) and sanidine ($K_2O{\cdot}Al_2O_3{\cdot}6SiO_2$) are mutually soluble, and the replacement of small amounts of potassium in leucite by sodium is possible. When the Na_2O in the glass composition is considered as K_2O, the cooling path of glass A, C and D suggests leucite and sanidine crystallisation in sequence, and leucite only for glass B. The deviation of glass D might be due to the additional TiO_2, which was suggested as the most effective nucleating agent for leucite crystallisation by Hermansson and Carlsson (1978). They also claimed that nucleating agents and modifiers were essential for leucite crystallisation in the K_2O-Al_2O_3-SiO_2 system. A potassium content higher than 12 wt% and 1 wt% CaO was also beneficial. Calcium rich spherical domains were previously reported in a leucite glass-ceramic system (Cattell et al., 2005), but might be associated with sanidine crystallisation.

5.3.1 Phase Separation

Scanning electron imaging photomicrographs of the experimental glass B, C and D showed spherical domains (Fig. 4.41 - Fig. 4.43 in section 4.9.2). A CaO-TiO_2 rich droplet phase was previously characterised in glass A (Cattell, 2003). Phase separation in the glass could lower the interfacial energy and provide an increased driving force for crystal nucleation (McMillan, 1979). Phase separation could also lead to compositional change and facilitate the nucleation process (James, 1982). If a new phase was formed, the residual glass composition might shift towards the desired crystal stoichiometry and then promote the crystallisation (Hermansson and Carlsson, 1978). However, EDS spot analysis on the spherical areas did not show a significant change in elemental composition. This might be due to the size of the domains (0.004 - 0.02 μm^2) and the limitation of the EDS beam width and penetration depth. Transmission Electron Microscopy might be useful to categorically characterise these areas.

5.4 Effect of Attritor Milling on Leucite Crystallisation

Particle size analysis results of the Attritor milled glass A showed an “L” shape relationship with milling time (Fig. 4.1). A remarkable powder size reduction was achieved within the first 30 minutes milling and little reduction was noticed for prolonged milling after 1 hour. Further powder size reduction was achieved when a smaller grinding media was used (4hr A and 8hr A, Table 4.3). This agrees with the claims given by Mclaughlin (1999), which suggested the particle size reduction tends to stop when the average particle size reaches about 1/2000 of the diameter of the grinding media, and more than 90% reduction occurs at the beginning of milling. The zirconium, yttrium and hafnium contents of the glass increased with the milling time as showed in Fig. 4.2 and Fig. 4.3. This might be due to the continuous wear of the yttrium stabilised zirconium oxide (YTZ) grinding media during Attritor milling, where Hafnium commonly exists in the YTZ grinding media. These elemental increases might have influenced the leucite crystallisation of the parent glass and contributed to the glass-ceramic property changes. Especially, since zirconia has been utilised as a nucleating agent for leucite glass-ceramics. Prolonged milling was associated with an increase in leucite area fraction (Table 4.31), however, there were signs of a few glassy domains (Fig. 4.114) and the BFS values were lowered. Ball milling has previously been associated with the amorphorisation of secondary phases in glasses and the precipitation of another phase (Suryanarayana, 2001).

Glass-ceramics produced using the Attritor milled glass with a two-step heat treatment (650ºC/1h - 1120ºC/1h) showed copious tetragonal leucite crystals within the glass matrix (Fig. 4.44 - Fig. 4.47). A reduction in powder size led to a steady decrease in crystal size (r^2 = 0.9329, Fig. 4.48) and increase in crystal number (r^2 = 0.9891, Fig. 4.49). The crystal size was reduced from Mean (SD) 0.99 (0.59) μm^2 to 0.39 (0.28) μm^2, and the crystal number was increased from 558 to 1434 with 4 hour milling and heat treatment. Prolonged milling with smaller grinding media, glass-ceramic A (8hr A) produced a uniform microstructure of leucite crystals with a narrow size range 0.01 - 1.25 μm^2, finer crystal size 0.16 (0.10) μm^2

and increased crystal number (3378). Surface nucleation and crystallisation was suggested for the leucite glass-ceramics derived from the K_2O-Al_2O_3-SiO_2 systems (Höland et al., 1995, Höland et al., 2003). A reduction in glass powder size may produce a large number of sharp edges and a change in particle shape, therefore, more nucleation sites for the nucleation of leucite (Müller et al., 2000). A possible trend of an increase in crystal number and reduction in crystal size with reduced parent glass powder size were given by Cattell et al., (2006). Powder size dependent leucite crystallisation was produced in aluminosilicate glass with low fluorine content, where a critical glass powder size (7.5 μm) was suggested for the bulk to surface nucleation mechanism switch (Tošić et al., 2000).

Another reason for the crystal number increase might be the existence of fine sized leucite crystals within the parent glass indicated by a few sharp peaks in the X-ray diffraction patterns of the Attritor milled glass A series (Fig. 4.21). These fine leucite crystals might work as isostructural nucleating sites during the crystallisation. Isotructural seeding can provide lower energy sites for crystallisation and results in lowering the crystallisation temperature (Selvaraj et al., 1991a, Selvaraj et al., 1991b). Smaller leucite seeds may provide more crystallisation sites. Nanocrystalline leucite seeding lowered the precursor crystallisation temperature and resulted in the crystallisation of leucite (Zhang et al., 2007a, Zhang et al., 2007c). Low levels of tetragonal leucite were present in the glasses A and HB (Fig. 4.21 and Fig. 4.22).

Glass-ceramics A (starting, 30min A, 60min A, 90min A and 120min A) showed an even leucite crystal structure with very few large crystals, crystal coalescence (Fig. 4.44 - Fig. 4.46) or matrix microcracking (Fig. 4.45). The existence of a few large crystals might be attributed to those large size powders within the as milled glass powder indicated by the D [v, 0.9] values (Table 4.3). Microcracking was limited to larger leucite crystals and correlated well with work presented by Mackert et al., (2001), which suggested the microcracking of dental porcelain could be minimised by a reduction of the mean leucite particle diameter to less than 4 μm. No discernible microcracks within the glass matrix and leucite crystal were

illustrated for glass-ceramic A (4hr A and 8hr A), especially for the evenly distributed glass-ceramic A (8hr A), and tetragonal leucite twinning was still visible at high magnification. This is thought to be associated with the narrow leucite crystal size range 0.01 - 1.25 μm^2 (Table 4.31), where no leucite crystals were larger than the critical size 4 μm for glass-ceramic microcracking (Mackert et al., 2001).

The mean a and c lattice parameters for the Attritor milled glass-ceramic A series (Table 4.17) do not show a linear reduction with the decrease in glass powder size and leucite crystal size. A possible explanation is different Attritor milled glass A powders have different powder distributions and size ranges (Table 4.3), therefore, the glass powder size distribution is not strictly linear, which might influence the crystal growth process.

Glass-ceramics with a fine crystal size, uniform leucite distribution and minor microcracking were successful produced by ball milling and a two step heat treatment (610ºC/1h - 1120ºC/1h). This microstructure can contribute to an improvement of the overall glass-ceramic translucency, mechanical strength (McMillan, 1979) and wear (Metzler et al., 1999).

5.5 Crystallisation Control of Glass A (4hr A)

5.5.1 Leucite Nucleation

Glass-ceramic A (4hr A, 610ºC/1h - 1120ºC/1h) gave the highest leucite crystal number (1751) and the lowest Mean (SD) leucite crystal size of 0.30 (0.24) μm^2 (Table 4.32) compared with other glass-ceramics with different nucleation temperatures. A relatively high leucite area fraction (24.5%) and very little crystal coalescence were present. A decrease in leucite crystal number was observed with an increase in nucleation temperature. McMillan (1979) suggested the optimum nucleation temperature normally lies between the glass transition temperature (T_g) and 50ºC above T_g, which corresponds to a viscosity in the range of 10^{10} to 10^{11} Pa·s. Hill and Gilbert (1993) found some glasses exhibit an optimum

nucleation temperature just above the glass transition temperature, which was later confirmed by Henry and Hill (2004). Glass A (4hr A) demonstrated a glass transition temperature of 581.9ºC (Table 4.11) according to the dilatometry measurement. Therefore, the optimum nucleation temperature of 610ºC (about 30ºC above T_g) was in agreement with both claims made by McMillan (1979) and Hill and Gilbert (1993) and the nucleation experiments (Table 4.32).

Glass-ceramics A (4hr A) with 1 hour nucleation hold at 610ºC gave the smallest leucite Mean (SD) crystal size when compared with other nucleation held glasses (Table 4.33). A linear relationship (r^2 = 0.9441) was found between the leucite area fraction and the nucleation holding time (Fig. 4.53). Small increases in crystal size were shown with a prolonged nucleation hold. During nucleation, a coarsening process controlled by diffusion may happen (Hing and McMillan, 1973) and an optimum nucleation duration for fine-grained glass-ceramic production was suggested (McMillan, 1974). Reduced leucite crystal size, increased leucite crystal number and area fraction were shown for two-step heat treated glasses compared to glasses without nucleation holds (Cattell et al., 2006). A one hour nucleation hold at 610ºC for glass A (4hr A) may have provided sufficient time to establish nucleating sites before coarsening. Although the 4 hours nucleation held glass-ceramic A (4hr A) gave the maximum crystal numbers (1853, Table 4.33), some leucite crystal necking was present (Fig. 4.52). This resulted in crystal coalescence and an increase in the crystal size (Table 4.33). Therefore a one hour nucleation hold at 610ºC was considered the optimum nucleation condition for fine leucite glass-ceramic A (4hr A) preparation.

5.5.2 Leucite Crystal Growth

Glass-ceramic A (4hr A, 610ºC/1h - 1000ºC/1h) showed extensive leucite crystals and signs of a secondary phase (lath shape) in the glassy matrix (Fig. 4.54). Similar structures were also found in the leucite glass-ceramic system (Barreiro et al., 1989, Cattell, 2003). The high temperature X-ray diffraction (HTXRD) patterns of glass A (4hr A) revealed the sanidine crystallisation from 760ºC to 1000ºC (Fig. 4.24 and Table 4.15), therefore, the lath shaped

secondary phase was thought to be sanidine crystals. According to the K_2O-Al_2O_3-SiO_2 ternary phase diagram (Schairer and Bowen, 1955). The presence of sanidine in the present study might be due to the transformation of leucite and silica to sanidine. Sanidine precipitation was previously identified in leucite glass-ceramics from 800ºC to 950ºC (Barreiro and Vicente, 1993).

Glass-ceramic A (4hr A, 610ºC/1h - 1050ºC/1h) (Fig. 4.55) produced a finer leucite structure with a narrow size range (0.01 - 0.91 μm^2). Reducing the crystal growth temperature from 1120ºC to 1050ºC increased the leucite crystal number from 1751 to 4895 (Table 4.34). The Mean (SD) crystal size was reduced by 50% to 0.15 (0.09) μm^2, and the leucite area fraction was increased by 10% (Table 4.34). Tošić et al., (2000) observed an early stage of leucite crystal growth where dendritic leucite grew in preferred crystallographic directions controlled by diffusion. An increase in crystallisation temperatures could reduce the glass viscosity, increase the mobility and therefore facilitate the crystal growth.

Different crystal growth holds for glass A (4hr A) at 1050ºC indicated that the optimum crystal growth hold for glass A (4hr A) was 1 hour. Prolonged holding led to crystal coalescence, reduction in leucite area fraction and increase in mean leucite crystal size (Table 4.35). Partial dissolution of leucite crystals was revealed with prolonged heating of leucite glass-ceramics in the range of 1000 - 1100°C (Denry et al., 2001) and was further confirmed by Cattell et al., (2005). A peak crystallisation temperature of 854.8ºC was indicated by differential thermal analysis, however, the overlap of leucite and sanidine crystallisations were suggested by HTXRD patterns. Therefore, 1050ºC was considered as the peak crystallisation temperature.

5.5.3 Sanidine Crystallisation

High temperature X-ray diffraction results suggested sanidine can be crystallised from glass A (4hr A) within the temperature range of 760ºC - 1000ºC. Sanidine crystallisation at 800ºC - 950ºC was previously identified in leucite containing glass-ceramics (Barreiro and Vicente,

1993). X-ray diffraction and the SEM micrograph of the two-step heat treated glass-ceramic A (4hr A) showed the coexistence of a sanidine and tetragonal leucite phase with a 1 hour hold at 850ºC (Fig. 4.59). Prolonged holding (2 hours) resulted in a reduction in leucite crystal size and number, and sanidine was therefore the major crystalline phase (Fig. 4.60). Leucite crystals were hardly discernable in the 3 hours held glass-ceramic specimen. This is in agreement with the K_2O-Al_2O_3-SiO_2 ternary phase diagram (Schairer and Bowen, 1955), in which leucite and a silica rich glass network results in sanidine precipitation. Therefore, with a suitable two-step heat treatment, glass-ceramics containing sanidine or a mixture of sanidine and leucite crystals can be produced. Sanidine however has a different structure and a thermal expansion coefficient of 4.1 x 10^{-6}/K, which is much lower than leucite (28.0 x 10^{-6}/K, 25ºC to 700ºC) (Mackert, 2000). This thermal expansion mismatch might develop a residual stress within the glass and cause microcracking. Nevertheless, a single phase sanidine glass-ceramic with a matched thermal expansion glass matrix might be useful for biomedical applications.

5.5.4 Effect of Zirconia on Leucite Crystallisation

Zirconia has been used as a nucleating agent for different glass-ceramic systems (Hermansson and Carlsson, 1978, Yu et al., 2002, Apel et al., 2007, Khater and Idris, 2007). The Zr^{4+} has a Field strength of 6.3 and was categorised as an intermediate ion (McMillan, 1979). Zirconia (0.7 mole %) was deliberately introduced into the glass A (4hr A) to study its effects as a nucleating agent (glass-ceramic E). Agglomeration of the zirconia nanopowder resulted in irregular shaped inclusions within the glass matrix (Fig. 4.116) and reduced the BFS value and reliability when compared to glass-ceramic A (4hr A) (Table 4.44). EDS confirmed these areas were zirconia rich (Table 4.48). In contrast, the zirconia introduced during Attritor millings (4 hours) may drive glass phase separation, lowering the crystallisation kinetics. The lack of crystal coalescence found in the microstructure of the Attritor milled glass-ceramics A could be associated with the zirconia hindering effect on crystal growth due to an increased viscosity as suggested by Apel et al., (2007). After

prolonged milling (8 hours) and crystallisation heat treatments the glass-ceramic A (8hr A) presented a few glassy areas within the BFS test specimens (Fig. 4.114). These areas may be associated with zirconia rich phase separated areas and there were also signs of another phase. The glass-ceramic A (8hr A) showed a reduced Mean (SD) BFS of 219.5 (54.1) MPa and Weibull modulus (m = 4.7) which may be a consequence of the milling contamination and the precipitation of another species of different thermal expansion.

5.6 Crystallisation of the Experimental Glasses

Differential Scanning Calorimetry (DSC) plots of the glass B, HB, NB and C showed very little shift in peak crystallisation temperatures versus glass powder sizes (Fig. 4.5, Fig. 4.7, Fig. 4.9 and Fig. 4.11). This suggests a bulk nucleation mechanism, and low activation energies were derived using the Kissinger Equation (Table 4.9), which indicated lower crystallisation barriers. Similar activation energy values of Mean (SD): 125 (4) $KJ \cdot mol^{-1}$ were reported for a leucite crystallisation precursor synthesised by a sol-gel process (Zhang et al., 2006), however, a higher activation energy of crystallisation of 319 (23) $KJ \cdot mol^{-1}$ was given for the fluorine containing aluminosilicate glass (Tošić et al., 2000). Leucite crystallisation has been mainly achieved by surface nucleation (Höland et al., 1995), although, size dependent bulk nucleation of leucite was also possible (Tošić et al., 2000, Tošić et al., 2002). A bulk mechanism is favourable if the glass composition is close to the stoichiometry of the crystalline phase (McMillan, 1979) and this may be a factor in the present glass compositions.

Glass-ceramic B (Fig. 4.62) produced a leucite glass-ceramic with a high area fraction of leucite crystals (58.9%) and minimal level of microcracking. The microstructure consisted of orientated fibre like crystals and a dense dispersal of spherical leucite crystals. A similar structure was present in glass-ceramic C (Fig. 4.71) with a slight reduced leucite content of 52.4%. This morphology could be controlled by using different crystallisation temperatures (Fig. 4.64 and Fig. 4.73). The microstructures produced were in contrast to current

commercial leucite glass-ceramic microstructures which contain large glassy areas, uneven crystal size and microcracking of the glassy area (Fig. 4.38 - Fig. 4.40 and (Guazzato et al., 2004a). An explanation for the microcracks free microstructure of glass-ceramic B and C could be that the residual glass may possess favourable thermal expansion coefficients which thermally match leucite and generate compressive stress within the glass and strengthen the material (Denry et al., 1996). Glass-ceramic D (670ºC/1h - 1000ºC/1h) showed a coarse leucite crystal microstructure with larger glassy areas and some microcracking. This might be related to the glass compositional difference. Glass D contains higher TiO_2 and lower K_2O content than the other glasses, and possesses a higher T_g and D_{sp} (Table 4.11). Increased glass transition temperature might lead to stress relaxation due to the overlap of cubic / tetragonal leucite transformation temperature (Kon et al., 1994). The TiO_2 might also agglomerate and influence the overall glass crystallisation.

Glass-ceramic HB (620ºC/1h - 870ºC/1h) produced a microstructure consisting of rosette shaped domains, orientated fibres surrounded by fine leucite crystals (Fig. 4.65). Hardly any microcracking was presented. A highly crystalline structure with finer leucite crystals was crystallised using an optimised two step heat treatment (Fig. 4.68). The densely dispersed areas of interconnected leucite crystallisation observed (Fig. 4.69) were thought to be the consequence of preferential crystal growth. High volume fraction leucite glass-ceramics with needle-shaped leucite crystals have been reported to grow in a star shaped morphology, and a bending strength of 200 MPa was reported (Beham, 2003). The microcrack free glass-ceramic HB in the present study had a highly crystalline structure and led to a high BFS (212.2 MPa).

Glass-ceramic NB produced a mixture of spherical and interconnected leucite crystals (Fig. 4.70). Hardly any microcracking was observed. Titanium oxide was thought to be essential for the crystallisation of leucite and the most effective nucleating agent for leucite glass-ceramic systems (Hermansson and Carlsson, 1978). In the present study, leucite crystallisation without the presence of TiO_2 was achieved. Niobium oxide was suggested to

prevent the crystal growth of fluorapatite glass-ceramics (Denry et al., 2005), however, no such hindering effect on crystal growth was observed at the 0.5 mole% level.

5.7 Biaxial Flexural Strength of Experimental Glass-Ceramics

5.7.1 Effect of Leucite Crystal Size on Glass-Ceramic A

Fine leucite glass-ceramics with reduced crystal size and increased crystal number were achieved by ball milling and a two-step heat treatment (650ºC/1h - 1120ºC/1h). The Mean (SD) BFS increased from 153.2 (21.7) MPa for glass-ceramic A (starting) to 253.8 (53.3) MPa for glass-ceramic A (4hr A)$_1$. The A (4hr A)$_1$ glass-ceramic also had a higher BFS and characteristic strength than the IPS Empress Esthetic control group. The increase in strength was associated with the reduction of leucite size and the uniformity of the microstructure. Zhang et al., (2008) considered the reduction in leucite crystal size from 5.0 to 0.5 μm have no influence on the flexural strength of the leucite glass-ceramic, but reduced the level of microcracking. The present study however produced leucite crystal sizes (<1 μm^2) below this range and showed an increase in flexural strength. Glass composition might be an important factor at this stage, and glass compositional differences should be taken into account. The 70% and 48% statistical ($p<0.05$) increase in characteristic strength for glass-ceramics A (4hr A) and (8hr A) compared with the glass-ceramic A (starting) were considered as a consequence of the reduction in leucite crystal size (Table 4.31), which improved the leucite distribution and prevented the occurrence of microcracking. Increased biaxial flexural strength with reduced leucite crystal size and more uniform structure were also proven by other researchers (Shareef et al., 1994, Cattell, 2003). Compositional changes to the residual glass due to crystallisation may also have resulted in favourable thermal properties in the residual glass, influencing the crystal/glass mismatch. The thermal expansion difference between the residual glass and the fine leucite crystals produced a tangential compressive stress around the leucite crystals

which may have strengthened the material (Denry et al., 1996). The decrease in BFS value for glass-ceramic A (8hr A) might be attributed to the increased ZrO_2 content in the parent glass introduced by milling, which might cause phase separation. This assumption was supported by a few glassy areas found in the BFS fracture surface (Fig. 4.114).

No statistical difference in BFS was found between the glass-ceramic A (starting) and commercial IPS Empress Esthetic ($P>0.05$), however, statistically higher Weibull modulus ($m = 8.5$) were given by the glass-ceramic A (starting). The lower Weibull ($m = 6.3$) of IPS Empress Esthetic was due to the propagation of the anisotropic microcracks and the presence of large glassy areas (Guazzato et al., 2004a).

Optimised glass-ceramic A (4hr A, 610ºC/1h - 1050ºC/1h), showed no statistical increase in BFS / characteristic strength against glass-ceramic A $(4hr\ A)_1$, but showed a statistically higher Weibull modulus. The higher Weibull modulus was thought to be associated with the copious crystallisation of fine leucite crystals in the glass matrix (Fig. 4.55 and Table 4.35). It seems with a 50% reduction in leucite crystal size after the crystallisation optimisation, no further increase in strength was achieved. Increases in compressive strength have been observed with an increase in leucite volume fraction up to 50% (Zhang et al., 2009). However reductions in flexural strength have been observed with increases in leucite volume fraction due to the compositional differences of the glass matrix (Kon et al., 1994).

Studies by Yang et al., (2005) indicated a relationship between increased thermal expansion and flexural strength in a nano sized (80 nm) leucite glass-ceramic frit produced by a sol gel method. These nano sized glass-ceramics only gave a maximum strength value of 106 MPa at an increased volume fraction of 25%. Other researchers has found flexural strength values of 76 - 109 MPa and weibull m values of 7.0 - 10.9 for fine sized (0.5 - 5.0 μm) leucite glass-ceramics. The present study showed dramatically higher Mean (SD) BFS values of 252.4 (38.7) MPa with Weibull m values from 8.7 to 11.9 for optimised fine grained leucite (Mean (SD): 0.15 (0.09) μm^2) glass-ceramics (Table 4.44). The BFS strength value is much higher than those reported for dental leucite glass in the range of 120 - 149 MPa.

Glass-ceramics with reduced leucite crystal size and even distribution might also contribute to less enamel wear as they produced fewer defects and less abrasive dimensions compared to larger grained varieties during wear testing. Reduced enamel and ceramic wear loss was associated with a reduction in leucite size in an in vitro study (Metzler et al., 1999, Suzuki, 1999). This assumption is supported by further studies by Theocharopoulos et al., (personal communication, 2009), indicating a reduced human enamel wear (ethics approval ref. 06/Q0603/98) against heat pressed experimental glass-ceramic A (4hr A) when compared with Ceramco 3 glass-ceramic. This suggests the glass composition and reduced leucite crystal size in the glass-ceramic A (4hr A) may reduce human enamel wear.

5.7.2 Biaxial Flexural Strength of the Experimental Glass-Ceramics

Crystal growth was noticed for experimental glass-ceramics B, HB, C and D after sintering in a dental furnace, which can be associated with viscous flow during sintering (Skinner and Phillips, 1982). Glass-ceramic HB possessed a densely dispersed leucite microstructure with signs of elongated fibre crystals. However, these elongated fibres had a lower aspect ratio than that found in the as heat treated glass-ceramic frit (Fig. 4.62). No discernible microcracking was found in both glass-ceramics B and HB. It was suggested microcracking could be eliminated when a critical leucite crystal size was achieved (Mackert et al., 2001) or by reducing the thermal mismatch between the residual glass and leucite (Miyata, 1986). In contrast, the sintered glass-ceramics C and D showed microstructures with crystal growth, larger glassy areas (Fig. 4.94 and Fig. 4.95) and a lack of homogeneity. The microstructrural difference has proven influencing the glass-ceramic strength and the Weibull modulus (Cattell, 2003), and is shown in the lower BFS values for the glass-ceramics C and D. Experimental glass-ceramics B and HB showed statistical higher Mean (SD) BFS values: 199.3 (20.6) MPa and 212.2 (28.2) MPa than glass-ceramics A (starting), C and D, where the BFS of glass-ceramics C and D was significantly lower than the other groups. This could be explained by the higher leucite fraction of glass-ceramics B and HB, and also the uniformity of glass-ceramic HB. The differences between the experimental groups were

associated with the glass-ceramic microstructure, leucite content, thermal expansion difference between glass and leucite, glass transition temperature and the transformation temperature of leucite (Kon et al., 1994). A linear increase in leucite content and the glass-ceramic compressive strength was given when leucite content was less than 50% volume fraction (Zhang et al., 2009). Glass-ceramic A (4hr A) showed higher BFS values although the leucite volume fraction was lower (33.4%). Glass-ceramics B and HB which have higher leucite area fractions did produce high strength in the current study, but were significantly lower than glass-ceramic A (4hr A). The leucite crystal size, homogeneity of the microstructure and lack of matrix microcracking were therefore thought to be important factors in the strength optimisation. Glass-ceramic B, C and D gave high weibull modulus values (m = 11.5 - 17.6), which were significantly higher than IPS Empress.

5.7.3 Effect of Heat Extrusion of the Experimental Glass-Ceramics

Heat extruded glass-ceramic A (4hr A) showed a Mean (SD) BFS value of 245.0 (24.3) MPa, a characteristic strength of 255.5 MPa and a Weibull modulus of 11.9. There were no statistical difference in strength compared to the sintered glass-ceramic A (4hr A), but an increase in reliability was indicated (Table 4.45). Similar fracture surfaces showing fine intergranular fractures were observed for the heat extruded and sintered glass-ceramic A (4hr A). Heat extrusion directly applies the pressure on the ceramic grain boundaries and eliminates the possibility of coarsening during densification (Chiang et al., 1996). Higher Weibull modulus can be explained by the elimination of glassy areas during heat extrusion. Heat extrusion of the glass-ceramic B dispersed the leucite crystals and eliminated large glassy areas. Minimal matrix microcracking was also found in the high leucite area fraction microstructure of glass-ceramic B (Fig. 4.93). This might lead to increased BFS strength and reliability due to the even leucite crystal distribution. The glass-ceramic A (4hr A) was successfully heat extruded to produce a dental restoration, which was finished using stain and glaze techniques to give high esthetics (Fig. 9.1 and Fig. 9.2 in Appendix).

6 CONCLUSIONS

6.1 Conclusions

Appen Factors were successfully used for glass thermal property, density and refractive index predictions, and the results correlated well with the experimental measurements carried out during the project. The effect of nucleating agents (ZrO_2, TiO_2 and Nb_2O_5) was evaluated and leucite crystallisation was possible without the presence of TiO_2 in the experimental glass NB.

A relationship between the glass powder size and the leucite crystal number and size was established after glass-ceramic heat treatments. A nano sized leucite glass-ceramic, Mean (SD): 0.15 (0.09) μm^2 with a uniform leucite distribution was produced by ball milling and controlled nucleation and growth heat treatments. This glass-ceramic was processable and possessed a high biaxial flexural strength (Mean (SD): 252.4 (38.7) MPa) which was statistically higher than the control IPS Empress Esthetic glass-ceramic ($p<0.05$). The glass-ceramic was successfully heat extruded and led to an improved reliability ($m = 11.9$).

A range of high flexural strength (131.7 - 212.2 MPa), reliable ($m = 8.5 - 17.6$) and translucent leucite glass-ceramics with unique microstructures including rosette shape domains, orientated fibres and densely dispersed spherical leucite crystals were synthesised (glass-ceramic B/HB/C). The residual glasses were thermally matched with the leucite crystals and there was an absence of matrix microcracking. The leucite glass-ceramic microstructure could be controlled using two-step heat treatments and the materials could be sintered in a dental porcelain furnace or heat extruded. Sanidine in glass-ceramic A and a high aspect ratio phase in glass-ceramic D were crystallised and may be useful as potential biomedical materials.

7 FUTURE WORK

7.1 Future Work

Phase separation in glasses A, B, C and D should be further explored by Transmission Electron Microscopy to study the phase separation mechanism and their effect on leucite crystallisation. The effect of nucleating agents on the leucite glass-ceramic microstructure would be an advantage as a route to increased control of the microstructure and to enhance the mechanical properties.

Crystallisation experiments should be carried out on glasses B and C to confirm the bulk crystallisation DSC assumptions and broadening of the glass compositional range may help to understand this process. Powder processing of the glass-ceramic B materials to reduce glass powder size should be attempted and testing of the heat extruded material may lead to enhance mechanical properties.

High temperature analysis on glasses A (4hr A) and B on cooling should be carried out, in order to establish the phase crystallisation upon cooling, so as to design the glass-ceramic cooling process and control the dental glass-ceramic firing cycles, in order to avoid the possibility of undesired phase crystallisation. Residual stress calculations based on the unit cell dimensions given by the XRD refinement should be carried out, in order to study how the stress influences the crystal structure and microcrack distribution.

Fracture analysis of the biaxial flexural test specimens should be carried out, to investigate the fracture mode of the glass-ceramic and study how these failures influence the glass-ceramic strength and the Weibull distribution. Fracture toughness testing of all glass-ceramics should be carried out in order to explore the relationship between the glass-ceramic fracture toughness and the leucite crystal size, morphology and distribution. Wear testing of the optimised nanoscale leucite glass-ceramic should be carried out to establish the clinical relevance.

8 REFERENCES

Abernethey, R.B. (1996) *The New Weibull Handbook,* Forida, self published, pp. (a)3.3 - 3.6, (b)7.1 - 7.14.

Adair, P.J. and Grossman, D.G. (1984) The castable ceramic crown. *Int. J. Periodontics. Restor. Den.,* 4 (2) 32-46.

Addison, O., Marquis, P.M. and Fleming, G.J.P. (2007) Resin elasticity and the strengthening of all-ceramic restorations. *J. Dent. Res.,* 86 (6) 519.

Albakry, M., Guazzato, M. and Swain, M.V. (2004a) Biaxial flexural strength and microstructure changes of two recycled pressable glass ceramics. *J. Prosthodont.,* 13 (3) 141-149.

Albakry, M., Guazzato, M. and Swain, M.V. (2004b) Influence of hot pressing on the microstructure and fracture toughness of two pressable dental glass-ceramics. *J. Biomed. Mater. Res. B: Appl. Biomater.,* 71 (1) 99-107.

Allen, R.M. (1962) *Practical Refractometry by Means of the Microscope: With Listings of Index Liquids and Other Aids for Mineralogists,* Cargille Laboratories, pp. 1-63.

Anusavice, K.J. (2003) *Phillips' Science of Dental Materials,* london, Saunders, pp. 3-18.

Anusavice, K.J. and Hojjatie, B. (1987) Stress distribution in metal-ceramic crowns with a facial porcelain margin. *J. Dent. Res.,* 66 (9) 1493-1498.

Apel, E., van't Hoen, C., Rheinberger, V. and Höland, W. (2007) Influence of ZrO_2 on the crystallisation and properties of lithium disilicate glass-ceramics derived from a multi-component system. *J. Eur. Ceram. Soc.,* 27 (2-3) 1571-1577.

Appen, A.A. (1956) Some anomalies in the properties of glass. In: *Travaux du Ive congrès international du verre, Paris*,

Appen, A.A. (1961) Toward the method for calculating the properties of glass. *Glass Ceram. ,* 18 (5) 235-237.

Assmann, S., Ermrich, M. and Kunzmann, K. (2000) Determination of quantitative leucite content in pressable ceramics compared to conventional dental porcelains. *J. Mater. Sci.: Mater. Med.,* 11 (12) 833-835.

ASTM (1941) Committee [Subcommittee 1, Committee C–14] Offers Definition of Glass. *Glass Ind.,* 22 (5) 216.

Börger, A., Supancic, P. and Danzer, R. (2004) The ball on three balls test for strength testing of brittle discs: Part II: analysis of possible errors in the strength determination. *J. Eur. Ceram. Soc.,* 24 (10-11) 2917-2928.

Bach, H. and Neuroth, N. (1998) *The Properties of Optical Glass,* Springer, pp. 73-81.

Baharav, H., Brosh, T., Pilo, R. and Cardash, H. (1997) Effect of irradiation time on tensile

properties of stiffness and strength of composites. *J. Prosthet. Dent.,* 77 (5) 471-474.

Balandis, A. and Sinkyavichene, I. (2005) Hydrothermal synthesis of leucite and its application in engineering ceramics. *Glass Ceram.,* 62 (1) 49-52.

Ban, S. and Anusavice, K.J. (1990) Influence of test method on failure stress of brittle dental materials. *J. Dent. Res.,* 69 (12) 1791-1799.

Barbieri, L., Corradi, A.B., Leonelli, C., Siligardi, C., Manfredini, T. and Pellacani, G.C. (1997) Effect of TiO_2 addition on the properties of complex aluminosilicate glasses and glass-ceramics. *Mater. Res. Bull.,* 32 (6) 637-648.

Barker, M. and James, P. (1988) Photomachinable glass-ceramics of controlled thermal expansion. *J. Non-Cryst. Solids* 104 (1) 1-16.

Barreiro, M.M., Rlesgo, O. and Vicente, E.E. (1989) Phase identification in dental porcelains for ceramo-metallic restorations. *Dent. Mater.,* 5 (1) 51-57.

Barreiro, M.M. and Vicente, E.E. (1993) Kinetics of isothermal phase transformations in a dental porcelain. *J. Mater. Sci.: Mater. Med.,* 4 (4) 431-436.

Barsoum, M.W. (1997) *Fundamentals of Ceramics,* London, New York, Toronto, McGraw-Hill Companies, Inc, pp. 292-330.

Beall, G.H. and Duke, D.A. (1969) Transparent glass-ceramics. *J. Mater. Sci.,* 4 (4) 340-352.

Beham, G. (1990) IPS Empress: a new ceramic technology. Ivoclar-Vivadent Report, no. 115.

Beham, G. (2003) *Glass-ceramic material for dental restoration and method for producing same*. US Patent 6527846 B1.

Berenbaum, R. and Brodie, I. (1959) Measurement of the tensile strength of brittle materials. *Br. J. Appl. Phys.,* 10, 281-287.

Binns, D. (1983) The Chemical and Physical Properties of Dental Procelains. In: McLean, J.W. (Ed.) *Dental Ceramics: Proceedings of the First International Symposium on Ceramics.* Chicago, Berlin, London, Rio de janeiro, Tokyo, Quintessence Pub. Co., pp. 41-82.

Bragg, W.H. and Bragg, W.L. (1924) *X-rays and Crystal Structure,* London, G.Bell and Sons, Ltd, pp. 1-30.

Brecker, S.C. (1956) Porcelain baked to gold: A new medium in prosthodontics. *J. Prosthet. Dent.,* 6 801-810.

Cahn, J.W. (1968) Spinodal decomposition. *Trans. metall. soc. of aime,* 242, 166-179.

Carter, C.B. and Norton, M.G. (2007) *Ceramic Materials: Science and Engineering,* Springer, pp. 360-362.

Cattell, M.J. (2003) *The crystallisation and flexural strength optimisation of leucite reinforced glass ceramics for dental applications*. PhD Thesis*,* Bart's and the London School of Medicine and Dentistry, Queen Mary University of London.

Cattell, M.J., Chadwick, T.C., Knowles, J.C. and Clarke, R.L. (2005) The crystallisation of an aluminosilicate glass in the K_2O-Al_2O_3-SiO_2 system. *Dent. Mater.,* 21 (9) 811-822.

Cattell, M.J., Chadwick, T.C., Knowles, J.C., Clarke, R.L. and Lynch, E. (2001) Flexural strength optimisation of a leucite reinforced glass ceramic. *Dent. Mater.,* 17 (1) 21-33.

Cattell, M.J., Chadwick, T.C., Knowles, J.C., Clarke, R.L. and Samarawickrama, D.Y. (2006) The nucleation and crystallisation of fine grained leucite glass-ceramics for dental applications. *Dent. Mater.,* 22 (10) 925-33.

Cattell, M.J., Clarke, R.L. and Lynch, E.J. (1997a) The transverse strength, reliability and microstructural features of four dental ceramics - Part I. *J. Dent.,* 25 (5) 399-407.

Cattell, M.J., Clarke, R.L. and Lynch, E.J.R. (1997b) The biaxial flexural strength and reliability of four dental ceramics - Part II. *J. Dent.,* 25 (5) 409-414.

Cattell, M.J., Knowles, J.C., Clarke, R.L. and Lynch, E. (1999) The biaxial flexural strength of two pressable ceramic systems. *J. Dent.,* 27 (3) 183-196.

Cheng, M., Chen, W. and Sridhar, K.R. (2003) Biaxial flexural strength distribution of thin ceramic substrates with surface defects. *Int. J. Solids and Struct.,* 40 (9) 2249-2266.

Cheung, K.C. and Darvell, B.W. (2002) Sintering of dental porcelain: effect of time and temperature on appearance and porosity. *Dent. Mater.,* 18 (2) 163-173.

Chiang, Y.-m., Birnie, D.P. and Kingery, W.D. (1996) *Physical Ceramics: Principles for Ceramic Science and Engineering,* J. Wiley, pp. 429-430.

Chong, K.H., Chai, J., Takahashi, Y. and Wozniak, W. (2002) Flexural strength of In-Ceram alumina and In-Ceram zirconia core materials. *Int. J. Prosthodont.,* 15 (2) 183-188.

Christian, J.W. (1975) *The Theory of Transformations in Metals and Alloys,* London, Pergamon Press, pp. 1-586.

Claus, H. (1989) The structure and microstructure of dental porcelain in relationship to the firing conditions. *Int. J. Prosthodont,* 2 (4) 376-384.

Craig, R.G. and Powers, J.M. (2002) *Restorative Dental Materials,* St. Louis, Mosby, pp. 2-15.

Cullity, B.D. and Stock, S.R. (2001) *Elements of x-ray diffraction,* New Jersey, Prentice Hall, pp. a:89-113, b:183, c:185-194.

Darvell, B.W. (1990) Uniaxial compression tests and the validity of indirect tensile strength. *J. Mater. Sci.: Mater. Med.,* 25 (2) 757-780.

Day, D.E. and Rindone, G.E. (1962) Properties of soda aluminosilicate glasses: I refractive index, density, molar refractivity and infrared absorption spectrum. *J. Am. Ceram. Soc.,* 45 489-496.

Deer, W.A., Howie, R.A. and Zussman, J. (1966) *An Introduction to the Rock-forming Minerals,* London, John Wiley and Sons Inc., pp. 276-288.

Deer, W.A., Howies, R.A., Zussman, J. and Wise, W.S. (2004) *Rock-forming Minerals,* Geological Society, pp. 304-315.

Demkina, L.I. (1960) A new system for calculating the coefficient of thermal expansion of silicate glasses. *Glass Ceram.,* 17 (10) 503-510.

Denry, I.L., Holloway, J.A. and Colijn, H.O. (2001) Phase transformations in a leucite-reinforced pressable dental ceramic. *Mater. Res.,* 54 351-359.

Denry, I.L., Holloway, J.A., Nakkula, R.J. and Walters, J.D. (2005) Effect of niobium content on the microstructure and thermal properties of fluorapatite glass-ceramics. *Journal of Biomedical Materials Research Part B: Applied Biomaterials,* 75B (1) 18-24.

Denry, I.L., J.R., M., Holloway J.A and SF, R. (1996) Effect of cubic leucite stabilisation on the flexural strength of feldspathic dental porcelain. *J. Dent. Res.,* 75 (12) 1928-1935.

Dietzel, A. (1942) The cation field strengths and their relation to devitrifying processes, to compound formation and to the melting points of silicates. *Z. Elektrochem. Angew. Phys. Chem.,* 48, 9-23.

Dong, J., Luthy, H., Wohlwend, A. and Schärer, P. (1992) Heat-pressed ceramics: technology and strength. *Int. J. Prosthodont,* 5 (1) 9-16.

Dorsch, P., Fesseler, A. and Pfeiffer, T. (1993) Influence of test conditions on biaxial strenth of dental ceramic. *J. Dent. Res.,* 76 980 (Abstr. No.331).

Dove, M.T., Cool, T., Palmer, D.C., Putnis, A., Salje, E.K.H. and Winkler, B. (1993) On the role of Al-Si ordering in the cubic-tetragonal phase transition in leucite. *Am. Mineral.,* 78 486-492.

Ediger, M.D., Angell, C.A. and Nagel, S.R. (1996) Supercooled Liquids and Glasses. *J. Phys. Chem.,* 100 (31) 13200-13212.

Engelmeier, R.L. (2003) The history and development of posterior denture teeth--Introduction, part I. *J. Prosthodont.,* 12 (3) 219-226.

English, S. and Turner, W.E.S. (1927) Relationship between chemichal composition and the thermal expansion of glasses. *J. Am. Ceram. Soc.,* 10 (8) 551-560.

Fairhurst, C.W., Anusavice, K.J., Hashinger, D.T., Ringle, R.D. and Twiggs, S.W. (1980) Thermal

expansion of dental alloys and porcelains. *J. Bio. Mater. Res.,* 14 (4) 435-446.

Fairhurst, C.W., Lockwood, P.E., Ringle, R.D. and Thompson, W.O. (1992) The effect of glaze on porcelain strength. *Dent. Mater.,* 8 (3) 203-207.

Ferracane, J.L. (2001) *Materials in Dentistry: Principles and Applications,* Lippincott Williams & Wilkins, pp. 161-162.

Fleming, G.J.P., El-Lakwah, S.F.A., Harris, J.J. and Marquis, P.M. (2004) The influence of interfacial surface roughness on bilayered ceramic specimen performance. *Dent. Mater.,* 20 (2) 142-149.

Fleming, G.J.P., Shaini, F.J. and Marquis, P.M. (2000) An assessment of the influence of mixing induced variability on the bi-axial flexure strength of dentine porcelain discs and the implications for laboratory testing of porcelain specimens. *Dent. Mater.,* 16 (2) 114-119.

Fleming, G.J.P., Shelton, R.M. and Marquis, P.M. (1999) The influence of clinically induced variability on the bi-axial fracture strength of aluminous core porcelain discs. *J. Dent.,* 27 (8) 587-594.

Fletcher, N.H. (1958) Size effect in heterogeneous nucleation. *J. Chem. Phys.,* 29 (3) 572-576.

Fletcher, N.H. (1959) Erratum: size effect in heterogeneous nucleation. *J. Chem. Phys.,* 31 (4) 1136-1137.

Fokin, V.M., Potapov, O.V., Zanotto, E.D., Spiandorello, F.M., Ugolkov, V.L. and Pevzner, B.Z. (2003) Mutant crystals in $Na_2O{\cdot}2CaO{\cdot}3SiO_2$ glasses. *J. Non-Cryst. Solids* 331 (1-3) 240-253.

Fokin, V.M., Yuritsyn, N.S. and Zanotto, E.D. (2005) Nucleation and Crystallisation Kinetics in Silicate Glasses: Theory and Experiment. In: Schmelzer, J. (Ed.) *Nucleation Theory and Applications.* Wiley-VCH, pp. 74-125.

Fokin, V.M. and Zanotto, E.D. (2000) Crystal nucleation in silicate glasses: the temperature and size dependence of crystal/liquid surface energy. *J. Non-Cryst. Solids* 265 (1-2) 105-112.

Garcia, F., Le Bolay, N. and Frances, C. (2002) Changes of surface and volume properties of calcite during a batch wet grinding process. *Chem. Eng. J.,* 85 (2-3) 177-187.

Gilman, P.S. and Benjamin, J.S. (1983) Mechanical alloying. *Annu. Rev. Mater. Sci.,* 13 (1) 279-300.

Giordano, R., Cima, M. and Pober, R. (1995) Effect of surface finish on the flexural strength of feldspathic and aluminous dental ceramics. *Int. J. Prosthodont,* 8 (4) 311-9.

Goldschmidt, V.M. (1926) Geochemische Verteilungsgesetze der Elemente 7. Die Gesetze der

Krystallochemie." *Naturvidenskapelig Klasse I, Skrifter* 89.

Goldstein, J.I., Newbury, D.E., Echlin, P., Joy, D.C., Fiori, C. and Lifshin, E. (1992) *Scanning Electron Microscopy and X-Ray Microanalysis : A Text for Biologists, Materials Scientists, and Geologists* New York Plenum Press, pp. a: 1-33, b: 123-299.

Gorman, C.M., McDevitt, W.E. and Hill, R.G. (2000) Comparison of two heat-pressed all-ceramic dental materials. *Dent. Mater.,* 16 (6) 389-95.

Guazzato, M., Albakry, M., Ringer, S.P. and Swain, M.V. (2004a) Strength, fracture toughness and microstructure of a selection of all-ceramic materials. Part I. Pressable and alumina glass-infiltrated ceramics. *Dent. Mater.,* 20 (5) 441-448.

Guazzato, M., Albakry, M., Ringer, S.P. and Swain, M.V. (2004b) Strength, fracture toughness and microstructure of a selection of all-ceramic materials. Part II. Zirconia-based dental ceramics. *Dent. Mater.,* 20 (5) 449-456.

Guo, W., Iasonna, A., Magini, M., Martelli, S. and Padella, F. (1994) Synthesis of amorphous and metastable $Ti_{40}Al_{60}$ alloys by mechanical alloying of elemental powders. *J. Mater. Sci.: Mater. Med.,* 29 (9) 2436-2444.

Guttorm, T., Finn, S.B., Cox, G.J., Bodecker, C.F. and Shaw, J.H. (1952) *A survey of the literature of dental caries* Washington D.C., National Research Council (U.S.). Committee on Dental Health, pp. 168-172.

Höland, W., Frank, M. and Rheinberger, V. (1995) Surface crystallisation of leucite in glasses. *J. Non-Cryst. Solids,* 180 (2-3) 292-307.

Höland, W., Rheinberger, V. and Schweiger, M. (2001) Nucleation and Crystallisation Phenomena in Glass-Ceramics. *Adv. Eng. Mater.,* 3 (10) 768-774.

Höland, W., Rheinberger, V. and Schweiger, M. (2003) Control of Nucleation in Glass Ceramics. *Philoso.Trans.: Math. Phys. Eng. Sci.,* 361 (1804) 575-589.

Höland, W., Schweiger, M., Frank, M. and Rheinberger, V. (2000) A comparison of the microstructure and properties of the IPS Empress 2 and the IPS Empress glass-ceramics. *J. Biomed. Mater. Res.,* 53 (4) 297-303.

Harper, H., James, P.F. and McMillan, P.W. (1970) Crystal nucleation in lithium silicate glasses. *Discuss. Faraday Soc.,* 50 206-213.

Hashimoto, S. and Yamaguchi, A. (2002) Size Control of Spherical Leucite Crystals. *J. Ceram. Soc. Jpn.,* 110 (1) 27-31.

Haynes, J.M. (1986) Porosity: Characteristics and Techniques of Investigation. In: Bever, M.B. (Ed.) *Encyclopedia of Materials Science and Engineering.* Oxford, Pergamon Press, pp. 3830-3839.

He, L.H. and Swain, M.V. (2008) Understanding the mechanical behaviour of human enamel from its structural and compositional characteristics. *J. Mech. Behav. Biomed. Mater.,* 1 (1) 18-29.

Heffernan, M.J., Aquilino, S.A., Diaz-Arnold, A.M., Haselton, D.R., Stanford, C.M. and Vargas, M.A. (2002) Relative translucency of six all-ceramic systems. Part II: Core and veneer materials. *J. Prosthet. Dent.,* 88 (1) 10-15.

Henry, J. and Hill, R.G. (2004) Influence of alumina content on the nucleation crystallization and microstructure of barium fluorphlogopite glass-ceramics based on $8SiO_2{\cdot}YAl_2O_3{\cdot}4MgO_2{\cdot}MgF_2{\cdot}BaO$, Part I Nucleation and crystallisation behaviour. *J. Mater. Sci.,* 39 (7) 2499-2507.

Hermansson, L. and Carlsson, R. (1976) High and low temperature forms of leucite. In: *Proceedings of the Eighth international symposium on the reactivity of solids*, Gothenberg, Sweden, Swedish Institute for Silicate Research. pp 541-545.

Hermansson, L. and Carlsson, R. (1978) Crystallisation of the glassy phase in whitewares. *Trans. J. Brit. Ceram. Soc.,* 77 (2) 32-35.

Hill, R. and Gilbert, P. (1993) High-temperature dynamic mechanical thermal analysis of a lithium zinc silicate glass-ceramic. *J. Am. Ceram. Soc.,* 76 (2) 417-425.

Hing, P. and McMillan, P.W. (1973) A transmission electron microscope study of glass-ceramics. *J. Mater. Sci.,* 8 (3) 340-348.

Hlaváč, J. (1983) *The Technology of Gass and Ceramics: An Introduction,* Amsterdam, Oxford, New York, Elsevier Scientific Pub. Co., pp. 262-266.

Hobo, S. and Iwata, T. (1985) Castable apatite ceramics as a new biocompatible restorative material. 1. theoretical considerations. *Quintessence Int.,* 2 135-141.

Hodson, J.T. (1959) Some physical properties of three dental porcelains. *J. Prosthet. Dent.,* 9 325-335.

Hoffman, J.D. (1958) Thermodynamic driving force in nucleation and growth processes. *J. Chem. Phys.,* 29 (5) 1192-1193.

Hopkins, K. (1981) A method of strengthening aluminous porcelain jacket crowns. *Br. Dent. J.,* 151 (7) 225-227.

Huggins, M.L. and Sun, K.H. (1943) Calculation of Dentisty and Optical Constants of a glass from its composition in weight. *J. Am. Ceram. Soc.,* 26 (1) 4-11.

Hummert, T., Barghi, N. and Berry, T. (1991) Effect of fitting adjustments on compressive strength of a new foil crown system. *J. Prosthet. Dent.,* 66 (2) 177-181.

ISO Standrad 6872 (2008) International Standard for Dentistry - Ceramic materials.

Jackson, K.A. (1967) *Progress in Solid State Chemistry* Oxford, Pergamon Press, pp. 53-80.

Jager, N.d., Feilzer, A.J. and Davidson, C.L. (2000) The influence of surface roughness on porcelain strength. *Dent. Mater.,* 16 (6) 381-388.

Jambi, S.M., Bubb, N.L. and Wood, D.J. (2007) Effect of zirconia additions to novel machinable mica based glass-ceramics. In: *IADR/AADR/CADR 85th General Session and Exhibition (March 21-24, 2007)* New Orleans, LA, USA, Abstr. No. 389.

James, P.F. (1975) Liquid-phase separation in glass-forming systems. *J. Mater. Sci.,* 10 (10) 1802-1825.

James, P.F. (1982) Nucleation in Glass-forming Systems. A review. In: Simmons, J.H., Uhlmann, D.R. and Beall, G.H. (eds.) *Advances in Ceramics. Nucleation and Crystallisation of Glasses, 83rd Annual Meeting of the American Ceramic Society.* Washington, D.C, American Ceramic Society, pp. 14-48.

James, P.F. (1985) Kinetics of crystal nucleation in silicate glasses. *J. Non-Cryst. Solids,* 73 517-540.

Jenkins, R. and Snyder, R.L. (1996) *Introduction to X-Ray Powder Diffractometry* New York, Chichester, Wiley pp. a:25, b:369-387.

Jones, D.W. (1985) Development of dental ceramics. An historical perspective. *Dent. Clin. North Am.,* 29 (4) 621-644.

Jones, G.O. (1956) *Glass,* London, Methuen, Wiley, pp. 1-34.

Karamanov, A. and Pelino, M. (1999) Evaluation of the degree of crystallisation in glass-ceramics by density measurements. *J. Euro. Ceram. Soc.,* 19 (5) 649.

Kelly, J.R. (1997) Ceramics in restorative and prosthetic dentistry. *Annu. Rev. Mater. Sci.,* 27 (1) 443-468.

Kelly, J.R., Nishimura, I. and Campbell, S.D. (1996) Ceramics in dentistry: historical roots and current perspectives. *J. Prosthet. Dent.,* 75 (1) 18-32.

Khater, G.A. and Idris, M.H. (2007) Role of TiO_2 and ZrO_2 on crystallising phases and microstructure in Li, Ba aluminosilicate glass. *Ceram. Int.,* 33 (2) 233-238.

Kingery, W.D., Bowen, H.K. and Uhlmann, D.R. (1976) *Introduction to Ceramics,* Wiley, New York, pp. 329-379.

Kirstein, A.F. and Woolley, R.M. (1967) Symmetrical bending of thin circular elastic plates on equally spaced point supports. *J. Res. Nat. Bur. Stand. - C.,* 71 (1) (C)1-10.

Kissinger, H.E. (1956) Variation of peak temperature with heating rate in differential thermal analysis. *J. Res. Nat. Bur. Stand.,* 57 (4) 217-221.

Klaus, I., Herbstman, W. and Lopez, J. (1986) *Dental compositions, fired dental porcelains and processes for making and using same*. US 4604059

Koch, C.C. (1989) Materials synthesis by mechanical alloying. *Annu. Rev. Mater. Sci.,* 19 (1) 121-143.

Koch, C.C. (1991) Mechanical milling and alloying. *Mater. Sci. Technol.,* 15 193-245.

Kon, M., Kawano, F., Asaoka, K. and Matsumoto, N. (1994) Effect of leucite crystals on the strength of glassy porcelain. *Dent. Mater. J.,* 13 (2) 138-47.

Kuczynski, G.C. (1949) Study of the sintering of glass. *J. Appl. Phys.,* 20 (12) 1160-1163.

Kulp, P.R., Lee, P.W. and Fox, J.E. (1961) An impact test for dental porcelain. *J. Dent. Res.,* 40 (6) 1136-1141.

Kurdvk, B. (1999) Giuseppangelo Fonzi: Industrial Fabrication Promoter of Porcelain Prosthetics. *J. Hist. Dent.,* 47 (2) 79-82.

Lange, F.F. (1984) Sinterability of agglomerated powders. *J. Am. Ceram. Soc.,* 67 (2) 83-89.

Larsen, A.C. and Von Dreele, R.B. (2004) General Structure Analysis System, GSAS, LAUR 86-748. *Los Alamos National Laboratory,*

Lee, H.H., Kon, M. and Asaoka, K. (1997) Influence of modification of Na_2O in a glass matrix on the strength of leucite-containing porcelains. *Dent. Mater. J.,* 16 (2) 134-143.

Müller, R., Zanotto, E.D. and Fokin, V.M. (2000) Surface crystallisation of silicate glasses: nucleation sites and kinetics. *J. Non-Cryst. Solids* 274 (1-3) 208-231.

MacCulloch, W.T. (1968) Advances in dental ceramics. *Br. Dent. J.,* 124 (8) 361-365.

Mackenzie, J.K. and Shuttleworth, R. (1949) A phenomenological theory of sintering. *Proc. Phys. Soc. London, Sect. B* 62 (12) 833-852.

Mackert, J.R. (1988) Effects of Thermally Induced Changes on Porcelain-Metal Compatibility. In: Preston, J.D. (Ed.) *Perspectives in Dental Ceramics, Proceedings of the Fourth International Symposium on Ceramics.* Chicago, Quintessence, pp. 53-64.

Mackert, J.R. (2000) High-temperature X-ray diffraction measurement of sanidine thermal expansion. *J. Dent. Res.,* 79 (8) 1590-1595.

Mackert, J.R., Butts, M.B., Morena, R. and Fairhurst, C.W. (1986) Phase changes in a leucite-containing dental porcelain frit. *J. Am. Ceram. Soc.,* 69 (4) C-69-72.

Mackert, J.R. and Evans, A.L. (1991) Quantitative X-ray Diffraction determination of leucite thermal instability in dental porcelain. *J. Am. Ceram. Soc.,* 74 (2) 450-453.

Mackert, J.R. and Evans, A.L. (1993) Multiple firing effect on microcrack density in dental porcelain. *J. Dent. Res. (abstract 1276),* 72 263.

Mackert, J.R., Twiggs, S.W., Russell, C.M. and Williams, A.L. (2001) Evidence of a critical leucite particle size for microcracking in dental porcelains. *J. Dent. Res.,* 80 (6) 1574-1579.

Mackert, J.R. and Williams, A.L. (1996) Microcracks in dental porcelain and their behavior during multiple firing. *J. Dent. Res.,* 75 (7) 1484-1490.

Marotta, A., Buri, A. and Branda, F. (1980) Surface and bulk crystallisation in non-isothermal devitrification of glasses. *Thermochim. Acta,* 40 397-403.

Matusita, K. and Sakka, S. (1979) Kinetic study of the crystallisation of glass by Differential Scanning Calorimetry. *Phys. Chem. Glasses* 20 (4) 81-84.

Matusita, K. and Sakka, S. (1980) Kinetic study of crystallisation of glass by differential thermal analysis--criterion on application of Kissinger plot. *J. Non-Cryst. Solids* 38-39 (Part 2) 741-746.

Matusita, K., Sakka, S. and Matsui, Y. (1975) Determination of the activation energy for crystal growth by differential thermal analysis *J. Mater. Sci.,* 10 (6) 961-966.

Maurer, R.D. (1962) Crystal nucleation in a glass containing titania. *J. Appl. Phys.,* 33 (6) 2132-2139.

Mazzi, F., Galli, E. and Gottardi, G. (1976) The crystal structure of tetragonal leucite. *Am. Mineral.,* 61 (1-2) 108-115.

McLaughlin, J.R. (1999) Bead size and mill efficiency-producing inorganic nanoparticles by milling with ultrafine ceramic beads. *Ceram. Int.,* 149 (13) 34,36,38-40.

McLean, J.W. (2001) Evolution of dental ceramics in the twentieth century. *J. Prosthet. Dent.,* 85 (1) 61-66.

McLean, J.W. and Hughes, T.H. (1965) The reinforcement of dental porcelain with ceramic oxides. *Br. Dent. J.,* 119 (6) 251-267.

McLean, J.W. and Sced, I.R. (1976) The bonded alumina crown. 1. The bonding of platinum to aluminous dental porcelain using tin oxide coatings. *Aust. Dent. J.,* 21 (2) 119-127.

McMillan, P.W. (1974) In: *Proceedings of the Xth International Congress on Glass* Kyoto, pp 1-2.

McMillan, P.W. (1979) *Glass-ceramics,* London, Academic Press, pp. a:1-60, b:97-142, c:61-63, d:155-244.

Metzler, K.T., Woody, R.D., Miller Iii, A.W. and Miller, B.H. (1999) In vitro investigation of the wear of human enamel by dental porcelain. *J. Prosthet. Dent.,* 81 (3) 356-364.

Miyata, N. (1986) Dispersion toughening of ceramics. *Ceram. Jap.,* 21 (7) 605-612.

Miyata, N. and Jinno, H. (1972) Theoretical approach to the fracture of two-phase glass-crystal composites. *J. Mater. Sci.,* 7 (9) 973-982.

Morrell, R. (1999) Biaxial flexural strength testing of ceramic materials. Measurement Good Practice Guide National Physical Laboratory, no. 12, 1-48.

Morrell, R., McCormick, N.J., Bevan, J., Lodeiro, M. and Margetson, J. (1999) Biaxial disc flexure: modulus and strength testing. *Br. Ceram. Trans.,* 98 (5) 234-240.

Novotna, M., Satava, V., Kostka, P., Lezal, D., Maixner, J. and Klouzkova, A. (2004) Synthesis of leucite for application in dentistry. *Glass Technol.,* 45 (2) 105-107.

Oh, S.C., Dong, J.K., Lüthy H and P, S. (2000) Strength and microstructure of IPS Empress 2 glass-ceramic after different treatments. *Int. J. Prosthodont,* 13 (6) 468-472.

Ohyama, T., Yoshinari, M. and Oda, Y. (1999) Effects of cyclic loading on the strength of all-ceramic materials. *Int. J. Prosthodont.,* 12 (1) 28-37.

Okada, K., Ono, Y., Kameshima, Y., Nakajima, A. and MacKenzie, K.J.D. (2007) Simultaneous uptake of ammonium and phosphate ions by compounds prepared from paper sludge ash. *J. Hazard. Mater.,* 141 (3) 622-629.

[online] available from: http://www.webmineral.com/data/Leucite.shtml [Accessed 20th Oct 2006].

Ong, J.L., Farley, D.W. and Norling, B.K. (2000) Quantification of leucite concentration using X-ray diffraction. *Dent. Mater.,* 16 (1) 20-25.

Padella, F., Paradiso, E., Burgio, N., Magini, M., Martelli, S., Guo, W. and Iasonna, A. (1991) Mechanical alloying of the Pd-Si system in controlled conditions of energy transfer. *J. Less Common Met.,* 175 (1) 79-90.

Palin, W.M., Fleming, G.J.P., Trevor Burke, F.J., Marquis, P.M. and Randall, R.C. (2003) The reliability in flexural strength testing of a novel dental composite. *J. Dent.,* 31 (8) 549-557.

Palmer, D.C., Putnis, A. and Salje, E.K.H. (1988) Twinning in tetragonal leucite. *Phys. Chem. Miner. ,* 16 (3) 298-303.

Park, J.-S., Kim, Y., Shin, H., Moon, J.-H. and Lim, W. (2008) Calcium zinc borosilicate glass with high thermal expansion coefficient for LTCC applications. *J. Am. Ceram. Soc.,* 91 (11) 3630-3633.

Park, Y.J., Moon, S.O. and Heo, J. (2003) Crystalline phase control of glass-ceramics obtained

from sewage sludge fly ash. *Ceram. Int.,* 29 (2) 223-227.

Pauling, L. (1932) The nature of the chemical bond. Iv. the energy of single bonds and the relative electronegativity of atoms. *J. Am. Ceram. Soc.,* 54 (9) 3570-3582.

Piché, P.W., O'Brien, W.J., Groh, C.L. and Boenke, K.M. (1994) Leucite content of selected dental porcelains. *J. Biomed. Mater. Res.,* 28 (5) 603-609.

Piddock, V., Marquis, P.M. and Wilson, H.J. (1986) Comparison of the strengths of aluminous porcelain fired on to platinum and palladium foils. *J. Oral Rehabil.,* 13 (1) 31-37.

Pisciella, P. and Pelino, M. (2008) Thermal expansion investigation of iron rich glass-ceramic. *J. Eur. Ceram. Soc.,* 28 (16) 3021-3026.

Postek, M., Howard, K., Johnson, A. and McMichael, K. (1980) *Scanning Electron Microscopy,* Ladd Research Industries, pp. 79-96.

Postek, M.T. (1980) Theory of Scanning Electron Microscopy. *Scanning Electron Microscopy : A Student's Handbook.* Ladd Research Industries, pp. 13-44.

Priven, A.I. (1986) Calculating batch weights with a programmable microcalculator. *Glass Ceram.,* 43 (11) 488-491.

Priven, A.I. (1988) Computation of refractive index of silicate glasses according to their composition and density. *Fizika i Khimiya Stekla,* 14 (4) 589-594.

Priven, A.I. (2004) General method for calculating the properties of oxide glasses and glass forming melts from their composition and temperature. *Glass Technol.,* 45 (6) 244-254.

Priven, A.I. and Mazurin, O.V. (2003) Comparison of methods used for the calculation of density, refractive index and thermal expansion of oxide glasses. *Glass Technol.,* 44 (4) 156-166.

Puclin, T., Kaczmarek, W.A. and Ninham, B.W. (1995) Mechanochemical processing of $ZrSiO_4$. *Mater. Chem. Phys.,* 40 (2) 73-81.

Putnis, A. (1992) *Introduction to Mineral Sciences,* London, Cambridge University Press, pp. 223-235.

Rahaman, M.N. (1995) *Ceramic Processing and Sintering,* New York, Basel, Hongkong, Marcel Dekker, Inc, pp. a: 46-50, b: 264-330, c: 331-347.

Rahaman, M.N. (2003) Synthesis of Powder. *Ceramic processing and sintering.* 2nd ed. New York, Basel, Hongkong, CRC Press, pp. 425-468.

Rasmussen, S., McLaren, C.I. and O'Brien, W. (2004) The effect of cesium-containing leucite additions on the thermal and mechanical properties of two leucite-based porcelains. *J. Biomed. Mater. Res. B: Appl. Biomater.,* 69B (2) 195-204.

Rasmussen, S.T., Groh, C.L. and O'Brien, W.J. (1998) Stress induced phase transformation of a cesium stabilized leucite porcelain and associated properties. *Dent. Mater.,* 14 (3) 202-211.

Rawson, H. (1956) In: *Proceedings of the Fourth International Glass Congress, Paris, (Travaux du IVe Congrès International du Verre). Imprimerie Chaix, Pairs, 1957*., pp 62–69.

Ray, C.S. and Day, D.E. (1990) Determining the nucleation rate curve for lithium disilicate glass by Differential Thermal Analysis. *J. Am. Ceram. Soc.,* 73 (2) 439-442.

Ray, C.S., Fang, X. and Day, D.E. (2000) New method for determining the nucleation and crystal-growth rates in glasses. *J. Am. Ceram. Soc.,* 83 (4) 865-872.

Ray, C.S., Huang, W. and Day, D.E. (1991) Crystallisation Kinetics of a Lithia-Silica Glass: Effect of Sample Characteristics and Thermal Analysis Measurement Techniques. *J. Am. Ceram. Soc.,* 74 (1) 60-66.

Ray, C.S., Yang, Q., Huang, W.-h. and Day, D.E. (1996) Surface and Internal Crystallisation in Glasses as Determined by Differential Thermal Analysis. *J. Am. Ceram. Soc.,* 79 (12) 3155-3160.

Reed, J.S. (1995) *Principles of Ceramics Processing,* New York, Chichester, Brisbane, Toronto, Singapore, Wiley & Sons, Inc., pp. a: 418-442, b: 583-619

Rekow, D. and Thompson, V. (2007) Engineering long term clinical success of advanced ceramic prostheses. *Journal of Materials Science: Materials in Medicine,* 18 (1) 47-56.

Riffel, M. and Schilz, J. (1998) Mill setting and microstructural evolution during mechanical alloying of Mg2Si. *J. Mater. Sci.: Mater. Med.,* 33 (13) 3427-3431.

Ritter, J.E. (1986) Fracture: Reliability Criteia for Brittle Materials. In: Bever, M.B. (Ed.) *Encyclopedia of materials science and engineering.* Oxford, Pergamon Press, pp. 1852-1858.

Rouf, M.A., Hermansson, L. and Carlsson, R. (1978) Crystallisation of glasses in the primary phase field of leucite in the $K_2O{\cdot}Al_2O_3{\cdot}SiO_2$ system. *Trans. J. Brit. Ceram. Soc.,* 77 36-39.

Schairer, J.F. and Bowen, N.L. (1955) The system K_2O-Al_2O_3-SiO_2. *Am. J. Sci.,* 253 (12) 681-746.

Schmelzer, J., Pascova, R., J., M. and Gutzow, I. (1993) Surface-induced devitrification of glasses: the influence of elastic strains. *J. Non-Cryst. Solids* 162 (1) 26-39.

Schmelzer, J.W.P., Potapov, O.V., Fokin, V.M., Müller, R. and Reinsch, S. (2004) The effect of elastic stress and relaxation on crystal nucleation in lithium disilicate glass. *J. Non-Cryst. Solids* 333 (2) 150-160.

Scholze, H. and Lakin, M.J. (1991) Calculation Based on Composition. *Glass: nature, structure, and properties.* Springer-Verlag, pp. 189-190.

Schweiger, M. (2003) Control of nucleation in glass ceramics. *Philos. Trans. R. Soc. London, Ser. A,* 361 (1804) 575-589.

Seghi, R.R., Denry, I.L. and Rosenstiel, S.F. (1995) Relative fracture toughness and hardness of new dental ceramics. *J. Prosthet. Dent.,* 74 (2) 145-50.

Seitz, F. and Turnbull, D. (1956) *Solid State Physics,* New York, Academic Press, pp. 226-306.

Selvaraj, U., Komarneni, S. and Roy, R. (1991a) Seeding effects on crystallisation temperatures of cordierite glass powder. *J. Mat. Sci.,* 26 (13) 3689-3692.

Selvaraj, U., Liu, C.L., Komarneni, S. and Roy, R. (1991b) Epitaxial crystallisation of seeded albite glass. *J. Am. Ceram. Soc.,* 74 (6) 1378-1381.

Shareef, M.Y., Noort, R., Messer, P.F. and Piddock, V. (1994) The effect of microstructural features on the biaxial flexural strength of leucite reinforced glass-ceramics. *J. Mater. Sci.: Mater. Med.,* 5 (2) 113-118.

Shartsis, L., Spinner, S. and Capps, W. (1952) Density, expansivity, and viscosity of molten alkali silicates. *J. Am. Ceram. Soc.,* 35 (6) 155-160.

Shelby, J.E. (1976) Thermal expansion of mixed-alkali silicate glasses. *J. Appl. Phys.,* 47 (10) 4489-4496.

Shermer, H.F. (1956) Thermal expansion of binary alkali silicate glasses. *J. Res. Nat. Bur. Stand.,* 57 (2) 97-101.

Shetty, D.K., Rosenfield, A.R., Duckworth, W.H. and Held, P.R. (1983) A biaxial-flexure test for evaluating ceramic strengths. *J. Am. Ceram. Soc.,* 66 (1) 36-42.

Shetty, D.K., Rosenfield, A.R., McGuire, P., Bansal, G.K. and Duckworth, W.H. (1980) Biaxial flexure tests for ceramics. *Am. Ceram. Soc. Bull.,* 59 1193-1197.

Skinner, E.W. and Phillips, R.W. (1982) *Skinner's Science of Dental Materials,* East Sussex, Saunders, pp. 513-519.

Smith, B.G.N. (1986) *Planning and making crowns and bridges,* London, Martin Dunitz Ltd, pp. 10-17.

Smykatz-Kloss, W. (1974) *Differential Thermal Analysis: Application and Results in Mineralogy,* Springer-Verlag, pp. 5-10.

Stanworth, J.E. (1946) The structure of glass *J. Soc. Glass Technol.,* 30 54-66.

Stanworth, J.E. (1971) Oxide glass formation from the melt. *J. Am. Ceram. Soc.,* 54 (1) 61-63.

Stevels, J.M. (1954) Glass considered as a polymer. *Glass Ind.,* 35 (2) 69-72.

Stookey, S.D. (1959) Catalysed crystallisation of glass in theory and practice. *Ind. Eng. Chem.,* 51 (7) 805-808.

Stookey, S.D. (1960) *Method of making ceramics and product thereof*. US Patent 2920971.

Strnad, Z.C. (1986) *Glass-ceramic Materials : Liquid Phase Separation, Nucleation and Crystallization in Glasses,* Amsterdam, Oxford, New York, Tokyo, Elsevier, pp. 9-75.

Sukumaran, V.G. and Bharadwaj, N. (2006) Ceramics in dental applications. *Trends Biomater. Artif. Organs.,* 20 (1) 7-11.

Sun, K.-H. (1947) Fundamental condition of glass formation. *J. Am. Ceram. Soc.,* 30 (9) 277-281.

Suryanarayana, C. (2001) Mechanical alloying and milling. *Progress in Materials Science,* 46 (1-2) 1-184.

Suryanarayana, C. (2004) Process Variables in Milling. *Mechanical alloying and milling.* CRC Press, pp. 59-82.

Suzuki, S. (1999) Antagonistic enamel wear of cerinate pressable ceamic. University of Alabama School of Dentistry.

Szegvari, A. and Yang, M. (1984) Attritor grinding and dispersing equipment. no. 1-8.

Takahashi, K. (1953) Thermal expansion coefficients and sructure of glass. *J. Soc. Glass Technol.,* 37 175.

Takahashi, K. and Yoshio, T. (1973) Thermodynamic quantities of alkali silicates in the temperature range from 25^{o}C to melting point. *Yogyo Kyokai-Shi,* 81 524-533.

Tamman, G. (1925) *The States of Aggregation,* New York, D.Van Nostrand and Co., pp. 234-236.

Theocharopoulos, A., Chen, X. and Cattell, M.J. (2009) Wear testing of heat pressed glass-ceramic A (4hr A) and Ceramco 3 against human enamel. London.

Thompson, J.Y., Anusavice, K.J., Balasubramaniam, B. and Mecholsky, J.J. (1995) Effect of micmcracking on the fracture toughness and fracture surface fractal dimension of lithia-based glass-ceramics. *J. Am. Ceram. Soc.,* 78 (11) 3045-3049.

Timoshenko, S. and Woinowsky-Krieger, S. (1959) *Theory of Plates and Shells,* New York, McGraw-Hill, pp. 70-71.

Tošić, M.B., Dimitrijević, R.Ž. and Mitrović, M.M. (2002) Crystallisation of leucite as the main phase in glass doped with fluorine anions. *J. Mater. Sci.,* 37 2293-2303.

Tošić, M.B., Mitrović, M.M. and Dimitrijević, R.Ž. (2000) Crystallisation of leucite as the main

phase in aluminosilicate glass with low fluorine content. *J. Mater. Sci.,* V35 (14) 3659-3667.

Tsetsekou, A., Papadopoulos, T. and Adamopoulos, O. (2002) Microstructure effect on the properties of a commercial low-fusing dental porcelain. *J. Mater. Sci.: Mater. Med.,* 13 (4) 407-416.

Tulyaganov, D.U., Ribeiro, M.J. and Labrincha, J.A. (2002) Development of glass-ceramics by sintering and crystallisation of fine powders of calcium-magnesium-aluminosilicate glass. *Ceram. Int.,* 28 (5) 515-520.

Turnbull, D. (1969) Under what conditions can a glass be formed? *Contemp. Phys.,* 10 473.

Turnbull, D. and Cohen, M.H. (1958) Concerning reconstructive transformation and formation of glass. *J. Chem. Phys.,* 29 (5) 1049-1054.

Turnbull, D. and Fisher, J.C. (1949) Rate of nucleation in condensed systems. *J. Chem. Phys. ,* 17 (1) 71-73.

Uhlmann, D.R. and Yinnon, H. (1983) *The Formation of Glass,* New York Academic Press, pp. 1-44.

Vargin, V.V. (1967) *Technology of Enamels,* London, Maclaren and Sons Ltd, pp. 3-12.

Vergano, P.J., Hill, D.C. and Uhlmann, D.R. (1967) Thermal expansion of feldspar glasses. *J. Am. Ceram. Soc.,* 50 (1) 59-60.

Vines, R.F. and Semmelman, J.O. (1957) Densification of dental porcelain *J. Dent. Res.,* 36 (6) 950-956.

Vogel, W. (1985) *Chemistry of Glass,* Columbus, Ohio, American Ceramic Society, pp. 33-47.

Wagner, W.C. and Chu, T.M. (1996) Biaxial flexural strength and indentation fracture toughness of three new dental core ceramics. *J Prosthet. Dent.,* 76 (2) 140-144.

Wang, P., Yu, L., Xiao, H., Cheng, Y. and Lian, S. (2009) Influence of nucleation agents on crystallisation and machinability of mica glass-ceramics. *Ceram. Int.,* In Press, Corrected Proof

Warren, B.E. (1933) X-Ray Diffraction of vitreous silica. *Z. Kristallogr.Mineralog.Petrogr.,* 86 349-358.

Weinberg, M.C. (1991) Interpretation of DTA experiments used for crystal nucleation rate determinations. *J. Am. Ceram. Soc.,* 74 (8) 1905-1909.

Weinstein, M., Katz, S. and Weinstein, A.B. (1962) *Fused porcelain-to-metal teeth*. US Patent 3,052,982.

Weitz, G. (1972) Die Struktur des Sanidins bei verschiedenen Ordnungsgraden. *Z. Kristallogr.,* 136 418-426.

Weyl, W.A. (1951) Coloured Glasses. *J. Soc. Glass Technol.,* 89.

Williams, P.D. and Smith, D.C. (1971) Measurement of the tensile strength of dental restorative materials by use of a diametral compression test. *J. Dent. Res.,* 50 (2) 436-442.

Williamson, R.T., Kovarik, R.E. and Mitchell, R.J. (1996) Effects of grinding, polishing, and overglazing on the flexure strength of a high-leucite feldspathic porcelain. *Int. J. Prosthodont.,* 9 (1) 30-7.

Winkelmann, A. and Schott, O. (1894) Expansion coefficients of glazes. *Ann. Physik.,* 51 730.

Wohlwend, A. and Schärer, P. (1990) Die Empress Technik. Ein neues Verfahren zur Herstellung von vollkeramischen Kronen, Inlays und Facetten. *Quintessenz Zahntech,* 16 (8) 966-78.

Wohlwend, A. and Schairer, P. (1990) The Empress technique: a new technique for the fabrication of full ceramic crowns, inlays, and veneers (in German). *Quitessenz Zahntech* 16 966-978 (English reprints, 1991).

Xu, X.J., Ray, C.S. and Day, D.E. (1991) Nucleation and crystallisation of $Na_2O \cdot 2CaO \cdot 3SiO_2$ glass by Differential Thermal Analysis. *J. Am. Ceram. Soc.,* 74 (5) 909-914.

Yang, J.P., Wu, J.Q., Rao, P.G., Xin, C.F. and Chen, D.D. (2005) The Influence of nano-sized leucite on porcelain properties. *Key Eng. Mater.,* 280-283 1605-1608.

Yilmaz, H., Aydin, C. and Gul, B.E. (2007) Flexural strength and fracture toughness of dental core ceramics. *J. Prosthet. Dent.,* 98 (2) 120-128.

Yu, B., Liang, K. and Gu, S. (2002) Effect of ZrO_2 on crystallisation of $CaO\text{-}P_2O_5\text{-}SiO_2$ glasses. *Ceram. Int.,* 28 (6) 695-698.

Zachariasen, W.H. (1932) The atomic arrangement in glass. *J. Am. Chem. Soc.,* 54 (10) 3841-3851.

Zarzycki, J. (1970) Phase-separated systems. *Faraday Soc.,* 50 122-134.

Zarzycki, J. (1991) *Glasses and the Vitreous State,* Cambridge, New York, Port Chester, Melbourne, Sydney, Cambridge University Press, pp. a:11-29, b:156-166, c:167-226.

Zdaniewski, W. (1975) DTA and X-Ray Analysis study of nucleation and crystallisation of $MgO\text{-}Al_2O_3\text{-}SiO_2$ glasses containing ZrO_2, TiO_2, and CeO_2. *J. Am. Ceram. Soc.,* 58 (5-6) 163-169.

Zeng, K., Oden, A. and Rowcliffe, D. (1996) Flexure tests on dental ceramics. *Int. J. Prosthodont.,* 9 (5) 434-9.

Zeng, K., Oden, A. and Rowcliffe, D. (1998) Evaluation of mechanical properties of dental ceramic core materials in combination with porcelains. *Int. J. Prosthodont,* 11 (2) 183-9.

Zhang, B., Qian, F., Duan, X. and Wu, B. (2002) Study on some mechanism of leucite microcrystallisation to reinforce dental glass ceramics. *Hua Xi Kou Qiang Yi Xue Za Zhi,* 37 (4) 260-264.

Zhang, B., Qian, F., Duan, X. and Wu, B. (2009) Relationship between leucite content and compressive strength of K_2O-Al_2O_3-SiO_2 system dental glass ceramics. *Journal of Wuhan University of Technology--Materials Science Edition,* 24 (1) 72-74.

Zhang, Y., Li, B., Rao, P., Lu, M. and Wu, J. (2007a) Seeded crystallisation of leucite. *J. Am. Ceram. Soc.,* 90 (5) 1615-1618.

Zhang, Y., Lv, M., Chen, D. and Wu, J. (2006) Leucite crystallisation kinetics with kalsilite as a transition phase. *Mater. Lett. ,* 61 (14-15) 2978-2981.

Zhang, Y., Lv, M., Rao, P., Shui, A. and Wu, J. (2007b) Quantitative XRD analysis of hydrothermally-derived leucite content in dental porcelain ceramics. *J. Ceram. Soc. Jpn.,* 115 329-332.

Zhang, Y., Qu, C., Rao, P., Lv, M. and Wu, J. (2007c) Nanocrystalline seeding effect on the crystallisation of two leucite precursors. *J. Am. Ceram. Soc.,* 90 (8) 2390-2398.

Zhang, Y., Rao, P., Lu, M. and Wu, J. (2008) Mechanical properties of dental porcelain with different leucite particle sizes. *J. Am. Ceram. Soc.,* 91 (2) 527-534.

Zidan, O., Asmussen, E. and Jorgensen, K.D. (1980) Tensile strength of restorative resins. *Eur. J. Oral. Sci.,* 88 (3) 285-290.

9 APPENDIX

9.1 Appendix

Table 9.1: Appen Factors for glass properties prediction.

Oxides	Appen Factors			Fusion Temperature (ºC, Winkelmann and Schott)
	Density ρ_i (g/cm^3)	Thermal Expansion Coefficient (TEC) (x10^{-6}/K, 20 - 400 ºC)	Refractive Index (R.I.) n_i	
SiO_2	26.1 - 27.25	0.5 - 3.8	1.4585 - 1.475	6.161
Al_2O_3	40.4	-3.0	1.520	34.585
K_2O	34.1 (33.5)	46.5 (42.0)	1.575 (1.595)	783.92
CaO	14.4	13.0	1.730	885.046
TiO_2	20.5	-1.5 - 3.0	2.080 - 2.230	-79.806
Na_2O	20.2	39.5	1.590	670.233
Li_2O	11.0	27.0	1.695	
MgO	12.5	6.0	1.610	1125.698

For some Appen Factors , the following remarks apply:

SiO_2: when $67 \leq p_{SiO_2} \leq 100$,

$\alpha_{SiO_2} = 10.5 - 0.1 \cdot p_{SiO_2}$, $\rho_{SiO_2} = 23.75 + 0.035 \cdot p_{SiO_2}$ and $n_{SiO_2} = 1.5085 - 0.0005 \cdot n_{SiO_2}$,

when $p_{SiO_2} \leq 67$, $\rho_{SiO_2} = 26.1$, $\alpha_{SiO_2} = 3.8$, and $n_{SiO_2} = 1.475$.

K_2O: the values in parentheses only apply to glass with composition of $p_{Na_2O} < 1\%$,

TiO_2: when $50 \leq p_{SiO_2} \leq 80$, $\alpha_{TiO_2} = 10.5 - 0.15 \cdot p_{SiO_2}$ and $\alpha_{TiO_2} = 2.480 - 0.005 \cdot p_{SiO_2}$.

The weight percentage of oxides p_i is expressed in mole percentage (Scholze and Lakin, 1991).

Table 9.2: Glass reagents.

Reagent	Description	Manufacturer	Lot No
Kasil @ SS Pwd	Potassium silicate (SiO_2/K_2O = 2.50)	The PQ corporation, USA	11-904w -112804
SS 20 @ Pwd	Sodium silicate (SiO_2/Na_2O = 3.22)		11-139w -110305
Aluminium oxide	purum	Fluka, Germany	06285
Calcium carbonate	Purum. p.a. >= 99.0%	Fluka, Italy	21060
Lithium carbonate	Purum. p.a. >= 98.0%	Fluka, USA	62372
Titanium (IV) oxide		Aldrich, USA	232033 (07119ED)
Magnesium oxide		Sigma-Aldrich UAS	220361 (08907BD)
Silica sand		Glassworks service Ltd, UK	

Table 9.3: Values of the n and m for various crystallisation mechanisms.

Mechanisms	n	m
Surface nucleation	1	1
Bulk nucleation		
Three dimensional growth	4	3
Two dimensional growth	3	2
One dimensional growth	2	1

Fig. 9.1: Occlusal view of a glass-ceramic crown heat extruded using the glass-ceramic A (4hr A) and finished using stain/glaze techniques, showing high translucency.

Fig. 9.2: A side view of a glass-ceramic crown heat extruded using glass-ceramic A (4hr A) and finished using stain/glaze techniques.

10 PUBLISHED PATENT

US 20090081104A1

(19) **United States**

(12) **Patent Application Publication**

Ibsen et al.

(10) **Pub. No.: US 2009/0081104 A1**

(43) **Pub. Date: Mar. 26, 2009**

(54) **CONTROL OF CERAMIC MICROSTRUCTURE**

(75) Inventors: **Robert Ibsen**, Santa Maria, CA (US); **Xiaohui Chen**, Santa Maria, CA (US); **Michael J. Cattell**, Santa Maria, CA (US); **Jacques V. Riodel**, Santa Maria, CA (US); **Thomas C. Chadwick**, Nipomo, CA (US)

Correspondence Address:
CROWELL & MORING LLP
INTELLECTUAL PROPERTY GROUP
P.O. BOX 14300
WASHINGTON, DC 20044-4300 (US)

(73) Assignee: **Den-Mat Holdings LLC**, Santa Maria, CA (US)

(21) Appl. No.: **11/902,496**

(22) Filed: **Sep. 21, 2007**

Publication Classification

(51) **Int. Cl.**
C01B 33/26 (2006.01)

(52) **U.S. Cl.** **423/328.2**

(57) **ABSTRACT**

The present invention provides for the production of a single frit, dental porcelain, glass-ceramic containing small, uniformly dispersed, single leucite crystals of ellipsoidal habit and very uniform size.

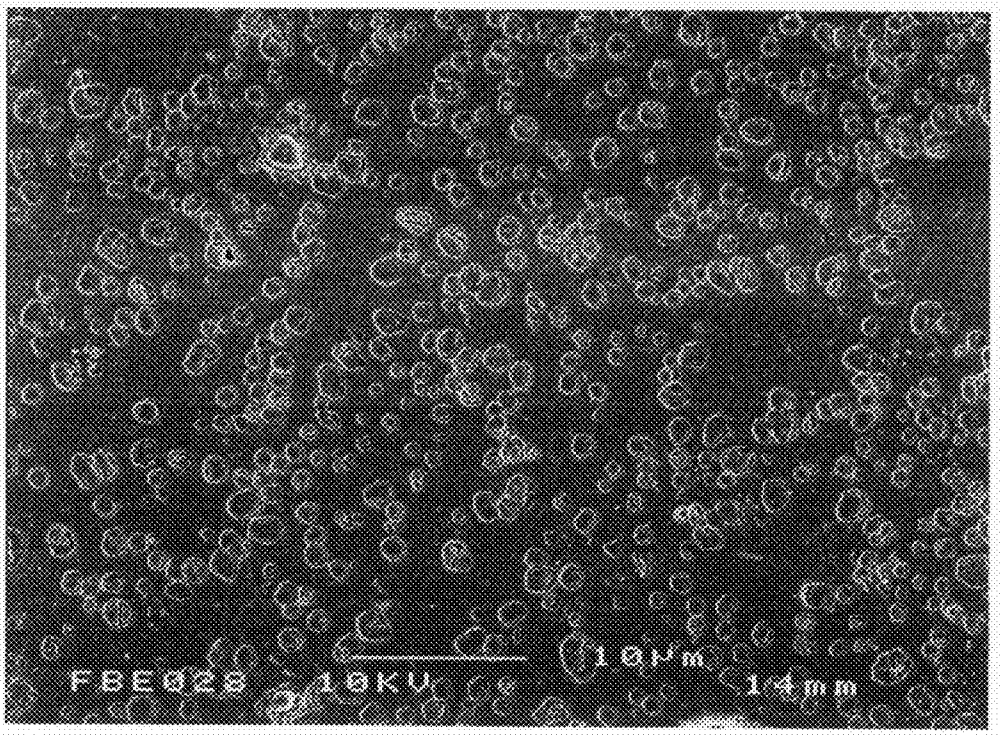

Figure 1-Leucite glass-ceramic produced according to Example 1 (feedstock for milling) and heat treated from 23 °C to 650/1 hour to 1120/1 hour holds.

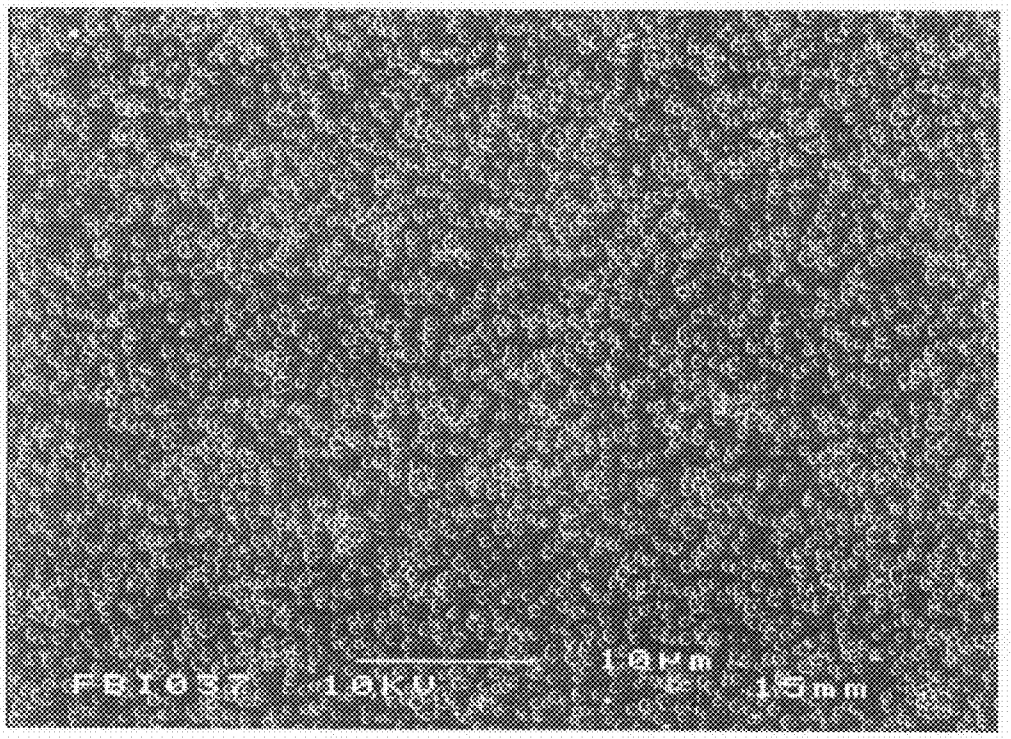

Figure 2-Leucite glass-ceramic produced according to Example 7 (480 mins milling time) and heat treated from 23 °C to 650/1 hour to 1120/1 hour holds.

CONTROL OF CERAMIC MICROSTRUCTURE

FIELD OF THE INVENTION

[0001] The present invention relates generally to dental ceramics. In particular, the invention relates to a low wear, dental glass-ceramic that contains very uniform, ellipsoidal reinforcing leucite crystals and a process for making it

BACKGROUND OF THE INVENTION

[0002] The use of porcelain facings or veneers (also called porcelain laminates) to cover unsightly teeth and thereby improve their appearance was pioneered by Dr. Charles Pincus in 1928. Dr. Pincus fabricated his porcelain veneers by firing packed dental porcelain powder on platinum foil.

[0003] Because of the limited range of adhesives available at the time, veneers were cemented in place only temporarily. Because of their expense and the limitations imposed by the available adhesives, porcelain veneers were used primarily by movie stars during performances before the camera (for a detailed account of the early history of porcelain veneers see: J. Cosmetic Dentistry, 1 (3), 6-8 (1985)).

[0004] During the 1970's great improvements were made in the area of dental adhesives, and the use of porcelain veneers became popular among the general public. Because of the limitations in the strengths of existing porcelain, the technique of building a metal substructure and firing porcelain to the outside was also developed. Although this technique was successful and useful, it had its limitations. Paramount among the difficulties associated with porcelain-metal restorations was the need to match the coefficient of thermal expansion of the porcelain and the underlying metal and the need to opacify heavily the porcelain, so that the metal substructure would remain well hidden. The use of porcelain-fused-to-metal construction also made it possible to fabricate more complicated structures, such as porcelain jacket crowns and bridges, but the previously mentioned problems and the difficulty of bonding metal reliably to tooth structure made all-porcelain restorations a desirable goal.

[0005] In order to avoid the need for a metal substructure, much effort has been directed to strengthening dental porcelain. Attempts to strengthen dental porcelain have usually involved the inclusion of strengthening oxide particles in the base porcelain. Examples of strengthening oxides include zirconium oxide and aluminum oxide. The inclusion of strengthening oxides opacifies the porcelain and makes simultaneous control of opacity and strength impossible.

[0006] An ideal porcelain for the fabrication of all-porcelain veneers, crowns and bridges should possess high strength. Ideally, it should possess the strength of the metal-oxide-reinforced porcelains. It should be available in a range of opacities which ideally could run from very opaque to clear. The coefficient of thermal expansion of the porcelain should match the coefficients of thermal expansion of the bonding agents and underlying teeth. It should be available in a variety of shades, and the colorants should be incorporated in, rather than painted on, the porcelain.

[0007] Finally, the porcelain should be easy to fabricate by either the platinum foil or refractory model fabrication techniques. It should not show a pronounced tendency to separate during the initial firing, and any separation cracks that do form should heal easily rather than separate further. The maturing temperature should be below 1093° C. (2000° F.) to avoid any unnecessarily severe service for the vacuum furnaces. As a final point, the coefficient of thermal expansion should be less than 15×10^{-6} C.$^{-1}$ in order to avoid difficulty in matching refractory expansion to that of the porcelain.

[0008] Glass-ceramics containing leucite are known. A number of patents discuss the importance of controlling either the volume fraction of leucite in leucite-containing glass-ceramics or the size distribution of the leucite crystallites. Some patents discuss the need to control both, but none of them discuss methods for control of crystal size. EP00155564 and U.S. Pat. No. 4,604,366 discuss the importance of controlling the amount of leucite to control the thermal expansion of these materials, but they do not discuss desirable sizes of leucite crystals nor do they discuss control of crystal size. EP0272745, U.S. Pat. No. 4,798,536; U.S. Pat. No. 6,428,614; U.S. Pat. No. 6,761,760; and US patent applications US20030122270 and US20040121894 each mention that the leucite crystallites should be less than 35 microns and in some cases preferably less than 5 microns but they do not describe how these crystallite sizes are achieved. U.S. Pat. No. 6,527,846 describes rod-like leucite crystals 0.3-1.5 microns wide and 7-20 microns in length but provides no indication of how to control the size of these rods. U.S. Pat. No. 5,653,791; U.S. Pat. No. 5,944,884; and U.S. Pat. No. 6,660,073 all discuss leucite glass-ceramics containing leucite crystals less than 10 microns in size but do not indicate the method of size control. Patents JP23048770, U.S. Pat. No. 6,706,654 and US patent application US20020198093 all describe a leucite glass-ceramic and lithium disilicate glass-ceramic blend in which the leucite is created from added leucite seed crystals. The role of leucite seed crystal size in determining the strength of the ceramic is discussed but there is no mention of the influence of glass particle size on ceramic properties. With the exception of U.S. Pat. No. 6,527,846, none of these patents discusses leucite crystal morphology.

[0009] U.S. Pat. No. 5,009,709, assigned to Den-Mat Corporation, describes a dental porcelain that was useful for application in refractory techniques, however, this patent does not discuss leucite or any method for controlling leucite crystal size. The present invention describes how to control leucite crystal size in a glass of that composition by controlling various processing variables. World patent application WO 00/48956 (abandoned) described a porcelain composition similar to that described in U.S. Pat. No. 5,009,709 that was useful for preparing dental restorations by the lost wax pressing technique. Again, this application did not describe any means for controlling the size of the leucite crystals in the finished glass-ceramic.

SUMMARY OF THE INVENTION

[0010] The present invention provides for the production of a single frit, dental porcelain, glass-ceramic containing small, uniformly dispersed, single leucite crystals of ellipsoidal habit and very uniform particle size. The powdered glass-ceramic can be used with the platinum foil or refractory investment technique to produce dental restorations or it can be pressed and sintered into blocks or ingots and used in a variation of the lost wax casting technique or CAD/CAM techniques to produce restorations.

[0011] One embodiment of the invention encompasses a method of making a leucite containing glass-ceramic comprising preparing a leucite-free glass, grinding the glass to the

desired particle size in order to control the size of the leucite crystal in the finished ceramic, and refiring to produce the glass-ceramic.

[0012] Another embodiment of the instant invention encompasses a method of controlling the particle size distribution of leucite in a glass-ceramic composition comprising blending glass-ceramic precursors until the precursors are well mixed, firing the glass-ceramic precursor mixture at a temperature above the liquidus for leucite, holding the mixture at a the temperature above the liquidus for leucite for 2-10 hours, allowing the mixture to cool to room temperature thereby forming a leucite-free glass frit, grinding the leucite-free glass frit to a desired particle size in order to control the particle size of the leucite in the finished glass-ceramic, firing the ground leucite-free glass frit to a temperature below the liquidus for leucite, and cooling until a leucite containing glass-ceramic is formed.

[0013] A further embodiment of the instant invention encompasses a single frit, dental porcelain, glass-ceramic containing small, uniformly dispersed, single leucite crystals of ellipsoidal habit and very uniform size.

BRIEF DESCRIPTION OF THE FIGURES

[0014] FIG. **1** shows a leucite glass-ceramic produced by a method in accordance with the instant invention.

[0015] FIG. **2** shows a leucite glass-ceramic produced by a method in accordance with the instant invention.

DETAILED DESCRIPTION OF THE INVENTION

[0016] For simplicity and illustrative purposes, the principles of the present invention are described by referring to various exemplary embodiments thereof. Although the preferred embodiments of the invention are particularly disclosed herein, one of ordinary skill in the art will readily recognize that the same principles are equally applicable to, and can be implemented in other systems, and that any such variation would be within such modifications that do not part from the scope of the present invention. Before explaining the disclosed embodiments of the present invention in detail, it is to be understood that the invention is not limited in its application to the details of any particular arrangement shown, since the invention is capable of other embodiments. The terminology used herein is for the purpose of description and not of limitation. Further, although certain methods are described with reference to certain steps that are presented herein in certain order, in many instances, these steps may be performed in any order as would be appreciated by one skilled in the art, and the methods are not limited to the particular arrangement of steps disclosed herein.

[0017] The present invention provides for the production of a single frit, dental porcelain, glass-ceramic containing small, uniformly dispersed, single leucite crystals of ellipsoidal habit and very uniform particle size. The powdered glass-ceramic can be used with the platinum foil or refractory investment technique to produce dental restorations or it can be pressed and sintered into blocks or ingots and used in a variation of the lost wax casting technique or CAD/CAM techniques to produce restorations.

[0018] Such a glass-ceramic is expected to cause only very low wear rates on opposing teeth without sacrificing strength, thermal or optical properties. Furthermore the average particle size of leucite crystals and the abrasivity of the leucite glass-ceramic can be controlled over a wide range of size by controlling the particle size of the leucite-free glass that is the precursor to the glass-ceramic. The process of the present invention avoids the need to make and then rapidly quench glass precursors that other processes use and it avoids the need a separate glass powder heat treatment step employed by other methods such as those described by Brodkin in U.S. Pat. Nos. 6,090,194; 6,120,591; 6,133,174; and 6,155,830.

[0019] It has been discovered that a single-frit, leucite-containing, glass-ceramic containing leucite crystals of uniform and selectable size can be produced via a two-step fritting process. In the first step suitable components for the production of a glass of the correct chemical composition are mixed and fired to produce the glass. Although potassium feldspar is the major ingredient for the usual method of production, other raw materials can be used for the preparation of the glass. Other minerals, pure chemicals or sol-gel precursors would all function perfectly well for the production of the leucite-free glass with the only requirement being that the raw materials have the correct overall chemical composition to produce the glass. After the glass precursors have been fired to produce the glass in the first firing, the glass is then ground and refired to produce the glass-ceramic. The glass powder can be shaped by compressing the powder in a die and firing directly to produce a dental glass-ceramic ingot for fabricating dental restorations by hot pressing or CAD/CAM. Alternatively the glass powder can be fired in bulk to produce chunks of dental glass-ceramic that can be crushed and ground to a powder and used in the stackable porcelain technique with either platinum foil or refractory investment models to produce porcelain restorations such as veneers, inlays, onlays and crowns or the powder can be pressed in a die and sintered to produce porcelain ingots that can be used to fabricate dental restorations by either the hot pressing or CAD/CAM techniques.

[0020] The production of single frit glass-ceramics containing uniformly dispersed single leucite crystals of reproducible, selectable and controllable size relies on several discoveries. First, it has been discovered that the control of leucite particle size in the finished glass-ceramic relies on the production of glass in the first firing stage that is leucite-free or nearly so. For our purposes here the term leucite-free means that there is no detectable leucite when powdered glass from the first firing is examined by powder x-ray diffraction. The detection limit by this technique for leucite in a glass matrix is less than 1% (w/w). The control of the particle size distribution also relies on the discovery that there is a direct relationship between the particle size distribution of the powdered glass that is made from the glass produced in the first firing and the particle size distribution of leucite crystals in the finished glass-ceramic. Thus it is possible to produce small leucite crystals in the finished glass-ceramic if the glass from the first firing is ground to a fine particle size (see FIG. **2**) and it is possible to produce larger leucite crystals if coarser glass powder is produced and used to make the glass-ceramic (see FIG. **1**). The rapid production of small uniform leucite crystals also relies on the discovery that crystal nucleation and growth are quite rapid and can be done within the context of a firing that does not require a hold time at the nucleation temperature (600-700° C.). Although it is possible to exert additional control by halting at the nucleation temperature range it is not necessary to do so. This feature facilitates the rapidity and throughput of the process without compromising the ability to produce leucite crystals in a specific size range.

The invention provides

[0021] 1) a glass-ceramic with reinforcing crystals of leucite where the leucite crystal size can be easily controlled

[0022] 2) a glass-ceramic that exhibits high flexural strength

[0023] 3) a glass-ceramic, which contains small, uniform, ellipsoidal reinforcing leucite crystals, and which has low abrasivity toward the natural enamel of opposing teeth

[0024] 4) a simple method of glass-ceramic production consisting of the steps of producing a leucite-free glass followed by grinding the glass to the desired degree of fineness (selected to control the particle size of the leucite in the finished ceramic) and refiring to produce the glass-ceramic.

[0025] 5) a method of glass-ceramic production in which it is unnecessary to heat the glass batch to a temperature sufficiently high to allow the glass to be poured into water.

[0026] 6) A glass-ceramic that, by virtue of uniformly sized, ellipsoidal crystals, low crystal loading and low viscosity residual glass has a very broad temperature range (1000-1100° C.) over which it can be processed by hot pressing.

[0027] 7) a low wear glass-ceramic which, when processed by the CAD/CAM technique, promotes machine tool longevity.

[0028] One embodiment of the invention begins with selecting suitable starting materials to make the leucite-free glass. The most convenient starting material, and the ingredient that contributes the majority of material to the glass, is high potassium feldspar. Feldspar with a chemical composition consisting of silica, 64-68%, alumina, 17-19%, calcium oxide, 0.1-1.0%, potassium oxide, 9-11%, and sodium oxide, 2-4% is satisfactory. The commercial material, G-200 Feldspar, presently produced by The Feldspar Corporation, a subsidiary of ZEMEX Industrial Minerals, Inc., supplied with a mean particle size of approximately 12 microns is quite useful. The second ingredient is a glass consisting of silica, 54-58%, alumina 5-9%, sodium oxide, 4-8%, potassium oxide, 18-22%, magnesium oxide, <4%, and calcium oxide, <4%. The third ingredient is another glass containing silica, 42-48%, alumina 0-2%, sodium oxide 18-22%, calcium oxide, <4%. The fourth ingredient is lithium carbonate. The particle size of the two glasses and the lithium carbonate should be similar to that of the feldspar.

[0029] The preparation of the leucite-free glass is accomplished by the usual methods of ceramic fabrication. The ingredients are weighed and then placed in a powder blender such as a twin cone or V cone blender and the ingredients are mixed to produce a uniform, homogenous powder. After the powders are a homogenous blend they are packed in refractory containers and fired to a temperature of at least 1300° C. and preferably 1350° C. and held at that temperature until a uniform, leucite-free melt is produced. This usually requires between 2 and 10 hours to accomplish. After the ingredients are thoroughly fused, the contents of the furnace are allowed to cool. The firing produces blocks of glass that are cleaned by sandblasting. After cleaning, the blocks are then crushed in a jaw crusher, screened to remove impurities from the crushing operation and then ground in a ball mill to produce glass powder with a mean particle size of approximately 25 microns.

[0030] The desired mean size of leucite crystals in the finished glass-ceramic can be selected using two equations.

[0031] For glass powder with a mean diameter above 3.5 microns the relationship between mean glass powder diameter and leucite crystal mean equivalent spherical diameter is described by:

mean leucite crystal diam, microns=0.0117×mean glass powder diameter, microns+0.8931

[0032] For glass powder with a mean diameter at or below 3.5 microns the relationship between mean glass powder diameter and leucite crystal mean equivalent spherical diameter is described by:

mean leucite crystal diam, microns=0.1463×mean glass powder diameter, microns+0.3792

[0033] The mean particle size of leucite-free glass feedstock is determined and the glass powder is wet ground to correct size in a Union Process attritor mill or other similar mill capable of reducing particle size into the 10 micron to 0.5 micron range. After the desired particle size is reached, the slurry of water and glass powder is discharged from the mill, the water is removed, the glass powder is dried by suitable means and the powder is then screened through a 325 mesh US series screen to remove agglomerates.

[0034] At this point, two alternatives can be used to produce the finished glass-ceramic. In the first alternative, the ground, powdered glass-ceramic precursor is mixed with opacifiers such as titanium oxide, zirconium oxide, zirconium silicate or tin oxide and single or multiple ceramic pigments that are necessary to give the glass-ceramic its proper final shade and opacity and the blended powders can then be pressed in a die to produce a powder compact. The powder compact can then be rapidly fired to 1120° C. to directly produce finished ingots that are suitable for use in hot pressing or CAD/CAM processes for the production of dental restorations.

[0035] Alternatively, the ground glass powders can be blended with opacifiers such as titanium oxide, zirconium oxide, zirconium silicate or tin oxide as well as individual ceramic pigments, packed in large refractory containers and the powder can be refired to 1120° C. The refractory containers are then removed from the furnace while hot and cooled rapidly in air. The resulting chunks of opacified, colored leucite glass-ceramic are then crushed and milled to produce a variety of glass-ceramic powders of different basic colors. These powders can then be blended to produce glass-ceramic powders of the correct final shade and opacity. These blended powders can be used directly to produce dental restorations by the stackable technique or the powder can be die pressed and sintered rapidly enough to preclude changes to the microstructure of the glass-ceramic so that ingots suitable for making dental restorations by the pressable technique or CAD/CAM technique can be produced. This latter process simplifies the problem of producing proper porcelain shades while the former process requires fewer steps to produce pressable, machineable ingots.

[0036] Note that the second firings associated with either process alternative can be modified to include a 0.50 to 4.0 hour hold at temperatures ranging from 600° C. to 700° C. These holds do allow some additional control over the nucleation process but they are not indispensable for satisfactory results.

[0037] The method of the present invention employs a two step process for the manufacture of a leucite containing glass-ceramic wherein the particle size distribution of leucite crystals in the product glass-ceramic is controlled to very narrow distributions over a wide range of average particle sizes. In the

first step porcelain glass-ceramic precursors selected from naturally occurring feldspar, glasses of appropriate composition or metal oxides, carbonates, nitrates in any combination that will provide the correct elemental composition for the glass-ceramic are blended, if the components are already finely divided, or ground and blended if they are not, until the precursor mixture is homogenous and well mixed. The precursor mixture is then placed in a container of cordierite, mullite, silica or other suitable refractory and fired to a temperature above the liquidus for leucite, which in the compositional system of the present invention is approximately 1300° C. The mixture is held at this temperature for 2-10 hours, the holding period providing an opportunity to allow dissolution of the starting materials as well as any leucite that has crystallized during the heating process. After the holding period the mixture is allowed to cool slowly to room temperature. The leucite-free glass frit is obtained as solid, unfractured blocks, which are cleaned, crushed and reground to carefully controlled particle sizes that are selected to provide the desired leucite particle size in the final glass-ceramic. After grinding, the powders are dried (if a wet grinding process is employed), blended with pigments and opacifiers such as titanium dioxide, tin oxide, zirconium oxide, zirconium silicate or other equivalent materials and pressed into powder compacts. These powder compacts can then be fired from room temperature to 1120° C. at heating rates up to 10° C./min. A hold time of 0.50 to 4.0 hours in the temperature range including 600° C. to 700° C. may be optionally included so that additional control may be exerted over the nucleation of leucite crystals. When the upper temperature has been reached, the sintered compacts are removed from the furnace and allowed to air cool.

[0038] Alternatively, the blended powders may be processed in bulk. The powders can be placed in cordierite saggers that have been coated with a 3 mm layer of 50 micron tabular alumina powder. The cordierite saggers are fired to 1100° C. at average rates of 2.0-3.5° C./min and held at the high temperature for 45 minutes. After the holding period the containers holding the glass-ceramic are withdrawn immediately from the furnace and allowed to cool in air. When the glass-ceramic has cooled it is removed as chunks from the container, the chunks are cleaned and then crushed, ground and sieved. Different colored powdered glass-ceramics may be produced by this method and the different shades of powder can then be blended to produce the shades required for dental restoration manufacture. The blending of basic shades makes the process of shade matching much simpler than if the powders are produced to a specific shade by adding concentrated pigments directly to the ceramic.

EXAMPLE 1

Preparation of the Leucite-Free Glass

[0039] All raw ingredients were obtained and used as powders (−325 mesh, US Series screen) A batch (~27 Kg) of frit was prepared by blending 22.226 Kg powdered potassium feldspar (composition of SiO_2, 66.3%, Al_2O_3, 18.50%, Na_2O, 3.04%, K_2O, 10.75%, CaO, 0.81% and MgO, 0.05%) with 3.922 Kg of a first glass powder (SiO_2, 55.4%, Al_2O_3, 7.19%, Na_2O, 6.68%, K_2O, 20.2%, MgO, 1.92%, CaO, 8.32%, SrO, 0.05%, BaO, 0.22% and TiO_2, 0.02%), 0.534 Kg of a second glass powder (SiO_2, 46.6%, Al_2O_3, 0.615%, B_2O_3, 6.09%, MgO, 0.052%, CaO, 4.83%, SrO, 2.57%, BaO, 10.5%, Na_2O, 17.0%, K_2O, 0.22%, TiO_2, 9.46%, F, 3.65%) and 0.334 Kg of powdered lithium carbonate. After the raw materials were thoroughly blended the powder mixture was packed into square cordierite saggers (25 cm width and length and 8.5 cm deep)) that had previously been coated with a 3 mm layer of tabular alumina (50 micron average particle size). The saggers were then stacked into an electric furnace, fired rapidly to 1316° C. and held at that temperature for 7 hours. Power was shut off to the furnace after the hold period and the furnace was allowed to cool to room temperature over 2 days. After cooling, the glass was removed from the saggers as intact blocks, the blocks were cleaned of aluminum oxide by sandblasting and the blocks were then crushed to 1-5 cm chips. These chips were then ball milled to produce a powdered glass with an average particle size of 11.4 microns. The powdered frit was examined by Dr. Sampeth Iyengar, Technology of Materials, Wildomar, Calif. (XRD analysis by the Rietveld technique) and Dr. Michael Cattell (XRD), Barts and the London Queen Mary's School of Dentistry, London, England and both confirmed that there was no detectable leucite (i.e. leucite content was <1%) in the ground glass. The yield of ground frit was 22 Kg.

EXAMPLES 2, 3, 4, 5 And 6

Preparation of Frit Specimens Ground to Different Particle Sizes

[0040] The frit of example 1 was used as the feedstock for the preparation of more finely ground glass powder. Grinding was carried out in a Union Process Attritor Mill (Union Process, 1925 Akron-Peninsula Road, Akron, Ohio 44313), Model 1-S. The mill was equipped with a 1 gallon water-jacketed grinding chamber, was driven by a 2 horsepower electric motor equipped with a variable speed drive and the grinding chamber was charged with 12.21 Kg of 5 mm spherical yttria stabilized zirconia grinding media. The particle size distributions of all ground ceramic powders were characterized with a Mastersizer/E particle analyzer (Malvern Instruments, UK).

EXAMPLE 2

[0041] The grinding chamber of the 1-S attritor was charged with 2.000 Kg of the glass frit of Example 1 and 2550 mL of distilled water. The mill agitator was run at 600 rpm for 30 minutes and the frit slurry was discharged to four Pyrex dishes and dried at 122 oC for 48 hours to yield 1.902 Kg of glass powder with a mean particle size of 4.73 microns.

EXAMPLE 3

[0042] Following Example 1, the grinding chamber was charged with 2.000 Kg of the glass frit of Example 1 and 2550 mL of distilled water. Milling was continued for 45 minutes and the slurry was processed in a fashion similar to Example 2 to yield 1.935 Kg of ground glass powder with a mean particle size of 3.54 microns.

EXAMPLE 4

[0043] The grinding chamber of the 1-S attritor was charged with 2.000 Kg of the glass frit of Example 1 and 2550 mL of distilled water. Milling was continued for 60 minutes

and the slurry was processed to give 1.878 Kg of ground glass powder with a mean particle size of 3.02 microns.

EXAMPLE 5

[0044] The grinding chamber of the 1-S attritor was charged with 2.000 Kg of the glass frit of Example 1 and 2550 mL of distilled water. Milling was continued for 90 minutes and the slurry was processed to give 1.876 Kg of ground glass powder with a mean particle size of 3.02 microns.

EXAMPLE 6

[0045] The grinding chamber of the 1-S attritor was charged with 2.000 Kg of the glass frit of Example 1 and 2550 mL of distilled water. Milling was continued for 120 minutes and the slurry was processed to give 1.662 Kg of ground glass powder with a mean particle size of. 2.76 microns.

EXAMPLE 7

[0046] A Union Process DMQ-07 small media mill equipped with a magnesia stabilized zirconia grinding chamber, yttria-stabilized zirconia impeller discs and 1589 g (0.429 L) of 0.65 mm yttria-stabilized zirconia grinding media was charged with 1.520 Kg of glass frit (11.4 microns average particle size) and 1.520 Kg of distilled water. The mill was run at 3700 rpm for 480 minutes. The mill contents were discharged at the end of the grinding period and the water was evaporated to yield glass frit with a mean particle size of 0.43 microns.

General Procedure for Crystallization of Leucite

[0047] Powder compacts of the milled powders were prepared by pressing the powders in a die at 3 bar for one minute. The powder compacts were then fired to 1120° C. at a rate of 10° C./min. The firing was interrupted by a one-hour hold at 650° C. When the high temperature was reached the sintered glass-ceramic compacts were removed from the furnace and allowed to cool. The leucite crystal size distributions in the glass-ceramic derived from the powders of Examples 1-7 were determined by analysis of scanning electron microscope images taken of each sample. The powder size and leucite crystal size are summarized in the table presented below. For photomicrographs of glass-ceramics prepared from the coarsest and finest glass powders see FIG. **1** and FIG. **2**, respectively.

Milling Time, minutes	Mean Glass Powder Size, Mean Equivalent Spherical Diameter, microns	Leucite Crystal Size, Mean Equivalent Spherical Diameter, microns
0	11.37	1.02
30	4.73	0.959
45	3.54	0.945
60	3.02	0.910
90	3.02	0.821
120	2.76	0.777
240	1.84	0.659
480	0.43	0.438

[0048] Powdered glass-ceramics as well as blends of different colored glass-ceramics, prepared as described above, may be used to fabricate dental restorations by the stackable refractory or platinum foil techniques or the blended powder can be compressed in a die and the resulting powder compacts can be sintered to produce ingots for use in dental restoration fabrication by hot pressing or CAD/CAM machining.

[0049] While the invention has been described with reference to certain exemplary embodiments thereof, those skilled in the art may make various modifications to the described embodiments of the invention without departing from the scope of the invention. The terms and descriptions used herein are set forth by way of illustration only and not meant as limitations. In particular, although the present invention has been described by way of examples, a variety of devices would practice the inventive concepts described herein. Although the invention has been described and disclosed in various terms and certain embodiments, the scope of the invention is not intended to be, nor should it be deemed to be, limited thereby and such other modifications or embodiments as may be suggested by the teachings herein are particularly reserved, especially as they fall within the breadth and scope of the claims here appended. Those skilled in the art will recognize that these and other variations are possible within the scope of the invention as defined in the following claims and their equivalents.

What is claimed is:

1. A method of making a leucite containing glass-ceramic comprising:

preparing a leucite-free glass;

grinding the glass to the desired particle size in order to control the size of the leucite crystal in the finished ceramic; and

refiring to produce the glass-ceramic.

2. The method of claim **1**, wherein the desired particle size is less than 15 microns.

3. The method of claim **1**, wherein the desired particle size is less than 5 microns.

4. The method of claim **1**, wherein the desired particle size is less than 4 microns.

5. The method of claim **1**, wherein the desired particle size is less than 3 microns.

6. A method of controlling the particle size distribution of leucite in a glass-ceramic composition comprising:

blending glass-ceramic precursors until the precursors are well mixed;

firing the glass-ceramic precursor mixture at a temperature above the liquidus for leucite;

holding the mixture at a the temperature above the liquidus for leucite for 2-10 hours;

allowing the mixture to cool to room temperature thereby forming a leucite-free glass frit;

grinding the leucite-free glass frit to a desired particle size in order to control the particle size of the leucite in the finished glass-ceramic;

firing the ground leucite-free glass frit to a temperature below the liquidus for leucite;

cooling until a leucite containing glass-ceramic is formed.

7. The method of claim **6**, wherein the precursor mixture is fired to a temperature of approximately 1300° C.

8. The method of claim **6**, wherein the ground leucite-free glass frit is fired to a temperature of approximately 1120° C.

9. The method of claim **8**, further comprising the step of holding the temperature of the ground leucite-free glass frit at 600 to 700° C. for 0.1 to 4.0 hours during the firing process.

10. The method of claim **6**, wherein the desired particle size is less than 15 microns.

11. The method of claim **6**, wherein the desired particle size is less than 5 microns.

12. The method of claim **6**, wherein the desired particle size is less than 4 microns.

13. The method of claim **6**, wherein the desired particle size is less than 3 microns.

14. The method of claim **6**, wherein the glass-glass ceramic precursors are selected from a group comprising feldspar, glass, metal oxides, carbonates, and nitrates.

15. The method of claim **6**, further comprising the step of adding pigments and opacifiers to the

16. A glass-ceramic containing leucite crystals of ellipsoidal habit and very uniform size.

17. The glass-ceramic of claim **16**, wherein the leucite crystals are less than one micron in size.

18. The glass-ceramic of claim **16**, wherein the leucite crystals are less than one half of one micron in size.

19. A method of making a leucite containing glass-ceramic comprising:

preparing a glass having less than 1% leucite;

grinding the glass to the desired particle size in order to control the size of the leucite crystal in the finished ceramic; and

refiring to produce the glass-ceramic.

* * * * *